Comparative study on the performance of photovoltaic modules and their sensitivity to external parameters based on an experimental analysis

Caio Felippe Abe

UNIVERSITE DE CORSE PASCAL PAOLI

ECOLE DOCTORALE ENVIRONNEMENT ET SOCIETE UMR CNRS 6134 (SPE)

UNIVERSIDADE DO VALE DO RIO DOS SINOS UNISINOS

Thèse en cotutelle présentée pour l'obtention du grade de

DOCTEUR de l'Université de Corse en MECANIQUE DES FLUIDES, ENERGETIQUE, THERMIQUE, COMBUSTION, ACOUSTIQUE
Mention : Energétique, Génie des Procédés

Thesis in co-supervision presented for the degree of

DOUTOR EM ENGENHARIA MECÂNICA

Soutenue publiquement par / publicly defended by

Caio Felippe ABE

Le 05 Mars 2024 – March, 05th, 2024

Etude comparative des performances de modules photovoltaïques et de leur sensibilité aux paramètres extérieurs basée sur une analyse expérimentale

Comparative study on the performance of photovoltaic modules and their sensitivity to external parameters based on an experimental analysis

Directeurs/Directors :
M Gilles NOTTON, Professor, Université de Corse
M Paulo Roberto WANDER, Professor, UNISINOS University

Rapporteurs/Reviewers :
M Michel AILLERIE, Professor, LMOPS, Université de Lorraine, Metz, France
M Giuliano RAMPINELLI, Professor, Federal University of Santa Catarina

Jury :
M Ghjuvan Antone FAGGIANELLI, Dr, Université de Corse
M Wilson Negrão MACÊDO, Professor, Federal University of Pará
M Gilles NOTTON, Professor, Université de Corse
M Giuliano Arns RAMPINELLI, Professor, Federal University of Santa Catarina
M Christian SCHAEFFER, Professor, Grenoble INP, Université Grenoble Alpes
Mme Flavia Schwarz Franceschini ZINANI, Professor, UNISINOS, São Leopoldo

Invité/Invited :
M João Batista DIAS, Professor, Atelier Solaire
M Michel AILLERIE, Professor, LMOPS, Université de Lorraine, Metz, France
M Paulo Roberto WANDER, Professor, UNISINOS University

COMPARATIVE STUDY ON THE PERFORMANCE OF PHOTOVOLTAIC MODULES AND THEIR SENSITIVITY TO EXTERNAL PARAMETERS BASED ON AN EXPERIMENTAL ANALYSIS

Caio Felippe Abe
Doctoral Candidate – Mechanical Engineering

This work has been submitted to the Postgraduate Program in Mechanical Engineering at UNISINOS (Brazil) and University of Corsica Pasquale Paoli (France) as a partial prerequisite for obtaining the title of Doutor em Engenharia Mecânica.

Thesis supervisor (Unisinos – Brazil): Prof. Dr. Paulo Roberto Wander
Thesis supervisor (University of Corsica – France): PRU. HDR. Dr. Gilles Notton

Jury:
Prof. Dr. Christian Schaeffer, Grenoble Inp, Université Grenoble Alpes
Profª. Drª. Flavia Schwarz Franceschini Zinani, Unisinos, São Leopoldo
Prof. Dr. Ghjuvan Antone Faggianelli, Université de Corse
Prof. Dr. Gilles Notton, Université de Corse
Prof. Dr. Giuliano Arns Rampinelli, Federal University of Santa Catarina
Prof. Dr. Wilson Negrão Macêdo, Professor, Federal University of Pará

This Doctoral Thesis was financed in part by the Coordenação de Aperfeiçoamento de Pessoal de Nível Superior - Brasil (CAPES) - Finance Code 001.

ABSTRACT

In this thesis, four photovoltaic (PV) technologies were experimentally compared, aiming to quantify the impact of the external parameters on PV performance. Two of the technologies studied are quite common in the market: polycrystalline (p-Si) and monocrystalline (m-Si). The third technology, bifacial, allows the conversion of the solar radiation reaching the back face of the modules, providing a yield gain. Modules with multi-junction cells under concentration (HCPV) were also included in the analysis. They use a larger solar spectrum range and lenses to concentrate the beam radiation thanks to a 2-axis tracker constantly following the Sun.

The PV modules were tested and had their ratings experimentally determined using modeling approaches developed in this thesis. All modules were assembled on the PV tracker to provide the same operating conditions, and the measurement campaign was carried out for 12 months. The experimental records, at one-minute timestep, were checked for synchronicity, interpolated, and aggregated. Several filtering approaches were discussed and applied to provide an adequate balance between noise removal and data retention.

The PV arrays were then studied concerning their particularities, starting with the identification of the most influencing operating parameters, in order of relevance, and their impact on the output power. Then, the effect of the operating temperature was assessed, and the actual temperature coefficients for the DC power were determined. Finally, a sensitivity analysis targeting the DC power relative to the operating parameters was performed based on filters and mathematical models developed for each PV array. Special attention was given to the bifacial array since this technology is very promising due to its interesting cost-benefit relation; novel methods to determine the effective irradiance and the bifacial gain were also developed.

Two different methods were applied to characterize the PV modules. It was found that their actual performance is not as good as reported on the datasheets. The m-Si array was the least sensitive to the operating temperature, followed by the p-Si and bifacial modules. In turn, the HCPV devices were the most impaired by the temperature, air mass, and humidity. The wind speed influence was small for the HCPV modules; the arrays most benefited by the wind were the p-Si and m-Si. The bifacial array presented the greatest final yield (with a bifacial gain of 6.2 %), followed by m-Si and p-Si. In turn, the HCPV array presented the poorest yield, mainly due to their responsiveness only to the beam irradiance and the high temperature coefficient for the DC power.

Keywords: Photovoltaic technologies; Performance comparison; Experimental study; Sensitivity analysis

RÉSUMÉ

Dans cette thèse, quatre technologies photovoltaïques (PV) ont été comparées expérimentalement afin de quantifier l'impact des paramètres externes sur leurs performances. Deux des technologies étudiées sont courantes sur le marché : le polycristallin (p-Si) et le monocristallin (m-Si). La troisième technologie, bifaciale, convertit également le rayonnement solaire atteignant la face arrière des modules, apportant ainsi un gain de rendement. Enfin, des modules à cellules multi-jonctions sous concentration (HCPV), permettant d'utiliser un plus large spectre solaire, sont également étudiés ; ils utilisent des lentilles pour concentrer le rayonnement et ont besoin d'un tracker biaxial pour recevoir et convertir le rayonnement direct perpendiculaire au plan des modules.

Les modules PV ont été testés et leurs caractéristiques déterminées expérimentalement à l'aide d'approches de modélisation développées dans cette thèse. Tous les modules ont été assemblés sur le même tracker pour offrir les mêmes conditions de fonctionnement, et la campagne de mesures a duré 12 mois. Les enregistrements expérimentaux – mesurés à un pas de temps d'une minute – ont été vérifiés pour leur synchronicité, interpolés et agrégés. Plusieurs approches de filtrage ont été appliquées et discutées pour atteindre un équilibre adéquat entre suppression du bruit et conservation des données.

Les paramètres les plus influents, par ordre de pertinence, et leur impact sur la puissance des quatre générateurs PV ont été étudiés. L'effet de la température a été évalué et les coefficients de température réels ont été déterminés. Une analyse de sensibilité de la puissance par rapport aux paramètres de fonctionnement a été réalisée sur la base de filtres et de modèles mathématiques développés pour chaque générateur PV. Une attention particulière a été accordée aux modules bifaciaux car cette technologie est très prometteuse du fait de son bon rapport coût-bénéfice ; de nouvelles méthodes pour déterminer l'irradiance efficace et le gain bifacial ont été développées.

Deux méthodes ont été appliquées pour caractériser les modules PV. Il a été constaté que leurs performances réelles n'étaient pas aussi bonnes que celles indiquées sur les fiches techniques. La technologie m-Si était la moins sensible à la température, suivi des modules p-Si et bifaciaux. Les modules HCPV étaient les plus altérés par la température, la masse d'air et l'humidité. L'influence du vent est moins marquée pour les modules HCPV mais plus importante pour le p-Si et le m-Si. Les modules bifaciaux ont des performances plus élevées (gain bifacial de 6,2 %), suivi du m-Si et du p-Si. Le générateur HCPV présentait la production la plus faible, principalement en raison de l'utilisation de la seule composante directe du rayonnement et du coefficient de température élevé.

Mots clés : Technologies photovoltaïques ; Comparaison des performances ; Etude expérimentale ; Analyse de sensitivité.

RESUMO

Nesta tese, quatro tecnologias fotovoltaicas (FV) foram comparadas experimentalmente, visando quantificar o impacto dos parâmetros externos no desempenho FV. Duas das tecnologias estudadas são bastante comuns no mercado: policristalina (p-Si) e monocristalina (m-Si). A terceira tecnologia, bifacial, permite a conversão da radiação solar que atinge a face traseira dos módulos, proporcionando ganho de produtividade. Módulos com células multijunção sob concentração (HCPV) também foram incluídos na análise. Eles utilizam um espectro solar maior e as lentes concentram a radiação do feixe graças a um tracker de 2 eixos que segue constantemente o sol.

Os módulos fotovoltaicos foram testados e tiveram suas classificações determinadas experimentalmente usando abordagens de modelagem desenvolvidas nesta tese. Todos os módulos foram montados no tracker fotovoltaico para proporcionar as mesmas condições de operação, e a campanha de medição foi realizada durante 12 meses. Os registros experimentais, em intervalos de um minuto, foram verificados quanto à sincronicidade, interpolados e agregados. Diversas abordagens de filtragem foram discutidas e aplicadas para fornecer um equilíbrio adequado entre remoção de ruído e retenção de dados.

Os arranjos fotovoltaicos foram então estudados quanto às suas particularidades, começando pela identificação dos parâmetros operacionais mais influentes, por ordem de relevância, e seu impacto na potência de saída. Em seguida, o efeito da temperatura operacional foi avaliado e os coeficientes reais de temperatura para a alimentação CC foram determinados. Por fim, foi realizada uma análise de sensibilidade para a potência CC em relação aos parâmetros operacionais com base em filtros e modelos matemáticos desenvolvidos para cada arranjo fotovoltaico. Especial atenção foi dada ao arranjo bifacial, uma vez que esta tecnologia é muito promissora devido à sua interessante relação custo-benefício; novos métodos para determinar a irradiância efetiva e o ganho bifacial também foram desenvolvidos.

Dois métodos diferentes foram aplicados para caracterizar os módulos fotovoltaicos. Verificou-se que o seu desempenho real não é tão bom como o relatado nas fichas técnicas. O arranjo m-Si foi o menos sensível à temperatura de operação, seguido pelos módulos p-Si e bifaciais. Por sua vez, os dispositivos HCPV foram os mais prejudicados pela temperatura, massa de ar e umidade. A influência da velocidade do vento foi pequena para os módulos HCPV; as os arranjos mais beneficiados pelo vento foram os p-Si e m-Si. O arranjo bifacial apresentou a maior produtividade final (com ganho bifacial de 6,2%), seguida por m-Si e p-Si. Por sua vez, o arranjo HCPV apresentou o pior rendimento, principalmente devido à sua capacidade de resposta apenas à irradiância direta e ao elevado coeficiente de temperatura para a potência CC.

Palavras-chave: Tecnologias fotovoltaicas; Comparação de desempenho; Estudo experimental; Análise de sensibilidade

Research is to see what everybody else has seen
and to think what nobody has thought

- Dr. Albert Szent-Györgyi.

to my mother Juraci (in memory),
who provided all I needed to start

and

to my wife Cláudia,
who supports me to keep advancing

ACKNOWLEDGMENTS

This work is the most recent outcome of a partnership that started in 2016, when professor João Batista Dias agreed to be the supervisor for my Final Project on Electrical Engineering. I was an unknown student to him, and I had no background in photovoltaics. Other than that, I already was a full-time employee at Petrobras, working over 40 h/week – thus being a part-time student, not a part-time worker – and I had no experience in scientific research at the university level. Despite this, Professor Batista not only accepted being my supervisor for that Final Project but also for the Master's and the present PhD. One remarkable aspect of Professor Batista's supervision is his ability to break problems into small tasks, each of them with a straightforward solution. This made my formation journey way less complicated. I am immensely grateful for Professor Batista's guidance and honored for the trust he places in me.

The supervision received an important reinforcement during the early development of this thesis, through the participation of Professor Gilles Notton. For months, he worked very hard with the École Doctorale at the Université de Corse and with Professor Batista to make a cotutelle agreement possible. I am highly thankful for Professor Notton's persistence in not giving up on the cotutelle and for his conviction in my ability to develop this thesis with international collaboration, while keeping my professional activities. I greatly appreciate the chance to benefit from professor Notton's experience in supervising PhD students; he can promptly tell what has worked and what has not, the reasons why, and possible alternative and innovative way-arounds.

The thesis supervision was changed in 2022: due to external factors, professor Batista left the supervision and Professor Paulo Roberto Wander – who had already been my professor at the Master's, and the director of the Graduation Program at Unisinos – became the new supervisor of this thesis at the Brazilian side. I thank Professor Paulo for his availability and his concise, focused assessments. They significantly helped improve the content, sequence and presentation of this thesis, always aiming to make all steps clear and meaningful, both to experts and non-specialist readers.

The experimental platform, which is the main object of study in this thesis, was assembled and monitored by an outstandingly capable engineering team: Guillaume Pigelet and David Ouvrard at the UMR SPE CNRS 6134, University of Corsica, Centre Georges Peri. I am very grateful for their dedicated work.

I also express here my gratitude to the Université de Corse, CNRS and CAPES, for the financial support during the development of this thesis; for the Mechanical Engineering Graduation Program at Unisinos; for the École Doctorale at Université de Corse; and for the administrative staff at Unisinos and UDCPP, for the hard work during the elaboration of the cotutelle documentation. In particular, the efforts made by Professor Gilles and the École Doctorale made it possible for me to travel two times from Brazil to Ajaccio, with the expenses paid by the Université de Corse. The visits to the Centre Georges Peri were exceptionally great opportunities to meet the Corsican team and to work on the experimental platform, allowing me to get in contact with people, laboratories, experiments, and scientific research overseas.

I am also grateful to my supervisors at Petrobras, who understood that I had to dedicate a great deal of time and energy to the PhD. In fact, the search for a correct time balance between work and research was the greatest management task – and the greatest challenge – during my PhD. I also thank my many colleagues and friends at work, for the encouragement they gave me during these four years of PhD journey.

Last but – definitely – not least, I must acknowledge the support provided by my wife, Cláudia. During the period I was developing this thesis, she helped me in every possible way despite developing her own professional career, foreign language studies, and her second MBA degree. If I could spend thousands of hours writing this thesis, preparing research papers, working with large datasets, developing Matlab codes, or just thinking quietly, it was because she was relentless in supporting and encouraging me, day after day, during all phases of the PhD, from 2020 to 2024.

Thank you all.
Caio F. Abe, March 2024

LIST OF SYMBOLS

Symbol	Meaning	Unit
a	Irradiance dependency factor (IEC-60891)	
A	Diode ideality factor for the SDM	
A_{PV}	Area of the PV array	m²
AH	Absolute humidity	$kgH_2O/kgda$
AM	Air mass	
AM_0	Air mass, reference	
BNI	Beam normal irradiance	W/m²
BNI_0	Beam normal irradiance, reference	W/m²
DHI	Diffuse horizontal irradiance	W/m²
DNI	Diffuse normal irradiance	W/m²
E_0	Orbit eccentricity	
E_g	Bandgap energy	eV
FF	Fill Factor	
FF_{bif}	Fill Factor, bifacial device	
G	Solar irradiance (POA, generic reference to irradiance)	W/m²
G_0HI	Extraterrestrial global horizontal irradiance	W/m²
G_0NI	Extraterrestrial global normal irradiance	W/m²
G_1	Original irradiance level	W/m²
G_2	Irradiance level for translation	W/m²
G_E	Effective irradiance	W/m²
GHI	Global horizontal irradiance	W/m²
GNI	Global normal irradiance	W/m²
GNI_0	Global normal irradiance, reference	W/m²
G_{front}	Front-side irradiance (bifacial modules)	W/m²
G_{meas}	Measured irradiance	W/m²
G_{rear}	Rear-side irradiance (bifacial modules)	W/m²
G_{ref}	Reference global irradiance	W/m²
G_{POA}	Global irradiance at the plane of the PV array.	W/m²

G_{STC}	Global irradiance (POA), STC	W/m²
h	Solar altitude angle	degrees
h_{site}	Site altitude	m
h	Planck constant	J.s
I_0	Reverse saturation current	A
I_0'	Translated reverse saturation current	A
I_1	Original PV current	A
I_2	Translated PV current	A
I_d	Diode current, SDM	A
I_{mp}	Current at the maximum power point	A
$I_{mp,STC}$	Current at the maximum power point for STC	A
I_0	Reverse saturation current	A
I_p	Parallel resistance current	A
I_{ph}	Photocurrent	A
I_{ph}'	Translated photocurrent	A
I_{pv}	Current at the output of the SDM	A
I_{sc}	Short-circuit current	A
$I_{sc,bif}$	Short-circuit current, bifacial device	A
$I_{sc,front}$	Short-circuit current, front-side	A
$I_{sc,STC}$	Short-circuit current, STC	A
$I_{sc,STC,front}$	Front-side short-circuit current, STC	A
$I_{sc,STC,rear}$	Rear-side short-circuit current, STC	A
$I_{sc,rear}$	Short-circuit current, rear-side	A
J_{sc}	Short-circuit current density	A/cm²
k	Boltzmann constant	J/K
k	Thermal dependency factor for the current	Ω/K
n_c	Number of cells within the PV module	
P_{DC}	DC power	W
$P_{inv,N}$	Nominal inverter power	W
pFF	Pseudo Fill Factor	

P_{mp}	Maximum power	W
$P_{mp,c}$	Calculated maximum power	W
$P_{mp,STC}$	Maximum power point, STC	W
PR	Performance Ratio	
PR_a	Annual Performance Ratio	
$P_{Rs,STC}$	Power loss in series-resistance	W
q	Electron charge	C
r	Exponential factor, SPR calculation	
r	Earth-Sun distance	m
r_0	Mean Earth-Sun distance	m
RH	Relative humidity	%
R_p	Parallel resistance	Ω
R_s	Series resistance	Ω
T_{air}	Ambient air temperature	°C
$T_{air,0}$	Ambient air temperature, reference	°C
T_c	Cell temperature	°C
$T_{c,0}$	Cell temperature, reference	°C
$T_{c,1}$	Original cell temperature level	°C
$T_{c,2}$	Cell temperature level for translation	°C
$T_{c,STC}$	Cell temperature, STC	°C
V_1	Original PV voltage	V
V_2	Translated PV voltage	V
V_{mp}	Voltage at the maximum power point	V
$V_{mp,STC}$	Voltage at the maximum power point, STC	V
V_{oc}	Open-circuit voltage	V
$V_{oc,bif}$	Open-circuit voltage, bifacial device	V
$V_{oc,NOCT}$	Open-circuit voltage, NOCT	V
$V_{\mathrm{oc,STC}}$	Open-circuit voltage, STC	V
$V_{\mathrm{oc,STC,front}}$	Open-circuit voltage, STC, front-side	V
$V_{\mathrm{oc,STC,rear}}$	Open-circuit voltage, STC, rear-side	V

V_{pv}	Voltage at the output of the SDM	V
v_{wind}	Wind speed	m/s
$v_{\mathrm{wind},0}$	Wind speed, reference	m/s
α	Temperature coefficient for I_{sc}	1/°C
β	Temperature coefficient for V_{oc}	1/°C
α_{rel}	Temperature coefficient I_{sc} (IEC-60891)	1/°C
β_{rel}	Temperature coefficient for V_{oc} (IEC-60891)	1/°C
φ	Bifaciality index	
Φ	Geographical latitude angle	degrees
γ	Temperature coefficient for P_{mp}	1/°C
γ_i	Current factor for the SPR calculation	
γ_v	Voltage factor for the SPR calculation	
Γ	Day angle	rad
η	Actual efficiency of the PV system	
η_{STC}	Nominal efficiency of the PV system	
δ	Solar declination	degrees
$\delta(T_{\mathrm{c}})$	Irradiance dependency factor for the voltage	
θ_{z}	Solar Zenith angle	degrees
ω	Solar angle	degrees
Ψ	Solar azimuth angle	degrees

LIST OF ACRONYMS

Acronym	Meaning
AC	Alternating Current
BG	Bifacial Gain
CEA	Commissariat à l'Énergie Atomique et aux Énergies Alternatives
DC	Direct Current
HCPV	High Concentration Photovoltaics
INES	Institut National de l'Énergie Solaire
m-Si	Monocrystalline
MJ	Multi-junction
MPP	Maximum Power Point
MPPT	Maximum Power Point Tracking
NOCT	Nominal Operating Cell Temperature
p-Si	Polycrystalline
POA	Plane of Array
PV	Photovoltaic
SDM	Single Diode Model
STC	Standard Test Condition
SPR	Series-Parallel Ratio
TST	True Solar Time
UDCPP	Université de Corse Pasquale Paoli

LIST OF FIGURES

LIST OF TABLES

CONTENTS

SECTION 1
INTRODUCTION

1 INTRODUCTION

On the way to a sustainable future, the energy transition is among the most critical factors. Worldwide power generation – still – strongly relies on coal, oil, and gas, which are fossil fuels, therefore not sustainable. In this context, the expansion of solar photovoltaic (PV) is an essential element of sustainable power generation, showing great potential since solar energy is abundant and free. Photovoltaic solar energy has been promoted as a renewable option both for centralized and distributed electricity generation, being adopted by several consumers in low, medium, and high power contracts.

As part of the University of Corsica Pascal Paoli renewable energy project, a great deal of work has been done on the intelligent management of energy flows within a photovoltaic micro-grid. To do this, it is necessary to control the electricity production and to precisely know the performance of the electricity sources. On the other hand, the Solar Photovoltaic Energy Laboratory at the Unisinos University has carried out, to date, numerous works with the Corsican team on the behavior of PV modules.

A thesis was defended in 2020 regarding the “Development of an Operational Power Model for Concentrated Photovoltaic Systems (HCPV)” (Benhammane, 2019), which made it possible to analyze the behavior of multi-junction (MJ) modules under high concentration in partnership with INES-CEA. The results of this work have been used and applied within the framework of the present thesis. The high-precision Sun tracking system that supported the HCPV modules has been reused to install other technologies; thus, the two "sails" of the tracker were separated into 4 independent sub-systems comprising different photovoltaic technologies: HCPV and bifacial monocrystalline on one sail, and monocrystalline and polycrystalline – both monofacial – on the other sail. Each subsystem is connected to an independent inverter input and integrated to the external electricity grid via the Paglia Orba micro-grid. The use of a solar tracker allows better control of the solar variables, since beam irradiance is always normal to the arrays.

Many meteorological quantities were measured and acquired, at the time step of 1 minute: normal beam solar irradiance, as well as diffuse, horizontal global, normal global (front face and rear face), ambient air temperature and wind speed. In addition to this, the DC voltage and current of the photovoltaic sources for each subsystem were also measured and registered, as well as the AC voltage and current injected into the grid. Finally, data referring to the temperature of the PV modules and to the irradiance sensors installed on the tracker were also recorded.

Calculated data were added to the dataset as well, such as the airmass and the clearness index; the first one can partially take into account the spectral distribution of the solar radiation, which is not measured because the measuring device is costly and not available at the experimental site. The second one characterizes the state of the sky.

This thesis allows grouping and pooling of knowledge and skills developed in recent years within the two solar energy laboratories (UDCPP and UNISINOS), namely solar resource prediction, modeling of PV systems, management algorithms and setting up of experiments. Besides this, it also enables the improvement of the performance models for the various photovoltaic subsystems, as well

as better knowledge of the influence of the solar radiation components and other meteorological quantities on the behavior of PV modules.

The theme presented is original due to the use of PV modules of different technologies – some of which are recent: HCPV and bifacial – mounted on a structure following the sun. All components were working in real operating conditions (generally they are tested in controlled conditions using an artificial solar device) on the micro-grid, in integration with the Paglia Orba R&D platform. The development of the subjects in this thesis is of interest to researchers, electricity producers and distribution system operators.

1.1 PROBLEM

Several PV module technologies are commercially available today. They are distinguished by their performance, by their cost and they react differently to variations in meteorological quantities and the state of the sky, according to the share of the different components of solar radiation and spectral distribution.

Monofacial
Polycrystalline (p-Si)

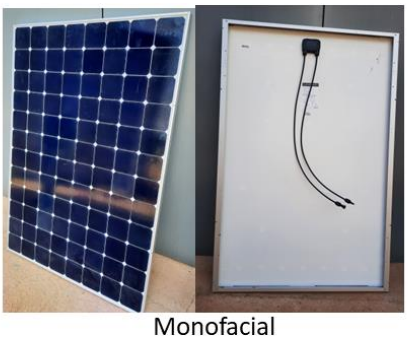

Monofacial
Monocrystalline (m-Si)

Bifacial
Monocrystalline

Multijunction with concentration (HCPV)

Figure 1-1: The four types of PV modules studied in this thesis.

It is desired to compare the following technologies, available on the Paglia Orba research and development platform:

- Multi-junction modules under high concentration (HCPV) and high conversion efficiency (around 34 % in standard condition), with triple-junction cells (GaInP/GaInAs/GaInNAs);
- Bifacial monocrystalline silicon modules;
- Conventional crystalline modules with single-sided production (mono and polycrystalline silicon technologies).

Images referring to these four types of PV modules are shown in Fig. 1-1.

While the conventional modules use the incident global solar radiation, bifacial crystalline modules also convert the radiation arriving on their rear face, consisting of radiation reflected by the ground and diffused by the sky (in a given angle depending on time); however, there is no direct radiation reaching this face. In turn, multi-junction modules under concentration convert only beam (direct) radiation, which is the only component that can be concentrated. A graphical scheme showing these concepts is provided in Fig. 1-2.

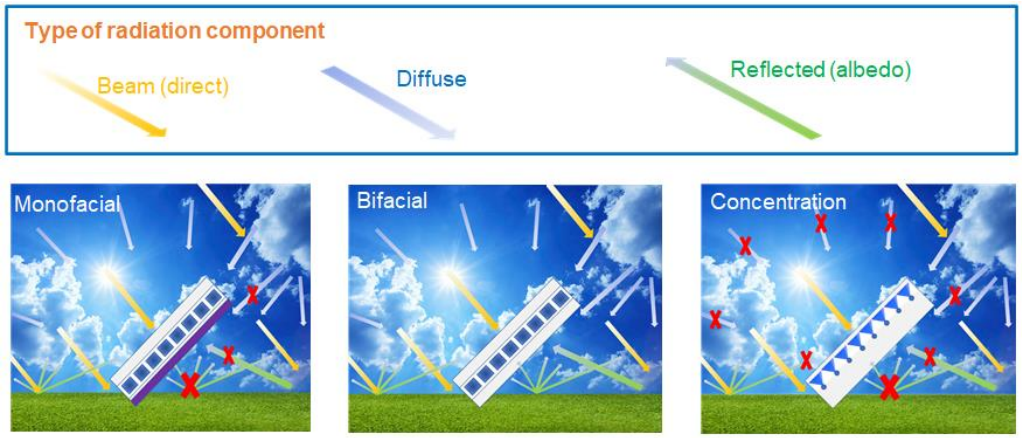

Figure 1-2: Different PV modules and usable radiation components

It is therefore important to take the peculiarities referring to the PV technologies into account and develop an experimental sensitivity analysis regarding various uncontrolled and intermittent parameters. This would allow to assess the main differences between the four PV technologies, in real operating conditions.

1.2 OBJECTIVE

The objective of the thesis is to compare the performance of different photovoltaic module technologies subject to the same weather conditions and mounted on a same sun tracking system. This work brings together a theoretical analysis, modeling, and an experimental analysis. Particular attention is given to the characteristics of each PV array and the sensitivity of electricity production as a function of external parameters, as well as the consequence on the power and energy behavior of the photovoltaic systems.

The specific objectives are:

1. Ensure that all PV modules are working well, by performing tests before they are assembled on the tracker;
2. Quantify the differences between datasheet ratings and actual outdoor performance, through the electrical characterization of the PV arrays;
3. Obtain a set of experimental records using the experimental platform developed specifically for this thesis;
4. Use the records to identify the influence of the external parameters on the PV performance;
5. Apply or develop new modeling methods, as necessary, to support a sensitivity study.

SECTION 2
LITERATURE REVIEW

2 LITERATURE REVIEW

The following sections present an overview of the concepts regarding solar radiation and the photovoltaic technologies studied in this thesis. In the sequence, relevant PV system performance metrics are introduced. This section ends with a discussion regarding previous studies on the comparison of PV technologies' performance.

2.1 SOLAR RADIATION

The radiation emitted by the Sun is distributed along a range of different wavelengths. Outside the Earth's atmosphere, the solar irradiance – that is, the power per area – presents a practically constant level: this value depends on some geometrical quantities and the Sun activity, which are considered by solar energy researchers as constant. This is the so-called solar constant, and its value might be different according to the reference source and the year of publication; it is generally taken as 1367 W/m². This section presents what happens to the extraterrestrial radiation when it enters the Earth's atmosphere.

2.1.1 **Solar radiation components**

Once the radiation enters the Earth's atmosphere, it is either absorbed or scattered and then, different components of this Sun radiation arrive on the Earth. For instance, the radiation is reflected by clouds; and gases such as oxygen, ozone and carbon dioxide – as well as water vapor – absorb radiation in different wavelengths, mainly infrared (Wenham et al. 2013). As a result, the radiation is decomposed into different components.

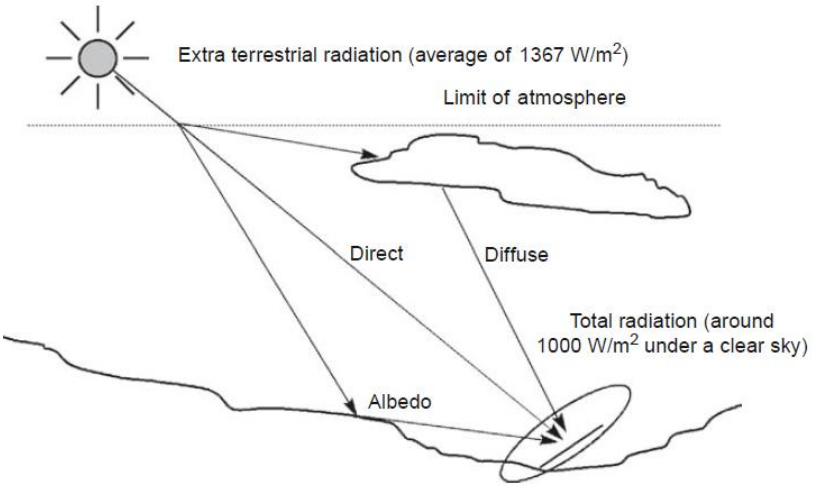

Figure 2-1: Beam (direct), diffuse and albedo radiation

Radiation that is not absorbed, reflected or scattered is defined as *beam radiation* (or *direct radiation*), and refers to light coming from the Sun in a straight path. The radiation which is scattered by the atmosphere and comes from the sky dome is named *diffuse radiation*, whereas the radiation which is reflected by the surroundings (ground, buildings or other objects) is termed *albedo radiation.* This last reflected radiation is a diffuse component, which depends on the albedo of the surrounding

(reflection coefficient), varying with the type of ground or surrounding buildings and season of the year. The extraterrestrial radiation is then considerably modified in terms of spectral distribution, as it passes through the atmosphere. In turn, the *global radiation* corresponds to the sum of these three components (beam, diffuse and albedo), and refers to the total radiation falling on a surface located on the Earth's surface (Luque and Hegedus, 2011). The illustration in Fig. 2-1, extracted from Labouret and Villoz (2010), shows these radiation components.

Even in clear-sky days – without any clouds – the irradiance reaching a surface depends on the turbidity of the sky: as the turbidity increases, the beam irradiance decreases, whereas the diffuse portion increases because of the scattering, according to Kalogirou (2017). In cases where the sky presents partial cloud coverage, the share of beam and diffuse radiation can be modified very rapidly, changing the predominant radiation component in a matter of seconds. Different sky conditions are shown in Figure 2-2.

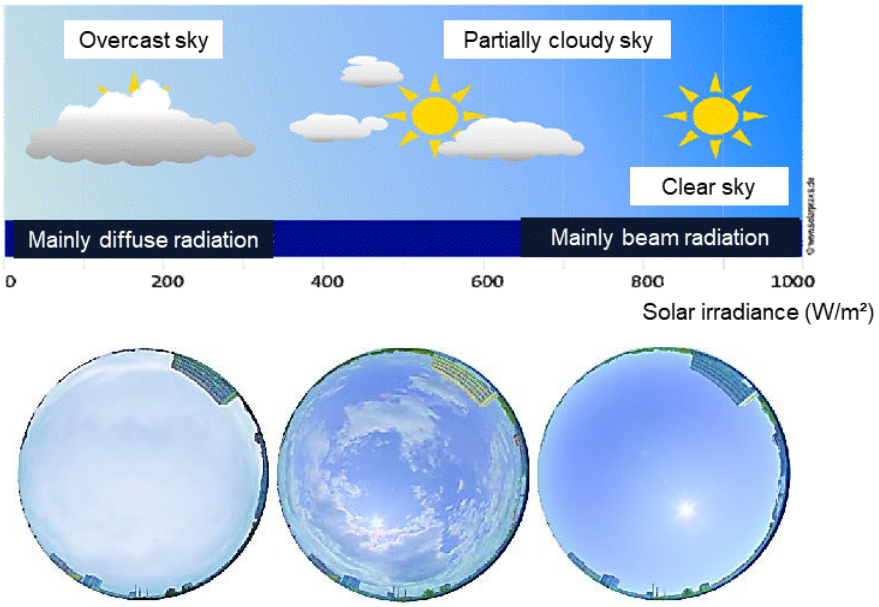

Figure 2-2: Different sky conditions: overcast, partially cloudy and clear.

Finally, in days with overcast sky, the beam radiation is practically not present, thus impairing the use of trackers and concentrators used for solar energy harvesting (Labouret and Villoz, 2010). However, the fact that the sky is completely covered by clouds does not mean that the diffuse radiation is constant: its magnitude depends on the thickness and type of cloud. Thus, changes in the cloud coverage cause variation on the diffuse irradiance reaching a surface; however, the rate of change is usually significantly lower as in comparison with partially clouded sky cases (Kalogirou, 2017).

2.1.2 **Sun position**

It is important to briefly describe the main angles defining the position of the Sun in the sky. The knowledge of the Sun position is required to determine, as an example, the atmosphere length crossed by the solar radiation (optical path), which influences the solar spectrum distribution, impacting the efficiency of the photovoltaic modules. It is also necessary to estimate the extraterrestrial irradiance, which will be used to determine the clearness index.

The Earth describes an ellipse about circular (eccentricity = 1/60) with the Sun at the focus. The rotation axis of the Earth makes an angle of 23°27’ (called obliquity) towards the perpendicular with the plan of the ecliptic, as illustrated in Fig. 2-3.

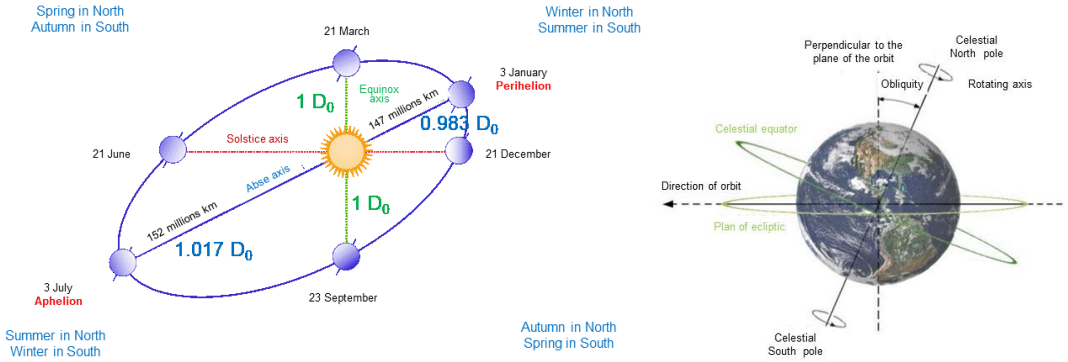

Figure 2-3: Representation of the Earth’s orbit around the Sun

The orbital eccentricity E_0 is a dimensionless parameter that determines the amount by which the orbit around another body deviates from a perfect circle (0 is a circular orbit, 1 is a parabolic escape orbit (or capture orbit), and greater than 1 is a hyperbola). The eccentricity can be calculated using different methods proposed in literature, and one of the most accurate is described in Eq. (2.1) (Iqbal, 2012):

$$E_0 = \left(\frac{r_0}{r}\right)^2 = 1.000110 + 0.034221\cos\Gamma + 0.001280\sin\Gamma + 0.000719\cos 2\Gamma + 0.000077\sin 2\Gamma \quad (2.1)$$

where Γ is the day angle in radian defined by $\Gamma = 2\pi\frac{(d-1)}{365}$ and d is the day number. For the northern and southern hemispheres, the eccentricity and the Sun-Earth distance behave as illustrated in Fig. 2-4, considering one year.

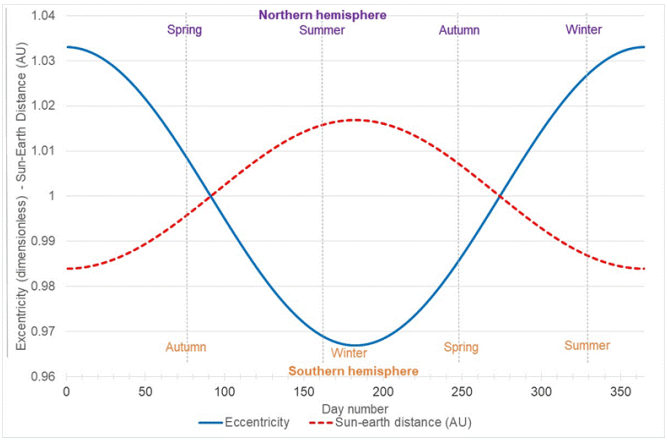

Figure 2-4: Eccentricity and the Sun-Earth distance plotted for one year.

The solar declination δ is the angle between the line joining the Earth to the Sun and the equatorial plane, as illustrated in Fig. 2-5. The declination is equal to zero for the equinoxes (the Sun crosses the equatorial plane) and it varies from + 23.45° (22 June) to – 23.45° (22 December).

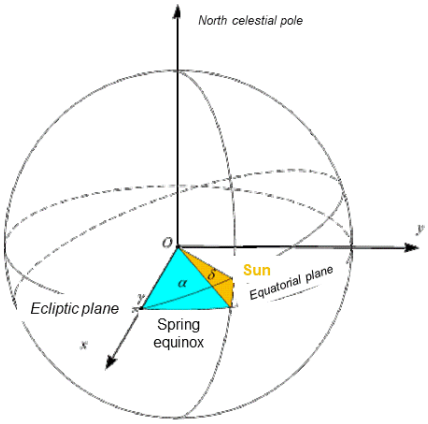

Figure 2-5: Representation of the solar declination angle

In 24 h, the maximal variation of declination (at equinoxes) is less than 0.5°, therefore it can be considered as constant over a day. The parameter δ can be determined by Eq. (2.2) (Iqbal, 2012), whose behavior during one year is illustrated in Fig. 2-6.

$$\delta = 0.006918 - 0.399912\cos\Gamma + 0.070257\sin\Gamma - 0.006758\cos 2\Gamma + 0.000907\sin 2\Gamma - 0.002697\cos 3\Gamma + 0.00148\sin 3\Gamma \quad (2.2)$$

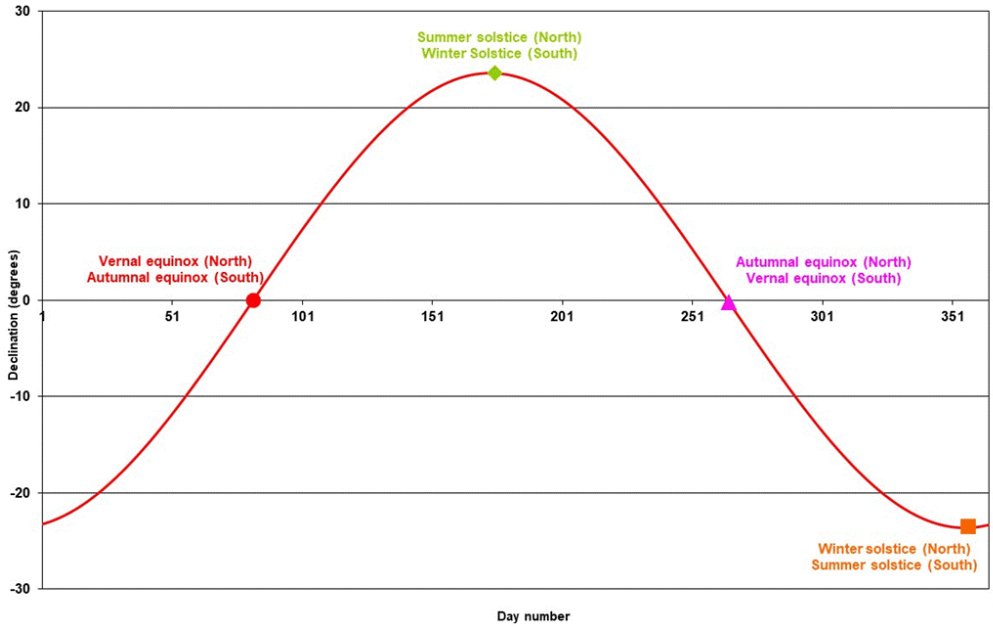

Figure 2-6: Behavior of the declination angle for one year

In geometrical formulation, the time scale is the true solar time calculated from the legal time by equations considering the position of the site (latitude and longitude) and the time equation. This true solar time, in hour, is then transformed in an hour angle ω. The solar angle ω is the arc of Sun trajectory between the Sun and the meridian plane of the location. This trajectory is 360° in 24h, or 15°/hour. The value 0° is for midday (True Solar Time = TST). Therefore, the solar angle is calculated using Eq. (2.3).

$$\omega = 15° \times (12 - \mathrm{TST}) \tag{2.3}$$

Figure 2-7 shows the main angles for determining the Sun's position for North (left) and South (right) hemispheres, for a horizontal surface.

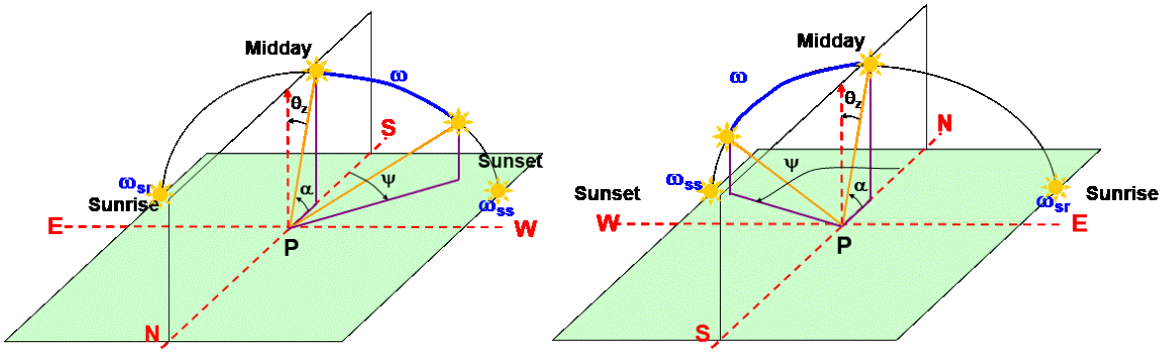

Figure 2-7: Angles describing the Sun's position.

To locate a point of the sky from a terrestrial observer, a coordinate system is chosen referring to the observer's location.

- The solar azimuth angle Ψ is the angular distance between the zero azimuth (either due South or due North, depending on the hemisphere) and the projection of the line of sight to the Sun on the ground. (> 0 towards East)
- The solar altitude angle *h* (also called sun height) is the angle between the Sun's rays and a horizontal plane.
- The zenith angle θ_z is the angle between the Sun's rays and the vertical, complementary to the angle of *h*.

θ_z and *h* are calculated by Eq. (2.4)

$$\cos\theta_z = \sin\delta \sin\Phi + \cos\delta \cos\Phi \cos\omega = \sin h \tag{2.4}$$

Relevant angles can be related by using Eq. (2.5), and they are illustrated in Fig. 2-8, where the solar azimuth is represented by Ψ.

$$\cos\theta = \cos\beta \cos\theta_z + \sin\beta \sin\theta_z \cos(\Psi - \gamma) \tag{2.5}$$

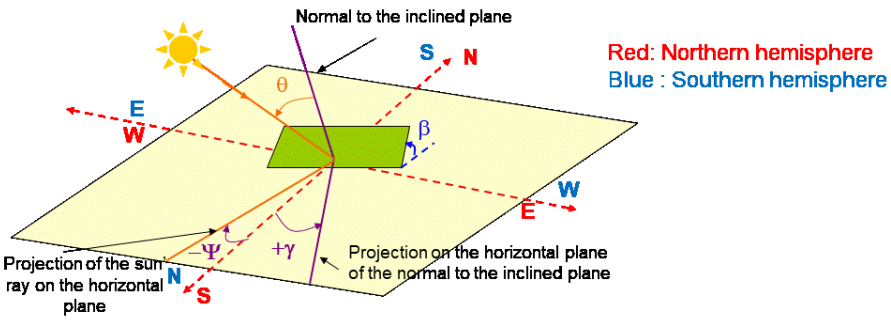

Figure 2-8: Angles for solar position

2.1.3 **Atmospheric radiation indexes**

Useful relations to describe the state of the sky can be derived by relating the various irradiance components. The horizontal clearness index expresses the relationship between the global horizontal irradiance (GHI) and the extraterrestrial irradiance converted to the horizontal plane (G_0HI). Another useful metric is the horizontal diffuse fraction, which relates the horizontal diffuse irradiance (DHI) and GHI.

Similarly, the normal global clearness index is a relation between the global normal irradiance (GNI) and the global normal extraterrestrial irradiance (G_0NI), whereas the normal diffuse fraction relates the normal diffuse irradiance (DNI) and GNI. A normal beam clearness index can be calculated relating the beam normal irradiance (BNI) and G_0NI. Table 2-1 summarizes the horizontal and normal atmospheric radiation indexes.

Table 2-1: Summary of atmospheric radiation indexes

Relation	Name
$\frac{\mathrm{GHI}}{\mathrm{G_0HI}}$	Horizontal clearness index
$\frac{\mathrm{DHI}}{\mathrm{GHI}}$	Horizontal diffuse fraction
$\frac{\mathrm{GNI}}{\mathrm{G_0NI}}$	Normal global clearness index
$\frac{\mathrm{BNI}}{\mathrm{G_0NI}}$	Normal beam clearness index
$\frac{\mathrm{DNI}}{\mathrm{GNI}} = \frac{\mathrm{GNI} - \mathrm{BNI}}{\mathrm{GNI}}$	Normal diffuse fraction

2.1.4 **Spectral distribution of solar radiation**

The solar radiation finds the shortest pathlength through the Earth's atmosphere when the Sun is directly overhead, that is, when the zenith angle (θ_z) is 0°. The thickness of the atmosphere can be expressed in terms of the *air mass*: when θ_z is zero, the air mass is 1 (AM1). In turn, air mass 2 (AM2) is found when θ_z is 60°, whereas AM1.5 – the standard air mass for photovoltaic work – is related to θ_z = 48.2° (Wenham et al. 2013). For zenith angles between 0° and 70°, Eq. (2.6) can be used to calculate AM:

$$\mathrm{AM} = \frac{1}{\cos\left(\theta_z\right)} \tag{2.6}$$

For θ_z with high values, the earth's curvature has to be taken into account, as stated by Duffie and Beckman (2020). An empirical expression to compute AM for θ_z approaching 90° is shown in Eq. (2.7), provided by Kasten and Young (1989). In Eq. (2.7), h_{site} represents the altitude of the site, in meters.

$$\mathrm{AM} = \frac{\exp\left(-0.0001184\ h_{\mathrm{site}}\right)}{\cos(\theta_z) + 0.5057(96.08 - \theta_z)^{-1.634}} \tag{2.7}$$

Figure 2-9 shows a schematic drawing for the air mass; as the zenith angle increases, so increases the thickness of the atmospheric layer.

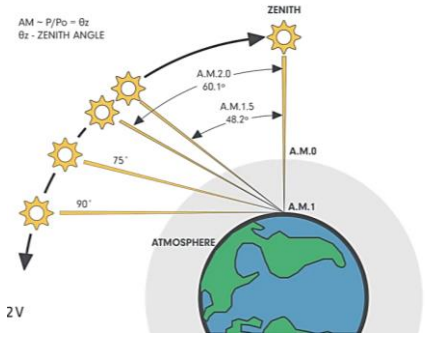

Figure 2-9: Schematic representation of the air mass concept

A plot showing the air mass and Sun's elevation variation according to daytime and year season is shown in Figure 2-10. The dashed lines represent the air mass, whereas the solid lines represent the solar elevation.

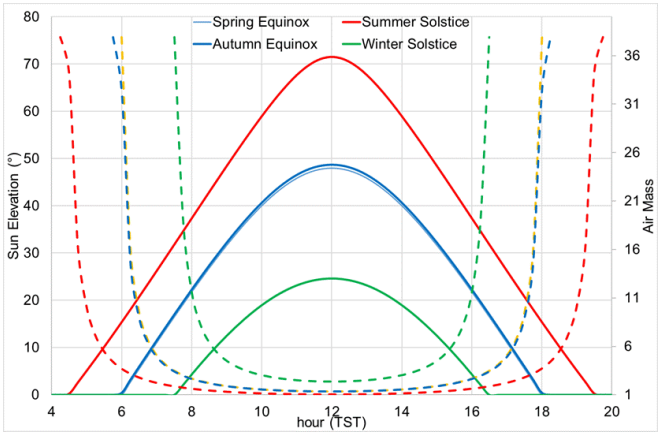

Figure 2-10: air mass and Sun elevation as functions of daytime

As mentioned earlier, solar radiation is emitted in different wavelengths, and it suffers absorption and scattering as it travels through the Earth's atmosphere. Such effects occur according to the wavelength and the air mass. To illustrate the relation between the spectral distribution and the air mass, Fig. 2-11 shows the spectral distribution of the solar radiation both for AM0 (extraterrestrial) and AM1.5 (Iqbal, 2012).

In Fig. 2-11, the vertical axis represents the spectral irradiance in W/m² per micrometer of bandwidth. The blackbody radiation at 5777 K is plotted to show its similarity to the extraterrestrial radiation curve (AM0). The cluttered yellow curve represents the spectral distribution for AM1.5, whereas the gases which absorb specific wavelengths – H_2O, CO_2, O_3 – are also related with the wavelength and irradiance amplitude. By integrating the AM1.5 curve with respect to the wavelength, 1000 W/m² irradiance is obtained, whereas an irradiance level of 1367 W/m² is found by integrating the AM0 curve with respect to the wavelength.

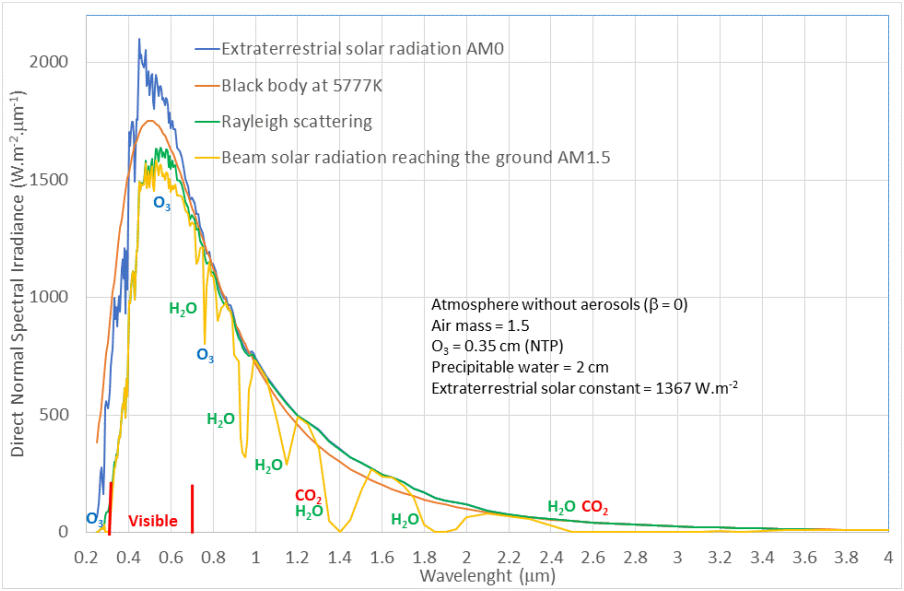

Figure 2-11: Spectral distribution of the solar radiation

Other factors that influence the shape of the spectral distribution of solar radiation are the aerosol optical depth (AOD) and the precipitable water (PW). The AOD represents the quantity of small particles in the atmosphere: low levels of AOD are related to a clear atmosphere, whereas high AOD levels are related to a hazy atmosphere (Kalogirou 2017). In turn, the PW indicates the amount of water in the direction of the zenith. High PW levels are related to a wet atmosphere, whereas low levels are related to a dry atmosphere.

It is worth mentioning that the AM1.5 spectrum does refer not only to a specific air mass, but to a set of specified parameters, which are described in the ASTM G173 international standard (ASTM 2020): a) the surface which receives the radiation is tilted to 37° (the U.S.A average latitude) facing the Sun, which is at an elevation of 41.8° above the horizon (that is, 48.2° zenith angle); b) the test site at sea level and 101.325 kPa atmospheric pressure; c) CO_2 concentration is 370 ppm in volume; and d) the aerosol optical depth is 0.084 for 500 nm wavelength. Given that such a condition is very specific, it would be desired to determine the spectral distribution when one or more of the environmental parameters change; this can be accomplished with an application named SMARTS (Simple Model for the Atmospheric Radiative Transfer of Sunshine), which was developed at the NREL – National Renewable Energy Laboratory, and published by Gueymard (1995) and Myers and Gueymard (2004).

2.1.5 **Solar radiation measurement instruments**

Quantifying the available solar resource is essential when deciding where to install a photovoltaic plant, what technology to choose and what the power rating should be. Moreover, such a quantification is paramount for monitoring the operation of an existing photovoltaic field and determine its efficiency, that is, the ratio between the converted and received solar power.

The horizontal global irradiance – GHI – can be measured by an instrument called *pyranometer*. Measuring the GHI allows comparison of local irradiance data with other monitoring systems or weather stations (it is the most common irradiance measurement in the World). The GHI can also be employed as an input in simulation tools. Pyranometers can be used, also, to measure the POA (plane-of-array) irradiance, that is, the global normal irradiance (GNI). In this case, the instrument is installed

with the same orientation and tilt angle as the photovoltaic array. Such a measurement is relevant because it quantifies the actual irradiance arriving on the plane of the PV modules. Two pyranometers are presented in Fig. 2-12: the one on the left side (a) is installed parallel to the ground, to measure GHI; and the one on the right side is installed with a tilt angle equal to that of the PV modules, to measure the GNI. The images shown in Figs. 2-12, 2-13 and 2-14 were adapted from a product catalog from Kipp & Zonen (Kipp&Zonen, 2021).

Figure 2-12: Pyranometers for monitoring GHI (a) and GNI (b)

Pyranometers can be also used to measure the diffuse irradiance. In this case, a moving shading element must be used to avoid the beam radiation component from reaching the pyranometer. An assembly to measure the diffuse horizontal irradiance (DHI) is presented in Fig. 2-13, where a Sun tracker (a) is used to move the beam irradiance blocking device (b). The pyranometer (c) is thus shaded for the beam irradiance, and measures only the diffuse component. The picture in Fig. 2-13 also shows a non-shaded pyranometer (d), to measure the GHI.

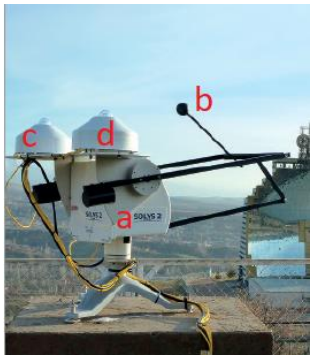

Figure 2-13: Assembly to measure GHI and DHI

In turn, the beam normal irradiance (BNI) can be measured using instruments named *pyrheliometers*. It is essential that such an instrument is mounted on a solar tracking device, to follow the Sun along its path. An assembly consisting of a pyrheliometer (a), and a solar tracker (b) is illustrated in Fig. 2-14.

Figure 2-14: Assembly to measure BNI.

2.2 PHOTOVOLTAIC MODULES AND THEIR PERFORMANCE

Photovoltaic devices convert solar radiation directly into electricity, consisting of a particular case in a generation fleet, since virtually all common power generation methods – namely hydroelectric, thermoelectric (solar thermal, coal, gas, biomass, nuclear and oil), wind and geothermal – require rotating electric machines to convert mechanical motion into electricity. However, the voltage provided by a single photovoltaic cell is too low for practical applications. For this reason, PV cells are associated in series – thus summing the voltage of various cells – forming a single structure denominated photovoltaic module. PV modules are currently available in many different sizes and employ different manufacturing technologies. In this thesis, four types of PV modules are considered: single-face, manufactured using polycrystalline (p-Si) and monocrystalline (m-Si) technologies; bifacial modules – that is, devices consisting of PV cells which are able to absorb radiation both on the front and rear faces; and finally, multi-junction modules, consisting of PV cells manufactured in such a way as to optimize the energy harvesting through the use of different semiconductor materials, covering a wider spectral response in comparison to conventional PV cells. In the following, performance models of three categories of PV modules are presented. This section is aimed at describing the behavior of these devices according to their temperature and the solar irradiance reaching their surface.

2.2.1 **Single face crystalline PV modules**

Single face (or monofacial) crystalline modules are the most common PV devices in the market. Therefore, several studies have been devoted to describing their performance, considering different levels of complexity and precision. Given the relevance of crystalline single-face PV modules and their significant market share, three different approaches for modeling their performance are presented in this thesis, starting from a simple power model. Then, in Section 3.7.1, an approach using IEC-60891 for voltage and current translations is presented, including a new coefficient adjustment procedure developed as part of the present thesis. Finally, in Section 3.7.2, an equivalent circuit for PV modules – the single-diode model (SDM) – is explored, combining different techniques available in literature for the outdoor characterization of crystalline PV modules.

Figure 2-15 illustrates a monocrystalline module – manufactured by LDK (LDK, 2018) – and a polycrystalline module, manufactured by Canadian Solar (Canadian Solar, 2020a).

Both modules present their back surface covered with opaque white polymeric material. Being so, the rear side of the PV cells is not visible.

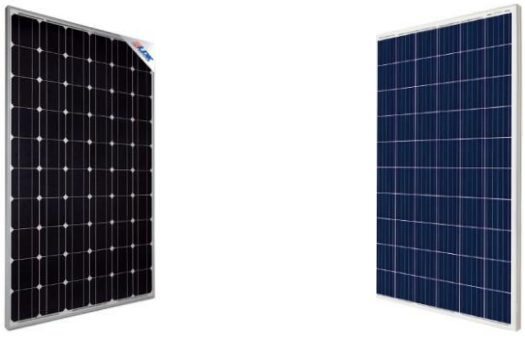

a) b)

Figure 2-15: PV modules: monocrystalline (a); and polycrystalline (b)

A relatively simple method for describing the performance of a single-face crystalline PV module – as a function of irradiance and temperature – is by using a power model. An example of a power model is provided in Eq. (2.8), which is the model adopted in the PVform photovoltaic system simulation program introduced by Menicucci (1985).

$$P_{\mathrm{mp}} = P_{\mathrm{mp,STC}} \ \frac{G}{G_{\mathrm{STC}}} \left[1 - \gamma \left(T_{\mathrm{C}} - T_{\mathrm{C,STC}}\right)\right] \tag{2.8}$$

In Eq. (2.8), G is the global irradiance at the plane of the PV array, G_{STC} is the reference irradiance, T_c is the cell temperature and $T_{c,STC}$ is the reference cell temperature. Such reference values refer to the Standard Test Condition (STC), where G = 1000 W/m², T_c = 25 °C and AM = 1.5. Manufacturers usually specify their products' ratings based on the STC. It is worth mentioning that the model presented in Eq. (2.8) does not consider the series resistance of the PV device under study.

Single-junction silicon PV cells present bandgap energy around 1.12 eV; this means that photons with energy below 1.12 eV are not able to transfer their energy to excite electrons lying within the semiconductor structure. In other words, photons with energy levels below the bandgap produce no useful effect on a PV cell. In turn, photons with energy above 1.12 eV are able to liberate electrons from the nucleus and create an electric current. However, the excess energy is converted into heat. This concept is represented in Fig. 2-16 (Labouret and Villoz, 2010), on the right-hand side – "energy not absorbed" and at the top – "energy dissipated in heat". From Fig. 2-16 it can be concluded that there are two inevitable losses related to the PV conversion: a) incident photons with energy levels below the bandgap level and b) the loss due to photons with energy levels that exceed the bandgap level. This makes it impossible for Si PV cells to convert more than 44 % of the total spectrum energy. To improve the efficiency, it would be necessary that all photons reaching the PV device to present a single energy level, thus avoiding the two categories of losses aforementioned – which unfortunately is not the case in practice.

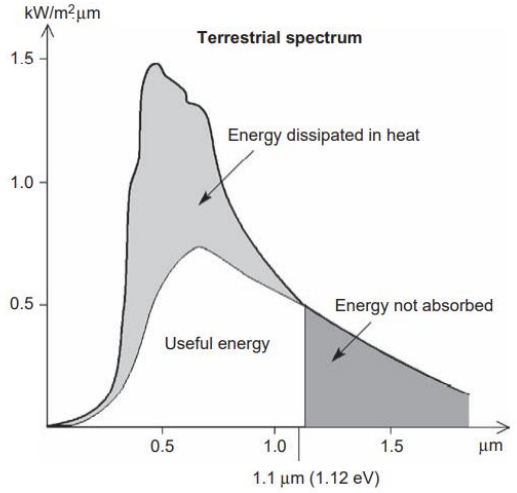

Figure 2-16: Use of the AM0 solar spectrum by crystalline PV

2.2.2 **Bifacial PV modules**

Bifacial PV modules are able to absorb solar irradiance in their front and rear sides, and this allows increased solar energy harvesting, with the same array area as monofacial modules (Kopecek

and Libal, 2018; Liang et al., 2019). The images in Fig. 2-17 show the difference between regular monofacial PV modules (a) and bifacial devices (b), where white ground cover was added to increase albedo (reflected radiation) incidence on the rear side of the array.

a) b)

Figure 2-17: Back side of PV modules: a) monofacial; b) bifacial

The research on bifacial PV devices started in the 60s, and around 2010, several companies started producing and selling bifacial modules in large scale. To date (2023), the biggest plant with bifacial modules is located in Bulgaria, with 123 MW nominal capacity.

The characterization of bifacial PV modules is a relevant topic because it allows manufacturers to offer their products with global reach – that is, adopting performance specifications that are recognized in various countries – and it helps the designers to correctly size the systems and estimate the electrical production.

ELECTRICAL DATA (STC)		
Peak Power Watts-PMAX (Wp)*		315
Power Output Tolerance-PMAX (W)		
Maximum Power Voltage-VMPP (V)		32.9
Maximum Power Current-IMPP (A)		9.58
Open Circuit Voltage-VOC (V)		40.0
Short Circuit Current-ISC (A)		10.15
Module Efficiency η m (%)		18.5
STC: Irradiance 1000W/m², Cell Temperature 25°C, Air Mass AM1.5.		
BI-FACIAL OUTPUT - Backside Power Gain		
10%	Power Output(W)	347
	Module Efficiency(%)	20.3
15%	Power Output(W)	362
	Module Efficiency(%)	21.2
25%	Power Output(W)	394
	Module Efficiency(%)	23.1

Figure 2-18: Excerpt of model TSM-DEG6MC datasheet

In bifacial modules, both sides produce electricity simultaneously, however, the STC does not specify the irradiance condition for the rear side. In datasheets, most producers report the front-side parameters under STC plus the contribution of the rear side, in terms of a “x % rear-face contribution”, which is simply a scale up of the P_{mp} specification at the STC. Examples illustrating this practice can be found in product datasheets modules provided by high quality manufacturers in the PV industry such

as Trina Solar (2019) (TSM-DEG6MC, monocrystalline), Canadian Solar (2020a)(CS3W-390, polycrystalline) and Canadian Solar (2020b) (CS3W-435, monocrystalline).

An excerpt of model TSM-DEG6MC datasheet from Trina Solar, (2019) is presented in Fig. 2-18, where one can observe that the *backside power gain* is simply the maximum power under the STC multiplied by a factor (1.1, 1.15 or 1.25), which is not satisfactory. The manufacturer does not include data which could allow comparing the performance of the rear and front sides. In this sense, relevant information would be a performance table referring to the rear side under STC – without any contribution from the front side – that is, the front side would have to be covered during the test. From these data, the rear face efficiency could be computed, allowing a designer to compare products from different manufacturers to determine the cost/benefit relation.

Since the datasheet information regarding the rear side does not relate to any operating condition, it is not possible to estimate the overall performance (front + rear side contributions), because the same condition which produces 10 % backside power gain for model TSM-DEG6MC could produce different gains when different bifacial PV module models are considered. The so-called backside power gain is actually a function of the conversion efficiency of the rear side, and such a parameter is not specified on the datasheets provided by Canadian Solar (2020b, 2020a) and Trina Solar (2019). For the determination of overall efficiency of a bifacial PV module – that is, quantifying the rear-side efficiency – experimental tests must be carried out, either indoors or outdoors. Datasheet specifications, as presented in Fig. 2-18 are not sufficient.

In search for standardization, the IEC (International Electrotechnical Commission) released the Technical Specification IEC TS 60904-1-2 - Measurement of current-voltage characteristics of bifacial photovoltaic (PV) devices (IEC 2021). The Technical Specification presents procedures for characterization tests, similar to what was proposed by (Deline et al., 2017).

Using a single light source, separated tests should be performed in STC (G = 1000 W/m², Tc = 25 °C) for both sides of the module, one side at a time. This allows calculating the ratio φ via Eq. (2.9), which relates the short-circuit current of the rear ($I_{\mathrm{sc,rear}}$) and front ($I_{\mathrm{sc,front}}$) sides of a bifacial PV module, according to IEC (2021). To carry out flash-tests of the two sides of a bifacial module, one at a time, the undesired interference of the side which is not under consideration can be avoided by using coverage such as with cloth or black mask (Liang et al., 2019).

$$\varphi = \frac{I_{\mathrm{sc,rear}}}{I_{\mathrm{sc,front}}} \tag{2.9}$$

The effective irradiance (G_{E}), which is the irradiance level that replicates the effect of radiation reaching the front and rear surfaces simultaneously, is computed from Eq. (2.10)

$$G_{\mathrm{E}} = G_{\mathrm{STC}} + \varphi\, G_{\mathrm{rear}} \tag{2.10}$$

The irradiance level G_{E} takes into account G_{STC} (1000 W/m²) reaching the front surface of the bifacial module, as well as the G_{rear} level. This way, since φ has been defined, it is possible to compare indoor tests with field measurements.

Concerning further mathematical derivations for the electric response of bifacial modules, Singh et al. (2014) defined the equivalent short-circuit current ($I_{\mathrm{sc,bif}}$) as Eq. (2.11).

$$I_{\mathrm{sc,bif}} = \frac{G_{\mathrm{E}}}{G_{\mathrm{STC}}} I_{\mathrm{sc,STC,front}} \tag{2.11}$$

whereas the open-circuit voltage ($V_{\mathrm{oc,bif}}$) is computed from Eq. (2.12).

$$V_{\mathrm{oc,bif}} = V_{\mathrm{oc,STC,front}} + \frac{\left(V_{\mathrm{oc,STC,rear}} - V_{\mathrm{oc,STC,front}}\right) ln\left(\frac{G_{\mathrm{E}}}{G_{\mathrm{STC}}}\right)}{ln\left(\frac{I_{\mathrm{sc,STC,rear}}}{I_{\mathrm{sc,STC,front}}}\right)} I_{\mathrm{sc,STC,front}} \tag{2.12}$$

In the study presented by Singh et al. (2014), the authors introduced the term pFF, referring to a *pseudo fill factor* for a bifacial module, given that the loss effect due to the series-resistance is neglected. The $\mathrm{FF_{bif}}$ can be expressed as in Eq. (2.13)

$$\mathrm{FF_{bif}} = \mathrm{pFF} - \frac{G_{\mathrm{E}}}{G_{\mathrm{STC}}}\left(\frac{V_{\mathrm{oc,STC,front}}}{V_{\mathrm{oc,bif}}}\right)\left(\mathrm{pFF} - \mathrm{FF_{STC,front}}\right) \tag{2.13}$$

Deline et al. (2017) provide an alternative procedure for computing pFF, which starts from the expression of the power loss ($P_{R_{\mathrm{S,STC}}}$) due to the series resistance, from Eq. (2.14).

$$P_{R_{\mathrm{S,STC}}} = I^2 R_{\mathrm{S}} \tag{2.14}$$

As mentioned earlier, pFF is the fill factor disregarding the effect of R_{s} therefore, $P_{R_{\mathrm{S,STC}}}$ can be written

$$P_{R_{\mathrm{S,STC}}} = \left(\mathrm{pFF} - \mathrm{FF_{STC,front}}\right) V_{\mathrm{oc,STC,front}}\, I_{\mathrm{sc,STC,front}} \tag{2.15}$$

Finally, an expression for pFF can be written by combining Eqs. (2.14) and (2.15), which provides Eq. (2.16),

$$\mathrm{pFF} = \frac{R_{\mathrm{S}}\, I_{\mathrm{sc,STC,front}}}{V_{\mathrm{oc,STC,front}}} + \mathrm{FF_{STC,front}} \tag{2.16}$$

whereas the total power of the bifacial module can be computed using Eq. (2.17)

$$P_{\mathrm{mp,bif}} = V_{\mathrm{oc,bif}}\, I_{\mathrm{sc,bif}}\, \mathrm{FF_{bif}}\,. \tag{2.17}$$

The series resistance R_{S} can be estimated by the I-V curve slope at $V_{\mathrm{oc,STC,front}}$, as shown by Deline et al. (2017).

Considering a bifacial array operating outdoors, under real weather conditions, Eq. (2.10) can be adjusted to represent the effective irradiance for in-plane front-side irradiance levels different from G_{STC}, as proposed by Gostein et al. (2021). In this case, the effective irradiance is written as a function of G_{front}, as in Eq. (2.18).

$$G_{\mathrm{E}} = G_{\mathrm{front}} + \varphi\, G_{\mathrm{rear}} \tag{2.18}$$

It is known that the temperature distribution along the surface of a module is not likely to be uniform at outdoors. Also, the temperature measured by a temperature sensor attached to the back

of the PV module is not likely to equal the actual cell temperature, given the constant changing environmental conditions, as addressed in King (2008) and Krauter and Preiss (2009).

In the particular case of bifacial PV modules, the major concern refers to unwanted shading on the back surface, therefore, the sensor should be as small as possible. At the same time, these measurements have to be representative. In this sense, the study carried out by Kenny et al. (2018) reports that with seven temperature sensors attached to the back of a bifacial module, temperature differences up to 5.5 °C were found, whereas when using only two sensors, the maximum difference measured was 2 °C. Thus, there is a trade-off between accuracy and the occurrence of shading at the rear face of the bifacial modules due to the attachment of more sensors. Since the photo-generated currents of the front and rear faces are summed up to compose the total cell current, differences in current capacity of the cells are unwanted, given the fact that the cells in a module are connected in series and share the same current level during normal operation.

The Technical Specification IEC-60904-1-2, *Photovoltaic devices – Part 1-2* from IEC (2021a) is the first-line reference on the subject of characterizing bifacial modules. However, it does not make any reference regarding temperature measurement of these devices. Instead, it just makes reference to IEC-60904-1 from IEC (2003), which is a well-established set of standards regarding the characterization of PV devices. A more detailed description referring to the position of sensors is given by the IEC (2009), which is IEC-60891 international standard.

2.2.3 **Concentrate multi-junction PV modules**

Two main points differentiate concentrate (HCPV) multi-junction (MJ) PV modules from flat-plate technologies. First, the MJ cells are composed of different semiconductor materials, covering different bandgap energy levels, allowing a larger use of the solar spectrum. Second, the modules employ optical elements to concentrate the beam radiation on the cells. Concentration is required due to the fact that MJ cells are much more expensive than regular PV cells, thus, they are manufactured in very small sizes. To illustrate this: the poly-Si modules considered in this work contain cells measuring 100 x 100 mm, whereas the HCPV modules are composed by cells measuring only 0.4 x 0.4 mm. An image showing a CPV module is provided in Fig. 2-19, where the most striking difference in comparison to regular PV modules is the presence of lenses (called Fresnel lenses) on the front face, in addition to a noticeable greater thickness.

Figure 2-19: A CPV module with lenses

The particular HCPV modules employed in this work are composed by three junctions, namely InGaP (top cells), InGaAs (middle cells) and Ge (bottom cells), presenting different bandgap energy levels, which are respectively 1.86 eV, 1.4 eV and 0.65 eV.

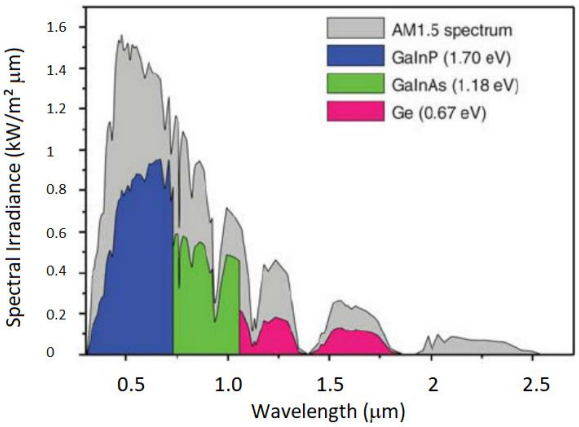

Figure 2-20: Use of AM0 solar spectrum by multi junction PV cells

The presence of different bandgap levels is precisely what allows a better use of the solar spectrum, in comparison with the adoption of a single bandgap level. On the one hand, the low bandgap junction allows the rightmost part of the spectrum to be used. On the other hand, the higher bandgap level presented by the top cell acts reducing thermalization, according to Pérez-Higueras and Fernández (2015). An illustration of the use of the AM0 spectrum by MJ cells is shown in Fig. 2-20 (Yastrebova, 2007).

This thesis is being developed using the same solar tracker (and some of the HCPV modules) employed in the doctoral thesis of Benhammane (2019), and in the publication of Benhammane et al. (2021). The objective of the Benhammane's work was to develop and to validate an operational PV power model for HCPV power plants, avoiding the requirement for numerous data inputs. In these works, the authors presented a study concerning seven different modeling methods to estimate the output power of HCPV arrays. The model described in Eq. (2.19) was found as the best in terms of minimizing the root-mean-square error between measured and predicted power. $P_{\mathrm{DC},0}$ refers to the HCPV array's nominal power, whereas BNI_0 is 1000 W/m² and $T_{\mathrm{air},0}$ is 25 °C.

$$P_{\mathrm{mp,c}} = P_{\mathrm{DC},0} \cdot \mathrm{a}\,\frac{\mathrm{BNI}}{\mathrm{BNI}_0} + \mathrm{b}\left(\frac{\mathrm{BNI}}{\mathrm{BNI}_0}\right)^2 + \mathrm{c}\,\frac{\mathrm{BNI}}{\mathrm{BNI}_0}\ln\left(\frac{\mathrm{BNI}}{\mathrm{BNI}_0}\right)\left(1+\mathrm{d}.\left(T_{\mathrm{air}}-T_{\mathrm{air},0}\right)\right)\left(1+\mathrm{e}.\left(\mathrm{AM}-\mathrm{AM}_0\right)\right) \tag{2.19}$$

In Eq. (2.19), the coefficients a, b, c, d and e were calculated using a least-squares regression technique. A relevant advantage shown by Eq. (2.19) is the use of ambient temperature instead of PV cell temperature. Multi-junction PV cells are usually much smaller than regular PV cells, therefore, measuring actual cell temperature is not a trivial task.

2.2.4 **Remarks regarding the temperature of PV modules**

Measuring the temperature of PV modules is a challenging task since the cells are not accessible. Therefore, a usual way of measuring the temperature of PV devices if by attaching sensors

at the back surface of the modules. However, this introduces a temperature error: a temperature difference between the cell and the back sheet of PV modules up to 3 °C has been reported in literature King (2008) and Rao Golive et al. (2022). For glass-glass encapsulation, Rao Golive et al. (2022) suggest adopting a 5.5 °C temperature difference between the cell and the rear glass cover. Considering concentration modules, a 13 °C temperature difference between the multi-junction cell and the heat-sink was reported by researchers at the Sandia Laboratories (King et al., 2004). All mentioned temperature differences were reported for irradiance (GNI for flat-plate and BNI for HCPV modules) levels of 1000 W/m². In this thesis, suitable temperature corrections were applied to the measured datasets via the use of Eq. (2.20), (King, 2008) which scales the temperature differences according to the irradiance. In Eq. (2.20), *G* represents GNI for the flat-plate PV arrays, and BNI for the HCPV array.

$$T_{\mathrm{C,corrected}} = T_{\mathrm{C,measured}} + \frac{G}{G_{STC}} . \Delta T \tag{2.20}$$

The PV cells' temperature can be calculated using the open-circuit voltage (V_{oc}), as proposed by the international standard IEC-60604-5 (IEC, 2011) and by Abe et al. (2019). However, in this thesis, the PV arrays are always in operation via the inverters, at the maximum power point, that is, the P_{mp}, with voltage V_{mp} and current I_{mp}. Therefore, V_{oc} measurements are not performed.

2.3 ASSESSING THE PERFORMANCE OF PV SYSTEMS

The conversion efficiency of PV devices is mainly influenced by the PV technology, the amount of solar irradiance and the operating cell temperature. The international standard IEC-61724 (IEC 2021b) provides guidelines for the performance assessment of PV systems. It recommends the use of the Performance Ratio (PR) parameter as an indicator of system performance. The PR is a dimensionless quantity, which considers the output power of a PV system, as well as the incident solar radiation. PR can be interpreted as a ratio relating the actual efficiency (η) of the system and the nominal efficiency (η_{STC}), as shown by Eq. (2.21).

$$\mathrm{PR} = \frac{\eta}{\eta_{\mathrm{STC}}} \tag{2.21}$$

The terms in Eq. (2.21) are defined by Eqs. (2.22) and (2.23).

$$\eta = \frac{P_{\mathrm{mp}}}{A_{\mathrm{PV}}\, G} \tag{2.22}$$

In Eq. (2.22), P_{mp} is the maximum power point of the PV system for a given operating condition, whereas A_{PV} is the area of the PV array and *G* is the global irradiance at the plane of the PV array (GNI), for the case of the p-Si and m-Si modules. For the case of bifacial modules, *G* is the effective irradiance G_E, whereas for the case of HCPV modules, *G* is BNI.

It is worth noting that the instantaneous (power) efficiency referring to the HCPV modules is high, in comparison to the efficiency presented by the other three technologies. However, this does not necessarily mean that the energy harvested by an HCPV array is higher than that harvested by a p-Si, m-Si or bifacial array. The reason is that an HCPV array only converts the BNI radiation component,

which is usually not as available as the global irradiance component used by the other technologies. It should be highlighted that p-Si, m-Si and bifacial arrays also convert the diffuse component, whereas such a component is not useful for HCPV systems.

$$\eta_{\mathrm{STC}} = \frac{P_{\mathrm{mp,STC}}}{A_{\mathrm{PV}}\, G_{\mathrm{STC}}} \tag{2.23}$$

In Eq. (2.23), $P_{\mathrm{mp,STC}}$ and G_{STC} are, respectively, the nominal maximum power of the PV array and the nominal irradiance, which is 1000 W/m² in STC condition. Important factors that contribute to reduce PR are the cell temperature (if different from 25 °C), soiling, losses in cables, connectors and in the inverter, spectral losses and ageing effects. In Eq. (2.23), G_{STC} is 1000 W/m² for the p-Si, m-Si and bifacial technologies. The STC ratings for bifacial technologies consider only the front-side performance. In turn, for the HCPV, G_{STC} represents BNI of 1000 W/m².

By combining Eqs. (2.22) and (2.23), a new format for PR (Eq. 2.24) is obtained.

$$\mathrm{PR} = \frac{P_{\mathrm{mp}}}{P_{\mathrm{mp,STC}}}\,\frac{G_{\mathrm{STC}}}{G} \tag{2.24}$$

2.4 THE DURISCH EFFICIENCY MODEL

An efficiency model was introduced by Durisch et al. (2007) based on solar irradiance, cell temperature and air mass. The efficiency model is provided in Eq. (2.25), where coefficients p, q, m, r, s and u are usually identified based on experimental measurements, fitting techniques to minimize the squared error referring to the experimental and modeled efficiencies. The reference parameters (with subscript 0) are G_0 (1000 W/m²), $T_{c,0}$ (25 °C) and AM_0 (1.5).

$$\eta_c = \mathrm{p}\left[\mathrm{q}\frac{G}{G_0} + \left(\frac{G}{G_0}\right)^{\mathrm{m}}\right]\left[1 + \mathrm{r}\frac{T_c}{T_{c,0}} + \mathrm{s}\frac{\mathrm{AM}}{\mathrm{AM}_0} + \left(\frac{\mathrm{AM}}{\mathrm{AM}_0}\right)^{\mathrm{u}}\right] \tag{2.25}$$

Relevant parameters can be calculated based on Eq. (2.25): the STC efficiency (Eq. (2.26)), the temperature coefficient for the STC efficiency (Eq. (2.27)), and the STC power (Eq. (2.28)).

$$\eta_{\mathrm{STC}} = \mathrm{p}[\mathrm{q}+1][2+\mathrm{r}+\mathrm{s}] \tag{2.26}$$

$$\alpha_{\mathrm{STC}} = \frac{\mathrm{p}(\mathrm{q}+1)\mathrm{r}}{T_{c,\mathrm{STC}}} \tag{2.27}$$

$$P_{\mathrm{STC}} = \eta_{\mathrm{STC}}\, G_{\mathrm{STC}}\, A_{PV} \tag{2.28}$$

Durisch et al. (2007) provided, also, transformation equations, allowing to express the efficiency at constant irradiance and cell temperature; constant irradiance and air mass; or at constant cell temperature and air mass. The model can be adjusted to respond according to a single variable, while keeping the other two constant. This way, two-dimensional analysis can be carried out, for

example, by plotting the measured and modelled efficiency levels versus one of the three external variables, one at a time. The transformation equations are presented in detail by Durisch et al., (2000); Eqs. (2.29) to (2.31) refer to the model, whereas Eqs. (2.32) to (2.34) refer to the measurements.

$$\eta_{c,1000,1.5} = \mathrm{p}[\mathrm{q}+1]\left[2+\mathrm{s}+\mathrm{r}\frac{T_c}{T_{c,0}}\right] \tag{2.29}$$

$$\eta_{c,25,1.5} = \mathrm{p}\left[\mathrm{q}\frac{G}{G_0}+\left(\frac{G}{G_0}\right)^{\mathrm{m}}\right][2+\mathrm{r}+\mathrm{s}] \tag{2.30}$$

$$\eta_{c,1000,25} = \mathrm{p}[\mathrm{q}+1]\left[1+\mathrm{r}+\mathrm{s}\frac{\mathrm{AM}}{\mathrm{AM}_0}+\left(\frac{\mathrm{AM}}{\mathrm{AM}_0}\right)^{\mathrm{u}}\right] \tag{2.31}$$

$$\eta_{meas,25,1.5} = \eta_{meas}(G,\ T_{\mathrm{c}},\mathrm{AM}) - \eta_c(G,\ T_{\mathrm{c}},\mathrm{AM}) + \eta_{c,25,1.5} \tag{2.32}$$

$$\eta_{meas,1000,1.5} = \eta_{meas}(G,\ T_{\mathrm{c}},\mathrm{AM}) - \eta_c(G,\ T_{\mathrm{c}},\mathrm{AM}) + \eta_{c,1000,1.5} \tag{2.33}$$

$$\eta_{meas,1000,25} = \eta_{meas}(G,\ T_{\mathrm{c}},\mathrm{AM}) - \eta_c(G,\ T_{\mathrm{c}},\mathrm{AM}) + \eta_{c,1000,25} \tag{2.34}$$

Works conducted by Hamou et al. (2014) and Bërdufi et al. (2016) are examples of application of the Durisch model and the transformation equations.

2.5 STUDIES COMPARING DIFFERENT PV TECHNOLOGIES

Different PV technologies present distinguished characteristics – for instance, spectral response and temperature factors – therefore they may perform differently even when operating side-by-side at the same site and using identical installation methods. When considering conventional single junction monofacial modules, in contrast to multi-junction or bifacial technologies, the differences in performance are even more significant, given the particularities of these two types of PV modules.

Manufacturers report the performance of PV modules under STC; however, this refers to a single condition (GNI = 1000 W/m², T_c = 25 °C and AM1.5) which is hardly found in real field operation. Therefore, studying the performance of different PV technologies under the same operating condition becomes relevant as it allows to identify which type of PV module is more sensitive to particular environmental parameters.

When comparing the performance of different PV technologies, two important parameters to be evaluated are the energy yield over a certain period of time and the performance ratio, which take into account both the solar resource and the electricity production. These parameters have largely been employed in works concerning the performance of PV systems and are significant indicators for the long-term performance assessment. To study the sensitivity of PV devices to external parameters in detail, it is necessary to measure irradiance levels, module temperature and electrical parameters

such as voltage, current and power using a time step sized to allow short-term analysis of the parameter variations and the respective impact on system operation.

Solar trackers have been used to actively position a PV array facing the Sun, allowing increased electricity production, in comparison to fixed-tilt mounting. Drury et al. (2013) report that dual-axis trackers can achieve 30 – 45% increase in generation when compared to a fixed-tilt system. The use of tracking is more significant in regions which do not suffer from persistent cloud coverage, as tracking takes advantage of maximizing the beam radiation component.

2.5.1 **Monocrystalline and polycrystalline PV systems**

Literature on the comparison of PV systems is extensive and concerns cases where different technologies operate in the same site, as well as cases considering a given PV technology operating in different sites. Many works are focused on the long-term performance assessment of PV technologies which are commonly found in rooftops and PV fields, such as polycrystalline and monocrystalline; for instance, Nour-eddine et al. (2020) employed a PV array containing monocrystalline (m-Si) and polycrystalline (p-Si) technologies in a semi-arid climate (Morocco). Measurements were made for 12 months and different performance indicators were computed as per IEC-61724 (IEC 2021b). The authors found that the m-Si technology was the most suitable for that climate type, performing slightly better as in comparison to p-Si. However, given the higher cost associated with the m-Si technology, the technology of choice should be the p-Si, although the authors did not present a quantitative financial analysis. Although the m-Si array performed better than the p-Si, the first presents a thermal coefficient for P_{mp} which is higher (in modulus) than that of p-Si, whereas the STC efficiency is the same for the two technologies. This fact could indicate that p-Si would outperform m-Si; however, this point was not discussed by Nour-eddine et al. (2020). Another technology comparison is presented by Adar et al. (2020), where the authors carried out a 19-months measurement campaign in Morocco covering three PV technologies, among them, p-Si and m-Si. Similarly to Nour-eddine et al. (2020), the authors based their performance study on the indexes provided in IEC-61724; however, they employed the Principal Component Analysis (PCA) to study the experimental dataset. The work presented by Elibol et al. (2017) considered an experimental photovoltaic assembly located in Turkey, which is among the European countries with greatest solar potential. The authors found the p-Si technology to increase its efficiency as the temperature increases. This is a curious finding due to the fact that the temperature coefficient of power is negative for that technology. Other studies focusing on the comparison of different PV technologies were carried out in different countries: Balaska et al. (2017) considered an experimental assembly located in Algeria; the study presented by Tossa et al. (2016) concerns an experiment carried out in Burkina Faso for roughly one year, where four PV technologies, among them, one m-Si and two p-Si modules. Differently from the studies of Adar et al. (2020), Balaska et al. (2017), Elibol et al. (2017) and Nour-eddine et al. (2020), the modules were tested by means of an acquisition system capable of measuring I-V curves automatically according to predetermined time intervals. This means that the P_{mp} was determined regardless of any maximum power point tracking (MPPT) system. In turn, the study presented by Guenounou et al. (2016) also employed an experimental measurement system capable of performing continuous I-V curve measurements for four PV modules of different technologies. The authors employed an interesting approach for the performance calculations, using a) datasheet information; and b) outdoor measurements. By correcting the outdoor measurements to

STC, the authors were then able to calculate the performance ratio using both datasheet information and outdoor measurements. Both for m-Si and p-Si technologies, it was found that datasheet values for $P_{mp,STC}$ were higher than the value provided by outdoor measurements translated to STC. This produced higher annual PR values, for both technologies, when the outdoor measured data were used for the calculations. Table 2-2 summarizes the performance data obtained by the authors mentioned in this section.

Table 2-2: Summary of efficiency and performance ratio reported by other studies

Reference	Duration (months)	m-Si efficiency (%)	p-Si efficiency (%)	m-Si PR (%)	p-Si PR (%)
Nour-eddine et al. (2020)	12	14.94	14.91	85.51	85.37
Adar et al. (2020)	19	12.65	12.90	84.76	86.66
Balaska et al. (2017)	12	13.26	11.36	91	81
Elibol et al. (2017)	12	14.63	12.63	91.63	88.59
Guenounou et al. (2016)	12	13.49	11.01	88/95	80/98

To illustrate a fixed PV system mounting, Fig. 2-21 shows the experimental assembly used by Elibol et al. (2017).

Figure 2-21: Fixed PV system assembly

All the experimental PV systems previously mentioned in this section are fixed PV systems, that is, the modules were mounted on a structure presenting constant inclination and orientation angles.

In turn, the comparative study conducted by Visa et al. (2016) in Romania shows a remarkable difference in mounting: the authors implemented five types of flat-plate PV modules (among them, m-Si and p-Si) on a two-axis tracker, which is illustrated in Fig. 2-22. The authors used two platforms as the one presented in Fig. 2-22, allowing performance comparison when fixed tilt and orientation were employed. The results due to the use of a tracker with different crystalline PV modules are of interest in the context of the present thesis. With the use of the tracker, Visa et al. (2016) collected measured data for 16 months, regarding global irradiance, cell temperature, wind speed and electric output of the PV modules. The authors set one of the trackers with constant tilt (47°), south-oriented, and another one in dual-axis tracking mode. They found that tracking indeed improves the PV performance, however, it is the combination of relevant factors (irradiance, cell temperature and wind profile) that governs the amount of gain in terms of energy. The average efficiency levels for the tracker system were 16.49 % (p-Si) and 16.37 % (m-Si), whereas the authors report average 10 % gain on output power for the tracking system, as in comparison with the fixed mounting. The authors state that the higher

temperature of the modules on the tracker – compared to those installed on the fixed system – is an important factor that limits the gain in power. Besides this, they mention that snow takes longer to melt during sunrise on the tracker system, impairing the production. Moreover, during days with preponderant diffuse irradiance – where the ratio between the diffuse and global components is greater than 0.9 – the performance of both systems (tracked and fixed) is almost the same, and the use of a tracker is not justified.

Figure 2-22: Tracking PV system assembly

Also with PV trackers, the work conducted by Zarkov et al. (2016) considered five different PV technologies, which were compared in terms of measured and calculated performance. Two out of the five PV technologies coincide with the ones considered in this thesis: p-Si and m-Si. The PV modules were installed on 2-axis trackers, as shown in Fig. 2-23.

Figure 2-23: Different PV technologies installed on two-axis trackers.

The efficiency was adopted as the performance metric in the work of Zarkov et al. (2016). The measured efficiency was quantified using Eq. (2.22), whereas the theoretical efficiency was assessed using the Durisch efficiency model (Eq. 2.25). To determine the unknown parameters in the Durisch model, fitting procedures were consecutively executed aiming to minimize the squared error. The authors found the nRMSE between the measured and predicted efficiency to be within 3 %.

2.5.2 **Bifacial PV systems**

Bifacial technologies are among the most promising solutions for photovoltaic installations given that they currently present the same price per watt as conventional monofacial devices (Gu et al., 2020; Kopecek and Libal, 2021). The application of bifacial modules along with single-axis tracker systems provides the most cost-attractive solution for PV plants at present time, and bifacial PV devices are also a promising alternative for vertical and floating PV systems (Kopecek and Libal, 2021; Tina et al., 2021).

Several works in the literature focused on the comparison between bifacial and monofacial PV systems in terms of the electricity produced in a given time period. The goal of such studies was to determine the energy increase due to bifaciality, the so-called *bifacial gain*. In most cases, the monofacial and bifacial modules chosen by the authors were very similar in respect to their front-side performance specifications, therefore allowing direct comparison. For cases where the module specifications were not the same, a scaling factor based on datasheet power ratings was adopted, to allow a fair comparison in terms of normalized power rating of each PV system, as proposed by Stein et al. (2018).

A critical parameter for bifacial PV systems, which affects the bifacial gain, is the bifaciality index (φ), as defined in Eq. (2.9). It is a measure of how similar the module's rear-side performance is as in comparison to the front-side. The bifaciality index is a module-specific parameter and depends on the technology employed for the bifacial module production.

A study employing two dual-axis trackers with bifacial and monofacial modules is presented by Burnham et al. (2019). One of the systems contained bifacial modules with high bifaciality index (φ = 0.92), presenting bifacial gain of 14 %. In contrast, the other system studied by the authors used bifacial modules with lower bifaciality index (φ = 0.62), presenting a 4 % bifacial gain.

Regarding bifacial PV systems installed in snowy environments, Hayibo et al. (2022) compared monofacial and bifacial systems. In winter, bifacial modules take advantage of the increased amount of radiation reflected upwards due to snow ground coverage, which is an important contributor for increasing bifacial gain. The authors considered large fixed bifacial and monofacial PV arrays, consisting of over 4500 modules in total. A bifacial gain of 19 % was found during winter operation, however, the value of φ for the bifacial modules was not provided by Hayibo et al. (2022).

An annual bifacial gain of 14.8 % was reported by Gu et al. (2021), which compared fixed-tilt monofacial and bifacial modules (φ = 0.8). The authors assessed the bifacial gain for sunny and cloudy days, which presented average values of 13.1 and 16.5 %, respectively.

A comparison of monofacial and bifacial modules presenting different φ was carried out by Muehleisen et al. (2021). The module with φ = 0.7 presented bifacial gain ranging from 5 to 7 % (depending on the orientation), whereas the module with φ = 0.92 presented a 3 % higher yield than the module with lower φ. All modules were installed at the same site.

For experimental bifacial systems installed in desert environment, Baloch et al. (2020) reports bifacial gains of 8.6 and 16.3 %, respectively, for modules presenting φ = 0.65 and φ = 0.9.

It is therefore observed a wide range for the bifaciality index, which depends on the technology employed for the module manufacture. In turn, the bifacial gain also shows great variation since is a

function of the bifaciality and the characteristics of the installation site, where the ground albedo and module height are of great relevance.

A comprehensive techno-economic assessment carried out by Rodríguez-Gallegos et al. (2020) mentions a 40% gain in yield for bifacial systems using two-axis trackers, in comparison to fixed conventional systems. However, the authors state that two-axis tracker systems present significantly higher cost of energy produced: for latitudes within +/- 60°, the cost of the tracker should decrease by 60% for the system to present the lowest cost of electricity, in comparison with fixed PV installations. Rodríguez-Gallegos et al. (2020) concluded that bifacial PV systems with two-axis tracking produce 7% more electricity compared to monofacial PV systems with two-axis tracking; 4% more than bifacial with one-axis tracking; 11% more than monofacial with one-axis tracking; 31% more than bifacial with fixed tilt; and 40% more than monofacial with fixed tilt.

Burnham et al. (2019) conducted a two-year measurement campaign with two dual-axis bifacial systems in Vermont (USA). Monofacial modules were installed on the tracker as well, to provide a resource for comparison. Tracker 1 was fitted with 60-cell framed monofacial m-Si modules and 60-cell frameless m-Si bifacial modules. Tracker 2 had 72-cell framed monofacial m-Si modules and 72-cell m-Si framed bifacial modules. A picture of Tracker 2 is shown in Fig. 2-24.

The primary interest of Burnham et al. (2019) was on the performance of the bifacial modules in a site which receives snow from five to six months per year, thus providing a high-albedo surface to contribute to the bifacial gain. The authors concluded that dual-axis tracking systems with bifacial modules present 14 % energy gain in comparison with dual-axis tracking systems with monofacial modules during the winter. This tends to reduce the cost of energy in regions which present persistent snow cover. In comparison to a south-facing, 30° fixed-tilt bifacial system, the dual-axis tracking mounting with bifacial modules yielded 41 % more energy, in agreement with Rodríguez-Gallegos et al. (2020).

Figure 2-24 – A tracker with 10 monofacial modules (right) and 10 bifacial modules (left). Source: Burnham et al. (2019)

2.5.3 **Concentration PV systems**

Concentration multi-junction PV devices present unique features which significantly differ from flat-plate PV technologies – including bifacial modules. Given that the beam irradiance is the only component of the solar radiation which can be concentrated, the use of a tracker is necessary for HCPV devices to operate adequately. Such a requirement inevitably introduces additional cost to HCPV

plants; these trackers must have a high tracking precision, higher than for trackers using flat-plate PV modules. If the precision is low, the concentrated beam irradiance does not reach the very small PV cell and the electricity production is null. Consequently, the price of such a tracker is significantly high. Some works have been done to address the performance of HCPV devices in comparison to other PV technologies, and in order to provide all the modules with the same solar resource, it becomes necessary to install all the modules on a tracker; however, literature usually presents comparisons between HCPV modules mounted on trackers and conventional flat-plate PV modules mounted on fixed-tilt stands. Although this approach is more representative of real installations, it does not allow providing the same solar resource for all the technologies under study.

A study conducted by Bianchini et al. (2016) in Italy tackled both technical and economic aspects of different technologies of PV sources, including HCPV. Eight PV technologies were studied, among them monocrystalline and polycrystalline (both mounted on fixed-tilt stands) and a HCPV plant mounted on a dual-axis tracker. Since the PV arrays referring to each technology present different power specifications, the electricity produced by each PV plant over a specified period was divided by the respective nominal power. The resulting parameter, Y_a (array yield) is given in kWh/(kW_p.year). For the m-Si, p-Si and HCPV modules, the values of Y_a were respectively 1075, 1046 and 699 kWh/(kW_p.year). Regarding the cost of electricity, the authors report 0.129, 0.135 and 0.336 euros per kWh, respectively for m-Si, p-Si and HCPV technologies. The HCPV technology, although presenting greater efficiency (26 %, triple-junction gallium arsenide cells – GaAs) as in comparison to m-Si (heterojunction) (19 %) and p-Si (14.7 %), only converts the beam radiation component. The authors report that regarding the HCPV, the smaller Y_a is justified by the fact that the installation site receives a relatively low amount of beam radiation yearly. Moreover, the significantly greater cost of electricity produced by the HCPV plant refers not only for the higher initial installation cost, but also to the dual-axis maintenance requirements.

A side-by-side comparative study was carried out by Libby et al. (2015), in the USA. The authors compared the performance of different PV modules, being two polycrystalline, one monocrystalline and two HCPV, aiming to obtain typical operational profiles. As in other studies, the flat-plate modules were installed on fixed-tilt racks, whereas the HCPV modules were fitted on dual-axis trackers. Fig. 2-25 depicts the experimental assembly.

Figure 2-25: flat-plate and HCPV experimental plants. Source: Libby et al. (2015)

For a clear-sky day, the power profile is quite different, considering the fixed and tracking systems. Normalized power profiles are presented in Fig. 2-26. It shows that the output of the HCPV systems remains almost flat for roughly eight hours, whereas the flat-plate plants slowly ramp-up and down, remaining only about 2 hours near the peak power. The HCPV power profile is steep at the

beginning of the day because of the tracker operational range: there is a minimum solar altitude angle for the tracker to operate. A similar behavior is observed near the sunset. As a result, the flat-plate technologies supply power to the grid for a greater number of hours, however, at a low intensity during sunrise and sunset.

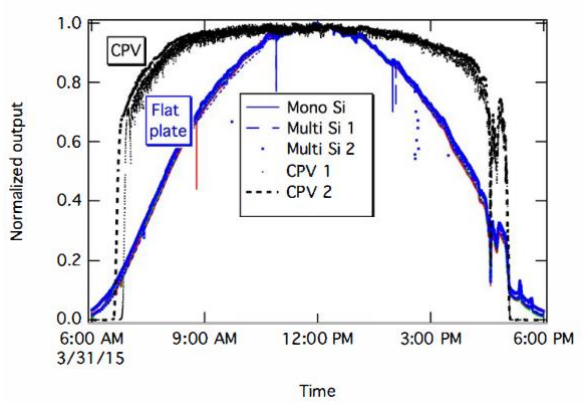

Figure 2-26: Power profile for fixed-tilt (flat-plate) and 2-axis tracker (HCPV). Libby et al. (2015)

The experimental assembly proposed in this thesis presents significant and novel differences and features in comparison with other systems described in literature. All PV modules – HCPV, bifacial, monocrystalline and polycrystalline – were installed on a 2-axis tracker. To date, this seems to be the only experimental system joining these four technologies on such a mounting scheme.

2.6 GRID-INTERACTIVE INVERTERS FOR PV SYSTEMS

Grid-connected inverters are key elements in PV systems. They provide not only the DC/AC conversion, but also determine the optimal operating point of the PV array, by means of an MPPT (maximum power point tracking) strategy. Besides this, they are responsible for connecting the PV system to the utility grid, performing automatic synchronization and voltage/current control.

The relationship between the nominal power ratings of the inverter and of the array is referred to as inverter sizing ratio (SR), computed using Eq. (2.35). The parameters $P_{\mathrm{mp,STC}}$ and $P_{\mathrm{inv,N}}$ are, respectively, the nominal peak power of the PV array and the nominal power rating of the inverter.

$$\mathrm{SR} = \frac{P_{\mathrm{inv,N}}}{P_{\mathrm{mp,STC}}} \tag{2.35}$$

The inverter sizing ratio dictates the typical inverter loading, which is a relevant aspect: strongly oversized or undersized inverters may operate with relatively low annual efficiency values. The reason for this is the efficiency x loading curve, shown in Fig. 2-27 (Wang et al., 2018). Macêdo and Zilles (2006) carried out an experimental campaign with eight PV systems, each with different SR configurations, ranging from 55 to 102 %, using inverters of the same model. For that entire SR range, the authors did not find a significant variation among the final yield of the PV systems studied. In fact, Rodrigues Neto et al. (2020) describe an experimental study in which the inverter was operated under 50% load; despite that, the DC/AC conversion efficiency was around 95 %. Such an inverter efficiency level is quite high, considering that the equipment is underloaded.

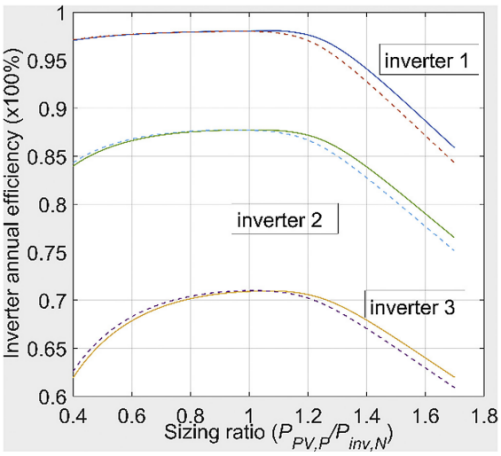

Figure 2-27: Annual inverter efficiency as a function of inverter sizing ratio for 3 different PV inverters. Source: Wang et al. (2018)

Wang et al. (2018) conducted a study to determine the optimal inverter sizing ratio for two PV systems, from the energetic and economic perspectives. The authors found that including the economic aspect causes the optimal sizing ratio interval to decrease. Moreover, the authors also considered a degradation rate for the PV array. This caused a 10% increase in the optimum sizing ratio. Toreti Scarabelot et al. (2021) made an assessment of how overirradiance affects the performance of PV systems when different inverter sizing ratios are considered. The authors studied two PV systems located in southern Brazil. System “A” and “B” were designed with different sizing ratio values, respectively, 0.76 and 0.92. Given that the two PV systems were installed in different locations (30 km apart), system “A” received 4.2 % more irradiation than system “B”. However, the average monthly final yield values, evaluated over one year, were 98.56 kWh/kW_p and 111.82 kWh/kW_p. This shows the relevance of the sizing ratio on PV systems’ performance.

Notton et al. (2010) proposed a method to determine the optimal inverter rating, considering site characteristics, inverter type and the PV technology. It was found that regarding inverter sizing ratio, the inverter's efficiency curve is more important than the PV module technology being used in the PV array. Regarding the efficiency of PV inverters, Rampinelli et al. (2014) developed mathematical models to describe system operation. The authors considered experimental and theoretical approaches to calculate fitting coefficients to describe the efficiency behavior of 9 different inverters. For each case, the authors compared the actual efficiency curves and the performance described by the model (adjusted for each particular inverter), where excellent correlation was observed.

The international standard IEC 61683 (IEC, 2019) provides guidelines for the in-factory efficiency tests of inverters. The tests must be carried out at 25 °C ambient temperature, with direct measurements of input and output power levels. Since IEC 61683 is aimed at assessing the intrinsic efficiency of the power conditioner, it does not consider the efficiency of the MPPT system. This way, the measurements are carried out with fixed DC voltage and current levels. On the other hand, the standard IEC 63156 (IEC, 2021b) is devoted to the efficiency assessment of PV inverters under dynamic conditions. The document specifies procedures for inverter performance calculation based on power efficiency, however, additional methods for energy efficiency calculation are also provided.

2.7 CONCLUSIONS FOR SECTION 2

This section introduced the basic aspects regarding solar radiation, which is composed by three components: beam radiation, which comes straight from the Sun; diffuse radiation, consisting of radiation that is scattered in the atmosphere, and diffused by the sky dome; and reflected radiation. The sum of these components forms the global irradiance. Instruments for irradiance measurement include pyranometers and reference solar cells, for the global irradiance; pyrheliometers, for the beam irradiance; and shaded pyranometers for the diffuse irradiance. The state of the sky can be defined by indexes such as the clearness index and the diffuse fraction, computed from the irradiance quantities.

The four PV technologies considered in this work are the polycrystalline (p-Si), monocrystalline (m-Si), bifacial and multi-junction cells under concentration (HCPV). p-Si and m-Si are the most common, consisting of regular flat-plate modules with glass-EVA encapsulation. The main differences between such two technologies are the efficiency and the behavior of the DC power with respect to the temperature. The efficiency of p-Si cells is typically lower than that of m-Si cells, meaning that for a same rated power, p-Si PV modules require more array area than m-Si. In turn, p-Si devices are usually more sensitive to the operating temperature, in comparison to m-Si cells. This means that, for the same temperature, p-Si modules present higher temperature-driven DC power reduction than m-Si modules. The bifacial modules present the remarkable ability to convert, also, the radiation reaching their rear surface, thus providing a gain in power and, therefore, in energy yield. Such a yield increase is the so-called bifacial gain, which is a function of three main variables: a) bifaciality index of the PV cells, which is the ratio between the rear and front-side efficiencies; b) system design, where the PV array's clearance from the ground is a relevant parameter; and c) the ground coverage, which influences the albedo. Bifacial modules usually present glass-glass encapsulation and are composed by modified m-Si cells. The HCPV technology presents two main characteristics. First, the cells are built using three different semiconductor materials, allowing a larger use of the solar spectrum. These cells present a much higher cost than regular PV cells; thus, they are built in small sizes since the cost is proportional to the cell's area. Second, the radiation is concentrated by lenses fitted onto the modules, to compensate the relatively small area of multi-junction cells. Due to the concentration, HCPV modules respond only to the beam irradiance. Thus, HCPV arrays must be constantly facing the Sun, requiring a dual-axis solar tracking system which further increases the initial cost of a HCPV system.

Photovoltaic systems can be compared using the performance ratio (PR), which is calculated from the ratio between the measured and rated PV efficiency. This allows the PR to be calculated as an instantaneous metric, that is, with a particular value in each time step. It is worth mentioning that the PR can also be calculated by integrating the output power and solar irradiance over a given time frame. This way, the PR is a function of the electrical energy and the solar irradiation for a given period.

Studies in the literature show bifacial gains ranging from 4 to over 19 %, relatively to regular p-Si or m-Si arrays. However, reported BG levels greater than 10 should be critically assessed since the conditions for the experimental measurements might not be representative of real-world applications, as typical BGs are around 5 %. Previous studies with HCPV devices did not include regular PV technologies installed on the same solar tracker; therefore, the operating conditions are not the same for all PV systems under study, particularly regarding the solar resource and operating temperature.

SECTION 3

EXPERIMENTAL RESOURCE AND ELECTRICAL CHARACTERIZATION OF PV MODULES

3 EXPERIMENTAL RESOURCE AND ELECTRICAL CHARACTERIZATION OF PV MODULES

This section introduces UDCPP's Renewable Energy Laboratory, and the experimental resource for this thesis. The PV tracker, the modules and the measurement instruments are presented in detail, and the modeling methods developed for the outdoor characterization of PV modules are explained.

3.1 THE RENEWABLE ENERGY LABORATORY IN AJACCIO

The Georges Peri UDCPP campus at Vignola – Ajaccio (UMR SPE CNRS 6134) features the Paglia Orba micro-grid research platform, which encompasses various renewable energy systems and different energy storage means. The electricity production, the dispatch to/from the external grid, as well as the storage charge/discharge can be managed using different operating modes. The site – which contains electric cars, offices, laboratories and even an apartment building for researchers and students – enables research to be carried out on a wide range of subjects, from solar resource prediction, solar thermal and solar PV conversion, electric mobility, chemical energy storage systems (batteries and hydrogen), pumped hydro storage and intelligent control and management systems. The Vignola campus is illustrated in Fig. 3-1.

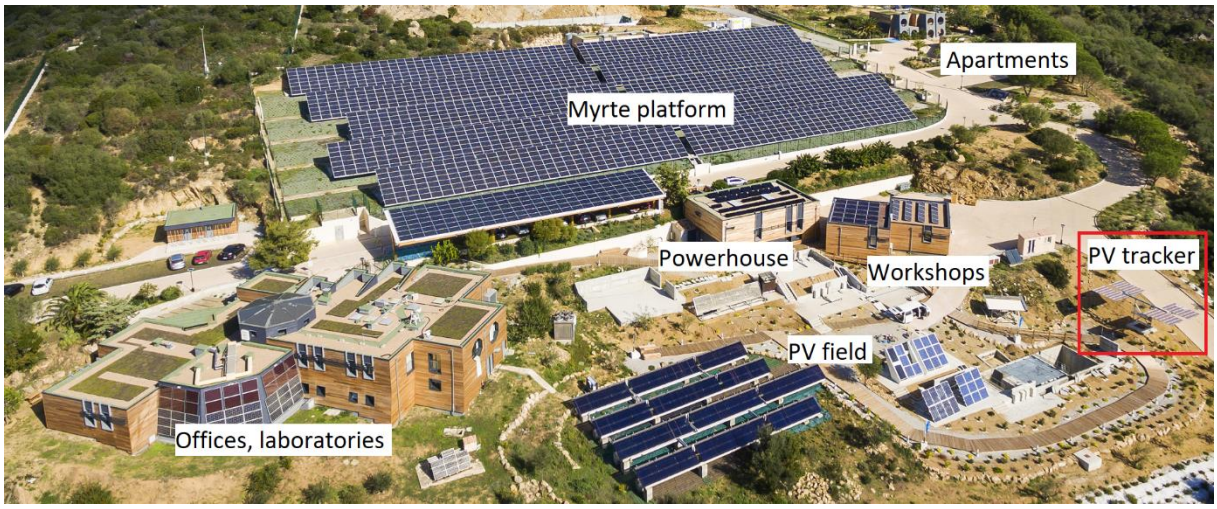

Figure 3-1: General view of the UDCPP campus at Vignola

The largest PV array belongs to the Myrte Platform, where the electricity is fed into electrolyzers, which produce hydrogen (H_2) and oxygen (O_2) from water. These gases and respective energy content are then stored in tanks (not seen in Fig. 3-1). When needed, the H_2 and O_2 are directed to fuel cells for electricity production. The 28 Myrte PV inverters, as well as the fuel cells are connected to the external utility grid. All other PV arrays have the respective inverter outputs sent to the powerhouse. The powerhouse contains different battery types (Fig. 3-2), whose charge is managed by special inverters, able to connect PV generators with batteries and with the grid at the same time.

In the powerhouse, a very smart electric panel arrangement has been adopted: it is possible to organize three independent micro-grids (Fig. 3-3), allowing different configurations between sources and loads, adopting different control strategies, with or without storage, while feeding loads with different power profiles over the time, being the grids isolated or grid-connected.

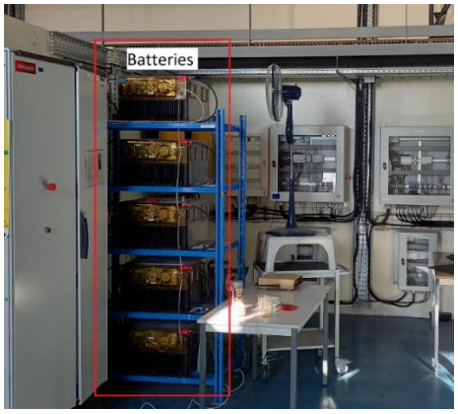

Figure 3-2: View of one of the battery banks (Zebra batteries) inside the powerhouse

In summary, the powerhouse offers flexible connections as it receives power from all sources and sends power to all loads, whereas allowing connection with the external grid and the battery storage systems.

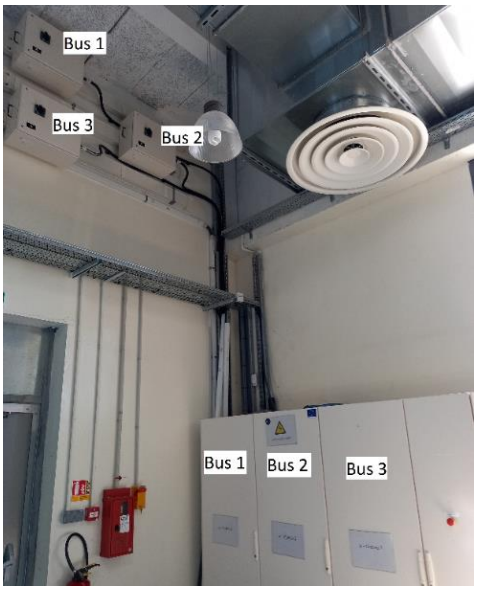

Figure 3-3: Panels and buses for the three flexible research micro-grids

Besides providing power connections, it is in the powerhouse that all field signals are concentrated (Fig. 3-4), processed and sent to the supervisory system. The powerhouse holds, also, the control room (Fig. 3-5). All signals from the field reach the powerhouse using optic fiber.

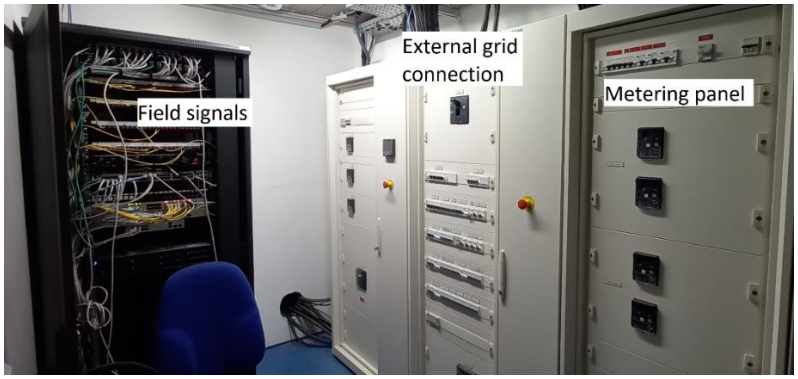

Figure 3-4: Field signals panel and external grid / metering panels

The use of optic fiber presents remarkable advantages: it is immune to magnetic interference; it avoids overvoltage caused by malfunctions or by lightning from reaching the signal receivers; and it does not suffer from voltage drop issues due to long transmission distances.

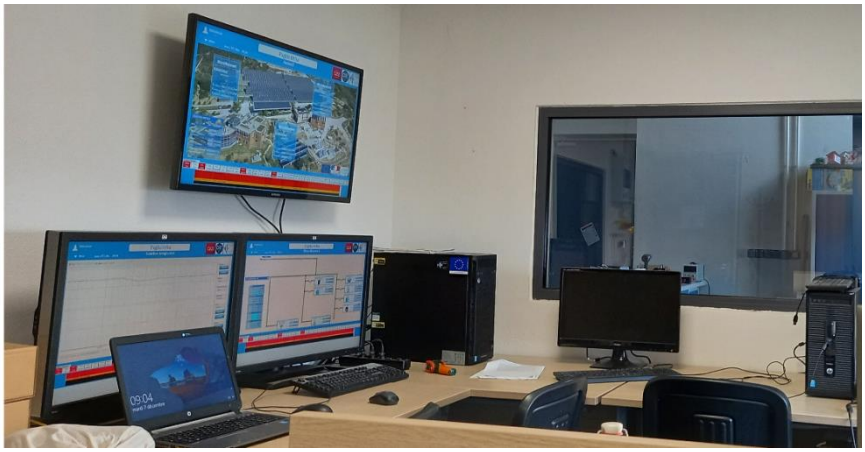

Figure 3-5: The control room inside the powerhouse

In Fig. 3-1, on the far-right side, there is a structure highlighted by a red square. This is the PV tracker, which is the experimental resource for this thesis. This system is detailed in the following.

3.2 THE SOLAR TRACKER AND THE PV MODULES

The HL-39 2-axis HeliosLite PV tracker was originally installed in UDCPP campus Vignola for the study of HCPV modules. Given that HCPV modules are provided with lenses, and that the only solar radiation component which can be concentrated is the beam, tracking is mandatory to keep the HCPV modules always facing the Sun. The original tracker assembly, containing only HCPV modules installed, as shown in Fig. 3-6 a), was modified: monocrystalline, polycrystalline and bifacial modules were included for the present thesis. This way, each of the four quadrants of the tracker is fitted with a different PV technology, as illustrated in Fig. 3-6 b).

a) b)

Figure 3-6: The HL-39 tracker: a) Original modules; b) With four different PV technologies

In cases where the wind speed is above 30 km/h, or the solar irradiance is too low – for example in overcast days or after sunset – the tracker goes to the so-called rest position, as shown in Fig. 3-7.

Figure 3-7: The PV tracker in its “rest” position

The HL-39 tracker datasheet (HeliosLite, 2019) presents relevant information regarding the tracker operation, such as average daily energy consumption of 200 Wh and tracking accuracy of 0.1° and 0.2°, respectively for wind speeds of 0-4 and 4-8 m/s.

The HCPV arrays’ voltage and current are continuously monitored by the tracker control system. When the Sun rises, the PV array voltage increases, and the tracker is initially positioned according to calculated angles of azimuth and altitude to make the PV modules face the sun. Then, the tracker applies small changes in the positioning angles while monitoring the maximum power point of the HCPV array to determine the optimal position. This power monitoring and position correction is constant during operation; however, it occurs in a time frame wider than the one used on the inverter’s MPPT since it is not desired that the two control schemes overlap each other.

In the specific assembly prepared for this thesis, the HCPV array is the one being monitored by the tracker, given the greater dependence of concentration PV on the radiation angle of incidence, as in comparison with the other technologies under study. The manufacturer states that the HL-39 tracker can increase energy yield of a PV plant by 30-50 %. Notton and Diaf (2016) carried out a study considering the solar irradiation observed for different mounting inclinations, as well as one and two-axis tracking. The authors found that tracking indeed increases the solar irradiation on PV modules. Given that tracking systems represent additional costs, the authors propose changing the PV array’s tilt seasonally (four times a year), as a measure to increase the solar energy harvested whereas avoiding the costs associated to trackers. Fig. 3-8 depicts the comparison between the performance ratio for fixed and tracking PV systems, as a function of daytime, clearly showing the increase in PR obtained from sunrise to sunset.

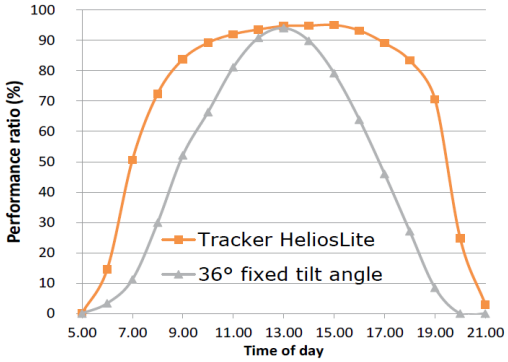

Figure 3-8: A plot from the HL-39 tracker datasheet: PR with and without tracking

3.3 PV MODULES INSTALLED ON THE TRACKER

The four PV technologies installed on the tracker refer to modules with specifications that differ widely in terms of electric characteristics, efficiency and size. Table 3-1 summarizes the datasheet information regarding the four models of modules, under STC.

Table 3-1: Datasheet specifications for the four PV modules installed on the tracker.

Parameter	Poly-Si Photowatt PW1650	Mono-Si Sunpower SPR-327	Bifacial Trina Solar TSM-335DEG6MC(II)	HCPV Semprius SM-U01
Maximum power, P_{mp} (W)	175	327	335	87.5
Voltage at maximum power, V_{mp} (V)	35.0	54.7	34.1	86.6
Current at maximum power, I_{mp} (A)	5.0	5.98	9.83	1.01
Open-circuit voltage, V_{oc} (V)	43.4	64.9	40.8	101.6
Short-circuit current, I_{sc} (A)	5.3	6.46	10.35	1.06
Module efficiency (%)	15.0	20.4	19.7	33.9
Module area (m²)	1.17	1.60	1.70	0.26
Temperature coefficient for I_{sc}, α (%)	0.03	0.04	0.05	-
Temperature coefficient for V_{oc}, β (%)	-0.36	-0.27	-0.29	-0.14
Temperature coefficient for P_{mp}, ϒ (%)	-0.42	-0.35	-0.37	-0.14
Number of cells	72	96	120 (half-cells)	660
Number of modules on the tracker	6	4	6	28

Besides its capability of absorbing radiation on both front and rear sides, the bifacial module installed on the tracker presents another differential: the half-cut cells. The major benefit of such a construction is the smaller loss from series-resistance, since a half cell produces half the current. This is the reason why Table 3-1 shows that the bifacial contains 120 cells, although the open-circuit voltage suggests that it actually has 60 cells. The 120 cells are divided in two groups of 60 series-connected half-cells, which are then internally connected in parallel.

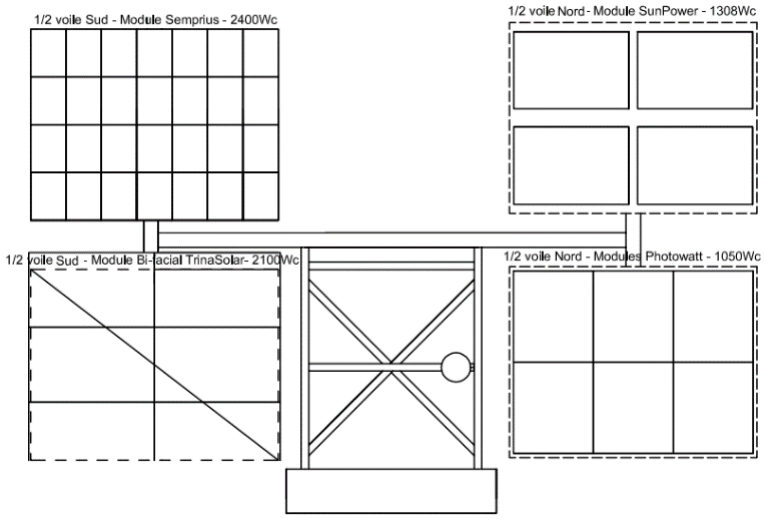

Figure 3-9: Schematic drawing of the tracker and the modules of each technology

A schematic illustration showing the position of the PV modules on the tracker is provided in Fig. 3-9. A particularity regarding the HCPV modules refer to the interconnections: in the HCPV array, there are four strings with seven modules each, and the strings are parallel connected. This means that the current at the inverter input is about 4 times greater than the current of a single module. The parallel connection was required because the HCPV modules' V_{mp} is significantly higher than that of common PV modules (refer to Table 3-1). Therefore, to reach the desired DC power, it was required to increase the current. This was achieved by connecting 4 strings in parallel. In contrast, for the other three PV arrays (p-Si, m-Si and bifacial), all similar modules are connected in series, in a single string.

3.4 IRRADIANCE (FRONT AND REAR) AND TEMPERATURE MEASUREMENT

Although the Campus Vignola is provided with several irradiance metering devices, (described in Section 3.6), two unique irradiance measurements are only possible with sensors installed on the tracker: it is the case for the global irradiance at the plane of array for the front (GNI) and rear (GNI_{rear}) sides of the PV panels. In Fig 3-10, the frontal irradiance sensor can be seen installed close to the m-Si modules.

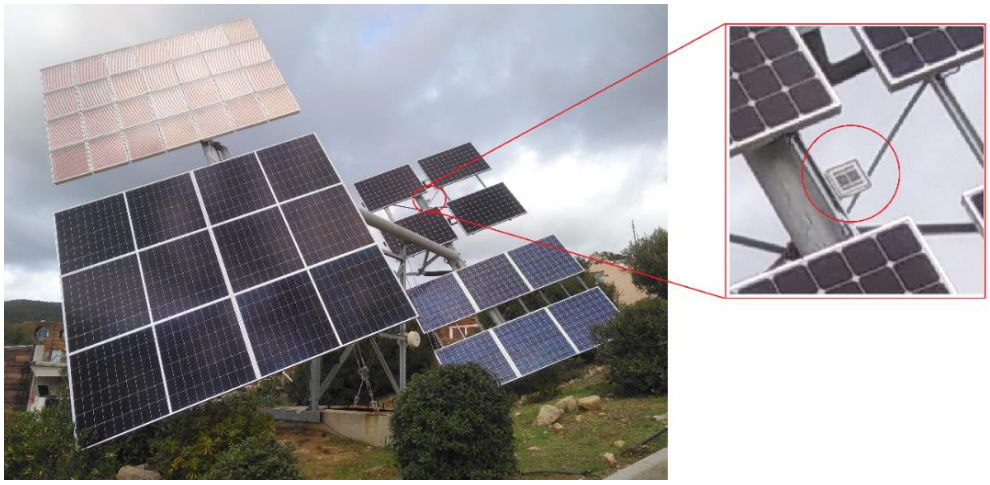

Figure 3-10: Frontal view or the tracker (left) and the front-side reference cell for irradiance measurement (detail, right)

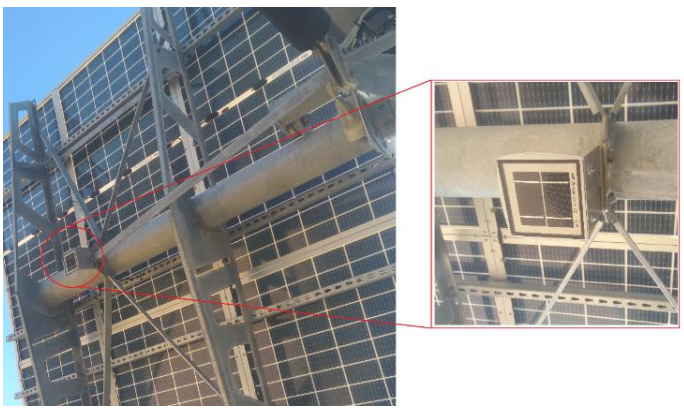

Figure 3-11: Rear view of the tracker (left) and the rear-side reference cell for irradiance measurement (detail, right)

In turn, Fig. 3-11 shows the irradiance sensor for the rear irradiance, installed just across the supporting axis behind the bifacial modules array. Its purpose is to measure the diffuse irradiance reaching the back surface of the bifacial modules. Both these sensors are calibrated m-Si cells, provided with built-in PT-100 temperature sensors. The temperature factor of each particular cell was determined by the manufacturer and is specified in a label attached to the sensor casing.

3.5 INVERTERS

Two 3000 W SMA Tri-Power inverters are used in the experiment. Each of the four PV arrays – HCPV, bifacial, mono-Si and poly-Si – is connected to an individual inverter input, that is, the maximum power point tracking (MPPT) is individual for each technology. This is actually a pre-requisite, given that the characteristics of the four PV module types vary widely. Each inverter provides two independent DC inputs, which are summed and result in a single AC output for grid connection. A picture showing the two inverters (in blue) and instrumentation panels is provided in Fig. 3-12.

Figure 3-12: Inverters and instrumentation panels

The modules and inverters are connected according to the illustration in Fig. 3-13, which shows that the HCPV array is supplied to input A of inverter 1, whereas the m-Si array is connected to the input B of inverter 1. In turn, the bifacial array feeds input A of inverter 2, while the p-Si array is linked to the input B of inverter 2. The sizing ratios for inverters 1 and 2 are, respectively, 0.798 and 0.980. The reason for keeping the inverter sizing ratio relatively high for inverter 2 is to accommodate the extra DC power provided by the bifacial array, since the STC ratings consider only the front-side.

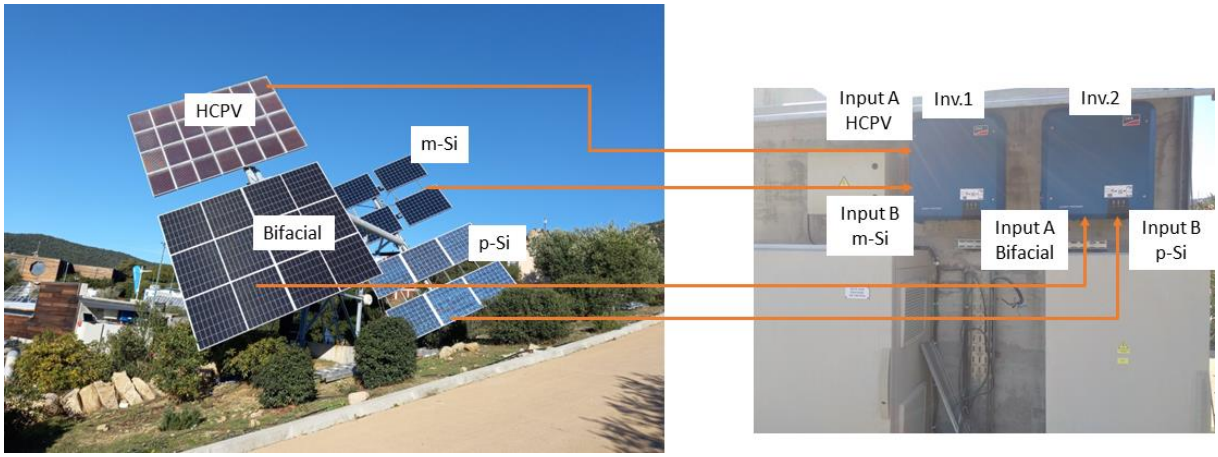

Figure 3-13: Modules on the tracker and their connection to the inverters

3.6 ON-SITE IRRADIANCE AND WEATHER MONITORING INSTRUMENTS

Various irradiance instruments are installed at the top of the Offices and Laboratories building (see Fig. 3-1 for reference). These meters acquire relevant irradiance parameters, and a dedicated supervisory system is responsible for recording the measurements. Tilted global irradiance levels are measured with the four pyranometers depicted in Fig. 3-14.

Figure 3-14: Pyranometers for tilted global irradiance measurement.

Besides this, a weather station (Fig. 3-15) measures ambient temperature and humidity, in addition to wind speed and direction.

Figure 3-15: A weather station installed for wind, humidity and temperature measurements.

A tracking assembly for measuring global, direct and diffuse irradiance components is shown in Fig. 3-16. The equipment is similar to the one whose explanation is given in Section 2.1.5.

Figure 3-16: Tracker assembly to measure GHI, BNI and DHI

Regarding the measurements made using these and other instruments, in this thesis, the main error metric is the normalized Root Mean Squared Error (nRMSE), calculated using Eq. (3.1).

$$\mathrm{nRMSE} = \sqrt{\frac{\sum_{i=1}^{n}(x_\mathrm{c} - x_\mathrm{r})^2}{n}}\,\frac{1}{\overline{x_\mathrm{r}}} \tag{3.1}$$

In cases where it is desired to check the direction of the error – for example, to determine if a model overestimates or underestimates a given variable – the nMBE (normalized Mean Biased Error) is used. The nMBE is computed via Eq. (3.2).

$$\mathrm{nMBE} = \frac{\sum_{i=1}^{n}(x_\mathrm{c} - x_\mathrm{r})}{n}\,\frac{1}{\overline{x_\mathrm{r}}} \tag{3.2}$$

In Eqs. (3.1) and (3.2), x_c and x_r are respectively the calculated and reference parameters, whereas $\overline{x_\mathrm{r}}$ represents the average of the reference parameter within the whole dataset, and *n* is the number of observations contained in the dataset.

In short, the nRMSE offers an absolute measurement of the average normalized error, providing more weight as the error increases (since it is squared). On the other hand, the nMBE provides a measure of the average normalized error. Since the error is not squared, the signal (+ or -) is preserved.

3.7 ALTERNATIVE APPROACHES FOR OUTDOOR CHARACTERIZATION OF PV MODULES

Two studies regarding outdoor characterization of PV modules were carried out during the development of this thesis. The first focuses on IEC-60891 international standard, and the second on the single-diode model (SDM) for PV sources.

The interest in outdoor characterization methods in the context of this thesis arises from the fact that all PV modules were individually tested before being installed on the tracker, through the measurement of I-V curves. The aim was to carry out performance checks to allow detecting failures before the measurement campaign started. Therefore, it became necessary to convert the field I-V measurements into a normalized condition, common for all PV modules. Such a common condition was chosen as the STC, thus allowing to compare the converted field measurements with the datasheet ratings. Another reason for the outdoor characterization of the PV modules is that all HCPV modules were not new as of the beginning of this thesis; they had been in operation for over 4 years, during the development of the thesis of Benhammane (2019). The exposition to sunlight – depending on the condition and duration – may introduce changes in the electric behavior of the PV device, which should be quantified so that the real specifications of the device are known. These specifications are essential for production performance assessment.

On the other hand, for the new bifacial PV modules, it is desired to carry out outdoor tests to confirm that the modules are not damaged and to check the specifications provided by the manufacturer. Moreover, the specific case of bifacial modules brings an additional need for tests: the quantification of the bifaciality index, which relates the short-circuit currents owing to the front and

rear sides of the module. It is not common practice for manufactures to include such an index in their products' documentation.

The series of studies resulted in two scientific papers, both of them already published: the alternative procedure for IEC-60891 (Abe et al. 2021); and the study regarding the single-diode model (Abe et al. 2023). For both studies, the validation was carried out using extensive experimental data coming from a PV system outside the scope of this thesis. The modules used for the validation were not the same as those installed on the tracker. Moreover, the tested modules were installed on a fixed mounting stand, not on a tracker. Using an experimental dataset obtained externally to this thesis was needed since the studies on outdoor characterization presented in this section started at the same time as the assembly and configuration of the PV tracker experiment. Therefore, it was not yet possible to use the tracker assembly to produce records. Appendix A and Appendix B present the validation of the methods described in the present section.

3.7.1 **Simplified approach to adjust IEC-60891 equation coefficients from experimental measurements**

A standard approach for modeling PV sources is by using current and voltage translation equations, notably as proposed in IEC-60891 (IEC, 2009) – 2nd procedure. They allow calculating the corresponding corrections in voltage and current, according to the operating condition, specified in terms of G and T_c. As the calculation is straightforward, providing voltage and current levels under known levels of G and T_c allows computing their translated values. It is worth mentioning that this does not require calculating the complete I-V curve: the I-V pair is directly translated by calculating just two equations. A concern regarding IEC-60891 is the need of adjusting some parameters in the voltage translation equation. To determine them according to the standard, two sets of I-V curves under specific conditions are needed. Therefore, it becomes necessary to use modeling techniques or advanced measurement equipment such as solar simulators.

This section presents a new procedure for adjusting the parameters of IEC-60891 (2nd procedure), based on simple experimental measurements. The method was designed in such a way to avoid the need for complex equipment and advanced modeling methods for PV devices. However, it is necessary to measure I-V curves of the module studied, under known levels of G and T_c. If a commercial instrument is not available, the I-V curve can be easily measured through the capacitive method, using simple current-voltage recording hardware. A review of methods to measure the I-V curve of PV modules is provided by Duran et al. (2008), whereas the capacitive method is discussed in detail by Spertino et al. (2015). Regarding the irradiance measurement, if a pyranometer or a calibrated PV cell are not available, measurements using a PV module as a sensor can be carried out. In this case, a module with known characteristics could be operated at the short-circuit point and positioned at the same inclination and orientation as that of the array under analysis. Measuring the current and the temperature of the sensor module allows computing the irradiance, as presented by Tan et al. (2013).

3.7.1.1 International standard IEC-60891

The IEC-60891 standard (IEC 2009) presents three different procedures for irradiance and temperature corrections regarding the current and voltage of PV devices. The second procedure

presented in the standard introduces Eqs. (3.3) and (3.4), and it is reported to provide better results when compared to the first procedure, considering large irradiance corrections. In turn, the third procedure is based on the interpolation of measured I-V characteristics and will not be covered in the present thesis. In Eqs. (3.3) and (3.4), α and β are the temperature coefficients for I_{sc} and V_{oc}, respectively. They are given in °C^{-1}. In turn, R_S is the series resistance of the module under test, in Ω, a is the irradiance dependence coefficient for the voltage (dimensionless), and k is the thermal correction factor of R_S, in Ω/K, which can present negative or positive values, depending on the experimental data used to adjust the parameters of Eqs. (3.3) and (3.4). The variables with subscript "1" refer to the input data, whereas the variables with subscript "2" refer to the translated data.

$$I_2 = I_1\left(1 + \alpha\left(T_{c,2} - T_{c,1}\right)\right)\left(\frac{G_2}{G_1}\right) \tag{3.3}$$

$$V_2 = V_1 + V_{oc,1}\left(\beta\left(T_{c,2} - T_{c,1}\right) + a\ln\left(\frac{G_2}{G_1}\right)\right) - R_S(I_2 - I_1) - kI_2\left(T_{c,2} - T_{c,1}\right) \tag{3.4}$$

A procedure for adjusting the parameters a, R_S and k is presented in the IEC-60891 standard (IEC 2009). Two I-V curve sets are required, with at least three I-V curves each: one set with the same T_c for all curves, varying G, for the adjustment of a and R_S; and another set under the same G, but with variable T_c, for adjusting k. Starting with the curve set under the same T_c and adopting a = 0 and R_S = 0, the current levels of the curves have to be scaled, so that all the curves coincide with the highest I_{sc} measured. At this point, the V_{oc} and the P_{mp} of the curves are not coincident. Then, assuming the highest irradiance as a reference in Eqs. (3.3) and (3.4), the parameter a has to be incremented in steps of 0.001 until the V_{oc} of the curves coincide. Once the parameter a has been defined, R_S is initially estimated by multiplying the number of cells connected in series by 0.01 Ω. The initial R_S has to be changed in steps of 0.01 Ω (positive or negative) until all curves coincide. Finally, the curve set containing curves under different T_c has to be used to adjust parameter k, taking the lowest temperature as a reference in Eqs. (3.3) and (3.4). The parameter k (initially set to 0) has to be changed in steps of 0.001 Ω/K until the transposed curves coincide.

The procedure presented in the standard requires at least six I-V curves, as well as computing resources to plot the translated curves at each step. A more straightforward method is presented in section in the following.

3.7.1.2 Alternative method for adjusting IEC-60891 voltage translation equation

An advantage of the novel method proposed in this thesis is the fact that fewer curves are required. In contrast to the original procedure, which requires one set of curves under the same G and another set under the same T_c, the proposed procedure requires only two I-V curves, which have to differ in terms of G and T_c. Datasheet information is needed only with regard to the temperature coefficients.

For adjusting the parameters in Eq. (3.4), the I-V curve under higher irradiance level is referred to as curve A and is associated with the condition G_a and $T_{c,a}$. The curve taken under lower irradiance,

referred to as curve B, refers to the condition G_b and $T_{c,b}$. The task of adjusting the parameters of Eq. (3.4) is complete when curve A points – being translated to G_b and $T_{c,b}$ – coincide with curve B.

Initially, R_S and k are set to zero. The first parameter to be adjusted is a, which is carried out based on the open-circuit voltage points of the curves. However, since a refers to the irradiance correction, the temperature must be constant for its adjustment. Aiming to avoid the case where I-V curves under different G and same T_c are required, the open-circuit point of curve B ($V_{oc,b}$, under $T_{c,b}$) is translated to $T_{c,a}$. This is carried out using an adaptation of Eq. (3.4) for the case of open-circuit and constant irradiance, where I_1 and I_2 are equal to zero, therefore yielding Eq. (3.5), where $V_{oc,c}$ refers to G_b and $T_{c,a}$. Equation (3.5) has been also used in (Abe et al., 2019), where a study regarding the relationship between V_{oc} and T_c was carried out. Once the V_{oc} of curve B has been translated to $T_{c,a}$, the open-circuit voltage of the two curves will only differ in terms of irradiance, and that is precisely what is needed in order to adjust a using Eq. (3.4).

$$V_{\mathrm{oc,c}} = V_{\mathrm{oc,b}}\left(1 + \beta\left(T_{\mathrm{c,a}} - T_{\mathrm{c,b}}\right)\right) \tag{3.5}$$

The proposed approach for the determination of a concerns only two voltage points – $V_{oc,c}$ and $V_{oc,a}$ – where the optimal value of a allows translating $V_{oc,a}$ to $V_{oc,c}$ using Eq. (3.4). This way, the trial-and-error procedure proposed in IEC-60891 for computing a is not necessary, since an explicit calculation is possible. This takes into account Eq. (3.4) written for open-circuit condition and constant temperature, and Eq. (3.5), yielding Eq. (3.6).

$$a = \frac{1}{\ln\left(\frac{G_b}{G_{\mathrm{a}}}\right)}\left(\frac{V_{\mathrm{oc,b}}\left(1 + \beta\left(T_{\mathrm{c,a}} - T_{\mathrm{c,b}}\right)\right)}{V_{\mathrm{oc,a}}} - 1\right) \tag{3.6}$$

The second step is adjusting R_S. This is carried out by writing Eqs. (3.3) and (3.4) for constant temperature, thus providing Eqs. (3.7) and (3.8), which are used to translate the curve A points to G_b.

$$I_2 = I_1\left(\frac{G_2}{G_1}\right) \tag{3.7}$$

$$V_2 = V_1 + V_{\mathrm{oc},1}\left(a\ln\left(\frac{G_2}{G_1}\right)\right) - R_{\mathrm{S}}(I_2 - I_1) \tag{3.8}$$

The parameter R_S has to be adjusted in such a way that the maximum power of the translated curve, that is, the product of Eqs. (3.7) and (3.8), coincides with $P_{mp,c}$, given by

$$P_{\mathrm{mp,c}} = P_{\mathrm{mp,b}}\left(1 + \gamma\left(T_{\mathrm{c,a}} - T_{\mathrm{c,b}}\right)\right), \tag{3.9}$$

which is the maximum power model adopted in the PVFORM simulation program for PV systems published by (Menicucci, 1985), written for constant irradiance. In Eq. (3.9), γ is the temperature coefficient for P_{mp}. The procedure of translating curve A points to G_b and determining the maximum power value has to be repeated for each adjustment of R_S, until its optimal value is determined. Given the discrete nature of measured I-V curves, a polynomial fit of the points could be performed, allowing a better estimation of the maximum power point. Such a procedure is explained in detail by Emery (2016), whereas an application case is described by Piliougine et al. (2021).

The last parameter in Eq. (3.4) to be adjusted is *k*. At this point, no intermediate conversion is needed, such as those provided by Eqs. (3.5) and (3.9); data referring to curves A and B are used directly in Eqs. (3.3) and (3.4). The curve A points are translated to G_b and $T_{c,b}$, whereas the parameter *k* is adjusted to make the power value resulting from the product of Eqs. (3.3) and (3.4) coincide with the measured $P_{mp,b}$. This completes the equation parameter adjustment procedure. It is worth mentioning that the task of translating curve A points to G_b and $T_{c,b}$, determining the maximum power value of the resulting curve, has to be repeated for each adjustment of *k*, until its optimal value is found. Besides that, as for the determination of R_S, polynomial fit should be applied if the measured curves present low definition.

The complete process of adjusting the parameters of Eq. (3.4) is presented in the flowchart illustrated in Fig. 3-17.

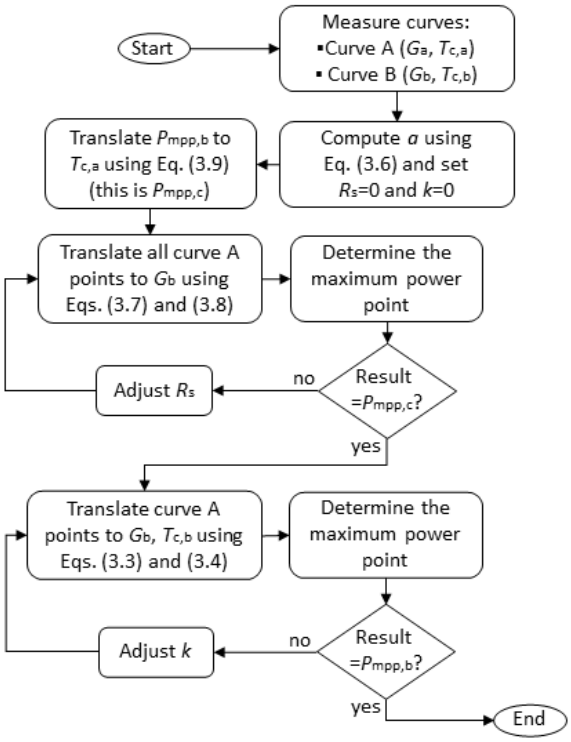

Figure 3-17: Process flowchart for adjusting the parameters of Eq. (3.4). Source: (Abe et al. 2021)

It is worth recalling that this procedure requires only two I-V curves, and plotting the translated curves is not required to complete the procedure. Two simple equations have been added to the original procedure. This way, the determination of *a* is explicit, and extensive outdoor measurements, tests using solar simulators, and further modeling methods are not needed. The validation of the proposed method is available on Appendix A.

3.7.2 **Using on-site measurements to identify and adjust PV single-diode model parameters for real operating conditions**

The single-diode model (SDM) is the most widely used approach to describe the behavior of PV modules, since it presents an adequate balance between complexity and precision, as described by

Femia et al. (2017) and Petrone et al. (2017). The electric circuit referring to the SDM is presented in Fig. 3-18, where the currents can be related by Eq. (3.10).

$$I_{\mathrm{pv}} = I_{\mathrm{ph}} - I_{\mathrm{d}} - I_{\mathrm{p}}\,, \tag{3.10}$$

where I_{pv} is the current at the output of the PV module and I_{ph} is the photo-generated current. Using the Shockley junction equation to express the diode current (I_d), and writing I_p as a function of I_{pv} and the PV cell voltage (V_{pv}) provides Eq. (3.11)

$$I_{\mathrm{pv}} = I_{\mathrm{ph}} - I_0\left[e^{\left(\frac{q\,(V_{\mathrm{pv}}+I_{\mathrm{pv}}\,R_{\mathrm{S}})}{n_{\mathrm{c}}\,A\,\mathrm{k}\,T_{\mathrm{c}}}\right)} - 1\right] - \frac{V_{\mathrm{pv}}+I_{\mathrm{pv}}\,R_{\mathrm{S}}}{R_{\mathrm{p}}}\,, \tag{3.11}$$

where I_0 is the diode reverse saturation current in A; R_s is the series resistance, in Ω; R_p is the parallel (or shunt) resistance, in Ω; q is the elementary charge (1.60217662 x10^{-19} C); A is the diode ideality factor; k is the Boltzmann constant (1.3806505 x10^{-23} J/K); and n_c is the number of cells connected in series in the module.

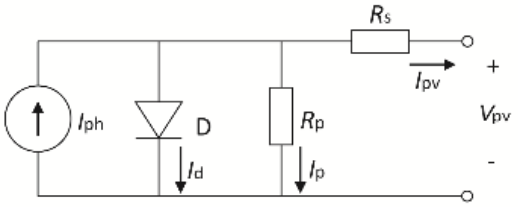

Figure 3-18: Single-diode model of a PV cell

To accomplish the crucial task of identifying the five SDM parameters (I_{ph}, I_0, A, R_s and R_p), different approaches have been presented, for instance exact iterative numerical methods, usually based on the solution of a system of non-linear equations; approximate methods, which allow explicit calculation of the SDM parameters due to the assumption of simplifications in the model; and optimization methods. A comprehensive review of consolidated methods to identify the SDM parameters is provided by Femia et al. (2017), Petrone et al. (2017) and Piazza and Vitale (2017).

Various identification methods presented in literature – for instance those proposed by Cannizzaro et al. (2014a), Lineykin et al. (2014), Di Piazza et al. (2015), Sera et al. (2007) and De Soto et al. (2006) – employ data referring to the Standard Test Condition (STC) as input, where the solar irradiance (G) on the plane of the PV module is 1000 W/m², whereas the module temperature (T_c) is 25 °C. In most cases, under such a high G level, the temperature of a PV module outdoors would hardly be equal to 25 °C. Thus, tests under STC are usually performed indoors, using specific equipment to allow controllable G and T_c levels. This is usually accomplished using the so-called solar simulators, which enable controllable temperature within the chamber where the PV module is positioned and are provided with a controllable light source, presenting AM 1.5 spectrum, which is similar to that of sunlight. Such an equipment presents high cost, which tends to restrict their use to PV module manufacturers and PV module characterization laboratories.

To avoid using datasheet information or solar simulators to obtain STC data, the SDM parameter identification of a particular PV module could be carried out based on outdoor measurements. In this sense, Hosseini et al. (2018) introduce a procedure to determine the five SDM parameters in real field conditions, using an iterative procedure and taking into account the effect of

spectral distribution on parameter I_{ph} by introducing a term dependent on the air mass (AM). In turn, Lappalainen et al. (2020) present a fitting method for on-site estimation of the five SDM parameters, as well as the G and T_c levels. This way, only datasheet information (under STC) and a measured I-V curve are needed for the SDM parametric identification. Piliougine et al. (2021) applied different explicit (approximate) identification methods using outdoor measured I-V curves of a PV module. The goal of the study was to evaluate the performance of such explicit methods for cases when the PV module presents degradation, which was emulated by adding series resistances during the I-V curve measurements, and no translation methods were considered.

In the works of Hosseini et al. (2018), Lappalainen et al. (2020) and Piliougine et al. (2021), once the SDM parameters were identified, the PV source terminal current and voltage can be predicted only for the condition under which the parameters were calculated. This means that if the operating condition changes, the SDM parameters have to be identified again. This can be overcome if translation methods for the SDM parameters are employed, allowing to reproduce the behavior of PV modules for any operating condition, according to Petrone et al. (2017). The study presented by Lineykin et al. (2014) introduces a method to adjust I_{ph} and I_0, which employs the semiconductor bandgap energy value. In contrast, the method presented by Piazza et al. (2017) does not require the bandgap energy value to calculate the corrected I_0; instead, it requires a second I-V curve under known G and T_c levels. Lineykin et al. (2014) and Piazza et al. (2017) evaluated such translation methods using original SDM parameters identified under STC, relying on datasheet information. Moreover, the use of such translation methods along with SDM parameters obtained from outdoor measurements has not been sufficiently documented in the literature.

3.7.2.1 SDM parameters identification methods

In this section, three methods for identifying the SDM parameters are considered. They regard the iterative, approximate, and optimization methods.

The first approach considered was presented by Sera et al. (2007), and relies on the iterative solution of a non-linear equations system and determines the five parameters of the SDM, using the Newton-Raphson method. Such a study has been employed as a reference in numerous studies over the last years; for instance, Chatterjee et al. (2011) employed derivations presented by Sera et al. (2007), however, they used the Gauss-Seidel numeric method to solve the non-linear equations system. Since the research of Sera et al. (2007) is regarded as a "classic" parameter extraction method, it was used as a reference to compare the performance of new methods proposed in the literature, as carried out by Piazza et al. (2015) and Hejri and Mokhtari (2017). Boutana et al. (2017) present a performance assessment of implicit and explicit identification methods for the SDM parameters, where the approach of Sera et al. (2007) is compared with six other methods.

According to Sera et al. (2007), the parameters R_s, R_p and A are computed iteratively by solving the system of non-linear equations formed by Eqs. (3.12) to (3.14).

$$I_{\mathrm{mp}} = I_{\mathrm{sc}} - \frac{V_{\mathrm{mp}} + I_{\mathrm{mp}}\,R_{\mathrm{s}} - I_{\mathrm{sc}}\,R_{\mathrm{s}}}{R_{\mathrm{p}}} - \left(I_{\mathrm{sc}} - \frac{V_{\mathrm{oc}} - I_{\mathrm{sc}}\,R_{\mathrm{s}}}{R_{\mathrm{p}}}\right) e^{\frac{q\,(V_{\mathrm{mp}} + I_{\mathrm{mp}}\,R_{\mathrm{s}} - V_{\mathrm{oc}})}{n_{\mathrm{c}}\,A\,K\,T_{\mathrm{c}}}} \tag{3.12}$$

$$\left.\frac{dP}{dV}\right|_{P_{\mathrm{mp}}} = I_{\mathrm{mp}} + V_{\mathrm{mp}} \frac{-\frac{q\left(I_{\mathrm{sc}} R_{\mathrm{p}} + I_{\mathrm{sc}} R_{\mathrm{s}} - V_{\mathrm{oc}}\right)}{n_{\mathrm{c}} A K T_{\mathrm{c}} R_{\mathrm{p}}} e^{\frac{q\left(V_{\mathrm{mp}} + I_{\mathrm{mp}} R_{\mathrm{s}} - V_{\mathrm{oc}}\right)}{n_{\mathrm{c}} A K T_{\mathrm{c}}}} - \frac{1}{R_{\mathrm{p}}}}{1 + \frac{q\left(I_{\mathrm{sc}} R_{\mathrm{p}} + I_{\mathrm{sc}} R_{\mathrm{s}} - V_{\mathrm{oc}}\right)}{n_{\mathrm{c}} A K T_{\mathrm{c}} R_{\mathrm{p}}} e^{\frac{q\left(V_{\mathrm{mp}} + I_{\mathrm{mp}} R_{\mathrm{s}} - V_{\mathrm{oc}}\right)}{n_{\mathrm{c}} A K T_{\mathrm{c}}}} + \frac{R_{\mathrm{s}}}{R_{\mathrm{p}}}} \tag{3.13}$$

$$\left.-\frac{1}{R_{\mathrm{p}}}\right|_{I_{\mathrm{sc}}} = \frac{-\frac{q\left(I_{\mathrm{sc}} R_{\mathrm{p}} + I_{\mathrm{sc}} R_{\mathrm{s}} - V_{\mathrm{oc}}\right)}{n_{\mathrm{c}} A K T_{\mathrm{c}} R_{\mathrm{p}}} e^{\frac{q\left(I_{\mathrm{sc}} R_{\mathrm{s}} - V_{\mathrm{oc}}\right)}{n_{\mathrm{c}} A K T_{\mathrm{c}}}} - \frac{1}{R_{\mathrm{p}}}}{1 + \frac{q\left(I_{\mathrm{sc}} R_{\mathrm{p}} + I_{\mathrm{sc}} R_{\mathrm{s}} - V_{\mathrm{oc}}\right)}{n_{\mathrm{c}} A K T_{\mathrm{c}} R_{\mathrm{p}}} e^{\frac{q\left(I_{\mathrm{sc}} R_{\mathrm{s}} - V_{\mathrm{oc}}\right)}{n_{\mathrm{c}} A K T_{\mathrm{c}}}} + \frac{R_{\mathrm{s}}}{R_{\mathrm{p}}}} \tag{3.14}$$

The parameter I_{ph} is computed via

$$I_{\mathrm{ph}} = I_0 \, e^{\left(\frac{q V_{\mathrm{oc}}}{n_{\mathrm{c}} A K T_{\mathrm{c}}}\right)} + \frac{V_{\mathrm{oc}}}{R_{\mathrm{p}}}, \tag{3.15}$$

whereas I_0 is calculated by

$$I_0 = \frac{I_{\mathrm{sc}} - \frac{V_{\mathrm{oc}} - I_{\mathrm{sc}} R_{\mathrm{s}}}{R_{\mathrm{p}}}}{e^{\left(\frac{q V_{\mathrm{oc}}}{n_{\mathrm{c}} A K T_{\mathrm{c}}}\right)}}. \tag{3.16}$$

The procedure described by Cannizzaro et al. (2014a) and Di Piazza et al. (2015) – regarded as an approximate method – presents an explicit solution, and since it neglects the effect of one of the resistances of the SDM, it always provides four parameters. The approach presented by Cannizzaro et al. (2014a) and Di Piazza et al. (2015) was selected as the approximate identification method for this section since their authors have also authored the translation method presented by Piazza et al. (2017). Moreover, the method presented by Cannizzaro et al. (2014a) and Di Piazza et al. (2015) was employed by Cannizzaro et al. (2014b), which describes a MATLAB-based software that calculates the SDM parameters using either iterative or explicit methods, allowing to compare the reconstructed I-V curves.

The simplification introduced by Cannizzaro et al. (2014a) and Di Piazza et al. (2015) consists in considering R_{s} equal to zero or R_{p} equal to infinite, and the criteria to neglect R_{s} or R_{p} is also described by Cannizzaro et al. (2014a) and Di Piazza et al. (2015). It refers to a new indicator called “series-parallel ratio” (SPR), calculated by

$$\mathrm{SPR} = \frac{1 - \gamma_i}{e^{-\mathrm{r}}}, \tag{3.17}$$

with

$$\gamma_i = \frac{I_{\mathrm{mp}}}{I_{\mathrm{sc}}}, \gamma_v = \frac{V_{\mathrm{mp}}}{V_{\mathrm{oc}}}, \mathrm{r} = \frac{\gamma_i(1 - \gamma_v)}{\gamma_v(1 - \gamma_i)}. \tag{3.18}$$

In cases where SPR > 1, R_{p} can be set as infinite; therefore, a set of four parameters is to be determined, which is conducted by solving Eqs. (3.19) to (3.22). The cases with SPR < 1 are usually found for modules composed by non-crystalline cells, according to Petrone et al. (2017). Such cases are not covered in the present work, since usually SPR > 1.

$$I_{\mathrm{ph}} = I_{\mathrm{sc}} \tag{3.19}$$

$$R_{\mathrm{s}} = \frac{V_{\mathrm{oc}}}{I_{\mathrm{sc}}} \frac{\frac{\gamma_v}{\gamma_i}(1-\gamma_i)ln(1-\gamma_i) + (1-\gamma_v)}{(1-\gamma_i)ln(1-\gamma_i) + \gamma_i}\Bigg|_{R_{\mathrm{p}}=\infty} \tag{3.20}$$

$$A = \frac{q}{n_{\mathrm{c}}\, K\, T_{\mathrm{c}}} \frac{I_{\mathrm{mp}}\, R_{\mathrm{s}} - V_{\mathrm{oc}} + V_{\mathrm{mp}}}{ln\frac{\left(I_{\mathrm{sc}} - I_{\mathrm{mp}}\right)\left(R_{\mathrm{s}} + R_{\mathrm{p}}\right) - V_{\mathrm{mp}}}{I_{\mathrm{sc}}\left(R_{\mathrm{s}} + R_{\mathrm{p}}\right) - V_{\mathrm{oc}}}} \tag{3.21}$$

$$I_0 = \left(I_{\mathrm{ph}} - \frac{V_{\mathrm{oc}}}{R_{\mathrm{p}}}\right) e^{-\frac{q\, V_{\mathrm{oc}}}{n_{\mathrm{c}}\, A\, K\, T_{\mathrm{c}}}} \tag{3.22}$$

It is worth mentioning that, as suggested by Petrone et al. (2017), the present study employs the approximate method solution as an initial guess for the application of the implicit numerical approach of Sera et al. (2007), as this helps to achieve convergence.

To simplify further references to the identification methods, the numerical approach proposed by Sera et al. (2007) will be referred to as “5-Par”, whereas the approximate method of Cannizzaro et al. (2014a) and Di Piazza et al. (2015) will be referred to as “4-Par”.

Cannizzaro et al. (2014a), Di Piazza et al. (2015) and Sera et al. (2007) suggest using datasheet information – under STC – as input data for the calculations. In this work, however, the SDM parameters are identified under different outdoor conditions; therefore, all references to parameters under STC in the equations presented in sources Cannizzaro et al. (2014a), Di Piazza et al. (2015) and Sera et al. (2007) were disregarded.

The third identification approach is based on the work of Ye et al. (2009), which proposes a parameter identification process based on Particle Swarm Optimization (PSO). For this optimization method, all the I-V curve points are used for the calculations, in contrast to the iterative and approximate methods which employ only the I-V curve notable points, that is, V_{oc}, I_{sc}, V_{mp} and I_{mp}. A further development of the method proposed by Ye et al. (2009) is described by Faggianelli et al. (2015), where the authors wrote Eq. (3.11) for the I_{sc} and V_{oc} cases to further solve the resulting equations for A. This allows calculating only four parameters by means of the PSO (I_{ph}, I_0, R_{s}, and R_{p}) to further compute A using either I_{sc} or V_{oc} measurements. In the present work, the PSO was applied using the V_{oc} approach described by Faggianelli et al. (2015). Thus, from Eq. (3.11) written for the V_{oc} condition,

$$0 = I_{ph} - I_0\, e^{\left(\frac{q\, V_{oc}}{n_c\, A\, K\, T_c}\right)} - \frac{V_{oc}}{R_p}. \tag{3.23}$$

Solving Eq. (3.23) for A provides

$$A = \frac{q\, V_{oc}}{n_c\, K\, T_c\, ln\left(-\frac{V_{oc}}{I_0\, R_p} + \frac{I_{ph}}{I_0} + 1\right)}. \tag{3.24}$$

3.7.2.2 Translation methods for SDM parameters

Methods to translate the SDM parameters allow predicting the performance of a PV source for arbitrary operating conditions, that is, for multiple combinations of G and T_c. Such translations to various different conditions can be performed using the same originally identified SDM parameters; however, the error levels depend on a) the condition under which the SDM parameters were determined and b) the "target" condition, that is, the desired levels of G and T_c for the translation.

The translation methods studied in this section adjust only parameters I_{ph} and I_0, according to the operating condition, which is defined in terms of G and T_c. Thus, the parameters A, R_s, and R_p are considered constant, although R_p is known to change with respect to G, as described by De Soto et al. (2006).

The first translation method, which presents Eqs. (3.25) and (3.26), was proposed by Lineykin et al. (2014) and relies on the semiconductor bandgap energy E_g, which is 1.12 eV for crystalline silicon and 1.14 eV for polycrystalline silicon (Petrone et al. 2017). Also, in Eq. (3.26) α is the temperature coefficient for the short-circuit current, in °C^{-1}. The method introduced by Lineykin et al. (2014) is referred to as translation method A. In Eqs. (3.25) and (3.26) the subscripts were modified since the original procedure is based on STC data. This way, the subscript "1" refers to the condition under which the SDM parameters were identified (the base condition), whereas subscript "2" refers to the desired operating condition (the target condition). Translation method A was selected in the present work because of its simplicity – it presents only two equations – and also due to the fact that no advanced information regarding the PV device is required. Also, this translation method was adopted in the simulation tool PSIM (PSIM is an electronic circuit simulation software package), which offers the feature of simulating the SDM along with power electronics and control function blocks.

$$I_0{}' = I_0 \left(\frac{T_{c,2}}{T_{c,1}}\right)^3 e^{\left(\frac{q\,E_g}{A\,k}\right)\left(\frac{1}{T_{c,1}} - \frac{1}{T_{c,2}}\right)} \tag{3.25}$$

and

$$I'_{ph} = I_{ph}\left(\frac{G_2}{G_1}\right)\left(1 + \alpha\left(T_{c,2} - T_{c,1}\right)\right). \tag{3.26}$$

The second translation procedure was introduced by Piazza et al. (2017) and originally employs datasheet information, considering measurements under STC and under the condition specified for the Nominal Operating Cell Temperature (NOCT). The method is referred to as translation method B, where the same equation performs the adjustment of I_{ph} as in Lineykin et al. (2014), and I_0 is adjusted using Eqs. (3.27) to (3.29).

Since the present study considers only outdoor measurements, all "STC" subscripts in the publication of Piazza et al. (2017) now refer to the condition under which the SDM parameters were computed; therefore, they were changed to "1", denoting "condition 1". The subscripts "NOCT" in Piazza et al. (2017) denote a second reference condition; thus, in Eq. (3.29), this auxiliary condition is identified by the subscript "3". This third auxiliary condition is needed so that the influence of the irradiance on V_{oc} can be quantified, which is expressed in terms of the $\delta(T_c)$ parameter.

The translation method proposed by Piazza et al. (2017) was selected to be included in the present thesis because it was proposed by the same authors of the non-iterative translation method (4-Par) (Cannizzaro et al. (2014a) and Di Piazza et al. (2015)). As mentioned earlier, the identification

method of Cannizzaro et al. (2014a) and Di Piazza et al. (2015) was employed – under STC – along with the translation method of Piazza et al. (2017) presenting relatively good translation results, as reported by the authors. Therefore, with the proposed combination of methods, the performance of the 4-Par method (Cannizzaro et al. (2014a) and Di Piazza et al. (2015)), in conjunction with the translation method of (Piazza et al., 2017), can be assessed for cases in which the parametric identification is based on outdoor measurements. The validation of the proposed approach is available on Appendix B of this thesis.

$$I_0{}' = \frac{I_{ph}}{e^{\left(\frac{q\,V_{oc}}{n_c\,A\,k\,T_c}\right)} - 1} \tag{3.27}$$

$$V_{oc} = V_{oc,1}\left(1 + \beta\,\left(T_{c,2} - T_{c,1}\right)\right)\left(1 + \delta(T_c)\,ln\frac{G_2}{G_1}\right) \tag{3.28}$$

In Eq. (3.28), $V_{oc,1}$is the V_{oc} referring to the base curve, β is the temperature coefficient of $V_{oc,1}$ given in °C^{-1} and $\delta(T_c)$ is computed using

$$\delta(T_c) = \frac{1}{ln\left(\frac{G_3}{G_1}\right)}\left(\frac{V_{oc,3}}{V_{oc,1}\left(1 + \beta\left(T_{c,3} - T_{c,1}\right)\right)} - 1\right). \tag{3.29}$$

3.8 PV MODULES TESTING OUTDOORS: ACTUAL STC RATINGS

The present section provides a connection between the alternative characterization methods described in Section 3.7 and the PV modules used in the experimental assembly with the PV tracker built for this thesis. Functionality checks were conducted before installing the modules on the tracker, as shown in Fig. 3-19.

Figure 3-19: I-V tests with the PV modules before installation on the tracker

Special care has been taken with respect to the bifacial modules: for each module, tests were carried out with one face at a time, covering the face not being used. This was an important test to determine the individual performances of each side of the bifacial modules, allowing the bifaciality index φ to be quantified. Figure 3-20 illustrates these tests, whereas section 5.7 presents specific details and in-depth analysis of the particularities presented by bifacial modules.

Figure 3-20: I-V tests with the bifacial modules, individually for each face

Given the fact that the HCPV modules were not new, it became necessary to clean and inspect every module (Fig. 3-21) and perform I-V tests (Fig. 3-22) to further determine the modules' actual STC ratings using the modeling methods described in Section 3.7.

Figure 3-21: Cleaning and inspection of all HCPV modules

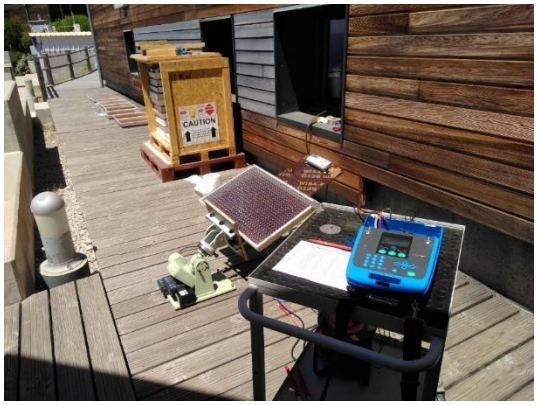

Figure 3-22: I-V curve tracing with the HCPV modules

The STC ratings are a relevant metric for each PV technology since the STC is regarded as the reference performance. Among the modeling methods presented in Section 3.7, the simplest approach is the 4-Par,A: it requires only one reference (field-measured) I-V curve and it does not require the SDM parameters to be identified by simultaneously solving a set of non-linear equations, as it is the case for method 5-Par. However, the 5-Par method combined with translation method A (5-Par,A)

provided the smallest translation error for the studies considered in Section 3.7, whose validation is presented in Appendix B. This way, the method 5-Par,A has been adopted for the determination of the actual STC ratings for the PV modules mounted on the tracker, except for the HCPV. Relevant data regarding the rated performance of the mono-Si, poly-Si and bifacial modules, as well as the measured and actual STC metrics, are organized in Tables 3-2, 3-3, and 3-4.

Table 3-2: Metrics referring to the poly-Si PV modules.

	Datasheet	Measured	Calculated STC (5-Par,A)
V_{oc} (V)	43.40	39.50	42.86
I_{sc} (A)	5.30	5.45	5.21
V_{mp} (V)	35.00	30.40	33.86
I_{mp} (A)	5.00	4.94	4.82
P_{mp} (W)	175.0	150.2	163.2
G (W/m²)	1000	1038	1000
T_c (°C)	25	60	25
Efficiency (%)	15.0	10.8	14.0

Table 3-3: Metrics referring to the mono-Si PV modules.

	Datasheet	Measured	Calculated STC (5-Par,A)
V_{oc} (V)	64.90	63.50	67.02
I_{sc} (A)	6.46	5.39	6.34
V_{mp} (V)	54.70	49.10	51.87
I_{mp} (A)	5.98	4.97	5.88
P_{mp} (W)	327.1	244.0	305.0
G (W/m²)	1000	845	1000
T_c (°C)	25.0	43.5	25.0
Efficiency (%)	20.4	17.7	19.0

Table 3-4: Metrics referring to the bifacial PV modules.

	Datasheet	Measured	Calculated STC (5-Par,A)
V_{oc} (V)	40.80	37.30	40.56
I_{sc} (A)	10.35	10.37	10.25
V_{mp} (V)	34.10	28.30	33.0
I_{mp} (A)	9.83	9.78	9.83
P_{mp} (W)	335.2	276.8	324.4
G (W/m²)	1000	949	1000
T_c (°C)	25.0	59.2	25.0
Efficiency (%)	19.7	17.2	19.1

The HCPV technology concerns the use of different semiconductor materials to achieve an enhanced use of solar radiation in terms of spectral distribution. Therefore, translation method A is not suitable for such a technology given the reliance on a single value for the bandgap energy E_g. Instead, for the HCPV, the 4-Par,B approach was used to determine the actual STC ratings. The 4-Par,B

combination shows the disadvantage of requiring two field-measured I-V curves, however, it was taken as the best cost/benefit option for the case of the HCPV modules. Table 3-5 presents the translated STC data referring to the HCPV modules.

Table 3-5: Metrics referring to the HCPV modules.

	Datasheet	Measured 1	Measured 2	Calculated STC 4-Par,B
V_{oc} (V)	101.60	97.40	96.30	103.4
I_{sc} (A)	1.06	0.94	0.89	0.99
V_{mp} (V)	86.6	82.30	82.50	88.83
I_{mp} (A)	1.01	0.88	0.83	0.94
P_{mp} (W)	87.5	72.4	68.5	83.5
G (W/m²)	1000	932	853	1000
T_c (°C)	25.0	74.6	67.3	25.0
Efficiency (%)	33.9	25.9	26.8	32.3

3.9 UNCERTAINTY STUDY

This section presents an uncertainty study covering all steps, from initial testing of the PV modules with the I-V curve tracer to the final relative efficiency calculations. In this sense, it becomes necessary to list all uncertainty levels referring to the sensors, methods and reference parameters employed in the experimental and analysis phases.

3.9.1 **Individual uncertainty levels**

The most relevant measured parameter for PV performance evaluation is the irradiance. GNI was measured using a reference PV sensor installed at the front-side of the tracker. The sensor manufacturer (Photovoltaik, 2020) reports a measurement uncertainty of +/- 4 %. For the BNI measurements, Kipp & Zonen documentation regarding the Solys2 meter reports +/- 2 % error on BNI measurements (Kipp & Zonen, 2018).

In turn, for the temperature measurements, the uncertainty for flat PT- temperature sensors is reported as +/- 0.4 °C by Dubois et al. (2021). In addition to the sensor uncertainty, the authors added a second uncertainty factor (+/- 1%), referring to the uncertainty due to the temperature difference between the module's back surface and the PV cell, considering a regular glass-EVA encapsulation. For the purpose of the present thesis, this second uncertainty factor has been scaled according to the temperature difference found for different PV module encapsulations. Considering a 3 °C difference between the back surface of a PV module and the cell, as reported by King, (2008) and Rao Golive et al. (2022), and taking the +/- 1% level as a reference, the second uncertainty factor was extended for the glass-glass and HCPV encapsulations. For the glass-glass encapsulation, a 5.5 °C temperature gap (Rao Golive et al., 2022) relates to a 1.84 % uncertainty level; and for the HCPV module, a 13 °C temperature gap (King et al., 2004) relates to a 4.33 % uncertainty level.

Regarding the air temperature measurement carried out by weather stations, both studies (Dubois et al., 2021 and Mavromatakis et al., 2014) reported 0.5 °C uncertainty.

For the temperature coefficients for current (α), voltage (β) and power (γ), the uncertainty is usually not displayed in PV modules' datasheets. However, Salis et al. (2018) considered an inter-comparison between laboratories for the determination of temperature coefficients of crystalline PV modules, and the uncertainties were reported as 0.0129 %/°C, 0.0765 %/°C, and 0.0776 %/°C, respectively, for α, β and γ. Due to the scarcity of uncertainty data for different PV technologies, in this thesis the α, β and γ uncertainty levels are considered the same for all four technologies studied.

Table 3-6: Individual uncertainty levels for devices and parameters

Resource	Uncertainty	Unit
Reference PV cell	+/- 4	%
Pyranometer	+/- 2	%
Pyrheliometer	+/- 2	%
PT-100 temperature sensor	+/- 0.4	°C
Temperature gap between back surface and cell	+/- 1 (Glass-EVA) +/- 1.66 (Glass-Glass) +/- 4.33 (HCPV)	°C
α	+/- 0.0129	%/°C
β	+/- 0.0765	%/°C
γ	+/- 0.0776	%/°C
Voltage (inverter)	+/- 3	%
Current (inverter)	+/- 3	%
Voltage (I-V tracer)	+/- 1	%
Current (I-V tracer)	+/- 1	%

For the voltage and current measurements: in the present thesis, the voltage and current measurements referring to the PV arrays are conducted by the inverters. The inverter's manufacturer (SMA) does not report the uncertainty referring to such measurements in the product documentation. However, the Photovoltaic Power Systems Programme (PVPS), held by the International Energy Agency (IEA), reports in its Task 13 (Reise et al., 2018) an uncertainty level of +/- 3% of the max readable current and voltage for a commercial inverter.

Regarding the power under STC, outdoor tests using an EKO MP-11 I-V curve tracer have been carried out during this thesis, to further determine the PV modules' maximum power corrected to STC. The I-V curve tracer's documentation report +/- 1% for the voltage and current measurements. The uncertainty levels for the irradiance and temperature measured during the tests are respectively +/- 4% (reference PV cell) and +/-0.5% (PT-100 sensor) plus the second uncertainty factor referring to the temperature difference between module's back surface and the cell, according to the module encapsulation, as mentioned earlier in this section.

With all pertinent explanations being laid out, Table 3-6 summarizes the individual uncertainty levels presented in this section.

3.9.2 **Combined uncertainty levels: Monte Carlo simulation**

To assess the influence of the individual uncertainty levels on the combined uncertainty of a particular parameter, Monte Carlo simulations were applied to randomly introduce errors on the input

parameters of the mathematical expressions of interest in each case. Such models describe the power, voltage and current of the four PV technologies under study in this thesis. Finally, the uncertainty on the performance ratio was also determined. For all cases studied, the uncertainty was determined with respect to a confidence interval of 1.96, covering 95 % of the population of 10000 simulation steps.

The initial measurement campaign, conducted at the beginning of this thesis and described in Section 3.8, employed an I-V curve tracer to determine the I-V curves of all PV modules under certain irradiance and temperature conditions, which were measured using a reference cell and a temperature sensor built-in the curve tracer. By coupling the random errors introduced on voltage and current during the Monte Carlo simulation, the combined relative uncertainty on the measured power ($P = V.I$) was determined as +/- 1.6 %. Given that the same setup was used for all modules, this uncertainty level for the power measurements via the I-V tracer has been adopted for all next uncertainty assessment phases.

The following step is the determination of the uncertainty referring to the power under the STC. The conversion of field measurements into the STC equivalents was conducted using the techniques developed in Section 3.7, whereas the results considering the PV modules used in this thesis are presented in Section 3.8. The model used in the Monte Carlo simulation was the 4-parameter single-diode model coupled with translation methods for the parameters I_{ph} and I_0: translation method A was used for the m-Si, p-Si and bifacial modules, whereas translation method B was used for the HCPV technology. The input parameters for the simulations were the I-V curves measured outdoors and the irradiance and temperature levels recorded during the I-V curve acquisitions. From the simulations where random errors were introduced in such parameters, according to the individual uncertainty levels shown in Table 3-6, it was possible to compute the uncertainty on the SDM parameters. The last step was to apply the SDM equation (Eq. 3.11) to calculate the current and voltage values for each simulation step, to further calculate the power and the uncertainties on all electrical parameters. The final uncertainty levels for the maximum power at STC ($P_{mp,STC}$) are +/- 5.1 % for p-Si; +/- 5.5 % for m-Si; +/- 5.1 % for bifacial; and +/- 3.9 % for the HCPV technology.

It is worth noting that the uncertainty referring to the HCPV technology was found to be smaller in comparison to the other PV modules. This is related to the fact that the useful irradiance for the HCPV is the BNI, which was measured using a pyrheliometer, which presents +/- 2 % uncertainty, whereas the uncertainty on the GNI measurements (for m-Si, p-Si and bifacial) made via the reference PV cell is +/- 4 %. Therefore, the uncertainty referring to the irradiance measurements is reflected on the final uncertainty concerning the STC power calculation.

Power predictions using the power model described in Section 2.2.1 (Eq. 2.8) were also assessed in terms of uncertainty. In this case, the input parameters are the irradiance and temperature, as well as the $P_{mp,STC}$ and its temperature factor γ. The Monte Carlo simulation was applied to produce random errors according to the data organized in Table 3-6, resulting in uncertainty levels on the calculated maximum power P_{mp} of +/- 7.8 % for m-Si and p-Si; and +/- 7.4 % for the bifacial technology.

For the HCPV array, a different power model – accounting for the air mass – was applied. Such a model is described in Section 2.2.3 (Eq. 2.19). In this case, the input parameters are the BNI and air temperature, in addition to the power under the STC. The combined uncertainty on the calculated power is +/- 4.8 %. Relevant remarks on such an uncertainty level – which is lower than the power

uncertainties for the three other technologies – include the fact that the BNI presents half the uncertainty relative to the GNI and that the temperature input in the model is the air temperature. This means that the uncertainty referring to the temperature gap between the module's back surface and the cell is not present. These two facts thus cause the power uncertainty for the HCPV modules to be lower than for the m-Si, p-Si and bifacial technologies.

The international standard IEC-60891, explored in Section 3.7.1, was also evaluated in terms of the uncertainty on its predicted current and voltage levels. In such an assessment only the flat-plate PV modules were considered, as IEC-60891 does not cover multi-junction devices. As in the case of the single-diode model, the first step was the calculation of the uncertainty on the model internal parameters, using the reference I-V curves measured during the initial testing campaign. Then Eqs. 3.3 and 3.4 were used to compute the voltage and current levels for the Monte Carlo simulation, allowing the uncertainty levels to be determined. For the current, the uncertainty levels are +/- 6.9 % for m-Si; +/- 6.6 % for p-Si and for bifacial. Concerning the voltage, the uncertainty values are +/- 6.9% for m-Si; +/- 6.1 % for p-Si; and +/- 4.8 % for the bifacial devices.

Finally, at this point all parameters needed for the PR calculation as per Eq. 2.24 (Section 2.3) are specified in terms of uncertainty. Using Eq. 2.24 as the reference model for the Monte Carlo simulations produces the uncertainty levels as follows: +/- 11.9 % for m-Si; +/- 10.7 % for p-Si; +/- 11.1 % for bifacial; and +/- 7.3 % for the HCPV technology.

3.10 CONCLUSIONS FOR SECTION 3

This section presented the UDCPP's Renewable Energy Laboratory, as well as the experimental resources available for the present thesis. The PV modules installed on the tracker present the following nominal specifications for power and efficiency: 175 W, 15 % (p-Si); 327 W, 20.4 % (m-Si); 335 W, 19.7 % (bifacial); 87.5 W, 33.9 % (HCPV).

From I-V curves traced with the PV modules outdoors, applied to modeling methods, the following power and efficiency metrics were obtained: 163.2 W, 14 % (p-Si); 305.0 W, 19 % (m-Si); 324.4 W, 19.1 % (bifacial); 83.5 W, 32.3 % (HCPV). The uncertainty levels for the calculated power levels are +/- 5.5 % for m-Si; +/- 5.1 % for p-Si; +/- 5.1 % for bifacial; and +/- 3.9 % for HCPV.

It is therefore seen that, for all PV technologies, the experimental power values are smaller than the datasheet ratings. Measurement errors are important limitations referring to the experimental determination of the STC power, particularly regarding the solar irradiance and module temperatures.

SECTION 4

DATA MEASUREMENT AND PROCESSING

4 DATA MEASUREMENT AND PROCESSING

The present section concerns the data aggregation and the filtering of the datasets in respect to invalid data. First, basic filtering was applied, and a visual identification of the factors for outlier production is carried out. Then, different filtering approaches are considered, aiming to find a suitable strategy for outlier removal.

The PV efficiency (Eq. 2.22) was taken as a reference parameter for the filters because it is a valuable indicator, which takes into account the output power and the available solar resource, expressed in terms of the in-plane irradiance. The efficiency is thus a useful metric to assess the quality of the data, since unusually high or low levels might be caused by inconsistent measurements or undesired conditions, such as strong transient conditions or shading on irradiance sensors or PV arrays.

4.1 DATA AGGREGATION

The measurements composing the experimental dataset produced during this thesis come from three different sources: the tracker measurement system, the Solys 2 irradiance measuring platform and a weather station (part of the Paglia Orba measuring system), as illustrated in Fig. 4-1.

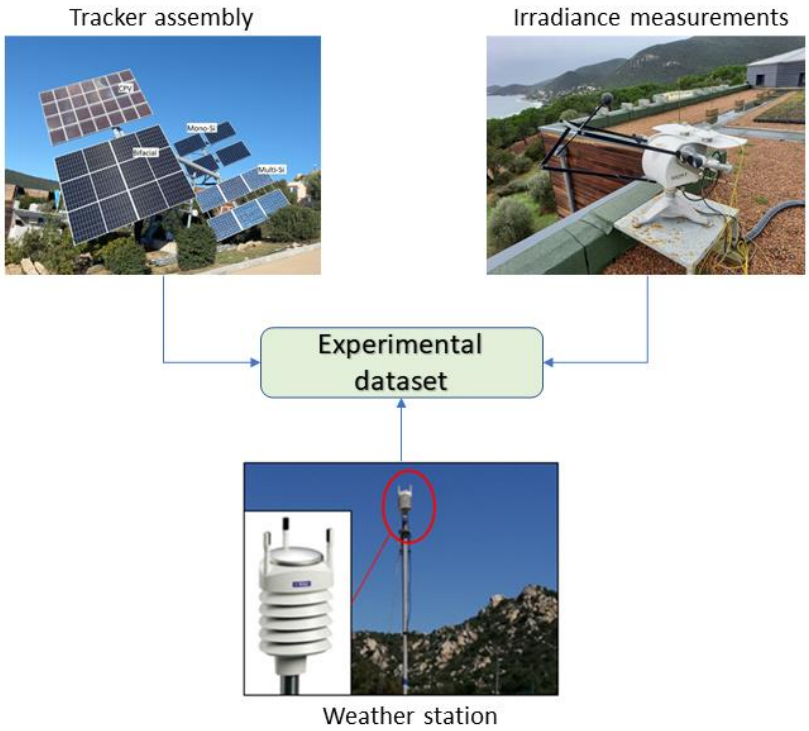

Figure 4-1: The three measurement sources for the experimental campaign

As mentioned in Section 3, the tracker assembly measurements comprise PV modules' temperature, rear and frontal normal global irradiance measurements (GNI and GNI_{rear}) and DC and AC voltage, current and power. In turn, the records from the Solys 2 irradiance measuring system include global horizontal irradiance (GHI), diffuse horizontal irradiance (DHI) and beam normal irradiance (BNI). Finally, the weather station provides metrics for ambient temperature and humidity, wind speed and direction.

The first task when receiving the data from these sources was to correct the date and time parameters: the records coming from the tracker system do not include DST (daylight saving time) corrections, whereas the records from the weather station automatically take the DST into consideration. In turn, the data coming from the Solys 2 station are based on UTC (coordinated universal time). It was therefore necessary to make the corrections to have all datasets under the same date and time setting. Once the local time and DST corrections were applied, it was still necessary to check for the synchronicity between the three data recordings. For that, the three files were scanned considering cloudy days in which the irradiance changed abruptly. GNI (tracker system) and BNI (Solys 2) were firstly checked for synchrony; then, GHI (Solys 2) and GHI (Paglia Orba weather station) were compared. There were no clock synchronicity issues detected, as the clocks were adjusted before the measurement campaign began and regular checks were carried out by the Laboratory's technical staff.

The second task was to aggregate the data coming from the three sources, to build a single dataset comprising all data within coincident timesteps. The data coming from the tracker assembly presents one-minute time steps. On the other hand, data coming from the Solys 2, and the weather station are recorded by the supervisory system, and new records are only stored when one of the parameters change (to save storage space). Consequently, the data coming from these two sources present a variable time step. To aggregate the data from the three sources, it was thus necessary to use the minute-stepped tracker data as the basis for interpolating the data acquired with the Solys 2 and the weather station. Such a task was conducted using Matlab's function *interpl*, whereas interpolating for the last recorded value in each dataset and parameter. As a result, a single dataset was obtained, with all measured parameters quantified at the minute-timestep.

Regarding data quality, the aggregated dataset contained NaN (Not a Number) values, as well as empty cells. Besides this, two measurement interruptions were noticed, one of which (March) was caused by a scheduled maintenance on the laboratory's general data recording system and the other (August) was caused by a crash affecting the main computer. In total, the aggregated dataset contains 450482 records at the minute-timestep, corresponding to 313 days. The next section discusses the filtering criteria applied to the dataset, to exclude non-useful and inconsistent data.

4.2 PRELIMINARY FILTERING OF THE MEASUREMENT RECORDS

Filtering must be applied to a raw dataset in order to remove spurious and incoherent data, allowing to focus on the useful measurements. Recent literature, such as the works of Jordan et al. (2018), Luo et al. (2019), and Øgaard et al. (2020) – which concern long-term data acquisition – employed filtering based on irradiance and clearness index. A minimum irradiance threshold (for example, 200 W/m²) was defined so that non-uniform irradiance, as well as inverter start-up issues were filtered out. In addition to that, width-filtering (i.e., +/- 10 %, +/- 30 %) was applied to the clearness index to remove records related to periods with high cloud coverage. Another filtering criteria applied by Jordan et al. (2018) excludes records in which the AC power is greater than 99 % of the rated inverter capacity, to avoid records affected by inverter saturation (also referred to as clipping). Regarding abrupt changes in the values of the recorded parameters, (IEC, 2016) in its IEC-61724 standard, part 3, recommends assessing the derivative of quantities such as temperature,

irradiance and power, filtering out records where the reference thresholds – adjusted according to the local conditions – were violated.

In the present thesis, however, filtering to remove low irradiance levels is not desired as it implies removing records related to high AM levels – and it is desired to evaluate the influence of AM on the PV arrays' performance. In turn, cloudy days usually present a shift in the spectral content, which influences the PV arrays' behavior. This way, filters based on clearness index were not applied to clean the dataset. However, the filtering based on the inverters' maximum power rating was applied since several records presented AC power exceeding the inverter's nominal capacity. During inverter clipping, the arrays were not operating on the maximum power point, which was noticed by the inconsistent relationships between irradiance and DC current levels at the inverters' inputs.

4.2.1 **Basic filters**

The basic filtering applied to the dataset studied in this thesis refers to parameters which are not PV technology-specific. Thus, the basic filters were applied equally to the datasets referring to the four PV technologies studied. The raw data, the filters and the remaining number of recorded observations are as follows.

Raw data: 450482 1-minute records (including night periods)

The useful data for this thesis refer to the daylight period; thus, the effects of the filtering are quantified in relation to the observations recorded for solar altitude angle > 0°. This way, the remaining data after the application of the sun altitude angle filter are regarded as 100 %, which is the basis for the calculation of the effects introduced by the filters applied afterwards.

Filter 1 – Sun altitude angle greater than 0°: 218787 records remaining (100 %)
Filter 2 – Removal of NaN records: 217544 records remaining (99.3 %)
Filter 3 – GNI greater than 0 W/m²: 212629 records remaining (97.1 %)
Filter 4 – Wind speed smaller than 6 m/s: 196711 records remaining (89.9 %)
Filter 5 – Atmospheric indexes between 0 and 1: 172517 records remaining (78.8 %)

The Sun's altitude angle filter was applied to remove periods in which the Sun is not yet over the horizon. The Sun's altitude angle – which is complementary to the zenith angle – was calculated according to the procedures presented in Section 2.1.2. In addition to that, Filter 3 was used to select only data records referring to situations in which the PV arrays are receiving solar radiation - that is, when the PV cells are active.

The wind speed is a critical factor for the PV tracker's operation, as the tracker is set to a rest (horizontal) position for cases where the wind speed is greater than 8 m/s. The reason for such a behavior is to avoid structural damages to the tracker structure. While the tracker is in the rest position, the PV arrays do not face the Sun, and the HCPV power output is greatly affected. In fact, during the initial checks of the measured data, it was found that wind speed greater than 6 m/s caused the HCPV power to be significantly low (sometimes close to zero) even for high BNI levels. Therefore, records referring to such a condition were removed by the application of Filter 4. Finally, the basic filtering considers the indexes introduced in Section 2.1.3. The dataset was filtered to remove records outside the 0 – 1 feasible limit for the indexes.

4.2.2 **DC power filter**

In addition to Filters 1 and 3, a filter for minimum DC power was applied to ensure that the PV modules are active. The reason is that filters 1 and 3 concern external factors to the PV arrays. The use of these two filters does not guarantee that the PV arrays are in operation, that is, supplying electricity. This is especially relevant for the HCPV array: GNI greater than zero does not necessarily mean that the HCPV PV array will present DC power greater than zero, since the HCPV modules respond to the BNI only. Therefore, for all four PV arrays, only records showing DC power greater than 0 were considered. It should be noted, though, that such a criterion does not mean that the PV arrays are operating at the maximum power point, given the operating limits referring to the internal power electronics stages of the inverters or occurrence of strong transient conditions caused by fast-moving clouds. This is a particularity of the present work, which focused on the analysis of the PV arrays in real operating conditions.

After applying the minimum DC power filter to the datasets referring to each technology, the number of records is as follows:

p-Si dataset: 156839 records remaining (71.6 %)
m-Si dataset: 148245 records remaining (67.7 %)
Bifacial dataset: 156972 records remaining (71.6 %)
HCPV dataset: 123262 records remaining (56.2 %)

It is observed that the remaining data points for the HCPV array is significantly lower than for the other technologies. This illustrates the HCPV array's dependence on the BNI, which is not as available as the GNI. Therefore, as previously stated, the electricity produced by a high-efficiency HCPV plant might be smaller than the amount produced by a conventional PV array, considering the same rated power for both.

4.2.3 **AC power filter**

The so-called inverter clipping is a potential cause for PV arrays to operate far from the maximum power point. Clipping (or inverter saturation) is defined as the situation in which the inverter's maximum AC power rating is reached. As a result, to keep the operating parameters within the specifications, the inverter shifts the operating point of the PV array connected to the DC side, reducing the PV array's current to reduce the DC power. This means that, during clipping, the DC power is not consistent with the irradiance and temperature levels, since the PV array is not operating on its maximum power point. In the context of this thesis, taking inverter clipping occurrences into consideration is not desired, given that PV power and the external operating conditions are studied together to find correlations. In other words, when the inverter's output is saturated, the PV power is no longer a function of the weather condition. This way, a filter based on maximum AC power was applied. Lindig et al. (2021) applied a clipping filter to their datasets, removing data in which the inverter power was greater than 99% of the rated inverter capacity. The same strategy was adopted by Jordan et al. (2018) and Øgaard et al. (2020). After applying the filter to remove records related to AC power equal or greater than 99% of the rated inverter capacity, the number of useful observations for the dataset is as follows:

p-Si dataset: 154323 records remaining (70.5 %)

m-Si dataset: 140985 records remaining (64.4 %)
Bifacial dataset: 154456 records remaining (70.6 %)
HCPV dataset: 118944 records remaining (54.4 %)

Up to this point, all filters were sequentially applied – that is, the filtering effects are cumulative. The cumulative filter setups applied up to the present section will be referred to as “basic and power filters”.

The scatter plots for the efficiency versus irradiance, considering the basic and power filters, show sparse points both in the upper and lower directions. Despite this, the main efficiency curves are clearly visible in the plots. Figures 4-2 to 4-5 show the efficiency levels plotted versus the irradiance: GNI for the p-Si and m-Si arrays; G_E (defined in Section 2.2.2) for the bifacial; and BNI for the HCPV. The dots are colored according to the measured module’s temperature, which allows observing the correlation between high temperature levels and low efficiency records, for a same irradiance range.

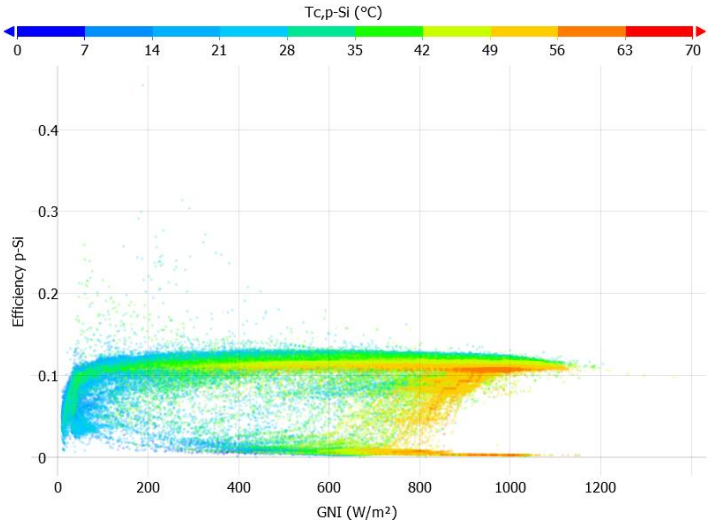

Figure 4-2: p-Si efficiency with basic and power filters

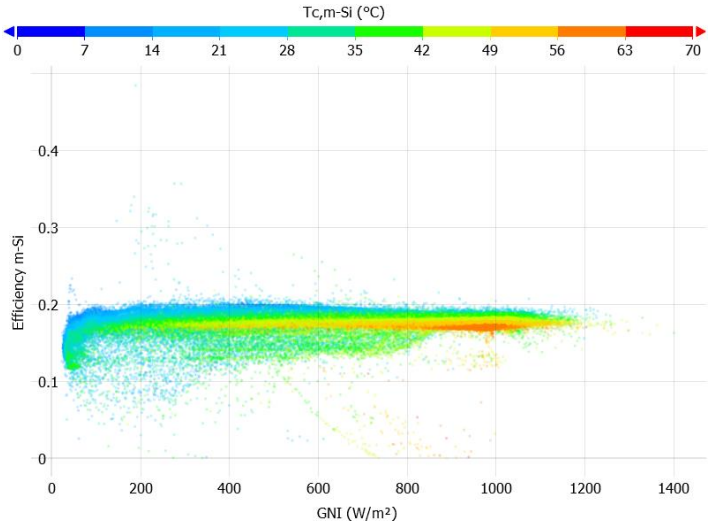

Figure 4-3: m-Si efficiency with basic and power filters

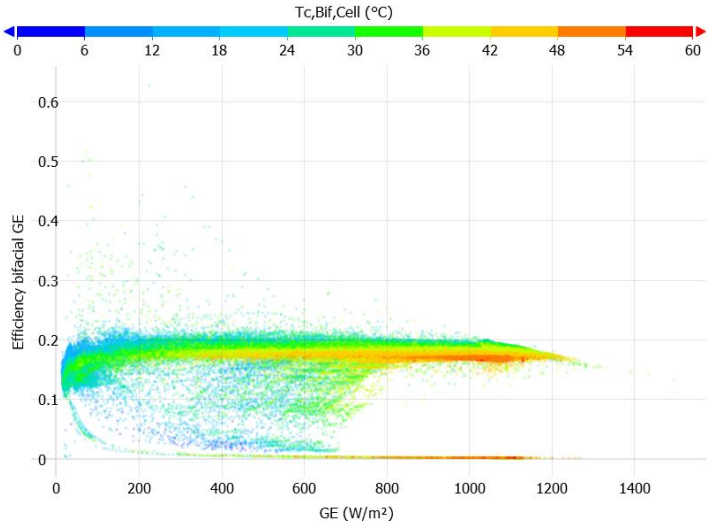

Figure 4-4: Bifacial efficiency with basic and power filters

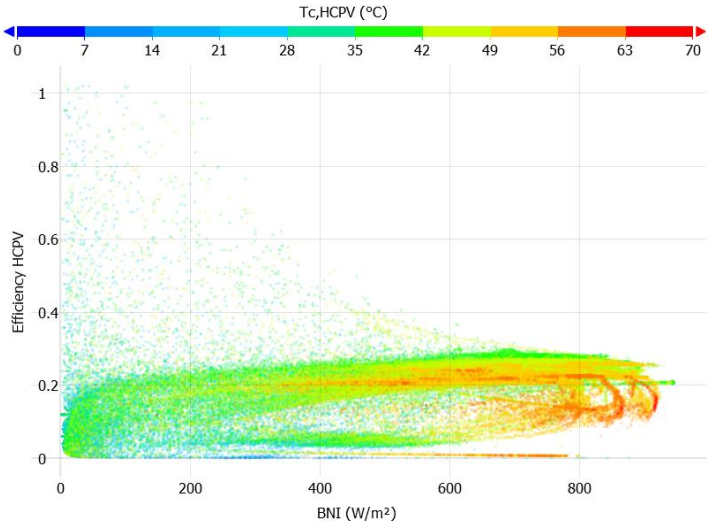

Figure 4-5: HCPV efficiency with basic and power filters

4.3 FILTERING STRATEGIES TO REMOVE OUTLIERS

After the basic and power filters described in Section 4.2, invalid data points were still present. This section considers further filtering schemes, aiming to better clean the datasets. The following filtering strategies were applied separately; thus, their effects are not cumulative, since the aim is to define what is the best filtering approach. All filters introduced in the following sections were applied in addition to the basic, DC and AC power filters shown in Section 4.2.

4.3.1 **IQR filter**

To filter the data for outlier removal, statistic filtering has been suggested in the literature. For instance, Lindig et al. (2021) applied the so-called inter quartile range (IQR) filter for outliers removal. The interquartile range holds 50% of the total data, whereas data outside the +/- 1.5 times que IQR limits are considered outliers. A filter with such a characteristic presents a behavior similar to a filter

based on a standard deviation of +/- 2.7. A visual representation of such a filtering technique, applied to a normal distribution, is presented in Fig. 4-6 (Galarnyk, 2023).

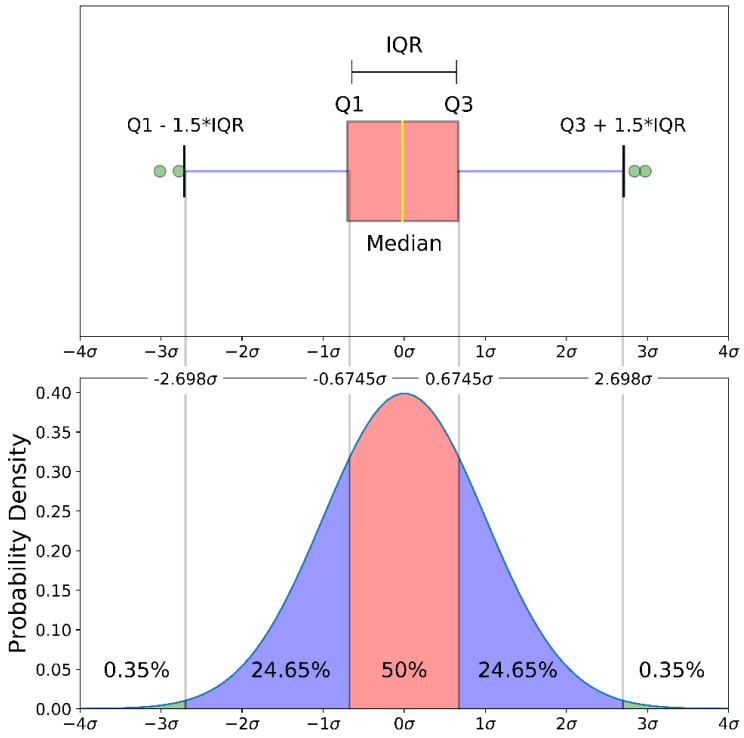

Figure 4-6: Graphical representation of the IQR filter scheme (Galarnyk, 2023)

Fig. 4-6 shows that using the +/- 1.5×IQR filter, 0.7% of the total data are considered outliers and therefore, removed.

In the work conducted by Livera et al. (2020), a comparison between three statistical outlier removal methods – namely the 1.5×IQR boxplot rule, the Hamper identifier and the 3-sigma were applied to a same dataset containing artificially added outliers, and the results were compared. Four cases were considered, namely 10, 20, 30 and 40% of outlier ratio in the dataset. In all cases, the 1.5×IQR method presented higher outlier detection rates, as in comparison to the other two methods. These three statistical outlier removal methods were also considered by Zhao et al. (2013), and the boxplot rule performed better than the other two methods, both in terms of accuracy and robustness. Due to the great performance shown by the 1.5×IQR method, it has been considered in the present thesis as an option for outlier removal.

After applying the IQR filtering, the dataset size for each PV technology is as follows:

p-Si dataset: 141245 records remaining (64.6 %)
m-Si dataset: 136950 records remaining (62.6 %)
Bifacial dataset: 144499 records remaining (66.0 %)
HCPV dataset: 118215 records remaining (54.0 %)

The scatter plots in Figs. 4-7 to 4-10 show clear cut-off on the efficiency levels. This was already expected given the nature of the IQR filter, which respects the boxplot limits.

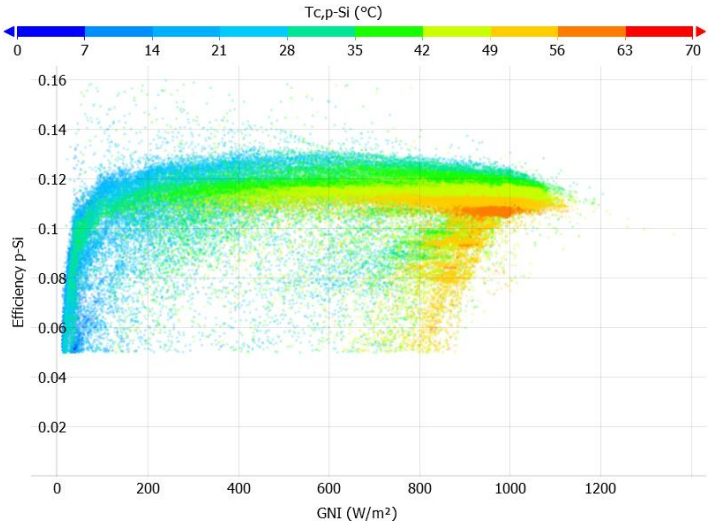

Figure 4-7: Efficiency plot after IQR filtering for the p-Si array.

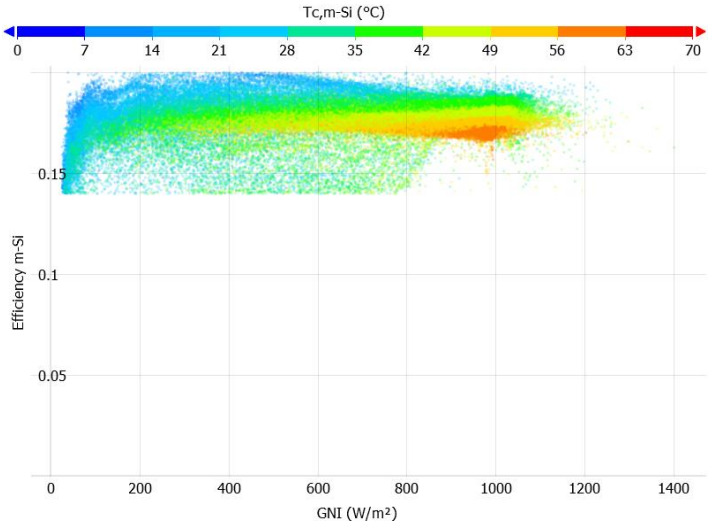

Figure 4-8: Efficiency plot after IQR filtering for the m-Si array.

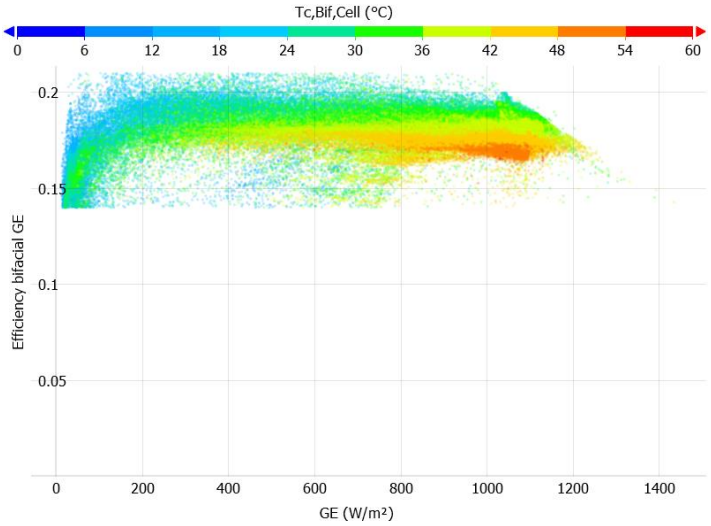

Figure 4-9: Efficiency plot after IQR filtering for the bifacial array.

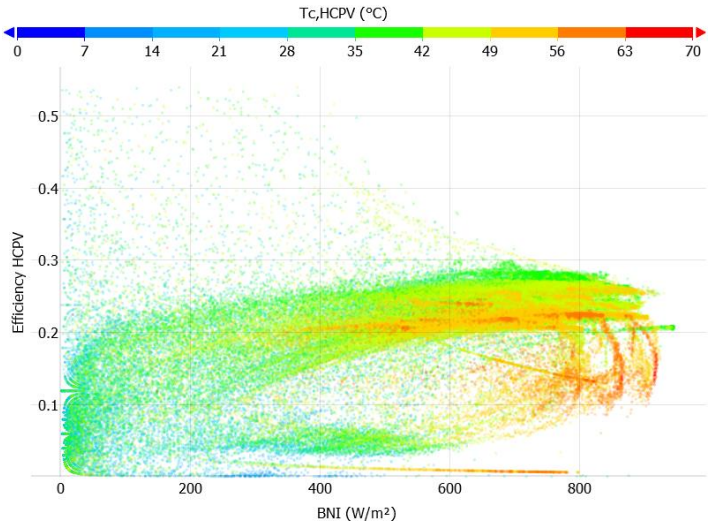

Figure 4-10: Efficiency plot after IQR filtering for the HCPV array.

It should be noted that for the HCPV, the low cut-off efficiency level is close to zero, which means that, in practice, few points were effectively filtered. In fact, the number of records referring to the HCPV presented only 0.4 % reduction, from the basic and power filters to the IQR filter. The reason for this is the high standard deviation found for the efficiency levels under a given BNI, for the whole range measured.

4.3.2 **Model-based filtering**

The IQR filtering scheme is not able to detect incoherences regarding the weather condition and the PV arrays' output power, given its statistical nature. To assess if the PV output is compatible with the irradiance and temperature, it becomes necessary to adopt a filter scheme that considers the coupling between the weather and the PV electric parameters; such a task can be accomplished by applying suitable modeling methods. A simple approach to make this relation is via the ratio of short-circuit current to irradiance, as carried out by Paudyal and Imenes (2021). However, in the present thesis, the experimental records are made on a PV system operating in real operating conditions, therefore short-circuit current measurements are not available. An alternative approach would be the use of the operating current instead of the short-circuit current, since the operating current and the irradiance are strongly related, as described by Abe et al. (2020b). A similar approach is described by Li et al. (2023), where the authors mention the relationship between the operating current I_{mp} and the irradiance; and between the operating voltage V_{mp} and the temperature T_c. The authors adopted a regression procedure of I_{mp} as a function of GNI and of V_{mp} as a function of T_c, whereas defining a threshold to determine the filter boundaries. In turn, Wang et al. (2018) employed mathematical expressions to calculate the PV array's voltage and current levels – and calculate the array power – for the observations where the inverter was saturated. All such works employed models to relate the PV array's output and the operating condition, which can be used for data filtering.

In the present thesis, three models were used to detect and filter out conditions in which the weather condition and the PV output parameters are not coherent. This covers cases where the PV arrays are not operating at the maximum power point. Such models are 1) a power model for the p-Si,

m-Si and bifacial arrays; 2) a power model for the HCPV array; and 3) IEC-60891 for current and voltage predictions.

The power model for the crystalline PV modules (Eq. 2.8) was introduced by Menicucci (1985), whereas the power model for the HCPV modules (Eq. 2.19) was proposed in a PhD thesis defended in 2020 at the University of Corsica (Benhammane, 2019; Benhammane et al., 2021); in his thesis, the author used the same PV tracker and HCPV modules that are employed in the present work.

In turn, IEC-60891 (IEC, 2009) as described in Section 3.7.1 presents Eqs. (3.3) and (3.4), and such a procedure has been applied using the simplified method proposed by Abe et al. (2021), developed within the context of the present thesis. The parametric identification referring to Eq. (3.4) concerns a, R_S and k. For the p-Si array, these values are respectively 0.042, 0.527 Ω and -0.009 Ω/K. For the m-Si array, the values are respectively 0.061, 0.740 Ω and 0.001 Ω/K; and finally, for the bifacial array, they are 0.013, 0.430 Ω and 0.002 Ω/K.

A relevant factor when using a power model and IEC-60891 as references to filter the data is to determine the admissible error, that is, the filter thresholds. For the P_{mp} model, irradiance and temperature measurements are used as inputs. Therefore, the uncertainty referring to such measurements has been used to estimate the combined uncertainty, as described in Section 3.9. In this thesis, the filter thresholds for the three model-based filters were set as two times the combined uncertainty for the measurements.

After implementing the power model-based filtering (Eqs. 2.8 and 2.19), the dataset size changed as follows:

p-Si dataset: 121473 records remaining (55.5 %)
m-Si dataset: 133251 records remaining (60.9 %)
Bifacial dataset: 136501 records remaining (62.4 %)
HCPV dataset: 80544 records remaining (36.8 %)

In the scatter plots (Figs. 4-11 to 4-14), great improvements in sparse points removal are observed, as in comparison to the scatter plots generated from the IQR filtering strategy.

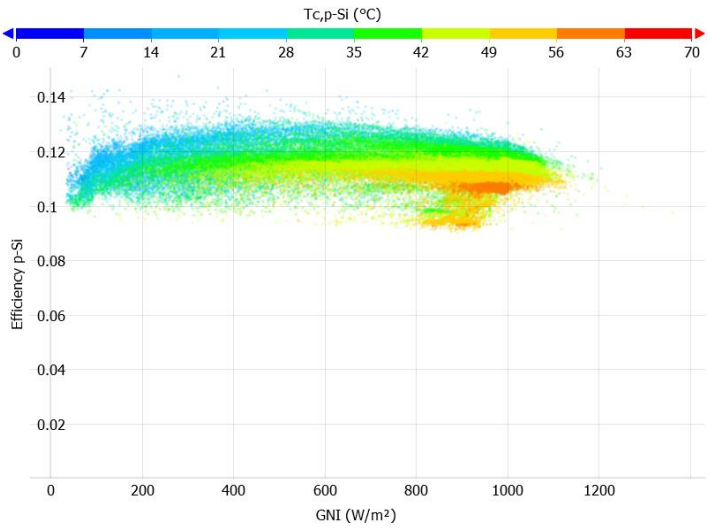

Figure 4-11: Efficiency plot after power model filtering for the m-Si array

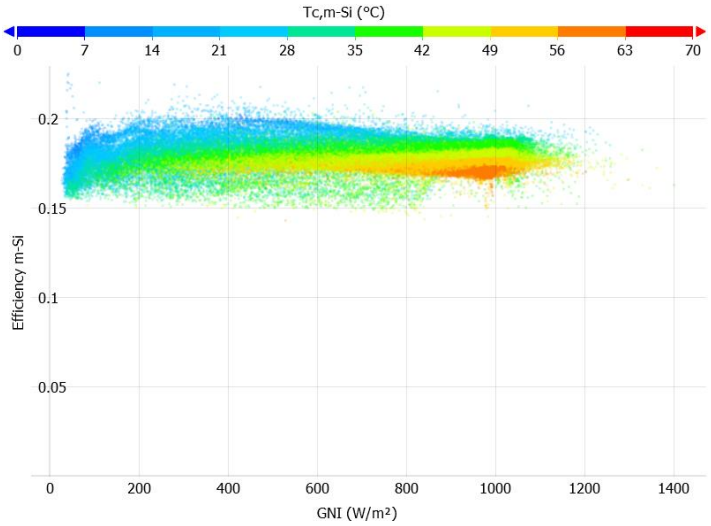

Figure 4-12: Efficiency plot after power model filtering for the m-Si array

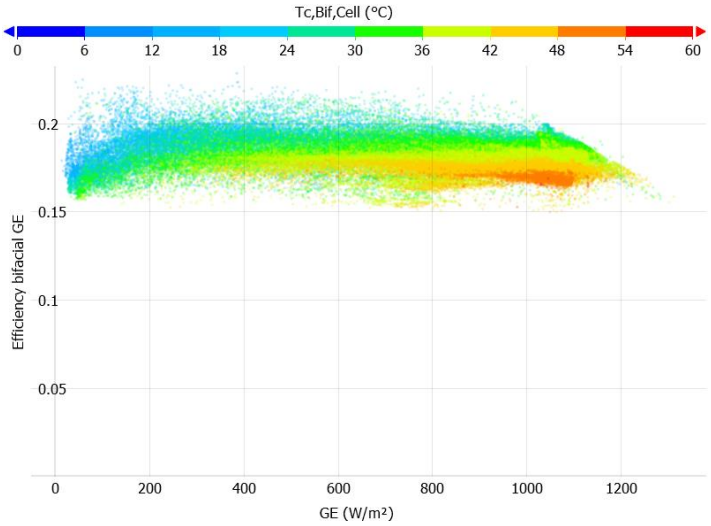

Figure 4-13: Efficiency plot after power model filtering for the bifacial array

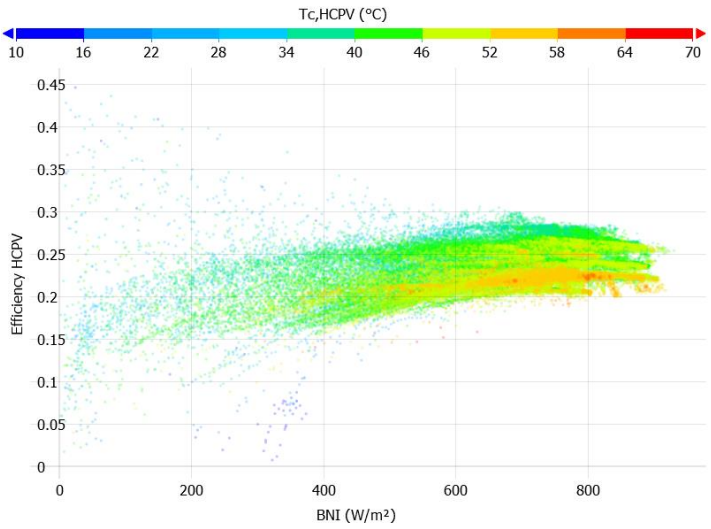

Figure 4-14: Efficiency plot after power model filtering for the HCPV array

After the application of the IEC-60891 filtering scheme, the remaining data points are as follows:

p-Si dataset: 121568 records remaining (55.6 %)
m-Si dataset: 132262 records remaining (60.5 %)
Bifacial dataset: 143373 records remaining (65.5 %)

Using IEC-60891 as a filtering strategy for the p-Si, m-Si and bifacial arrays datasets produced slight differences in terms of number of data records, as in comparison to the power models, especially for the p-Si array (0.1 % difference) and the m-Si array (-0.4 % difference). Despite the similar number of records removed with such filters, the shape of the efficiency scatter plots presents significant differences, particularly for low irradiance levels. The plots in Figs. 4-15 to 4-17 show an efficiency drop for low irradiance levels, whereas such records were removed when using the power model-based filtering. Keeping the group of points showing low efficiency under low irradiance levels could be of interest to evaluate the effect of the air mass on the efficiency.

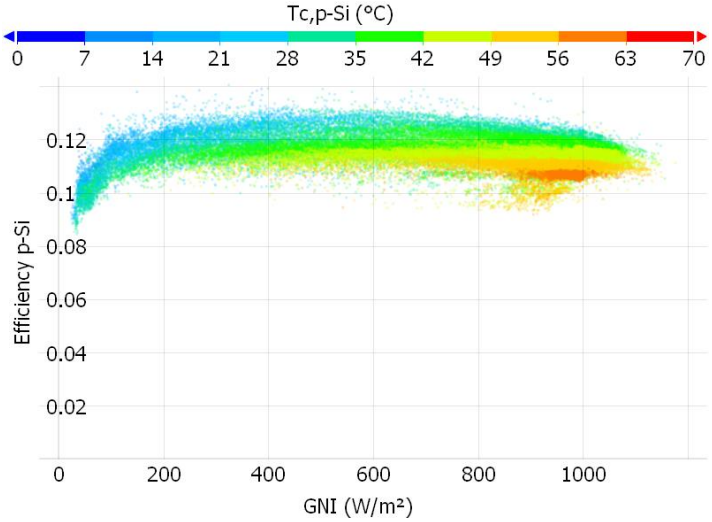

Figure 4-15: Efficiency plot after IEC-60891 model filtering for the p-Si array

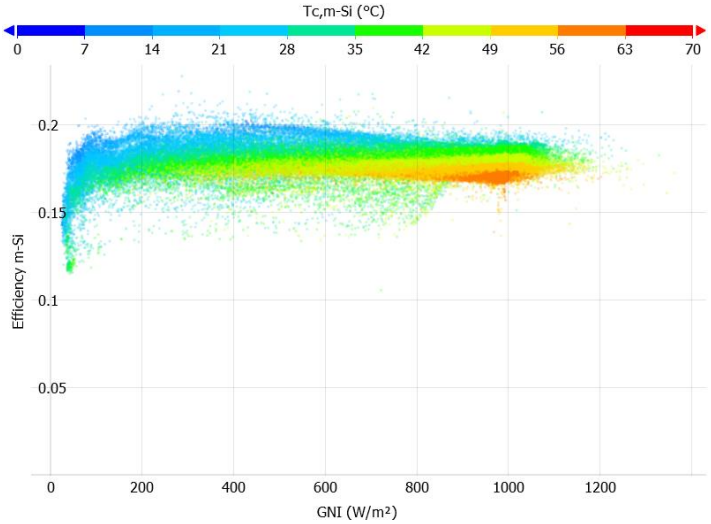

Figure 4-16: Efficiency plot after IEC-60891 model filtering for the m-Si array

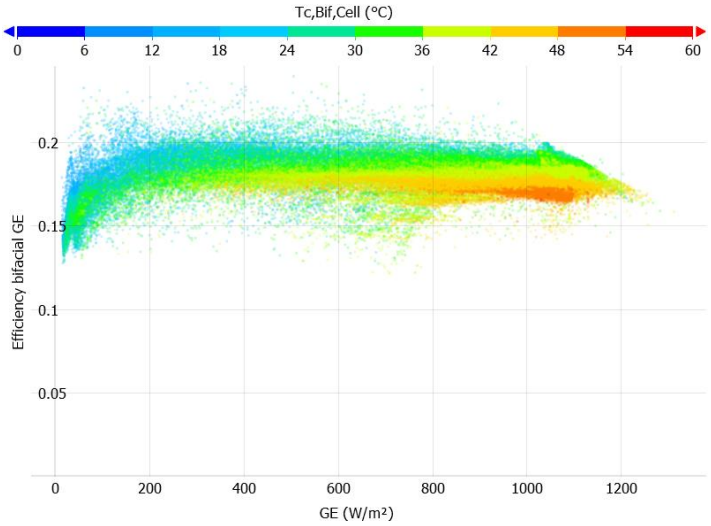

Figure 4-17: Efficiency plot after IEC-60891 model filtering for the bifacial array

For the HCPV array's dataset, the power model filtering retained a group of points presenting low efficiency at low irradiance, which allow further studying the influence of the air mass. Therefore, the filtering strategies selected to produce the datasets to be used in the upcoming sections of this thesis are the power model for the HCPV array; and the IEC-60891 model for the p-Si, m-Si and bifacial arrays. It should be noted that all models employed for filtering consider only voltage, current or power. Photovoltaic efficiency models were not used at this stage.

4.4 SUMMARY OF THE FILTERING APPROACHES

Section 4.2 considered the application of the basic filtering as the initial noise-removal strategy. A graphic summary is presented in Fig. 4-18, where the percent values refer to the remaining data amount after each filter stage.

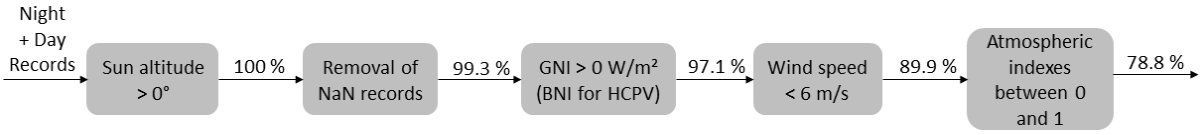

Figure 4-18: Graphical representation of the basic filters

Section 4.2 considered, also, the DC and AC power-based filters, to remove records in which the DC power levels was zero (PV array not in operation) and when the AC power was equal or above 3000 W (inverter saturation). Figure 4-19 illustrates the DC and AC filters.

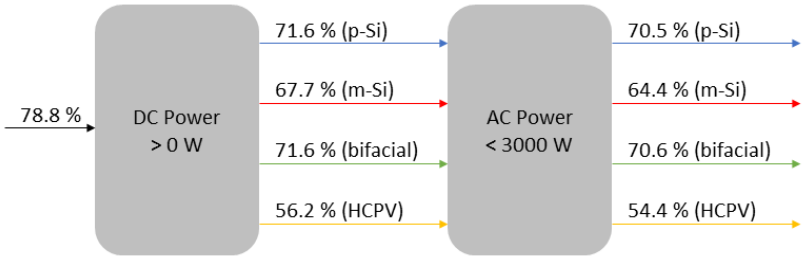

Figure 4-19: Graphical representation of the DC and AC power filters

Finally, Fig. 4-20 illustrates the application of the IQR, the P_{mp} and IEC-60891 filters, presented in Section 4.3. The selected filtering schemes, for each PV technology, are highlighted by the red squares.

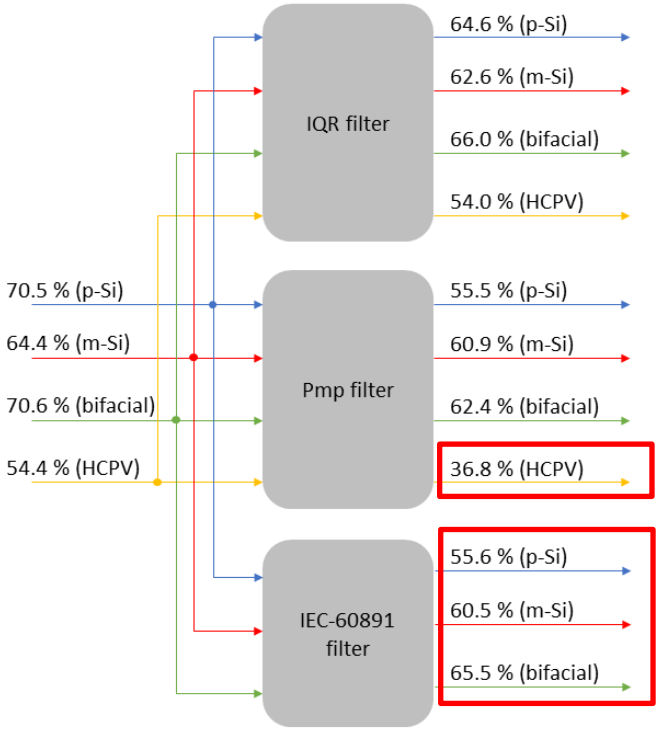

Figure 4-20: Graphical representation of the IQR, P_{mp} and IEC-60891 filters

A detailed time-series analysis, showing the reasons behind the production of outliers within the measured data, is available on Appendix C.

4.5 CONCLUSIONS FOR SECTION 4

The data recorded for this study comprised of measurements coming from three different platforms: a) the PV tracker system, with measurements referring to in-plane global irradiance for the front and rear sides of the PV arrays, backside temperature of one module per array, DC and AC voltage, current and power; b) the weather station, with measurements for the air temperature, wind speed, relative humidity and global horizontal irradiance; c) the Solys 2 pyrheliometer for the normal beam irradiance and pyranometers for horizontal global irradiance and diffuse horizontal irradiance.

The main platform refers to the tracker system, which was set to take measurements at the minute-timestep. The other two platforms presented variable timestep: therefore, it became necessary to interpolate the data so that the final dataset contained records referring to all variables, at the same timestep. The synchronicity between the platforms was periodically checked by the engineering staff, whereas the data synchronicity was confirmed by plotting the PV power and the irradiance measurements together, with special attention to situations with dynamic cloud cover.

An initial filtering was applied to the data, aiming to remove invalid records, night periods and data in which the DC power was zero, as it was desired to address only the cases where the PV arrays were in operation.

The PV efficiency is a useful parameter to assess the quality of the data since such a metric is calculated using the PV power and the solar irradiance. That is, the efficiency considers the most important variables at the PV output and solar resource sides. As a result, unusually high or low efficiency levels usually denote measurement problems, especially in regard to partial shade on the PV arrays or shaded irradiance sensors, situations which are likely to occur around the times of sunrise and sunset, given the extreme positions that the PV tracker assumes.

Using the efficiency as the main reference, different filtering strategies were then evaluated aiming to remove outliers, whereas closely assessing the balance between the removal of invalid records and the retention of data for the analysis.

Voltage and current models for the p-Si, m-Si and bifacial arrays, and a power model for the HCPV array were employed for filtering. Since these models provide a link between the operating condition and the electrical performance of the arrays, it was possible to exclude records which presented too much deviation between the observed and predicted parameters – be it power, voltage or current. Besides the model selection, the most crucial aspect is the filtering threshold, that is, the admissible deviation to cause a record to be removed. Setting the threshold too tightly might cause the dataset to be shaped by the model; on the contrary, setting the tolerances too high might cause a high amount of invalid data to be preserved. Among several strategies tested, the threshold set to 2 times the uncertainty referring to the parameter being modelled presented a good filtering balance.

SECTION 5

INFLUENCE OF EXTERNAL PARAMETERS ON PV ARRAYS' PERFORMANCE

5 INFLUENCE OF EXTERNAL PARAMETERS ON PV ARRAYS' PERFORMANCE

In this section, the output DC power referring to each of the four PV arrays is taken as the target parameter to assess the influence of the external meteorological parameters on the PV performance. As a starting point, a correlation matrix relating all measured parameters is constructed and presented, offering a general view of the correlation between the various parameters under consideration. Then, special attention was given to the influence of the air and cell temperature. In the sequence, multivariable models were created to rank the external parameters in order of relevance.

The sensitivity analysis is carried out in the middle subsections (5.4 and 5.5). First, a purely experimental approach is developed, based on data filtering. Then, a model-based analysis is carried out, allowing the quantification of the external parameters' influence on the DC power.

This section presents, also, the development of models to specify the DC power using the cell temperature instead of the air temperature, offering a secondary means of determining the STC ratings for the PV modules. Besides this, the present section brings an assessment covering the particularities of the bifacial array, with the introduction of novel methods to easily determine the effective irradiance and the bifacial gain. Such a focus on the bifacial array was not listed in the original objectives of this thesis. In fact, these new methods were designed to address potential difficulties associated with the performance analysis of bifacial devices. This topic becomes relevant given the peculiar behavior of bifacial PV modules, their interesting cost-benefit, and their ever-increasing use in new PV projects.

Finally, this section ends with a monthly summary of the performance metrics for the PV arrays and the average values for the relevant external parameters.

5.1 CORRELATIONS FOR THE MEASURED PARAMETERS

Two correlation metrics are usually employed in correlation studies: the Pearson correlation index, which measures the degree of linearity between two variables; and the Spearman correlation index, which offers a measure of the monotonicity in respect to the correlation between two variables. Even with the use of correlation indexes, plotting the data in scatter plots it is always a good practice, since it is possible that two variables are well correlated, however, not in a linear or monotonic fashion.

Fig. 5-1 illustrates a correlation matrix considering the DC power, cell temperature, and all relevant external parameters. In all cases, the strongest positive correlations are found for the BNI and GNI, as well as for the irradiance-related indexes: normal beam clearness index and normal global clearness index. The strongest negative correlation was found for the diffuse fraction, for all four PV technologies, given its calculation based on GNI and BNI (Table 2-1). The air mass has also shown significant negative correlation with the DC power, for all technologies studied. In the correlation matrix shown in this section, each cell is colored according to the correlation between two variables, allowing to assess the degree of correlation in one glance.

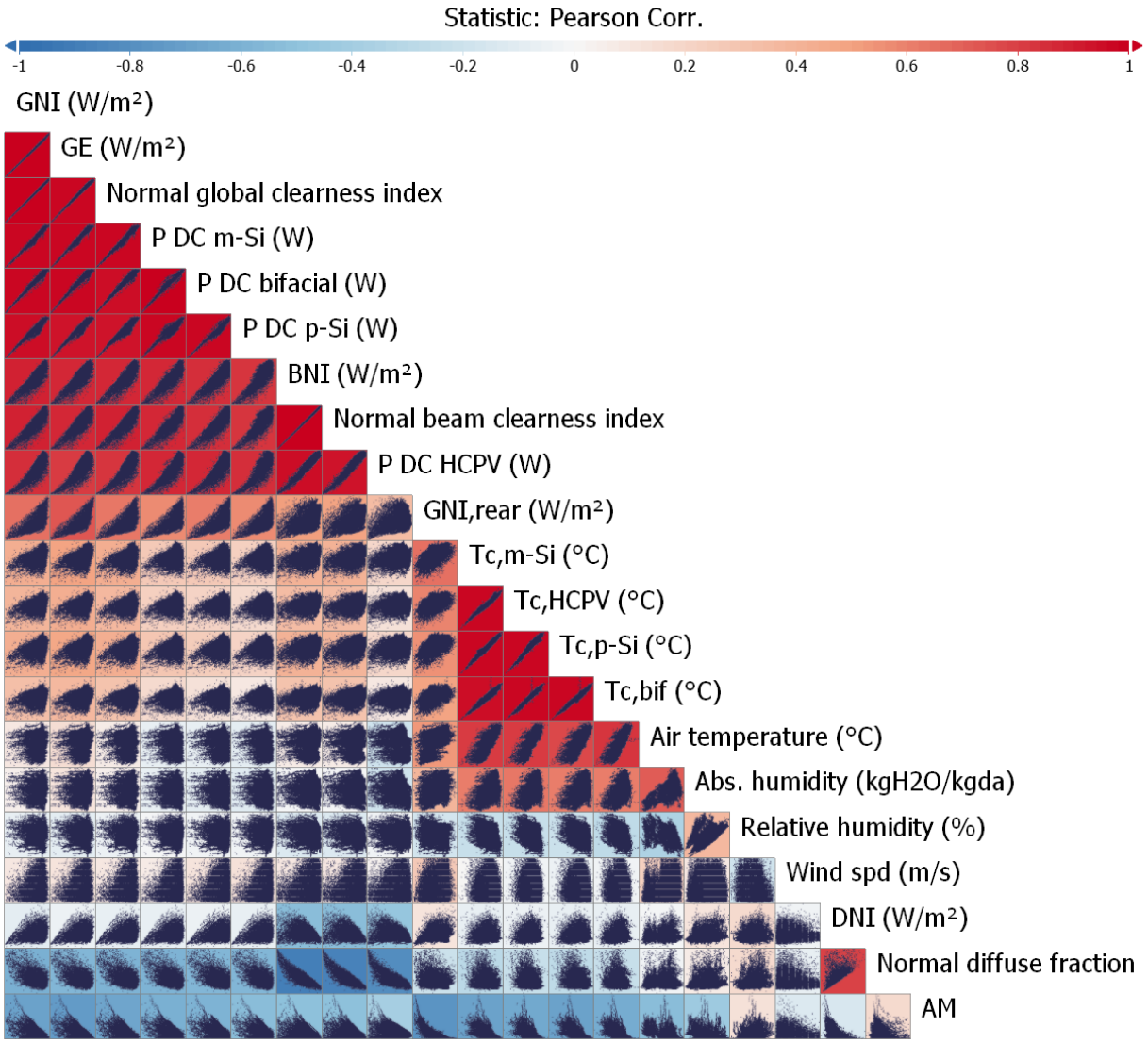

Figure 5-1: Correlation matrix for the DC power and relevant parameters

Strong correlations are found for the parameters at the upper portion of Fig. 5-1, more precisely at the first eight rows. Such parameters are the global and beam irradiance metrics, and the DC power referring to all four PV arrays. It is therefore clear that the irradiance is the variable which is most well correlated with the PV power, in all cases. The AC power was found to be well correlated with the DC power and irradiance; however, it was decided not to include the AC power in the analysis given that each PV inverter has only one AC output, which results from the contribution of two DC inputs. This way, it is not possible to separate the AC metrics by PV technology.

The measurement campaign included relative humidity (RH) measurements; however, such a quantity expresses the humidity as a percent of the humidity amount that the air could possibly hold at the current temperature. Therefore, given the outdoor nature of the present work, the air temperature is an uncontrolled parameter; and it is thus desired to base the analysis on a humidity quantity regardless of the air temperature. This can be achieved by computing the absolute humidity (AH) expressed in $kgH_2O/kgda$ (da=dry air) from the air temperature and relative humidity. Such a calculation was carried out using the procedure presented on the ASHRAE Handbook –Fundamentals (ASHRAE, 2009). Both metrics – RH and AH are included in Fig. 5-1.

A curious finding refers to the cell temperature: although it is known that increasing the cell temperature causes the PV power to decrease, the correlation matrix shows a weak, yet positive correlation between T_c and DC power, for all four PV arrays. It should be noted, though, that all T_c metrics are mildly correlated with GNI and BNI, and that the irradiance exerts a much stronger influence on the PV power than T_c. A focused assessment of the temperature influence on the DC power is provided in Section 5.2. The cell temperature is strongly correlated with the air temperature.

The air temperature correlates positively with the absolute humidity, since the hotter the air, the greater its capability of carrying water vapor. In turn, the air temperature correlates negatively with the relative humidity, given that it represents a percentage of the maximum amount of water vapor that the air could contain, as a function of its temperature. This way, increasing the air temperature increases its capability of holding water vapor, which causes the measured RH to decrease.

The air mass correlates negatively with all four PV arrays, since high AM levels are related with low global irradiance. High AM levels are associated with low solar altitude angles, which, for fixed PV systems, results in an increased angle of incidence and increased reflection of radiation. However, this is not the case for the present thesis since the PV arrays are mounted on the 2-axis tracker. Therefore, the AM influence refers, mainly, to a reduction of the global irradiance since the reflection losses are minimized by the tracking. It should be pointed that, for constant GNI and different AM, the spectral content is likely to be different; also, different PV technologies respond differently to spectral changes.

The normal diffuse fraction presents a negative correlation with the DC power of all PV arrays. However, such a correlation is more pronounced for the HCPV array. The reason is the use of lenses to concentrate the solar radiation, and the fact that such optic devices can only concentrate the BNI component.

Finally, the wind speed does not present a strong correlation with the DC power, although the wind increases the convective thermal exchanges and thus should reduce the cell temperature.

5.2 CORRELATING THE DC POWER AND TEMPERATURE

For all four PV technologies, the correlation matrix presented in Section 5.1 shows positive coefficients for the temperature correlation with the DC power.

As stated earlier, at first sight this seems contradictory, given the known negative influence of the cell temperature on the voltage, and therefore, on the power. In fact, the full-range data were used to produce the referred matrix, thus providing a first, general view on the correlation between the various parameters within the dataset. Given that high cell temperatures are usually related to high irradiance levels, and given that the power dependence of irradiance is significantly stronger than that of temperature, the cell temperature correlation with power becomes positive, in a general view. However, the same is not true when the irradiance is constant. In this section, the correlation plots are studied for constant irradiance levels, allowing to assess the power correlation with temperature in a more suitable and focused approach.

For the p-Si and m-Si technologies, the GNI levels were filtered in the range 990 – 1010 W/m², to allow direct comparison with the temperature coefficients for power provided on datasheets. In

turn, for the bifacial array, the effective irradiance (G_E) was filtered from 990 to 1010 W/m², whereas for the HCPV array, the BNI was filtered from 690 to 710 W/m².

5.2.1 **Constant irradiance for p-Si**

From the scatter plot in Fig. 5-2, the temperature coefficient for power is -0.44 %/°C, considering the STC power of 979 W for the p-Si array. The datasheet presents -0.42 %/°C, that is, a very close value.

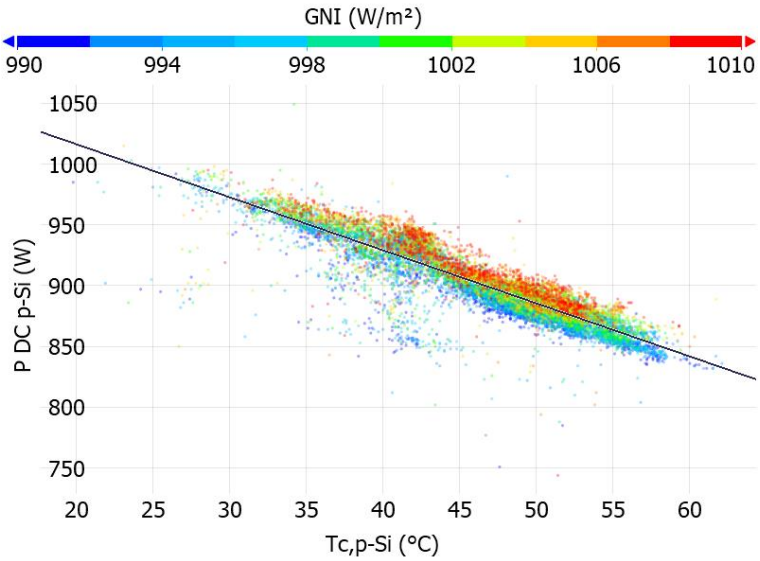

Figure 5-2: Scatter plot with regression line; p-Si

5.2.2 **Constant irradiance for m-Si**

From the scatter plot in Fig. 5-3, the temperature coefficient for the power is -0.36 %/°C, considering the power at STC of 1220 W for the m-Si array. The datasheet reports -0.35 %/°C, which agrees with the experimental finding.

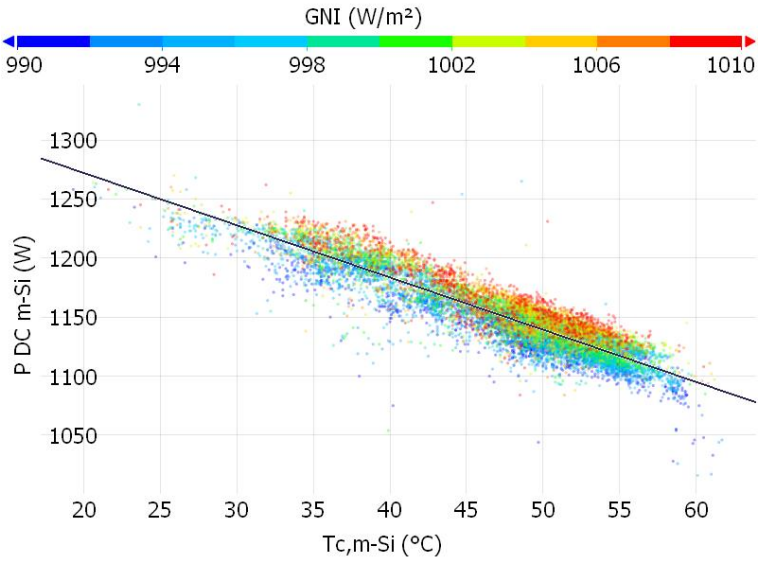

Figure 5-3: Scatter plot with regression line; m-Si

5.2.3 **Constant irradiance for Bifacial**

For the bifacial array, the temperature coefficient for power is -0.45 %/°C, considering the STC power of 1946 W for the bifacial array. It should be noted that the effective irradiance was used as the reference for coloring the points in the scatter plot. The datasheet value for γ is -0.37 %/°C. Possible reasons for such a difference are: 1) the temperature measurement method used in the context of this thesis, which consists of a flat temperature sensor attached to the rear-side glass (the PV module manufacturer does not specify the measurement method used for their test); and 2) the condition for the tests: the test carried out in this thesis consisted of a long-term experimental campaign, outdoors and therefore under uncontrolled conditions (the PV module manufacturer does not specify the condition for their test). All in all, it should be noted that the p-Si and m-Si present an EVA back-sheet encapsulant (0.35 mm thickness), which allows the temperature sensor to be closer to the PV cell. The same is not true for the bifacial modules, which present a total glass encapsulation (2 mm glass thickness on each side).

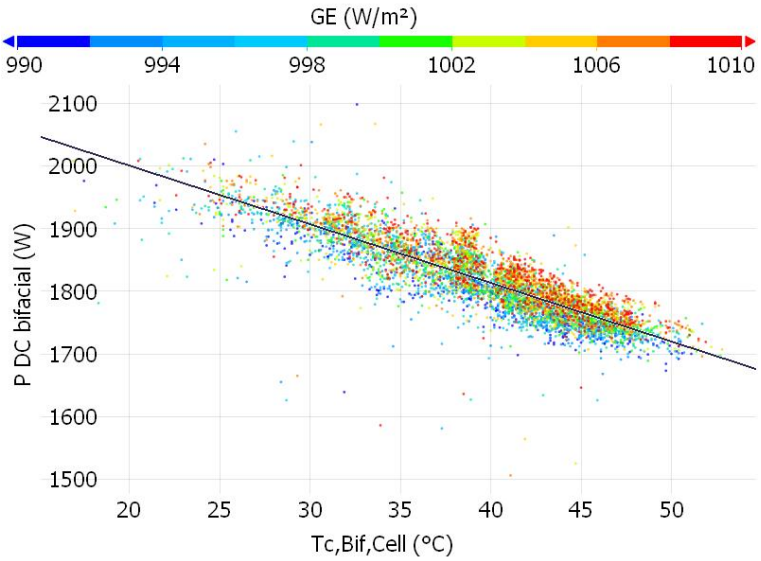

Figure 5-4: Scatter plot with regression line; bifacial

5.2.4 **Constant irradiance for HCPV**

For the HCPV array, the temperature coefficient for power was calculated as -0.57 %/°C. It should be noted, though, that the datasheet reports the power temperature coefficient as -0.14 %/°C. Also, the HCPV array temperature was measured on the heatsink of one of the modules; therefore, the temperature might not be representative of the actual cell temperature. For this reason, a temperature correction was applied using Eq. (2.20), presented in Section 2.2.4.

A more reliable way of determining the cell temperature is via open-circuit voltage measurements, as discussed by Rodrigo et al., (2014). However, measuring the V_{oc} is not practical in the context of this thesis, given that the PV arrays operate on the maximum power point, in real operating condition, supplying the external grid.

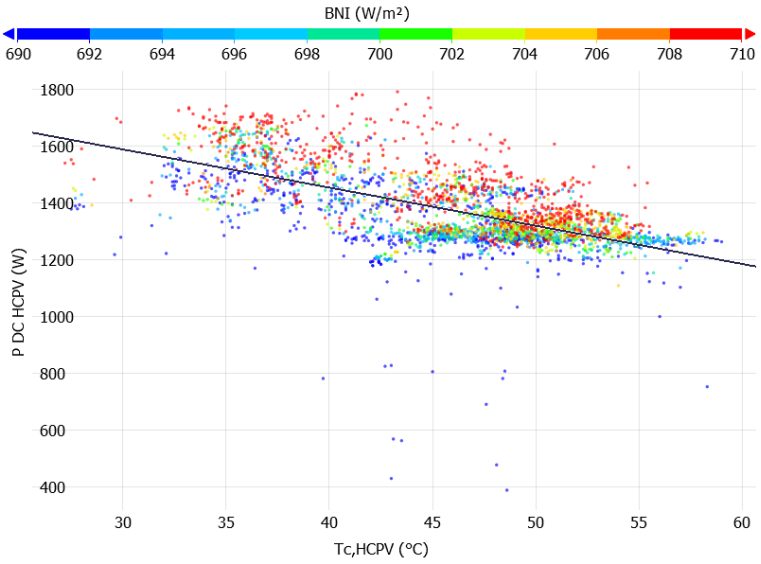

Figure 5-5: Scatter plot with regression line; HCPV

5.3 RELEVANCE OF THE EXTERNAL VARIABLES FOR DESCRIBING THE DC POWER

The relevance of each meteorological variable with respect to the DC power is the focus of the present section. For that, a polynomial multivariable regression was used to predict the DC power values, and the equation coefficients were adjusted to minimize the squared error between measured and predicted power levels.

The variables considered in the polynomial regression are: GNI, BNI, DNI, air temperature, AM, absolute humidity, wind speed, normal global clearness index (NGCI), normal beam clearness index (NBCI) and normal diffuse fraction (NDF). For the bifacial array, GNI_{rear} and G_E were also assessed.

Polynomial models were tested until the fourth degree; the best results were found using polynomial degrees up to two. Exhaustive tests were carried out with polynomial terms consisting of single and combined input variables, using the data analysis application Visplore®, which provides an automated feature to test different combinations between the equation variables, computing the optimal polynomial coefficients to minimize the RMSE error for the DC power. The best models were found to be the ones allowing combinations between variables (multiplication) to compose the polynomial equation terms. The model improvement was carried out including new equation terms until the nRMSE improvement was smaller than 0.001%. As expected, this termination condition is closely related to the complexity of the model obtained.

The allowed input variables for the models were sequentially introduced following two basic rules: 1) in each variable inclusion step, all variables were tested in the polynomial fit and the nRMSE were recorded. The variable associated with the greatest nRMSE reduction was effectively added to the model, and a new variable inclusion step was initiated; 2) new variables were added until the observed nRMSE error reduction was smaller than 0.01%; or until there were no variables left. This allowed ordering the variables by relevance, while building the optimal model in each trial. Such an approach consisted in classifying the external parameters in terms of their ability to describe the PV power. In this thesis, the external parameters – which define the operating condition – are also

referred to as descriptive variables, or input variables, or explanatory variables, when related to a model. In turn, the power – which is the observed variable – is referred to as output, or target, or outcome, when related to a model.

Table 5-1 shows the order of relevance for the different parameters when modeling the DC power according to the multivariate polynomial regression. For the p-Si, 6 variables were used as inputs in the model, whereas the smallest nRMSE was 3.37 % (R^2 = 0.9878). For the m-Si, 5 variables were inserted into the model, with minimum nRMSE of 1.84 % (R^2 = 0.9971). In turn, the polynomial regression for the bifacial array employed 6 variables, producing minimum nRMSE of 2.53 % (R^2 = 0.9951). Finally, 6 variables were used in the model for the HCPV array, which presented minimum nRMSE of 5.06 % (R^2 = 0.9621). The color-faded text was used to identify parameters whose inclusion to the model resulted in a nRMSE reduction of less than 0.1 %.

Table 5-1: Order of variable relevance, for the four PV technologies (including T_{air})

Variable relevance	p-Si	m-Si	Bifacial	HCPV
1	GNI	GNI	GNI	BNI
2	T_{air}	T_{air}	T_{air}	T_{air}
3	v_{wind}	BNI	GNI_{rear}	NDF
4	AM	AM	AM	AM
5	BNI	v_{wind}	v_{wind}	GNI
6	AH	-	BNI	AH

For comparison, the PV module's measured temperatures were also added to the polynomial regressions. The variable relevance analysis was carried out again, from the start – not only replacing the air temperature by the module temperature. Following the guidelines presented at the beginning of this section, the variables relevance order is organized in Table 5-2. It should be noted, though, that the module temperature is not an environmental parameter, but in fact, it results from the contributions of solar irradiance, air temperature and wind speed.

Table 5-2 Order of variable relevance, for the four PV technologies (including T_c)

Variable relevance	p-Si	m-Si	Bifacial	HCPV
1	GNI	GNI	GNI	BNI
2	T_c	T_c	T_c	T_c
3	AM	BNI	GNI_{rear}	AM
4	BNI	AM	AM	RH
5	v_{wind}	AH	AH	AH
6	-	RH	RH	GNI
7	-	DNI	v_{wind}	-

For the p-Si array, the nRMSE is 3.04 % (R^2 = 0.9901); for the m-Si, nRMSE = 1.62 % (R^2 = 0.9978); and for the bifacial array, nRMSE = 2.43 % (R^2 = 0.9956). It is therefore clear that including the module's temperature in the polynomial fit reduced the nRMSE, for the p-Si, m-Si and bifacial arrays.

For the HCPV array no nRMSE improvement was achieved when including the measured module temperature. The nRMSE was 5.12 % (R^2 = 0.9676). One possible reason for this outcome is the fact that the measurements were carried out with a sensor attached to the back of the board containing the cells, on the heatsink. Such a temperature level might not be representative of the actual cell temperature. Thus, for the HCPV, using the air temperature yielded the best modeling accuracy.

Such a modeling approach with several variables and terms is of questionable usefulness in practical applications: in some of the models, each term was composed by up to five parameters, whereas the total number of terms in a model was up to 30. Therefore, it should be highlighted that the models concerned in this section were chosen in such a way as to produce small errors while building models regardless of their complexity and size, aiming to determine the relevance of the operating parameters when describing the DC power. Details regarding the polynomial equation terms are provided in Appendix D.

5.4 SENSITIVITY ANALYSIS BASED ON THE EXPERIMENTAL RECORDS

Ideally, it would be possible to assess how strongly a given parameter affects the DC power by plotting both variables together, while keeping the remaining parameters constant. Repeating such a procedure for the four PV arrays, whereas considering only the data records which are common to all arrays, would allow to quantify the influence of the external parameters on each PV array. Thus, the PV technologies could be classified according to the dependency on specific environmental quantities.

However, when performing a sensitivity analysis based on the experimental measurements, two significant issues were observed. First, even using over 100,000 records, it is definitely not usual finding records in which one operational parameter varies widely while the others are constant. Second, the experimental resource for this thesis was designed to operate in real-world conditions, that is: the operational parameters are uncontrolled, and the PV arrays are connected to the grid via inverters. In turn, the inverters define the operating point for the PV arrays using the MPPT systems, which means that power fluctuations occur even when the external parameters are constant. That is precisely the essence of the MPPT algorithm, which constantly introduces changes (perturbations) on the operating point while seeking the maximum power (observations).

The first issue can be tackled by setting a tolerance for the parameters which are intended to be constant. On the one hand, this allows the number of points within a filter setting to be increased; on the other hand, this means increasing the variability allowed for all operating variables. All in all, there is a trade-off between the variability of parameters due to filtering tolerance, and the number of usable records.

Regarding the second issue, such power fluctuations were already expected. In fact, voltage variations up to 8 V (out of 200 V) were observed in intervals within 2 seconds. Likewise, current ripple up to 0.3 A (out of 5 A) was also recorded within a similar time interval. The dependence on MPPT systems would be eliminated if the experimental resource used I-V curve tracers to determine the complete electrical behavior of the PV arrays. However, this is not the proposal of the current thesis, which focuses on real operating conditions: PV arrays installed outdoors, supplying energy to the grid.

5.4.1 **Sensitivity analysis for the DC power via data filtering**

Plots regarding the sensitivity of the normalized DC power to several external parameters are shown in Figs. 5-6 to 5-13. They were built by applying filters to the dataset containing only the common points between the data records for the four PV arrays, to allow a fair comparison. The filter settings are as follows: 850-950 W/m² for GNI; 680-720 W/m² for BNI; 22-26 °C for T_{air}; 1.5-2.5 for AM; 1.5-2.5 m/s for v_{wind}; 0.009-0.012 kgH2O/kgda for AH; 100-125 W/m² for GNI_{rear}; and 0.2-0.4 for NDF. To construct Figs. 5-6 to 5-13, the filters referring to the variable on the horizontal axis were disabled. This way, the number of displayed records was defined by the remaining variables and their filter settings. It is worth noting that the normalized DC power was calculated dividing the observed power (in watts) by the experimental STC ratings defined in Section 3.7.

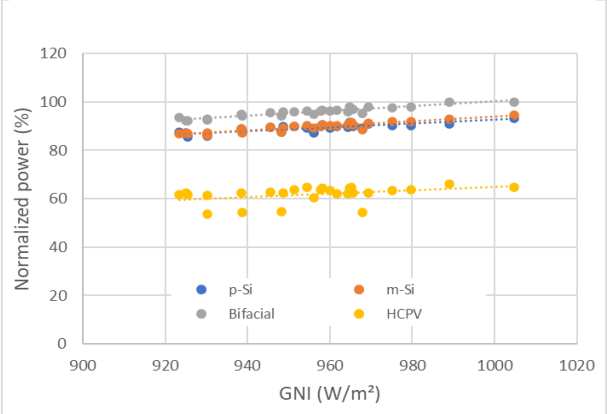

Figure 5-6: DC power sensitivity to GNI

For the m-Si and p-Si, Fig. 5-6 depicts records and linear fits which are closely matching, given that the DC power levels are normalized and both PV arrays refer to flat-plate, conventional modules. The offset for the bifacial technology refers to the contribution of the rear-side; it should be recalled that the STC power for bifacial devices refers to the front-face only. Therefore, a power gain is usually observed in outdoor operation, that is, when the modules receive irradiance, also, on the rear surface. In turn, the power levels referring to the HCPV array present levels between 60 and 70% of the STC power because the reference BNI is 1000 W/m², which is quite a high level for real operating conditions.

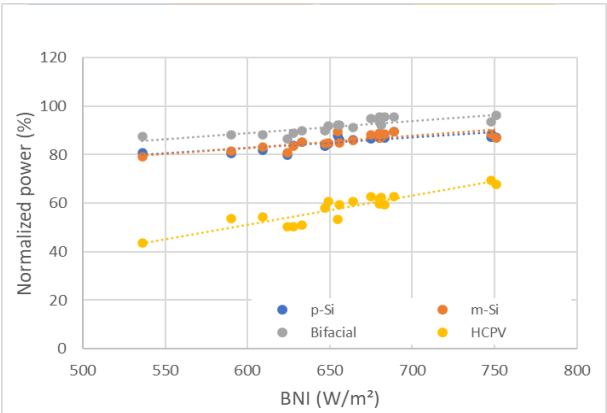

Figure 5-7: DC power sensitivity to BNI

In turn, Fig. 5-7 shows the normalized power response to BNI, where the rate of change is significantly greater for the HCPV than for the remaining PV technologies.

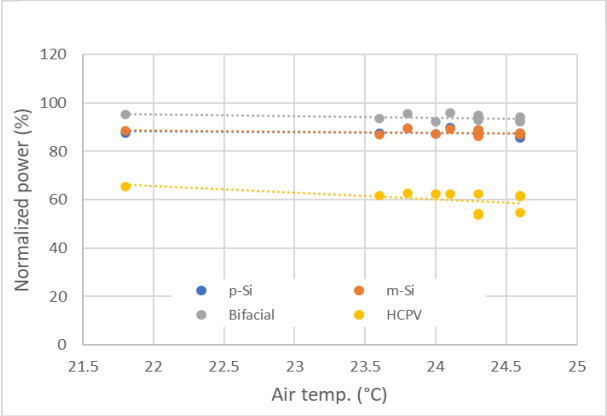

Figure 5-8: DC power sensitivity to the air temperature

For the influence of the air temperature, Fig. 5-8 shows a similar slope for the p-Si, m-Si and bifacial arrays. However, the slope is significantly more pronounced for the HCPV array. This is a curious finding, given that for the HCPV technology, the temperature factor the DC power is the smallest among all four arrays, as shown in Table 3-1. In fact, such a behavior was observed, also, when plotting the normalized power for filter settings other than the one considered in this section. The datasheet specification for the HCPV technology has already been questioned earlier: in Section 5.2.4, the temperature factor for the power was found as -0.57 %/°C, whereas the datasheet presents -0.14 %/°C (a 4x difference). In Fig. 5-8, the HCPV was found as the PV array presenting the greatest temperature effect on DC power, in agreement with the findings in Section 5.2.

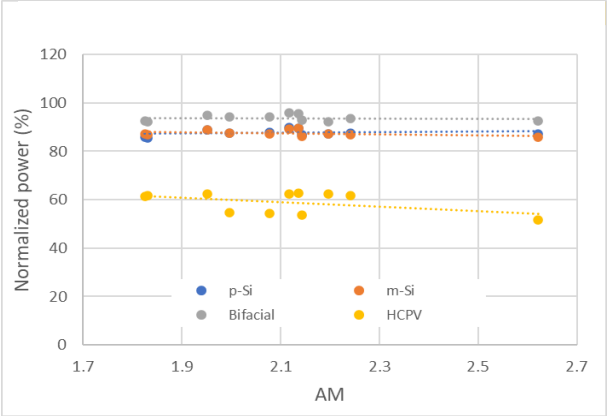

Figure 5-9: DC power sensitivity to AM

According to Fig. 5-9, increasing the AM caused more impact on the HCPV array than on the others. Although high AM levels are associated with reduced global irradiance, the slope for the p-Si technology presents a positive slope in Fig. 5-9. When plotting the cell temperature versus AM, it was found that for the points considered, the cell temperature of the p-Si array dropped significantly more than for the other technologies, considering the same AM increase. Such a temperature reduction could explain the slight gain in power for the p-Si array when increasing AM, as shown in Fig. 5-9. It is worth noting that the cell temperature presents a more pronounced impact on the PV output power than the AM.

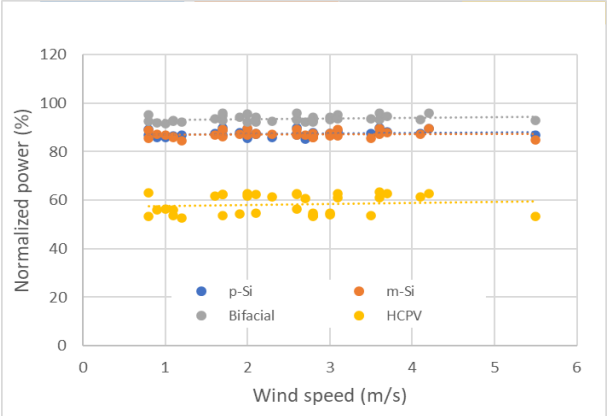

Figure 5-10: DC power sensitivity to wind speed

Considering the wind speed, the influence on the normalized DC power was found to be below 0.5 %/(m/s) for all four arrays, as shown in Fig. 5-10.

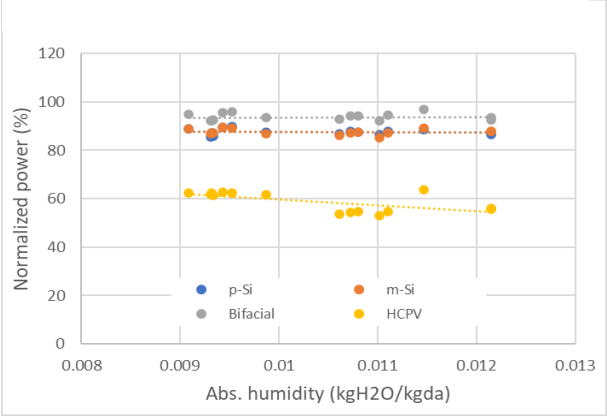

Figure 5-11: DC power sensitivity to the absolute humidity

The HCPV array is the most influenced by the absolute humidity variation, as illustrated in Fig. 5-11. When correlating the absolute humidity with other variables, no conclusions could be made. The spectral effect of increasing humidity cannot be quantitatively assessed since a spectroradiometer was not available at the measurement site.

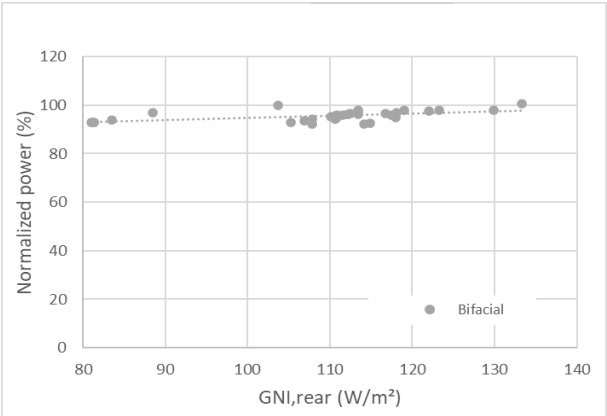

Figure 5-12: DC power sensitivity to GNI_{rear}

Concerning the bifacial array and GNI_{rear}, the slope is roughly 0.1 %/(W/m²). Once again, it should be noted that such an analysis considers GNI varying within a given range, as per the filter setting; therefore, the plot in Fig. 5-12 is biased by GNI.

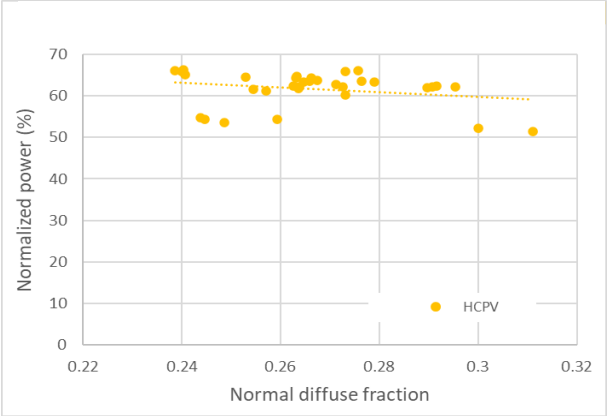

Figure 5-13: DC power sensitivity to NDF

Finally, the influence of the normal diffuse fraction was plotted for the HCPV only, since it was found as the only array for which the NDF was correlated to the DC power. In Fig. 5-13, the slope of the linear fit is -55.3 % per NDF unit.

5.4.2 **Sensitivity for the DC power in different scenarios**

Eight scenarios, in terms of operating condition, are considered for the sensitivity analysis in this section. Such scenarios were generated by filtering the dataset whereas keeping certain particularities according to the desired condition.

The clear sky scenario establishes the base for the other scenarios, since it is desired to assess the impact on the PV array's performance with respect to the individual weather parameters.

Table 5-3: Average values for the parameters defining the scenarios

Scenario	GNI (W/m²)	BNI (W/m²)	Tair (°C)	AM	Vwind (m/s)	AH $kgH_2O/kgda$	NGCI	NDF
Clear sky	992	752	22.2	1.56	2.10	0.010	0.73	0.24
Cloudy sky	**416**	**156**	22.8	1.64	1.82	0.012	**0.31**	**0.64**
High Ta	981	755	**30.8**	1.22	1.93	0.016	0.73	0.23
Low Ta	985	770	**17.4**	1.68	1.52	0.009	0.73	0.22
High AM	**624**	**465**	22.3	**4.92**	2.41	0.008	**0.45**	**0.25**
High Vwind	1001	785	22.7	1.23	**5.41**	0.010	0.74	0.22
Low AH	990	760	22.4	1.22	2.00	**0.007**	0.71	0.23
High AH	991	751	23.9	1.12	1.88	**0.014**	0.72	0.24

For each parameter – with values organized in each column of Table 5-3 – the items in bold text indicate values which make each scenario differ from the others: for instance, for the cloud sky

scenario, the GNI and BNI levels were filtered so as to produce a NGCI around 0.3, with the NDF around 0.65.

For the high AM scenario, the AM was filtered to select records around 5, which caused the GNI to be around 60% of GNI referring to the clear-sky scenario, producing NGCI levels around 0.45. It is desired to exclude cases with high AM and cloudy sky; this was accomplished by filtering the BNI so as to obtain NDF around 0.25.

The remaining scenarios – high/low T_{air}, high v_{wind}, and low/high AH were defined by filtering for the parameter of interest, while keeping the remaining parameters close to the setting referring to the clear sky scenario.

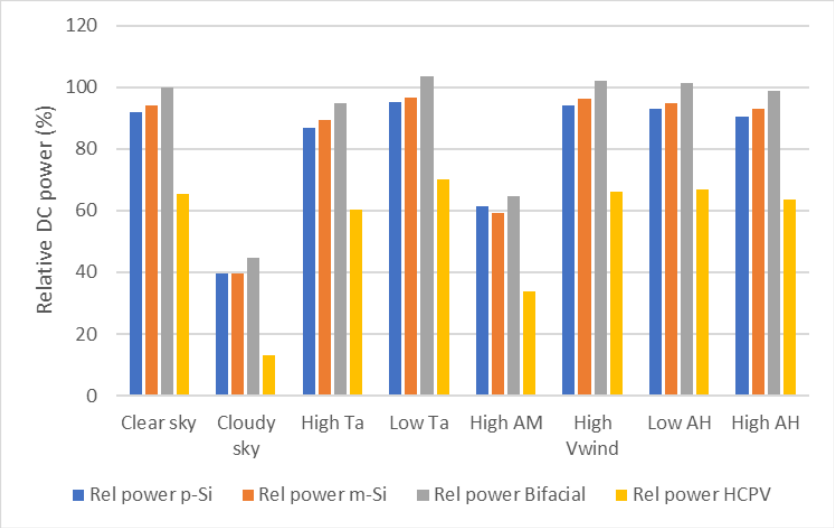

Figure 5-14: Relative DC power levels, per scenario and PV technology

The relative DC power levels displayed in Fig. 5-14 show how the operating condition impacts on the PV performance. As for the plots shown in Section 5.4.1 – for the sensitivity analysis – the greatest relative power values are related to the bifacial array, whereas the lowest are related to the HCPV technology. Regarding this subject, is worth recalling that the bifacial relative power exceeds 100% because the STC ratings for that technology are based on the front-side performance only. For the HCPV modules, the STC performance is based on BNI = 1000 W/m², that is, a condition rarely observed in real operating conditions; this explains the low relative DC power shown by the concentration PV array, in Fig. 5-14.

Regarding the p-Si and m-Si arrays, Fig. 5-14 shows that, except for the cloudy sky and high AM scenarios, the relative power referring to the p-Si is lower than that of the m-Si. When checking the cell temperature levels for both PV arrays, it was seen that the difference is within 0.3 °C, which is quite a low gap. However, the temperature coefficient for the DC power is higher for the p-Si than for the m-Si technology. This explains the lower performance of the p-Si array, in comparison to the m-Si when under high irradiance. It is clear from Fig. 5-14 that the highest power variations are related to scenarios which involve irradiance reduction – that is, cloudy sky and high AM cases. This should be no surprise since the irradiance is the most important external parameter for all PV technologies, as described in Section 5.3.

A better visualization of the cloudy sky and high AM data in Fig. 5-14 is provided in Fig. 5-15, where the relative power levels referring to the clear sky condition are taken as a reference, for a relative analysis. The bars in Fig. 5-15 are simply the variation of the levels in Fig. 5-14, relative to the clear sky scenario, expressed as percent values. For this reason, the power variation for the clear sky scenario is zero, whereas the levels for the cloudy sky and high AM scenarios are negative. Fig. 5-15 shows that, for the cloudy sky condition, the HCPV array was more impacted by the irradiance reduction than the other technologies. The reason is that the BNI is reduced in a greater scale than the GNI: taking the clear sky irradiance levels as a reference, in the cloudy sky scenario the GNI was reduced to 42%, whereas the BNI was reduced to 21% of the original level. It is worth recalling that the HCPV modules only respond to the BNI – because of the concentration – whereas the p-Si, m-Si and bifacial technologies are able to convert both BNI and DNI. This way, a sharp reduction in BNI results in a proportionally strong reduction of the HCPV array's output.

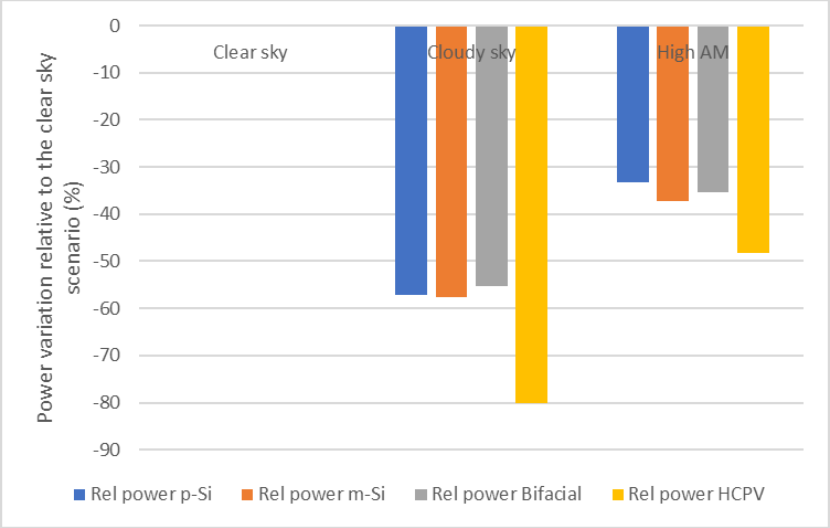

Figure 5-15: Power variations relative to the clear-sky scenario, for the clear sky and high AM scenarios, per PV technology

For the remaining parameters, Fig. 5-16 was built in a similar way as Fig. 5-15: the power variations, for each scenario and PV technology, are plotted with magnitudes relative to the clear sky case. Fig. 5-16 shows that the greatest variations in relative power refer to temperature changes. In both cases – high T_{air} and low T_{air} – the greatest power variations were shown by the HCPV array. Such a finding is consistent with the temperature coefficients for the DC power, which were experimentally determined and presented in Section 5.2. In that section, the HCPV modules were found to be the most sensitive for the temperature, among all four technologies. Also in Section 5.2, the p-Si and bifacial modules were found to be the second most sensitive for the temperature, which is coherent with the data in Fig. 5-16. Finally, the m-Si presents the lowest temperature coefficient for the DC power, among all four PV technologies considered in this thesis. This fact is corroborated by the data shown in Fig. 5-16.

The HCPV modules present quite a different construction, as in comparison with the other PV technologies considered in this work. The board which houses the multi-junction cells is contained within a metal housing, which acts as a barrier to the wind effect on the cells. In contrast, the PV cells

on the p-Si, m-Si modules are separated from the environment just by a glass cover – on the front – and by a thin polymer sheet, on the rear side. This means that the wind-induced thermal effect is more pronounced on these PV technologies than on the HCPV. By observing Fig. 5-16, with respect to the high v_{wind} scenario, it is seen that the HCPV array is significantly less influenced by the wind speed. Thus, the data in Fig. 5-16 agrees with the considerations previously presented, regarding the PV cells encapsulation. In fact, the wind speed was not identified as an important factor to describe the DC power for the HCPV array, as discussed in Section 5.3. The fact that the p-Si array presented the greatest power variation, in the high wind speed scenario, might be linked to the relatively high (in modulus) temperature factor for the DC power shown by this array. This, in turn, explains why the wind speed is more important for this PV technology than for the others, as discussed in Section 5.3.

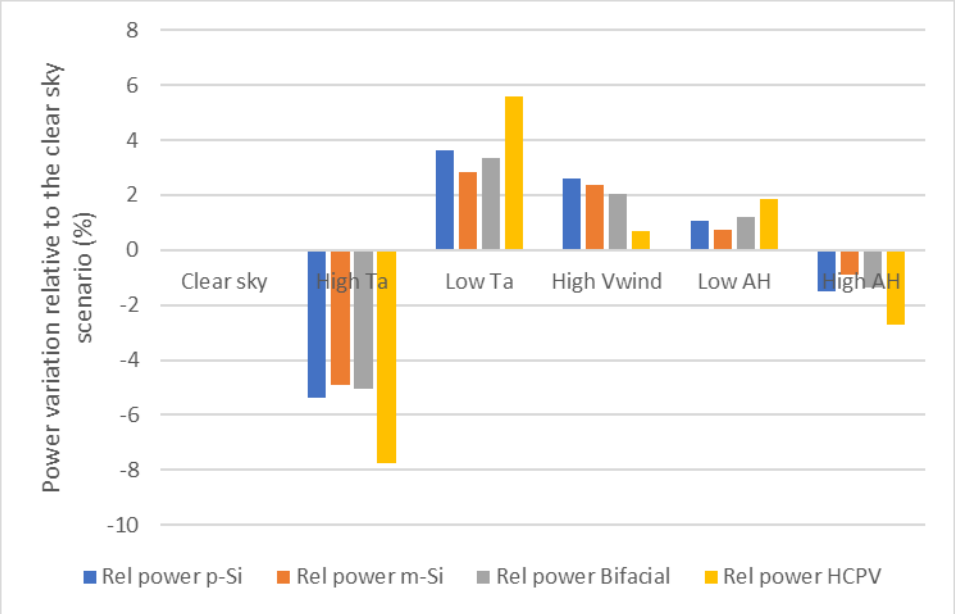

Figure 5-16: Power variations relative to the clear-sky scenario, per scenario and PV technology

Among all scenarios, the ones showing the smallest power variations are the high and low absolute humidity. The HCPV array was found to be the most affected PV array in both cases. This agrees with the results shown in Section 5.4.1, where the change rate of power per absolute humidity unit was found to be significantly more pronounced for the HCPV than for the other technologies. In fact, water in the atmosphere affects the spectral distribution of irradiance, as shown in Fig. 2-11. However, further analysis is beyond the scope of this work since the spectral irradiance was not measured. It is worth noting that when defining the scenarios referring to high and low AH, care was taken to keep the average air temperature as stable as possible, while allowing a sufficient variation in AH. In fact, between the two scenarios, the difference in the average T_{air} is only 1.5 °C.

5.4.3 **Remarks regarding the experimental sensitivity analysis**

Given the experimental nature of this work, it is not possible to obtain a set of records with all but one parameter constant. Such a case would be the ideal condition to perform a sensitivity analysis, however, in practice, not only some parameters change at the same time, but they are linearly related, that is, they present collinearity. This is particularly important for the irradiance components and the related indexes.

Since the external parameters are uncontrollable and are thus constantly changing, filtering has been used to keep them within a constant range. This means that a variation tolerance has been assumed. The smaller the tolerance, the smaller the number of points remaining; likewise, the greater the tolerance, the greater the variability introduced on the parameters. This means that when the power sensitivity with respect to a given parameter is studied, the remaining external parameters are also influencing the power. The greater the importance of the parameter, the greater the influence on the power, and the greater the difficulty in studying parameters with a light influence on the power, as it is the case for the air mass, wind speed and humidity.

The next section addresses these problems and presents a more refined sensitivity study.

5.5 MODEL-BASED SENSITIVITY ANALYSIS FOR THE DC POWER

Thus far in this thesis, the most important operating parameters for each PV array have been identified, and their effect on the PV power has been assessed based purely on assessments of the measured data. As a continuation, in the present section, the external parameters are used along with mathematical models to express the DC power, allowing to predict the PV arrays' output for any combination of inputs. The adoption of models to express the power as a function of the external variables allows, also, to carry out a sensitivity analysis with reduced interference of one parameter on another.

5.5.1 **A first approach for multivariate models to describe the DC power.**

For each PV array, models for the DC power were built considering the relevant parameters shown in Table 5-5. Linear and exponential terms were included for each operating parameter, whereas a least square fitting procedure was employed to determine the linear and exponential coefficients in the models.

The model proposed by Durisch et al. (2007), shown in Eq. (2.25), uses linear and exponential coefficients to express the influence of a given parameter for the PV array efficiency. A similar approach is followed in the present section. In fact, the general form of Eq. (2.25) was preserved, being the new parameters included along with the existing terms.

For the p-Si array, the model built for the sensitivity analysis is presented in Eq. (5.1).

$$P_{\mathrm{mp,c}} = A\ \mathrm{GNI}\ a_1 \left[a_2 \frac{\mathrm{GNI}}{\mathrm{GNI}_0} + \left(\frac{\mathrm{GNI}}{\mathrm{GNI}_0}\right)^{a_3} + a_4 \frac{\mathrm{BNI}}{\mathrm{BNI}_0} + \left(\frac{\mathrm{BNI}}{\mathrm{BNI}_0}\right)^{a_5} \right] \left[1 + a_6 \frac{T_{\mathrm{air}}}{T_{\mathrm{air},0}} + \left(\frac{T_{\mathrm{air}}}{T_{\mathrm{air},0}}\right)^{a_7} + a_8 \frac{\mathrm{AM}}{\mathrm{AM}_0} + \left(\frac{\mathrm{AM}}{\mathrm{AM}_0}\right)^{a_9} + a_{10} \frac{V_{\mathrm{wind}}}{V_{\mathrm{wind},0}} + \left(\frac{V_{\mathrm{wind}}}{V_{\mathrm{wind},0}}\right)^{a_{11}} + a_{12} \frac{\mathrm{AH}}{\mathrm{AH}_0} + \left(\frac{\mathrm{AH}}{\mathrm{AH}_0}\right)^{a_{13}} \right] \tag{5.1}$$

The model for the p-Si array in Eq. (5.1) presented nRMSE of 3.40 % and nMBE of 0.002 % (R^2 = 0.98605). Fig. 5-17 shows the correlation plot for the measured and predicted values for the p-Si DC power.

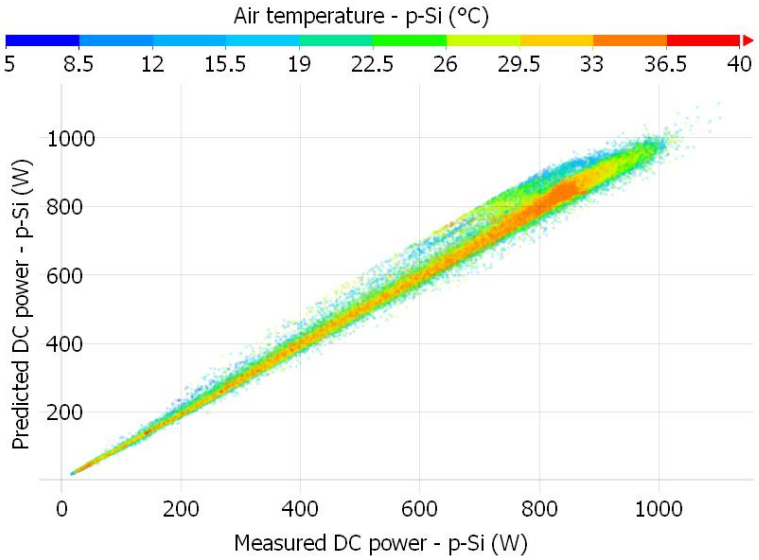

Figure 5-17: Correlation between measured and predicted DC power; p-Si model

Regarding the m-Si array, the model for the sensitivity analysis is shown in Eq. (5.2) and presented nRMSE of 1.84 % and nMBE of -0.019 % (R^2 = 0.99674). Fig. 5-18 shows the correlation plot for the measured and predicted values for the m-Si DC power.

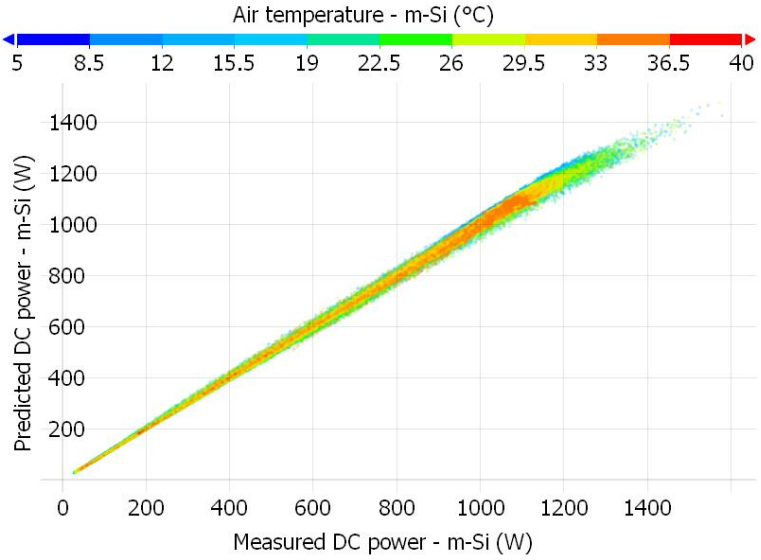

Figure 5-18: Correlation between measured and predicted DC power; m-Si model

$$P_{\mathrm{mp,c}} = A\ \mathrm{GNI}\ a_1\left[a_2\frac{\mathrm{GNI}}{\mathrm{GNI}_0}+\left(\frac{\mathrm{GNI}}{\mathrm{GNI}_0}\right)^{a_3}+a_4\frac{\mathrm{BNI}}{\mathrm{BNI}_0}+\left(\frac{\mathrm{BNI}}{\mathrm{BNI}_0}\right)^{a_5}\right]\left[1+a_6\frac{T_{\mathrm{air}}}{T_{\mathrm{air},0}}+\left(\frac{T_{\mathrm{air}}}{T_{\mathrm{air},0}}\right)^{a_7}+a_8\frac{\mathrm{AM}}{\mathrm{AM}_0}+\left(\frac{\mathrm{AM}}{\mathrm{AM}_0}\right)^{a_9}+a_{10}\frac{V_{\mathrm{wind}}}{V_{\mathrm{wind},0}}+\left(\frac{V_{\mathrm{wind}}}{V_{\mathrm{wind},0}}\right)^{a_{11}}\right] \quad (5.2)$$

In turn, the multivariate model built for the bifacial array is presented in Eq. (5.3). It presented nRMSE of 2.56 %, whereas the nMBE was -0.067 % (R^2 = 0.99378).

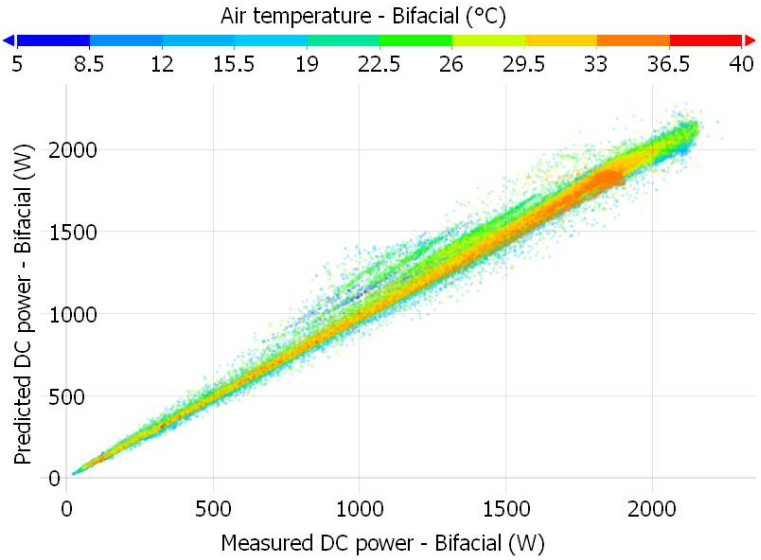

Figure 5-19: Correlation between measured and predicted DC power; bifacial model

Fig. 5-19 shows the correlation plot for the measured and predicted values for the bifacial array's DC power.

$$P_{\mathrm{mp,c}} = A\, G_E\, a_1 \left[a_2 \frac{\mathrm{GNI}}{\mathrm{GNI}_0} + \left(\frac{\mathrm{GNI}}{\mathrm{GNI}_0}\right)^{a_3} + a_4 \frac{\mathrm{GNI_{rear}}}{\mathrm{GNI_{rear,0}}} + \left(\frac{\mathrm{GNI_{rear}}}{\mathrm{GNI_{rear,0}}}\right)^{a_5} + a_6 \frac{\mathrm{BNI}}{\mathrm{BNI}_0} + \left(\frac{\mathrm{BNI}}{\mathrm{BNI}_0}\right)^{a_7} \right] \left[1 + a_8 \frac{T_{\mathrm{air}}}{T_{\mathrm{air,0}}} + \left(\frac{T_{\mathrm{air}}}{T_{\mathrm{air,0}}}\right)^{a_9} + a_{10} \frac{\mathrm{AM}}{\mathrm{AM}_0} + \left(\frac{\mathrm{AM}}{\mathrm{AM}_0}\right)^{a_{11}} + a_{12} \frac{V_{\mathrm{wind}}}{V_{\mathrm{wind,0}}} + \left(\frac{V_{\mathrm{wind}}}{V_{\mathrm{wind,0}}}\right)^{a_{13}} \right] \tag{5.3}$$

Finally, the HCPV array model is shown in Eq. (5.4). A nRMSE level of 5.96 % was found using such a model, while the nMBE was -0.027 % (R^2 = 0.94922). Fig. 5-20 shows the correlation plot for the measured and predicted values for the HCPV array's DC power.

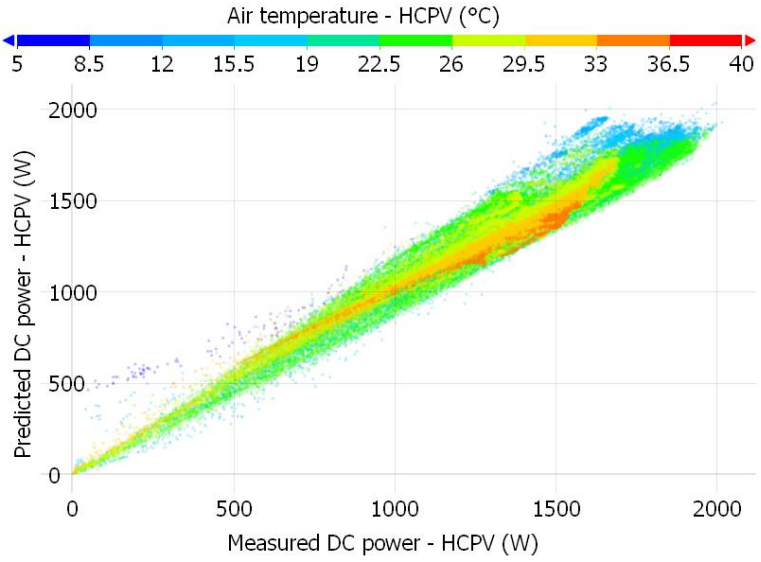

Figure 5-20: Correlation between measured and predicted DC power; HCPV model

$$P_{\mathrm{mp,c}} = A\,\mathrm{BNI}\,a_1\left[a_2\frac{\mathrm{BNI}}{\mathrm{BNI}_0}+\left(\frac{\mathrm{BNI}}{\mathrm{BNI}_0}\right)^{a_3}+a_4\frac{\mathrm{GNI}}{\mathrm{GNI}_0}+\left(\frac{\mathrm{GNI}}{\mathrm{GNI}_0}\right)^{a_5}\right]\left[1+a_6\frac{T_{\mathrm{air}}}{T_{\mathrm{air},0}}+\left(\frac{T_{\mathrm{air}}}{T_{\mathrm{air},0}}\right)^{a_7}+a_8\frac{\mathrm{NDF}}{\mathrm{NDF}_0}+\left(\frac{\mathrm{NDF}}{\mathrm{NDF}_0}\right)^{a_9}+a_{10}\frac{\mathrm{AM}}{\mathrm{AM}_0}+\left(\frac{\mathrm{AM}}{\mathrm{AM}_0}\right)^{a_{11}}+a_{12}\frac{\mathrm{AH}}{\mathrm{AH}_0}+\left(\frac{\mathrm{AH}}{\mathrm{AH}_0}\right)^{a_{13}}\right] \quad (5.4)$$

The coefficients for Eqs. (5.1) to (5.4) are organized in Table 5-8.

Table 5-4: Model coefficients for the four PV arrays

	p-Si Eq. (12.1)	m-Si Eq. (12.2)	Bifacial Eq. (12.3)	HCPV Eq. (12.4)
a1	1.65786	7.99127	2.24666	4.81050
a2	-0.41245	-0.13110	-0.28344	-2.20248
a3	0.27939	0.05812	0.14368	-0.31710
a4	-0.03581	-0.98891	-1.11118	1.88213
a5	0.00081	0.98610	0.25081	0.69816
a6	-0.85068	-1.50741	0.00073	-1.66275
a7	0.46277	1.24399	-0.00465	1.01973
a8	0.08320	-0.02145	-0.46951	-0.88468
a9	-0.06090	-0.02180	0.00063	-0.21310
a10	0.03807	0.00824	0.02483	-0.54901
a11	0.00005	-0.00087	0.00303	0.63630
a12	0.00691	-	0.01685	-0.62372
a13	-0.07281	-	0.00005	0.70732

Section 5.3 was devoted to present the order of relevance of the external parameters with respect to their ability to describe the PV power, for each of the four arrays being studied. In fact, when new parameters are successively added to the models developed in the present section, the error between the measured and predicted power levels decreases. Consequently, there is a trade-off between the number of variables to be measured and the admissible model error: smaller error levels come at the cost of more input variables.

The data in Table 5-5 show, for each PV array, the relevant external parameters (in order of relevance), along with the cumulative nRMSE according to the inclusion of new parameters as inputs.

Table 5-5: cumulative nRMSE due to the inclusion of parameters as model inputs

Order of relevance	p-Si		m-Si		Bifacial		HCPV	
	Param.	nRMSE	Param.	nRMSE	Param.	nRMSE	Param.	nRMSE
1	GNI	4.52%	GNI	3.19%	GNI	4.28%	BNI	9.05%
2	T_{air}	3.66%	T_{air}	1.97%	T_{air}	2.75%	T_{air}	6.56%
3	V_{wind}	3.50%	BNI	1.92%	$\mathrm{GNI}_{\mathrm{rear}}$	2.61%	NDF	6.47%
4	AM	3.43%	AM	1.88%	AM	2.58%	AM	6.12%
5	BNI	3.42%	V_{wind}	1.84%	V_{wind}	2.53%	GNI	6.03%
6	AH	3.40%	-	-	BNI	2.52%	AH	5.96%

For the p-Si array, including only the 4 most important external parameters (GNI, T_{air}, V_{wind} and AM) results in a modeling error of 3.43 %. After the inclusion of the 4th most relevant parameter, further including more parameters (BNI and AH) to the model does not provide a significant nRMSE reduction.

In turn, for the m-Si, including the parameters up to the 4th most relevant (that is, GNI, T_{air}, BNI and AM) results in a modeling error of 1.88 %, whereas adding the 5th most important parameter (which is V_{wind}) reduces the nRMSE only by 0.04 %. For the bifacial array, the minimum error of 2.52 % was achieved when applying all 6 parameters to the model; however, it is noted that the inclusion of the 6th parameter (that is, BNI), contributed to the error reduction with only 0.01 %. Finally, for the HCPV array, it is observed that including only the BNI produces a modeling error of roughly 9 %. As in the previous cases, the nRMSE is progressively reduced as more variables are included, reaching a level slightly below 6 % only after the 6th variable (AH) was included in the model.

Reasons for the relatively high nRMSE levels shown by the HCPV array's model are related to: a) PV tracking errors: tracking error of 0.3° can potentially reduce the HCPV array's power in 10 %, whereas 1° error makes the DC power virtually decrease to zero; b) differences between the orientation of the PV tracker and the pyrheliometer installed on the Solys 2 measurement system; c) divergences between the BNI levels measured at the roof of the Laboratory building and the BNI actually reaching the HCPV array, especially when under transient, partially cloudy condition.

It is worth noting that the Solys 2 irradiance meter and the PV tracker holding the HCPV array are roughly 90 m apart, as illustrated in Fig. 5-21. All these factors – which are particular for the HCPV array – act producing differences between the measured and actual BNI levels, therefore introducing errors both on the data analysis and on the power modeling. In fact, such factors explain, also, the greater number of inconsistent records detected during the filtering phase, as described in Section 4.

Figure 5-21: Distance between the BNI meter and the HCPV array

The modeling approach developed up to this point does not address the dependences which exist between the irradiance components; between AM and the irradiance components; and between T_{air} and AH. As a result, the models are not able to adequately differ the influence of two well correlated input variables on the power, that is, the output variable (Katz, 2006). Therefore, despite the models perform well when describing the DC power, they are not suitable for the sensitivity analysis, since the

model's coefficients attribution is not reliable at the individual variables level. It should be remembered that the models' parameters a_1 to a_{13} were defined based on the experimental dataset, in which many variables present collinearity. This poses a problem regarding the model specification.

Despite this drawback, the models (Eqs. 5.1 to 5.4) are useful for straightforwardly describing the DC power, in contrast with the significantly more complex models used in Section 5.3.

5.5.2 **Principal Component Regression**

The Pearson's coefficient correlation matrix in Fig. 5-1 shows that some of the explanatory variables are correlated. As previously mentioned, this is the case for the irradiance components – among each other and each of them with the AM. Also, the humidity and air temperature are correlated as well. It is said that such well correlated variables present collinearity. Katz (2006) states that one possible approach to avoid building models based on collinear explanatory variables is to eliminate one of them. However, such a solution is not suitable in the context of the present thesis, given that the study of the effects of the external variables on the PV performance is precisely what is addressed.

The Principal Component Regression (PCR) is a viable alternative to the multivariate modeling in the presence of collinearity between the descriptive variables. The PCR allows expressing a set of correlated multivariate data in terms of a smaller set of uncorrelated variables, yet keeping most information regarding the original dataset (Ziegel, 2002). Mathematically, the principal components are calculated from the eigenvectors of the covariance matrix referring to the dataset containing the explanatory variables, and the explanatory variables their selves. Detailed descriptions of the PCR method are provided by Katz (2006) and Ziegel (2002).

The principal components data (PC1 to PC5), for the four PV arrays, are presented in Tables 5-6 to 5-9. The columns show the coefficients for each explanatory variable, to compose each principal component.

Table 5-6: Principal component factors: p-Si array

	PC1	PC2	PC3	PC4	PC5
GNI (W/m²)	0.684	0.730	-0.010	-0.003	0.007
BNI (W/m²)	0.730	-0.684	0.007	0.001	-0.004
Air temperature (°C)	0.002	0.012	0.997	-0.055	0.058
AM	-0.002	-0.009	-0.074	-0.376	0.924
Wind speed (m/s)	0.000	0.000	0.029	0.925	0.379
Abs. humidity (kgH2O/kgda)	0.000	0.000	0.000	0.000	0.000

Table 5-7: Principal component factors: m-Si array

	PC1	PC2	PC3	PC4	PC5
GNI (W/m²)	0.697	0.717	-0.013	-0.003	0.006
BNI (W/m²)	0.717	-0.697	0.008	0.001	-0.004
Air temperature (°C)	0.003	0.014	0.995	-0.060	0.073
AM	-0.002	-0.009	-0.090	-0.388	0.917
Wind speed (m/s)	0.000	0.001	0.026	0.920	0.392
Abs. humidity (kgH2O/kgda)	0.000	0.000	0.000	0.000	0.000

Table 5-8: Principal component factors: bifacial array

	PC1	PC2	PC3	PC4	PC5
GNI (W/m²)	0.696	0.695	-0.182	0.012	0.004
GNI_{rear} (W/m²)	0.067	0.189	0.969	-0.144	0.000
BNI (W/m²)	0.715	-0.694	0.085	-0.002	-0.002
Air temperature (°C)	0.003	0.017	0.143	0.989	0.018
AM	-0.002	-0.009	-0.027	-0.031	0.528
Wind speed (m/s)	0.000	0.001	0.015	-0.001	0.849
Abs. humidity (kgH2O/kgda)	0.000	0.000	0.000	0.000	0.000

Table 5-9: Principal component factors: HCPV array

	PC1	PC2	PC3	PC4	PC5
GNI (W/m²)	0.665	-0.747	-0.008	0.000	0.010
BNI (W/m²)	0.747	0.665	0.005	0.000	-0.004
Air temperature (°C)	0.002	-0.008	0.995	-0.033	0.094
AM	-0.004	0.010	-0.092	0.048	0.994
Wind speed (m/s)	0.001	-0.001	0.037	0.998	-0.045
Abs. humidity (kgH2O/kgda)	0.000	0.000	0.000	0.000	0.000
Normal diffuse fraction	0.000	-0.001	0.000	0.001	-0.024

After the principal components were obtained, a linear regression was carried out to obtain the DC power model coefficients by means of least squares fit, using Eq. 5.5, for each of the four PV arrays.

$$P_{\mathrm{mp,c,PCR}} = a_0 + a_1\mathrm{PC}_1 + \cdots + a_n\mathrm{PC}_n \tag{5.5}$$

Finally, the resulting model, which is a function of the weighted principal components, is rewritten as a function of the original explanatory variables.

The weight parameters for the models, obtained by means of the principal component, are presented in Table 5-10, considering the four PV arrays.

Table 5-10: Linear regression coefficients for the PCR models, per PV array

	p-Si	m-Si	Bifacial	HCPV
a_0	20.28323	84.28078	125.3873	242.8357
a_1	0.601369	0.796309	1.317458	1.629572
a_2	0.637233	0.831221	1.451464	1.228822
a_3	-3.06754	-3.63619	-0.35972	-13.9475
a_4	3.593338	3.535421	-7.63391	-2.14483
a_5	8.939336	-1.15239	10.09917	-15.6766

When running simulations using the obtained models, for the complete PV dataset, the following performance metrics were obtained: nRMSE = 3.57%, R^2 = 0.98464 (p-Si array); nRMSE = 2.04%, R^2 = 0.99608 (m-Si array); nRMSE = 2.94 %, R^2 = 0.99182 (bifacial array); and nRMSE = 6.61%, R^2 = 0.93950 (HCPV array).

All nRMSE levels are greater than the ones presented in Section 5.5.1; however, it should be highlighted that the models developed using the PCR are expected to present a greater specificity in terms of the weights attributed to the various explanatory variables. This way, the models are suitable for the sensitivity analysis, which is explained in the next section.

5.5.3 **Sensitivity analysis using the PCR models.**

Even with models built upon linearly independent variables – as carried out in the previous section – proper sensitivity analysis cannot be carried out if some of the input variables keep a linear relationship between each other. This means that simply applying the original variables (GNI, BNI, T_{air}, AM, V_{wind} and AH) to the PCR models will not set the analysis free from the collinearity problem. In other words, it will not be possible to decouple the relationships between the variables, therefore impairing the study of the influence of the individual parameters on the observed variable – the DC power.

This way, in this section, instead of the external variables within the dataset, artificial variables were applied to the models' inputs, using a Monte Carlo simulation in 10,000 iterations. Each artificial variable was created from maximum and minimum limits (X_{max} and X_{min}), specified for each explanatory variable. The variables were computed using Eq. 5.6, where "rand" is a random real number between 0 and 1.

$$X_{\mathrm{rand}} = \mathrm{rand}(X_{\mathrm{max}} - X_{\mathrm{min}}) + X_{\mathrm{min}} \tag{5.6}$$

Maximum and minimum limits for the variables were set so as to represent conditions practically plausible, respecting the observations contained in the measured dataset. The limits are presented in Table 5-11, along with the average parameters for the 10,000 artificial values generated (last column, to the right).

Table 5-11: Limits attributed to the random variables for the model inputs

	Min	Max	Average X_{rand}
GNI (W/m²)	100	1100	603.1
BNI (W/m²)	1	750	446.6
Air temperature (°C)	0	40	20.3
AM	1	5	2.4
Wind speed (m/s)	0	5	2.5
Abs. humidity (kgH2O/kgda)	0.005	0.018	0.011

To enable the introduction of variations on the variables – which is a requirement for the sensitivity analysis – a bias was introduced in Eq. 5.6, which turns into Eq. 5.7.

$$X_{\mathrm{rand,biased}} = (\mathrm{rand}(X_{\mathrm{max}} - X_{\mathrm{min}}) + X_{\mathrm{min}}) * \mathrm{bias} \tag{5.7}$$

For the generation of the random variables, initially the bias in all equations is set to 1. This allows computing reference levels for all descriptive variables, as well as for the power. Then, the bias

is changed to 1.1 – to introduce a 10% gain – one equation at a time, whereas the new modelled DC power value is recorded. Other values for the bias were tested as well (15 %, 25 %), with similar results.

Repeating this procedure until all random variables were covered enables the construction of tables showing the sensitivity coefficients, which were calculated as the ratio between the percent variation of the normalized DC power and the percent variation of one individual input parameter.

The DC power levels were normalized using the reference (STC), in order to allow an easy and fair comparison between the four PV arrays. Also, to enable the use of comparable figures between the various external parameters, their variation was also set to a relative metric, using the average reference levels previously defined (Table 5-11). This way, the unit for the outcome of the sensitivity analysis is specified in % variation of relative power per % variation of the explanatory random variable, allowing comparison by means of a normalized score, covering all PV arrays.

The results regarding the sensitivity analysis, carried out with the PCR and the Monte Carlo simulations, are summarized in Fig. 5-22.

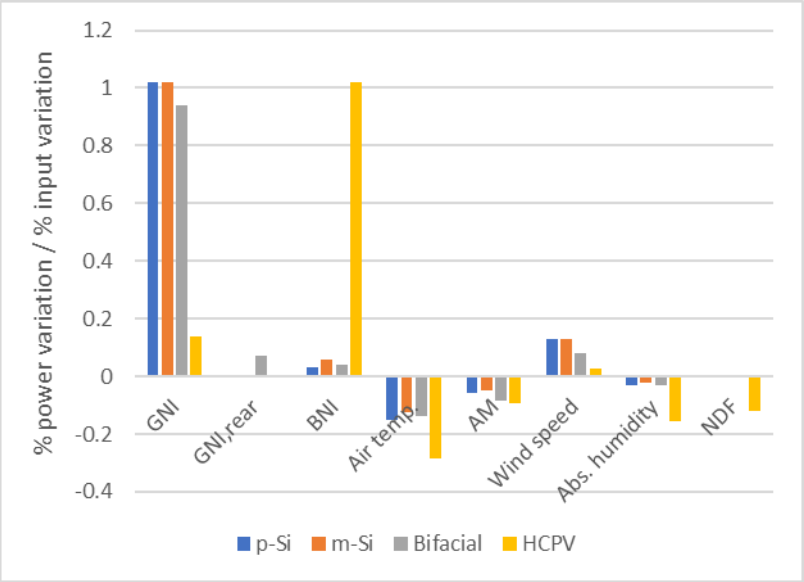

Figure 5-22: Scores for the sensitivity analysis, per parameter and PV array

Overall, the results depicted in Fig. 5-22 agree with the outcomes of Section 5.4: the effect of GNI on the HCPV is relatively low; however, such a PV array is the most sensitive to the BNI. The behavior presented by the HCPV array, with respect to GNI and BNI, remarkably differs from the other three PV technologies. Also, the HCPV presented the greatest influence by the air temperature, among all PV technologies studied. For all technologies, the results agree with Section 5.4.2, in Fig. 5-16. For the AM, the most influenced arrays were the HCPV and the bifacial, thus partially agreeing with the results of Section 5.4. In turn, the wind speed assessments do agree with the results in Section 5.4, with the HCPV array showing the smallest sensitivity to such a parameter. Also, the p-Si and m-Si were the most influenced by the wind speed, in close agreement with Section 5.4.2 (Fig. 5-16). Again, as in Section 5.4, the most impacted technology, with respect to the absolute humidity, was the HCPV, showing a significantly greater power reduction as the AH increases.

5.6 DESCRIBING THE PV ARRAYS' BEHAVIOR USING T_C INSTEAD OF T_{AIR}

The use of the measured array temperature, instead of the air temperature, is considered in this section. The aim is to assess the performance of the consolidated model presented by Durisch et al. (2007), which uses the irradiance, cell temperature and AM to describe the PV efficiency and power, comparing the results with those provided by the models using the air temperature. Also, as previously mentioned in Section 2.4, the method introduced by Durisch et al. (2007) includes useful equations for the determination of the STC power (Eq. 2.28) and efficiency (Eq. 2.26). Therefore, the results shown in the present section consist of a cross-check for the STC power ratings obtained in Section 3.8.

5.6.1 **Adapting the Durisch efficiency model for bifacial and HCPV arrays**

The efficiency model introduced by Durisch et al., (2007) was applied to predict the efficiency, and therefore, the DC power using the array area and the irradiance level. The aim is to verify the performance when the model is used in its standard form, which calculates the efficiency and power as a function of the irradiance, cell temperature and air mass.

The application of the Durisch model with p-Si and m-Si PV arrays has been well explored in the literature, for instance, in the works of Zarkov et al. (2016), Hamou et al. (2014) and Bërdufi et al. (2016). However, the model's use along bifacial and HCPV devices has not yet been documented. Therefore, one of the contributions of the present section is to propose, test and compare approaches for adapting the original Durisch model to bifacial and HCPV devices.

In this chapter, it is proposed to calculate the DC power from the Durisch model as shown in Eq. (5.8), where $P_{\mathrm{mp,c}}$ refers to the calculated power and GNI_0 is 1000 W/m².

$$P_{\mathrm{mp,c}} = A\ \mathrm{GNI}\ p\left[q\frac{\mathrm{GNI}}{\mathrm{GNI}_0} + \left(\frac{\mathrm{GNI}}{\mathrm{GNI}_0}\right)^m\right]\left[1 + r\frac{T_c}{T_{c,0}} + s\frac{\mathrm{AM}}{\mathrm{AM}_0} + \left(\frac{\mathrm{AM}}{\mathrm{AM}_0}\right)^u\right] \tag{5.8}$$

5.6.1.1 Durisch model: p-Si array

For the m-Si array, the coefficients in Eq. (5.8) were calculated to minimize the squared error on the PV efficiency, as defined in the original publications of Durisch et al. (2007), and the values are: p=15.891; q=-0.146; r=-0.092; s=-1.005; m=0.124; and u=1.007. The model adjusted with such parameters yielded nRMSE of 3.08 % (R^2 = 0.990083) on the DC power. In turn, relevant STC data referring to an individual p-Si module in the array, calculated using Eqs. (2.28) and (2.26), provided $P_{mp,STC}$=164.0 W, and η_{STC}=14.0 %. The difference relatively to the STC metrics found in Section 3.8 is 0.5 %.

5.6.1.2 Durisch model: m-Si array

For the m-Si array, the adjusted parameters in Eq. (5.8) are p=22.882; q=-0.055; r=-0.091; s=-1.010; m=0.068; and u=1.000. With these coefficients, the nRMSE for the DC power is 1.73 %, whereas

$P_{mp,STC}$=316.3 W, and η_{STC}=19.8 % (R^2 = 0.997259). Relatively to the data in Section 3.8, such STC metrics present a 3.7 % difference.

5.6.1.3 Durisch model: bifacial array

Applying the Durisch model to bifacial PV arrays is not as straightforward as in the case of p-Si and m-Si. The reason is that both sides of bifacial modules – front and rear – influence the amount of power conversion. Therefore, the GNI term in Eq. (5.8) must be adjusted accordingly to account for the irradiance falling on both sides.

However, adding the front and rear irradiance levels reaching the bifacial PV module is not a consistent way of representing the total irradiance, given that the front and rear sides of a bifacial device do not present the same efficiency. Therefore, the total irradiance must be calculated taking this particularity into account, for instance, using the concept of effective irradiance (G_E), as defined in Eq. (2.18). Therefore, GNI in Eq. (5.8) now refers to G_E = GNI + φ GNI_{rear}. This way, modifying Eq. (5.8) results in Eq. (5.9).

It is worth noting that the reference irradiance in Eq. (5.9) is GNI_0, as in Eq. (5.8) since the datasheets for bifacial modules present the performance considering only the front side. Therefore, the reference irradiance is 1000 W/m², as in the case of monofacial PV modules. This is consistent with the concept of effective irradiance since it is the irradiance that would produce the same output power if the module was monofacial (Gostein et al., 2021).

$$P_{\mathrm{mp,c}} = A\, G_E\, p \left[q \frac{G_E}{\mathrm{GNI}_0} + \left(\frac{G_E}{\mathrm{GNI}_0} \right)^m \right] \left[1 + r \frac{T_c}{T_{c,0}} + s \frac{\mathrm{AM}}{\mathrm{AM}_0} + \left(\frac{\mathrm{AM}}{\mathrm{AM}_0} \right)^u \right] \tag{5.9}$$

Using a least square error fitting procedure, the parameters in Eq. (5.9) are defined as p=12.118; q=-0.126; r=-0.2055; s=-0.006; m=0.103; and u=0.016. In turn, the nRMSE for the DC power is 2.67 %. The $P_{mp,STC}$ is 323.2 W, and η_{STC} is 19 % (R^2 = 0.995867). Relatively to the STC data in Section 3.8, such metrics present a -0.4 % difference.

5.6.1.4 Durisch model: HCPV array

This section tackles the problem of adapting the Durisch model to HCPV devices. The first task is to address the irradiance GNI in Eq. (5.8). Since HCPV devices respond only to the beam irradiance, GNI must be replaced by BNI. Besides the irradiance, the temperature is another factor that has to be considered: given that HCPV modules are more complex than flat-plate devices, measuring the cell temperature becomes a challenging task given that the cells are mounted on a circuit board, inside the PV module's housing. Therefore, a common practice is to measure the heatsink temperature in HCPV modules. However, adopting such an approach leads to relatively high temperature deviations due to the thermal resistance presented by the several materials between the cells and the heatsink.

In the present section, the Durisch model applied for HCPV modules is considered employing both the air and heatsink temperature measurements, and the results are compared in terms of the nRMSE, allowing the best-performing approach to be identified.

Using the heatsink temperature, Eq. (5.8) adapted for HCPV arrays becomes Eq. (5.10), where $T_{\mathrm{hs},0}$ is 25 °C.

$$P_{\mathrm{mp,c}} = A\ \mathrm{BNI}\ p\left[q\frac{\mathrm{BNI}}{\mathrm{BNI}_0} + \left(\frac{\mathrm{BNI}}{\mathrm{BNI}_0}\right)^m\right]\left[1 + r\frac{T_{\mathrm{hs}}}{T_{\mathrm{hs},0}} + s\frac{\mathrm{AM}}{\mathrm{AM}_0} + \left(\frac{\mathrm{AM}}{\mathrm{AM}_0}\right)^u\right] \tag{5.10}$$

In Eq. (5.10), the reference irradiance BNI_0 is 1000 W/m², and T_{hs} denotes the heatsink temperature. The parameters in Eq. (5.10) were identified as p=18.978; q=0.344; r=-0.206; s=-0.625; m=0.034; and u=0.735. The nRMSE on the DC power was found as 6.61 % (R^2 = 0.936606), while the $P_{\mathrm{mp,STC}}$ = 87.4 W and η_{STC} = 33.4 %. Compared to the STC metrics found in Section 3.8, this represents a difference of 4.7 %.

It is worth recalling that the STC data calculated in Section 3.8 comes from single I-V measurements and translation methods, whereas the STC data in the present section were calculated with the contribution of all measurements within each PV array's dataset.

When using the air temperature, the model equation takes the form of Eq. (5.11), where $T_{\mathrm{air},0}$ is 25 °C.

$$P_{\mathrm{mp,c}} = A\ \mathrm{BNI}\ p\left[q\frac{\mathrm{BNI}}{\mathrm{BNI}_0} + \left(\frac{\mathrm{BNI}}{\mathrm{BNI}_0}\right)^m\right]\left[1 + r\frac{T_{\mathrm{air}}}{T_{\mathrm{air},0}} + s\frac{\mathrm{AM}}{\mathrm{AM}_0} + \left(\frac{\mathrm{AM}}{\mathrm{AM}_0}\right)^u\right] \tag{5.11}$$

In this case, p=16.194; q=0.118; r=-0.361; s=-0.3000; m=0.046; and u=0.384, and the nRMSE on the DC power is 6.15 % (R^2 = 0.945996), which is below the nRMSE observed when using the heatsink temperature to model the power with Eq. (5.10).

As a comparison resource, the model developed by Benhammane et al. (2021), when applied to the same dataset, produced an nRMSE of 6.38 %, standing between the results provided by Eqs. (5.10) and (5.11).

5.6.2 Comparison of models using T_{air} and T_{c}

Figure 5.23 summarizes the nRMSE levels found when using the models given in Section 3.8 and the ones provided in the present section, to compute the power for the four PV arrays.

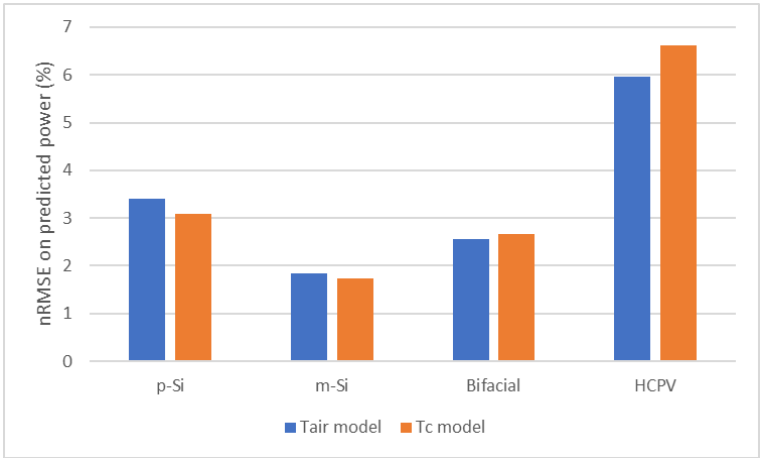

Figure 5-23: nRMSE levels per technology and model method

In Fig. 5-23, the "T_{air} model" refers to the models given in Section 5.5.1 (Eqs. (5.1) to (5.4)), which use the relevant external parameters, for each PV array. In turn, the "T_c model" refers to the models given by Eqs. (5.8) to (5.10). For the p-Si and m-Si technologies, the models provided in this section – relying on GNI, T_c and AM – presented smaller error levels, despite the fact that fewer input parameters are used, in comparison with the models using T_{air}. The bifacial and HCPV arrays were better described by the models given in Section 5.5.1. The greatest modeling error difference was found for the HCPV array: in this case, the model given by Eq. (5.10) relies on the heatsink temperature. In contrast, the model provided in Section 5.5.1 (Eq. 5.4), besides using the air temperature instead of the heatsink temperature, also includes the normal diffuse fraction and the absolute humidity. It should be noted, though, that including more variables as inputs to a model does not necessarily lead to a better model performance. This is precisely the case of the models for the p-Si and m-Si arrays studied in this thesis. Such arrays were better modelled by the Durisch model, which uses only GNI, T_c and AM as inputs.

5.6.3 **STC power using the Durisch models**

As mentioned earlier, the model introduced by Durisch et al. (2007) offers the valuable capability of allowing the STC efficiency and power to be easily calculated, by means of Eqs. (2.26) and (2.28). Since the STC power levels determined in Section 3.8 were, for all PV modules, lower than the datasheet specifications, an extra confirmation is highly desired. The STC efficiency and power presented in this section were computed based on an approach that differs from the methods used in Section 3 in the following respects:

- The measurements described in Section 3.8 consider only one I-V curve for each PV module. In contrast, the coefficients for the Durisch model were calculated based on all measurements within the datasets;
- The techniques developed in Section 3.7 and applied in Section 3.8 rely on analytical models based on the electrical circuit for a PV cell. In contrast, the Durisch model relies on optimization of parameters, targeting the minimization of the total squared error;
- The measurement hardware used to perform the calculations of Section 3.8 is totally different from the equipment used during the one-year measurement campaign. It is worth noting that the measurements described in Section 3.8 were carried out before the modules were assembled on the tracker. That is, not only the irradiance and temperature meters were not the same; but the PV data acquisition itself was different in concept: 200 ms I-V sweeps as described in Section 3.8, and a year-long campaign considered in this section, to adjust the model coefficients.

Despite the differences, the STC efficiency and power levels, found via Eqs. (2.26) and (2.28), agree with the STC data found in Section 3.8, as shown in Table 5-12. This is a relevant finding, since Section 3.8 presents significant differences between the manufacturers' datasheets STC specifications and the STC ratings calculated using the translation methods of Section 3.7, especially for the m-Si and bifacial devices. The power values in Table 5-12 are per module, to allow easier comparison with the datasheet ratings. The greatest deviation referring to the STC power in Table 5-12 regards the m-Si modules. The difference, however, is within the uncertainty level determined in Section 3.9.

Table 5-12: STC metrics for power, per module, for the four PV arrays

Source	STC power rating (W)			
	p-Si	m-Si	Bifacial	HCPV
Section 3.8 (single-diode model)	163.2	305.0	324.4	83.5
Section 5.6.3 (Durisch model)	164.0	316.3	322.5	85.7
Datasheet	175.0	327	335	87.5

5.7 BIFACIAL ARRAY: EQUIVALENT IRRADIANCE AND BIFACIAL GAIN

This section is devoted to exploring particularities regarding the bifacial PV array, which remarkably differs from the p-Si, m-Si and HCPV in terms of operation. Given that bifacial devices are considered very promising in terms of cost-effectiveness, this thesis includes the present chapter as a means of contributing to the PV scientific community and the industry, with novel approaches to simplify the quantification of the effective irradiance being converted by the bifacial PV array and the bifacial gain (BG). The validation of the proposed methods was carried out using the data acquired during the development of the thesis.

Due to the difficulty in assessing the rear-side irradiance (G_{rear}) on bifacial modules (especially for large PV arrays), the present work concerns the determination of the bifacial gain without the need of measuring G_{rear}, and without relying on monofacial PV modules for the calculation of the bifacial gain. For the validation, monitoring of a bifacial PV array in real operating conditions was carried out. This study differs from literature in the following:

- All bifacial modules were individually tested before the array was assembled. Even though the modules were new, I-V testing was carried out (Section 3.8) to ensure that all modules were performing correctly, but most importantly, to allow accurate outdoor measurements with each side (covering the other side). This allowed quantifying the bifaciality factor φ for each module – necessary for the validation phase – as well as the actual STC ratings, obtained through modeling methods explained in Section 3.7.

- A novel method to quantify the effective irradiance is introduced; such a method uses the operating current as an input, that is, front and rear-side irradiance, module mismatch and uneven irradiance distribution are automatically taken into account because such factors impact the electrical performance of the PV array. Testing of this method was carried out with the bifacial array operating in real field conditions, that is, using a non-ideal setup and under uncontrolled conditions;

- I-V curves of the entire array (on the tracker) were measured before the measurement campaign started. They are representative of all modules operating in series, thus considering the effects of module mismatch, and serve to check that the series-connected modules are performing well and presenting a smooth I-V curve;

- Another advantage of the proposed method is that the bifacial gain is calculated without the need of a reference monofacial PV system. While the studies of Baloch et al. (2020), Burnham et al. (2019), Gu et al. (2021), Hayibo et al. (2022), Muehleisen et al. (2021), and Stein et al. (2018) considered

monofacial modules as a comparison resource for the calculation of the bifacial gains, the present section presents a novel method for bifacial gain determination relying solely on monitoring of the bifacial array. The bifacial module's front-side individual contribution is quantified, thus being representative of a monofacial module with the same ratings as the bifacial.

5.7.1 **Consolidated bifacial modules theory**

Basic concepts regarding bifacial modules were introduced in Section 2.2.2. The present section regards further particular aspects of bifacial modules, along with the relationship of the total current and power with the contributions of each side of the devices.

The bifaciality φ was defined in Section 2.2.2 as

$$\varphi = \frac{I_{\mathrm{sc,rear}}}{I_{\mathrm{sc,front}}}, \tag{2.9}$$

whereas the effective irradiance was introduced in Section 2.2.2 as

$$G_{\mathrm{E}} = G_{\mathrm{front}} + \varphi\, G_{\mathrm{rear}}\,. \tag{2.18}$$

Such equations were rewritten in this section because they consist of the foundation for the method presented further in the following.

The classical expression for the BG is expressed by Eq. (5.12). It has been employed in several works in the literature and relies on the performance of a monofacial PV system as a reference to calculate bifacial gain.

$$\mathrm{BG} = \frac{\sum P_{\mathrm{mp,bifacial}}}{\sum P_{\mathrm{mp,monofacial}}} \frac{P_{\mathrm{mp,STC,monofacial}}}{P_{\mathrm{mp,STC,bifacial}}} - 1 \tag{5.12}$$

5.7.2 **Novel method: calculating G_E from the I_{mp}**

It is known that, given the strong correlation between the I_{sc} and GNI parameters, a short-circuited PV module can be employed as an irradiance sensor. In fact, Razongles et al. (2016) studied the validity of such a concept for bifacial modules, and concluded that considering I_{sc}, the behavior of a bifacial module is the same when the current is produced by the front or rear-side. However, for the case of a bifacial PV array in real operating condition, it is undesirable to shift the operating point (V, I) from (V_{mp}, I_{mp}) to (0, I_{sc}) to calculate the irradiance since this fatally results in a yield loss, given that the output power of a PV module at I_{sc} is zero.

The approach proposed in the following method for G_E calculation is based on the dependence of I_{mp} on the irradiance, as described by Abe et al. (2020b) and experimentally tested by Abe et al. (2020a). The method is based on the fact that the temperature coefficient for I_{mp} is small, as discussed by Abe et al. (2020b) and Seapan et al. (2020). This way, being I_{mp} mostly a function of the irradiance, the I_{mp} of a bifacial module can be used as a reference to calculate the equivalent irradiance G_E by means of Eq. (5.13), which is newly introduced in this thesis.

The equivalent irradiance for a bifacial module, as calculated by Eq. (5.13), considers the irradiance effectively being converted by the PV device, thus, it intrinsically considers the effect of non-uniform irradiance distribution on the rear-side.

$$G_{\mathrm{E}} = 1000 \frac{I_{\mathrm{mp}}}{I_{\mathrm{mp,front,STC}}} \tag{5.13}$$

Equation (5.13) is a linear relation of the instantaneous I_{mp} value with $I_{\mathrm{mp,STC}}$, which refers to the front surface of the bifacial module for STC condition. For this reason, the current is written $I_{\mathrm{mp,front,STC}}$ in Eq. (5.13), to ensure clarity. In a similar way, the front irradiance G_{front} is expressed by Eq. (5.14), where $I_{\mathrm{mp,front}}$ is the portion of I_{mp} referring to the front-side contribution. It should be mentioned that G_{front} is the GNI; however, the subscripts "front" and "rear" have been adopted in the present section to ensure clarity and avoid confusion. Similarly, G_{rear} is $\mathrm{GNI}_{\mathrm{rear}}$.

$$G_{\mathrm{front}} = 1000 \frac{I_{\mathrm{mp,front}}}{I_{\mathrm{mp,front,STC}}} \tag{5.14}$$

Following the same idea, G_{rear} is calculated using Eq. (5.15), where $I_{\mathrm{mp,rear}}$ is the portion of I_{mp} owing to the rear-side contribution, whereas $I_{\mathrm{mp,rear,STC}}$ is the current of maximum power for STC referring to the rear-side.

$$G_{\mathrm{rear}} = 1000 \frac{I_{\mathrm{mp,rear}}}{I_{\mathrm{mp,rear,STC}}} \tag{5.15}$$

Considering the ratio I_{sc} / I_{mp} constant for both sides of the bifacial module, the expression for φ is rewritten as Eq. (5.16).

$$\varphi = \frac{I_{\mathrm{mp,rear,STC}}}{I_{\mathrm{mp,front,STC}}} \tag{5.16}$$

Then, from Eq. (5.16) in Eq. (5.15), G_{rear} is expressed in Eq. (5.17) in terms of $I_{\mathrm{mp,front,STC}}$ to keep the same denominator as for G_{E} in Eq. (5.13) and G_{front} in Eq. (5.14).

$$G_{\mathrm{rear}} = 1000 \frac{I_{\mathrm{mp,rear}}}{\varphi\, I_{\mathrm{mp,front,STC}}} \tag{5.17}$$

From Eqs. (5.13), (5.14) and (5.17) substituted in Eq. (2.18) results Eq. (5.18).

$$1000 \frac{I_{\mathrm{mp}}}{I_{\mathrm{mp,front,STC}}} = 1000 \frac{I_{\mathrm{mp,front}}}{I_{\mathrm{mp,front,STC}}} + \varphi\, 1000 \frac{I_{\mathrm{mp,rear}}}{\varphi\, I_{\mathrm{mp,front,STC}}} \tag{5.18}$$

Equation (5.18) can be simplified to yield Eq. (5.19), which is the relation between the operating currents in a bifacial module. Equation (5.19) is precisely the relation which allows extending the proposal described in Abe et al. (2020b) for bifacial modules.

$$I_{\mathrm{mp}} = I_{\mathrm{mp,front}} + I_{\mathrm{mp,rear}} \tag{5.19}$$

5.7.3 Separating the power contributions of each side of a bifacial module

The previous sections presented the assumptions and calculations to relate the irradiance (G_E, G_{rear}, G_{front}) and the current contributions (I_{mp}, $I_{mp,front}$, $I_{mp,rear}$). The present section, in turn, presents expressions for computing the power contributions referring to the front and rear sides, respectively, $P_{mp,front}$ and $P_{mp,rear}$. The operating current I_{mp} can be easily measured during the operation of a PV array. This can be accomplished using built-in metering from the inverter (for example, via digital communication as in this study) or using dedicated measuring hardware. The inverter positions the operating point at the maximum power point (MPP), that is, voltage V_{mp} and current I_{mp}. Once the I_{mp} value is known, the equivalent irradiance (G_E) can be computed using Eq. (5.13).

The power contributions of the front and rear-sides are expressed by scaling P_{mp} and using a power balance, as shown in Eq. (5.20) and Eq. (5.21). It is worth noting that the relations in (5.20) and (5.21) already account for the temperature effect because the P_{mp} value comes from an on-site measurement. The G_{front}, which is an input for Eq. (5.20), should be measured with a device presenting reasonable spectral match with the bifacial array. In this thesis, the G_{front} sensor is a monocrystalline PV cell, therefore, spectrally matched with the bifacial array.

$$P_{\mathrm{mp,front}} = P_{\mathrm{mp}} \frac{G_{\mathrm{front}}}{G_{\mathrm{E}}} \tag{5.20}$$

$$P_{\mathrm{mp,rear}} = P_{\mathrm{mp}} - P_{\mathrm{mp,front}} \tag{5.21}$$

5.7.4 Novel method: bifacial gain calculation without a reference PV system

Differently from the classic approach of Eq. (5.12), the BG calculation proposed in this section, given in Eq. (5.22), relies on G_{front}, I_{mp} and P_{mp} measurements referring to the bifacial device, allowing the contributions of the front and rear-sides of the PV array to be quantified separately.

$$\mathrm{BG} = \frac{\sum P_{\mathrm{mp}}}{\sum P_{\mathrm{mp,front}}} - 1 \tag{5.22}$$

In Eq. (5.22), P_{mp} is a measurement coming from the inverter's metering system, whereas $P_{\mathrm{mp,front}}$ is computed via Eq. (5.20), with G_{E} given by Eq. (5.13).

5.7.5 Validation of the proposed method for computing G_E, $P_{mp,front}$ and BG

The validation phase for the method proposed in this study consists of three steps. First, the calculation of G_E using Eq. (5.13) is compared to G_E computed via Eq. (2.18), which considers G_{front} and G_{rear} measurements. Then, a reference $P_{mp,front}$ is determined from G_{front} and T_C measurements applied to the international standard IEC-60891 (IEC, 2009), as developed in Section 3.7.1, and compared with $P_{mp,front}$ obtained from Eq. (5.20). Finally, the bifacial gain (BG) is computed taking into account the m-Si PV array installed on the same tracker as the bifacial array, using Eq. (5.12), and compared with the BG computed using Eq. (5.22). A schematic illustration of the validation process is provided in Fig. 5-24.

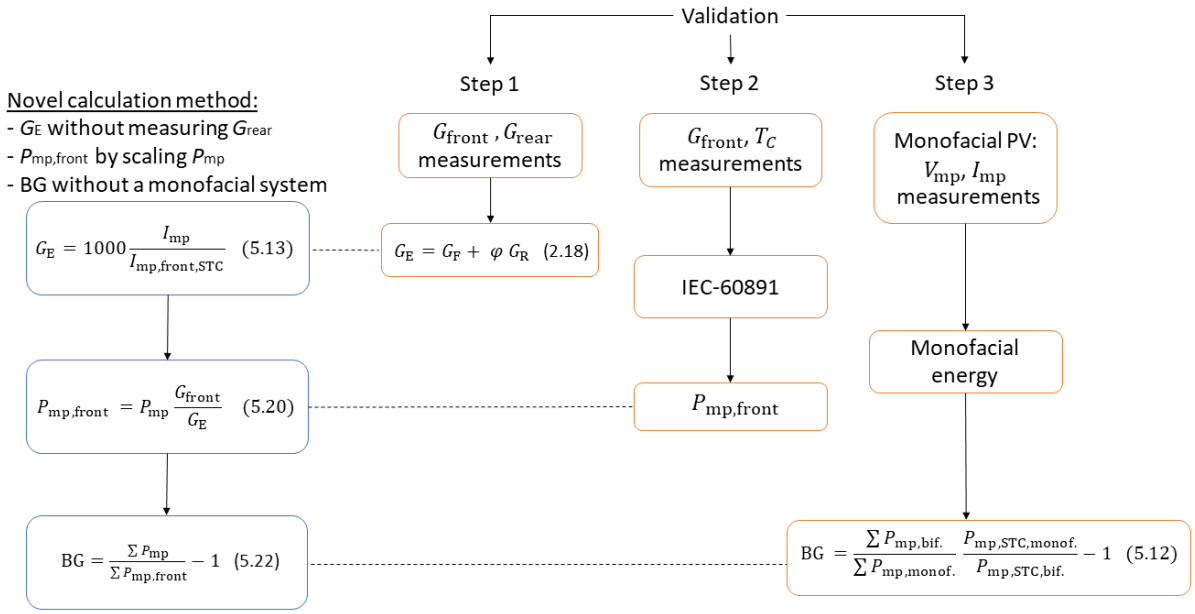

Figure 5-24: Schematic representation for the validation of the proposed method

5.7.6 Application: estimation of G_E and decomposition into G_{front} and G_{rear}

The present section concerns the estimation of the effective irradiance G_E being converted by the bifacial PV array. Given that the array operating point is determined by the inverter's maximum power point tracker (MPPT), some oscillations in current and voltage occur because the MPPT is constantly shifting the operating point, seeking for the maximum power. Since I_{mp} presents noise due to this constant variation, the G_E calculated using Eq. (5.13) inevitably presents noise as well, as illustrated in Fig. 5-25.

An undesirable effect of the noise in G_E is the fact that, in some cases, its value becomes lower than the front irradiance G_{front}. Consequently, the rear irradiance calculated using Eq. (5.17) presents negative magnitude, which is inconsistent with the physical meaning of G_{rear}.

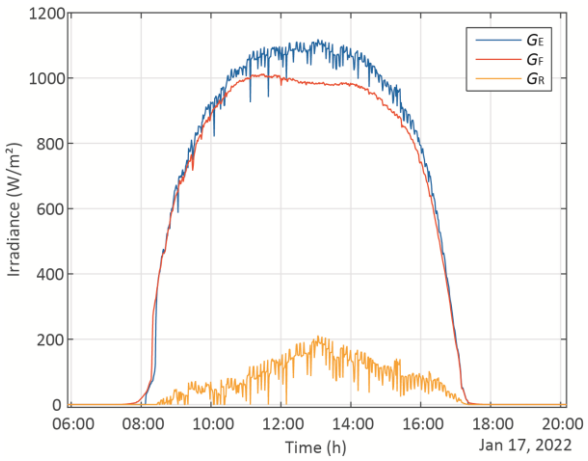

Figure 5-25: Unfiltered irradiance levels for G_E, G_{front} and G_{rear}

To reduce the MPPT-induced noise on I_{mp}, an averaging filter was applied. In this study, a 10-period moving average was employed as a noise-reduction measure. The resulting curves are presented in Fig. 5-26, where a significant improvement in noise is observed.

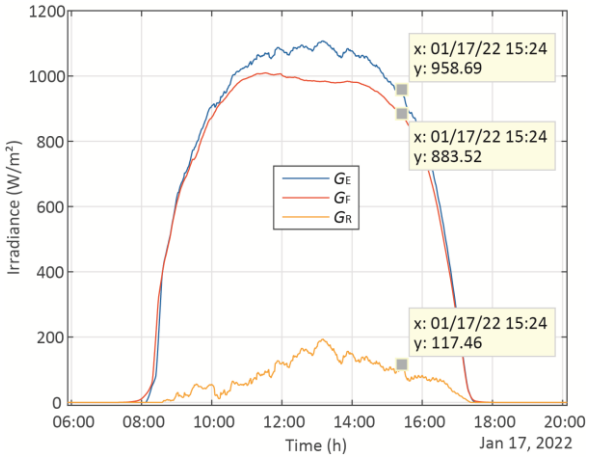

Figure 5-26: Filtered irradiance levels for G_E, G_{front} and G_{rear}

Despite the filtering, there are still situations where the resulting G_{rear} is a negative value, for instance, during steep variations in front-side irradiance, where the MPPT cannot quickly track the optimal I_{mp} level. To avoid negative G_{rear} values, the rear-side irradiance is only calculated for cases where $G_E > G_{front}$, otherwise, G_{rear} is set as zero.

Considering the irradiance curves depicted in Fig. 5-26, the magnitude balance follows Eq. (2.18), that is, if G_{rear} is scaled by a factor φ and then added to G_{front}, the result is G_E.

Correlating the temperature-corrected array P_{mp} with the G_E calculated using Eq. (5.13) results in the plot shown in Fig. 5-27. A linear fit presents angular coefficient equal to 1.958 and linear coefficient of -2.688, that is, for an irradiance level of 1000 W/m², the power is roughly 1955 W. Such a power value is close to the array $P_{mp,STC}$ found during the initial tests: 6 x 324.4 W = 1946.4 W, that is, a 0.45 % relative difference. This shows that the estimation of G_E by means of Eq. (5.13) provides a suitable measure for the total irradiance reaching the bifacial module.

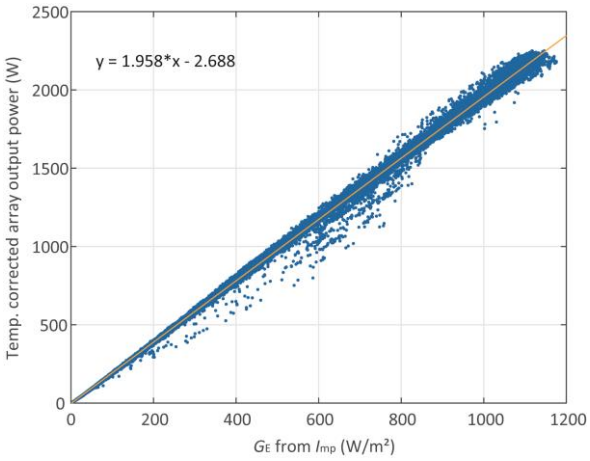

Figure 5-27: Correlation between temperature corrected array P_{mp} and G_E calculated via Eq. (5.13)

5.7.7 Application: determination of $I_{mp,front}$ from G_{front} and $I_{mp,rear}$ from G_{rear}

The decomposition of I_{mp} into $I_{mp,front}$ and $I_{mp,rear}$ presented in this section is for verification purpose only, since this step is not necessary for the calculation of the power contribution of each face of the bifacial module.

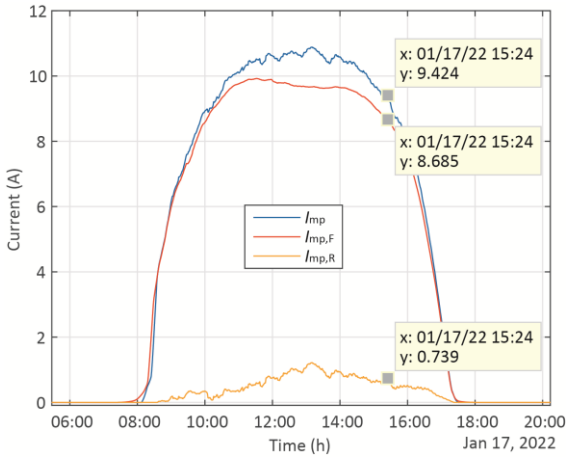

Figure 5-28: Decomposition of I_{mp} into $I_{mp,front}$ and $I_{mp,rear}$

The front-side irradiance is a measured quantity, therefore, the respective value of current produced by the front-side individually is computed using Eq. (5.14) solved for $I_{mp,front}$. Similarly, $I_{mp,rear}$ is obtained from Eq. (5.17) using the G_{rear} calculated in the previous steps, from Eq. (2.18).

In Fig. 5-28 it is shown that $I_{mp} = I_{mp,front} + I_{mp,rear}$, and such a relation is valid for every time step contained in the dataset.

5.7.8 Application: decomposition of P_{mp} into $P_{mp,front}$ and $P_{mp,rear}$

The power fractions of P_{mp} owing to the front and rear-sides of the bifacial module were calculated using Eqs. (5.20) and (5.21). The resulting curves for a given day are illustrated in Fig. 5-29, where it can be observed that $P_{mp} = P_{mp,front} + P_{mp,rear}$.

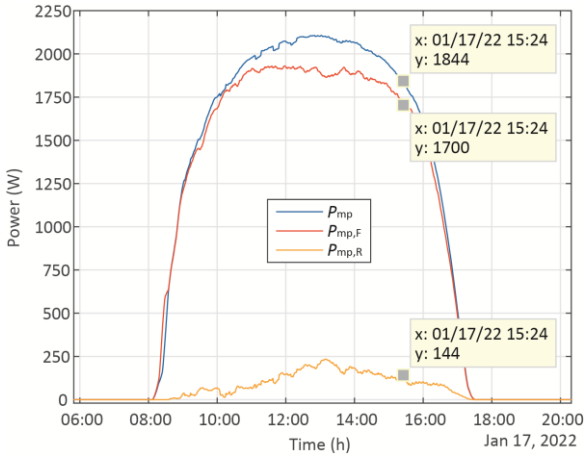

Figure 5-29: Decomposition of P_{mp} into $P_{mp,front}$ and $P_{mp,rear}$

5.7.9 Application: bifacial gain calculation

From the novel method proposed in this study, the BG for the modules under study could be computed without a monofacial PV array and without measurements of the rear-side irradiance. The BG value found using Eq. (5.22) is 6.24 %.

The study conducted by Burnham et al. (2019) also considered a dual-axis tracker and bifacial modules with $\varphi = 0.62$ (in the present study, $\varphi = 0.64$). Despite the similarities, Burnham et al. (2019) found BG = 4 %, which is 35 % smaller than the BG found in the present work. This fact illustrates how similar bifacial systems can perform differently because of site-specific parameters.

5.7.10 **Validation, step 1: using a back-side irradiance sensor to calculate G_E**

This section provides an assessment on how the method proposed in Section 5.7.2 compares with G_E calculated using actual rear-side irradiance ($G_{rear,meas}$) measurements. The values for $G_{rear,meas}$ were measured using a small calibrated PV irradiance sensor positioned at the center of the rear-side of the PV array, as mentioned in Section 3.4. The sensor model is identical to that used to measure the front-side global irradiance. It is worth emphasizing that the use of a rear-side irradiance sensor is considered in this section of the section only for checking purposes since the proposed method does not require G_{rear} measurements for the calculation of G_E, $P_{mp,front}$ and BG using Eqs. (5.13), (5.20) and (5.22).

The two vectors for G_E – calculated using Eqs. (5.13) and (2.18) are presented in Fig. 5-30 as a function of time for four days, each with a different sky condition. Fig. 5-30 shows a good agreement between the G_E calculated as a function of I_{mp} (Eq. 5.13) and the G_E computed using G_{front} and G_{rear} (Eq. 2.18), even in transient and low-irradiance conditions. The plots in Fig. 5-30 illustrate the suitability of the calculation of G_E using the I_{mp} determined by the inverter's MPPT.

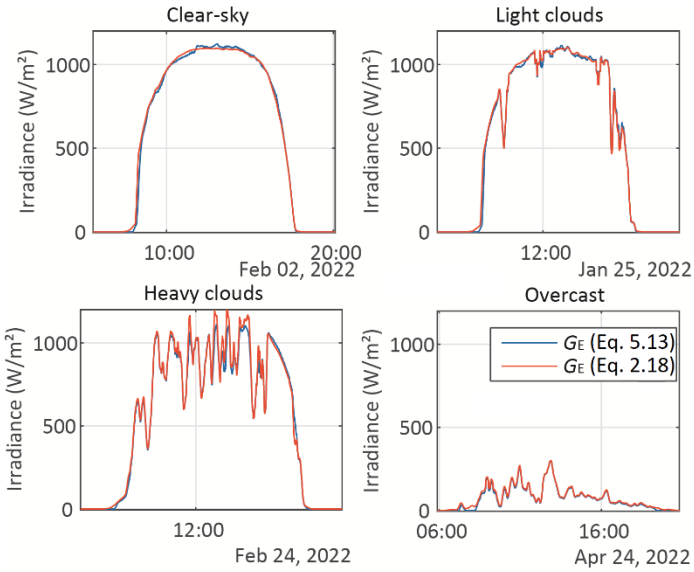

Figure 5-30: G_E calculated using Eqs. (5.13) and (2.18)

Plotting the levels of G_E obtained from Eqs. (5.13) and (2.18) results in Fig. 5-31.

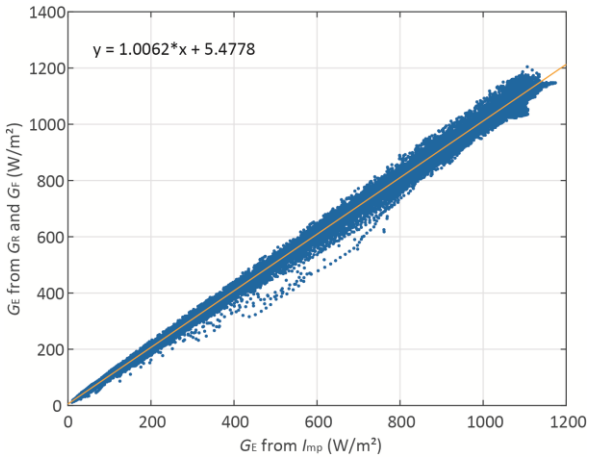

Figure 5-31: Correlation for G_E from Eq. (5.13) x G_E from Eq. (2.18)

In Fig. 5-31, a correlation factor greater than 0.999 was found using the Matlab function *corrcoef* (Pearson correlation coefficient). The nRMSE level for the data is 2.88 %, whereas the correlation slope is 1.0062. Factors which contribute to the spread shown in Fig. 5-31 are the MPPT, which introduces fluctuations in the operating current, which is not compensated in Eq. (5.13).

5.7.11 **Validation, step 2: calculating the front-face power using IEC-60891**

This part of the validation process deals with the P_{mp} decomposition method proposed in Section 5.7.3. Given that P_{mp} and G_{front} are measured quantities, the quantification of $P_{mp,front}$ by means of another method allows indirect assessment of the correctness of the G_E estimation via Eq. (5.13). The method introduced in Section 3.7.1, was employed for the determination of the reference $P_{mp,front}$. IEC-60891 was applied to model the electric behavior of the module's front-side only, as if the bifacial module were a monofacial device. For that, two I-V curves referring to the bifacial module (with the rear-side covered) were used to identify the three unknown parameters for the IEC-60891 voltage correction equation (from Section 4.3.2: a = 0.013, R_s = 0.43 Ω and k = 0.002 Ω/K). This way, using T_c and G_{front} as inputs, the voltage and current provided by IEC-60891 refer to a theoretical monofacial module, and the product between voltage and current results in the front-face power contribution.

The comparison between the $P_{mp,front}$ calculated using Eq. (5.20) and $P_{mp,F}$ calculated using IEC-60891 was carried out both as a function of time (Fig. 5-32, considering four days with different sky condition) and as a correlation plot (Fig. 5-33), considering all measurement points within the dataset.

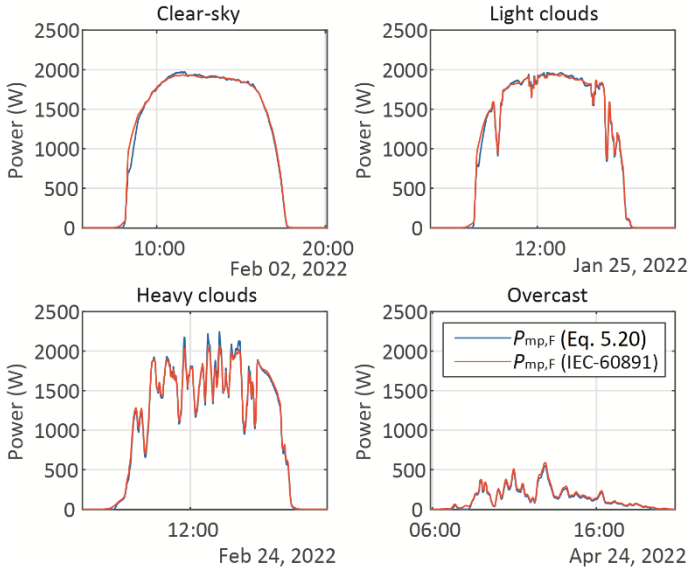

Figure 5-32: Comparison of the $P_{mp,front}$ calculated from Eq. (5.20) and from IEC-60891

The plots of $P_{mp,front}$ illustrated in Fig. 5-32 show a good fit: the general form of the curves agree; however, some low-amplitude noise is observed in the curve of $P_{mp,front}$ calculated using Eq. (5.20). The reason for the noise is the propagation of the residual noise on G_E, which in turn is caused by the oscillations on I_{mp} introduced by the MPPT, even after filtering was applied.

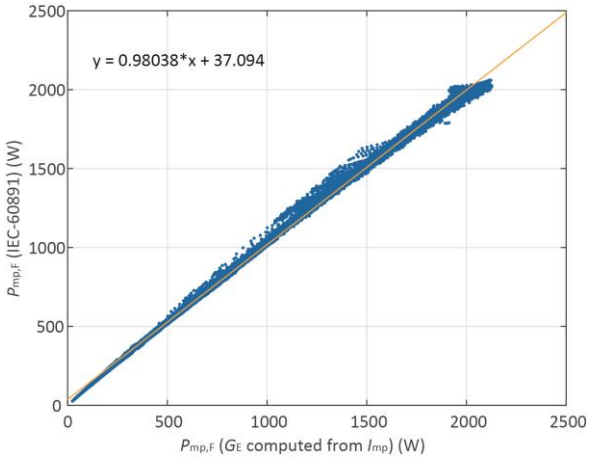

Figure 5-33: Correlation between $P_{mp,front}$ from Eq. (5.20) and from IEC-60891

Constructing a plot of $P_{mp,F}$ from Eq. (5.20) and $P_{mp,F}$ (IEC-60891) results in Fig. 5-33, where the correlation coefficient is greater than 0.999. This way, it is shown that the decomposition of P_{mp} into $P_{mp,F}$ + $P_{mp,R}$ is consistent with the front-side irradiance and module temperature registered in the dataset, which were used to specify the operating condition for the application of the IEC-60891 correction method. Consequently, the calculation of G_E via Eq. (5.13) is also consistent, given that G_E is the only calculated input parameter in Eq. (5.20). Calculating the nRMSE for the data points of Fig. 5-33 results in 2.68 %.

5.7.12 **Validation, step 3: using a monofacial PV array to calculate the bifacial gain**

The BG calculated using the method proposed in Section 5.7.4, using Eq. (5.22) resulted in 6.24 %. In turn, calculating the BG based on the performance of a monofacial PV array added for comparison, as carried out in numerous studies in literature using Eq. (5.12), provides BG = 6.69 %, which corresponds to a relative difference of 7.2 %. Such a deviation results from the coupled errors associated to the calculations via Eqs. (5.13) and (5.20).

It is worth noting that Eq. (5.12) takes the STC power ratings into account. When this experiment began, both bifacial and monofacial modules were new, and the STC ratings were identified outdoors during the initial I-V tests described in Section 3.7. Therefore, irradiance and temperature measurement errors are possible sources for deviations between the real and calculated STC ratings, which affects the calculation of the BG via Eq. (5.12).

On the other hand, the BG calculated using Eq. (5.22) relies on the bifacial module's operating current, which is not temperature-compensated and presents fluctuations due to the MPPT action. These factors are error sources for the calculation of BG via Eq. (5.22).

5.7.13 **Limitations of the proposed method**

Since the method to compute G_E relies on the maximum power current, it is essential that the PV array operates at the maximum theoretical power point, according to the operating condition defined by G_E and T_c. However, in practice there are a number of factors that can potentially shift or prevent the operating point to be at the maximum power point.

The MPPT might force the PV array to operate far from the MPP during fast-changing irradiance levels, for example, in windy, cloudy days, where the irradiance profile shows steep

variations. Given that it is not possible for the MPPT action to be instantaneous, the array's operating point is likely to be out of the MPP short after abrupt irradiance changes.

Another reason for a PV array to operate far from the MPP is the so-called clipping. Such an effect occurs when the DC power is greater than the inverter's rated power. Unusually high DC power levels can be found in cold, clear-sky days, in which the low temperature leads to relatively high voltage levels, whereas high irradiance leads to relatively high current levels. As a result, it is possible for the DC power to be significantly higher than usual, and if such a level is greater than the inverter's rating, the operating point of the PV array will be intentionally shifted. This will reduce the PV array power output to a level within the inverter's capacity, and as a result, the DC power will not be coherent with the operating condition defined by G_E and T_c, and Eq. (5.13) will not produce reliable results.

As for the clipping, a condition termed curtailment also might force the PV array to operate outside the MPP. Inverters can sense the grid operating condition, and in cases where the AC voltage is above the rated limit – for example due to a local excess of reactive power – the inverter would reduce the supply of electricity to the grid, forcing the PV array to operate outside the MPP. Another parameter monitored by the inverters is the grid AC frequency. Frequency levels above the nominal reference are an indication of an imbalance between instantaneous demand and supply. If a system presents more supply than demand, the grid frequency is likely to rise, and the PV inverters will respond reducing the power supplied to the grid. As a result, the operating power of the PV array will not be coherent with the current levels of G_E and T_c; therefore, Eq. (5.13) will not provide valid results for G_E.

One way to overcome the method's dependency on the inverter's MPPT is through the use of module-level I-V trace equipment, as proposed by Marquis et al., (2022) and Quiroz et al. (2015). This would allow Eq. (5.13) to be used in all operating conditions, regardless of the inverter's state.

Finally, the proposed method considers that the bifacial PV array is not faulty, shaded or soiled.

5.7.14 **Remarks on the proposed method to calculate G_E and BG**

Section 5.7 considered the problem of determining the effective irradiance for bifacial PV modules from the operating current, without requiring rear-side irradiance measurements. Measuring the rear-irradiance of PV arrays in real operating conditions is a challenging task given the non-uniformity of radiation along the rear surface of the PV modules.

The greatest advantage of the method proposed in this section is that the total irradiance effectively being converted by the PV array is quantified, since the operating current I_{mp} is used as the source for G_E calculation. The technique thus allows splitting P_{mp} into two fractions, $P_{mp,front}$ and $P_{mp,rear}$, which are the power contributions of each side of the bifacial PV array, allowing the bifacial gain to be computed without the need of a reference monofacial PV system.

The main limitation of the proposed method is the strong dependency on the inverter's MPPT. Thus, the method will not provide reliable estimations of G_E for cases where the PV array is not operating at the maximum power point. However, the method can still be implemented using I-V tracers, which are able to determine the MPP without relying on the inverter's MPPT.

The method was validated in the following respects:

- The G_E calculation using I_{mp} via Eq. (5.13) was checked against the consolidated approach based on the bifaciality index and rear-side irradiance measurements using (2.18), presenting nRMSE of 2.88 %;

- The $P_{mp,front}$ calculated using Eq. (5.20) was compared with the results from IEC-60891, showing nRMSE of 2.68 %;

- Finally, the bifacial gain calculated with Eq. (5.22) was compared to the BG provided by Eq. (5.12), resulting in 6.24 % and 6.69 %, respectively.

The study presented in this section was published in 2023, in the IEEE Journal of Photovoltaics (Abe et al., 2023). It consists the third scientific article published within the context of this thesis.

5.8 SUMMARY OF PV ARRAYS PERFORMANCE: MONTHLY AVERAGES

The data in Fig. 5-34*a,b* show the monthly average values for the environmental parameters, whereas the PV arrays' operational metrics are displayed in Fig. 5-34*c*,*d*. The aim of this section is to present a general view regarding the behavior of the arrays, and correlate them with the operating condition, monthly.

The metrics displayed in Fig. 5-34*a* are the irradiance components (left-side axis) and the air temperature (right-side axis). The average GNI and BNI vary according to the number of days with cloudy sky, showing no regular pattern throughout the year. On the other hand, GNI_{rear} presents a smooth variation, with its maximum value being reached during summer. Unsurprisingly, the average air temperature shows a correlation with the season of the year. For all PV arrays studied, the parameters shown in Fig. 5-34*a* are the most influencing. On the other hand, the data in Fig. 5-34*b* show the AM and v_{wind} sharing the left-side axis; and the absolute humidity on the right-side axis. The AM is a calculated metric, and thus presents a smooth variation through the year. The absolute humidity shows a correlation with the ambient temperature, illustrating the fact that the hotter the air, the greater its capacity of holding water vapor.

The plot in Fig. 5-34*c* shows the average PR, as calculated by Eq. (2.24). Although PR is calculated from P_{mp} and irradiance (GNI for p-Si and m-Si; G_E for bifacial; and BNI for HCPV), it does not follow the irradiance behavior. The reason is the strong influence of the irradiance on P_{mp}, and the fact that the latter composes the numerator of Eq. (2.24), whereas the former composes the denominator. The variations are thus partially compensated in the calculation of PR. In turn, the air temperature, along with the irradiance, strongly influence the arrays' temperature, which is not compensated in Eq. (2.24). This way, PR correlates well with the air temperature, for all PV arrays. In Fig. 5-34*c*, the HCPV array presented the smallest PR levels, since this is the most temperature-sensitive array. Similarly, the p-Si array presented the second smallest PR levels; the temperature coefficient for power (γ) for this array is located between the γ referring to the HCPV and m-Si and bifacial arrays – the two present similar γ. These conclusions show that Fig. 5-34*c* is a valuable resource to visualize the temperature influence on the PV arrays through the year.

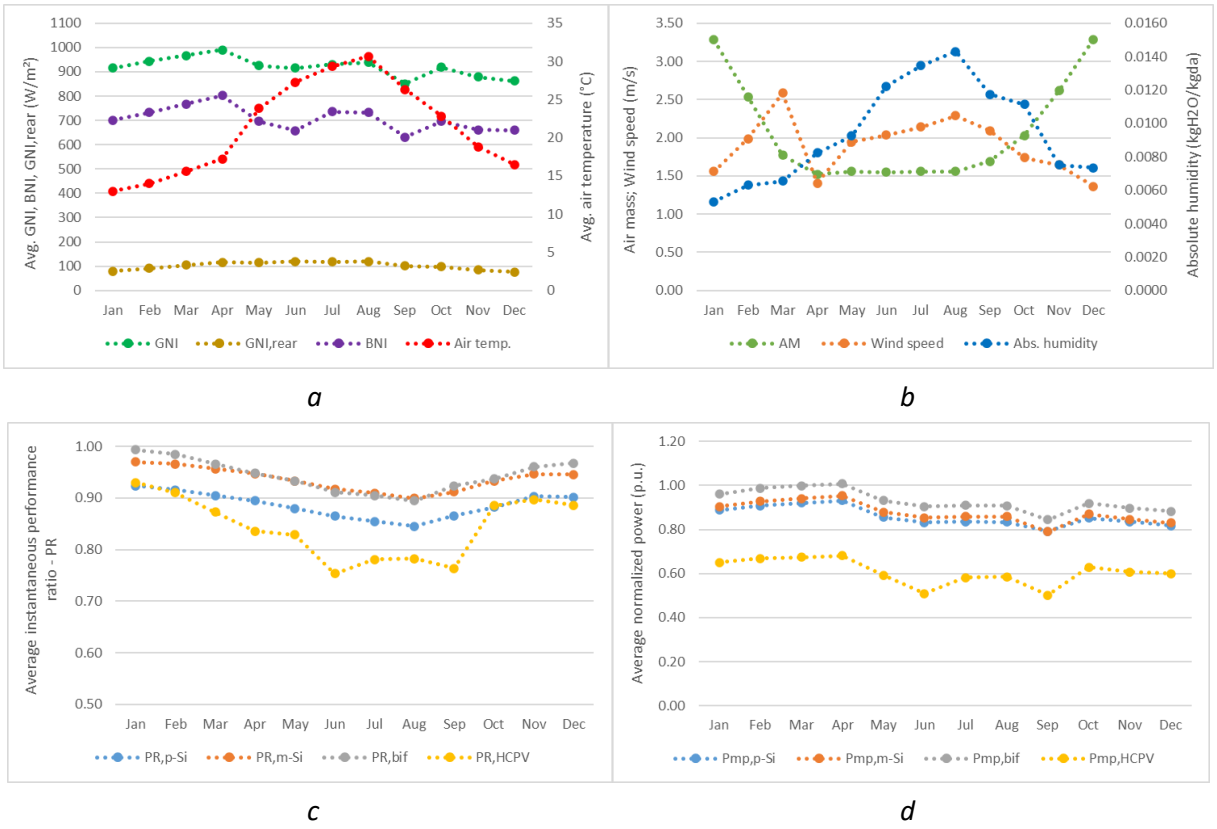

Figure 5-34: Monthly average values for the external parameters and PV array metrics

In turn, the plot in Fig. 5-34*d* shows the average normalized array power. Differently from the PR plots, which compensate the irradiance changes, the power plots clearly show the deficient power delivered by the HCPV array. As mentioned before, although this array presents the greatest efficiency, its irradiance source – BNI – is not as available as the GNI. Since the rated power is referenced to BNI = 1000 W/m², the normalized power is shown well below the power curves referring to the remaining technologies studied. Fig. 5-34*d* also shows that the normalized power referring to the p-Si and m-Si arrays are quite similar, with the p-Si array showing slightly smaller levels in comparison to the m-Si array. This is explained by the greater γ of the p-Si array, compared to the m-Si. The normalized power referring to the bifacial array is the greatest among all arrays. The reason for such high normalized power levels lies in the use of the STC ratings as the reference, which consider only the front-side contribution. Thus, given the contribution of the rear-side of the bifacial PV array operating outdoors, the normalized power presents a gain.

5.9 SUMMARY OF PV ARRAYS PERFORMANCE: ANNUAL YIELD

A reasonable way to summarize the performance of the PV arrays is by means of the annual normalized PV energy, of final yield. It is calculated by the ratio between the energy (in kWh) and STC power (in kW), resulting in an indicator with unit in hours. This results in 1536 h for p-Si; 1726 h for m-Si; 1833 h for bifacial; and 995 h for HCPV.

Similarly, the solar resource is calculated by the ratio between the solar energy (in kWh/m²) and the reference irradiance (in kW/m²). This is the reference yield, measured in hours. The results are 1987 h for G_E; 1846 h for GNI; and 1312 h for BNI.

The annual PR (PR_a) is thus computed by the ratio between the final yield and the reference yield, resulting in 0.83 for p-Si; 0.94 for m-Si; 0.93 for bifacial; and 0.76 for HCPV.

These results are debatable: the final yield represents the energy supplied by a PV array per unit of installed power. In this sense, the PV arrays considered in this work can be ordered from greatest to smallest productivity as follows: bifacial, m-Si, p-Si and HCPV. However, the PR_a is not in agreement with such an ordering, since it presents PR_a =0.93 for the bifacial array and PR_a =0.94 for the m-Si. It is worth recalling that the calculation of PR_a for the m-Si modules considers GNI, whereas for the bifacial array, it considers the effective irradiance G_E. Thus, the PR_a calculation is compensated for the irradiance; but it is not for the temperature. As stated in Section 5.6, the temperature referring to the bifacial array is 2 °C smaller than for the m-Si modules. However, the temperature coefficient for the DC power is -0.35 %/°C for the m-Si modules, and -0.45 %/°C for the bifacial (as per Section 5.2). For the m-Si array operating at 38.5 °C and the bifacial at 36.5 °C (the average annual values), the power losses referring to the temperature are 9.5 % greater for the bifacial modules than for the m-Si. This means that, considering the average annual records, the higher temperature coefficient of the bifacial modules is more significant than the lower operating temperature; as a result, the final effect on the bifacial array's power is a reduction. This consists of a plausible explanation for the bifacial array's PR_a being lower than the PR_a for the m-Si. Despite the lower PR_a, the normalized energy delivered by the bifacial modules is higher. Considering the current scenario, where bifacial and m-Si modules present virtually the same cost per watt, the bifacial technologies are undoubtedly the best option, especially for cases where: a) the bifaciality factor φ is high, thus increasing the bifacial gain; b) the system is installed with enough clearance from the ground, to enable uniform rear-side irradiance; and c) the ground is covered with paint or materials favorable to provide a high albedo.

The final yield referring to the m-Si array was 12.5 % greater than that of the p-Si. The fact that the p-Si modules present smaller efficiency than that of m-Si is already accounted in the calculations, which consider the nominal power ratings whereas the array area is not concerned. When checking the temperature records, very close T_c levels (0.2 °C difference, on average) were found for the two arrays. The difference lies in the temperature coefficients for power: -0.42 %/°C for p-Si and -0.35 %/°C for m-Si, thus justifying the smaller PR_a for the p-Si array.

In turn, the HCPV modules presented the poorest performance in this study. Not only they present the highest cost per watt among the four technologies studied; they presented, also, the smallest final yield and PR_a. In fact, these PV modules usually operate far from the STC ratings, since the reference BNI is 1000 W/m², which is quite a high level. Also, the HCPV array presented the highest power degradation with respect to the operating temperature. Moreover, due to the use of the Fresnel lenses for concentration, the HCPV array requires a high-precision dual-axis tracker, which further increases the initial investment and operating costs, both with maintenance and electricity consumption. Finally, the tracking is sensitive to the wind speed, and for certain wind speeds (30 km/h for the tracker used in this work), the HCPV array is set to the horizontal position to protect the tracker, at the expense of severely impairing the electricity production.

5.10 CONCLUSIONS FOR SECTION 5

The studies regarding the effects of the external parameters on the PV arrays' performance consist of the main tasks in this thesis, as they concern its main objectives.

In this sense, the present section explored several different assessment approaches, enabling the identification of the most influencing variables for the DC power, for each technology.

The analysis started with the correlations between the measured variables, with especial attention given to the relationship between the operating temperature and the power, under constant irradiance. Then, multivariable models were built and applied to classify the external parameters according to their ability to describe the arrays' output power. Following, the sensitivity analysis was carried out based on filters and mathematical models. The influence of the back-side irradiance on the bifacial array's performance was evaluated using traditional methods and novel approaches proposed in this work. Finally, a summary of the arrays' performance used the energy metrics to present indicators such as the yield and annual performance ratios.

The m-Si array was the least affected by the operating temperature, showing a coefficient of -0.36 %/°C for the DC power. In turn, the p-Si and bifacial technologies presented similar thermal performance, showing temperature coefficients for power of -0.44 and -0.45 %/°C, respectively. The HCPV array presented the greatest dependence on the operating temperature, with a -0.57 %/°C factor for the output power.

By using models for the DC power, the irradiance (GNI for m-Si and p-Si; G_E for bifacial; BNI for HCPV) and temperature (T_{air} or T_c) were identified as the most important variables to describe the DC power, for all PV arrays; such a finding was already expected since PV literature largely presents models based on these two parameters. The models were built strictly in view to present low errors; their size and complexity were not regarded as relevant factors. The performance metric was the nRMSE, presenting 3.37 %, 1.84 %, 2.53 % and 5.06 %, respectively, for p-Si, m-Si, bifacial and HCPV. Due to the complexity and size, these models are not suitable for straightforward application.

Operational models were built aiming to provide an adequate balance between simplicity and accuracy. Their complexity and size are significantly lower in comparison with the models previously mentioned; however, the performances are quite comparable: the nRMSE levels are 3.40 %, 1.84 %, 2.56 % and 5.96 %, respectively, for p-Si, m-Si, bifacial and HCPV. This shows that using the external parameters in several terms and interactions, forming complex models, does not necessarily lead to a significantly better description of the DC power.

Plots for the normalized power versus the external parameters showed that the HCPV array is the most sensitive for high levels of temperature, air mass and air humidity. When the records were filtered to consider cloudy days, the HCPV array was once again the most impaired, given its irresponsiveness to diffuse irradiance. Increasing wind speed presented a positive influence for all PV technologies; however, the HCPV array was the least benefited, given that the cells are enclosed within a metal housing. Since the external parameters present collinearity, a model-based multivariate sensitivity analysis was developed using the Principal Component Regression and artificial, independent variables, as inputs. The results provide quantitative scores for the sensitivity and corroborate the observations made via the filter-based analysis mentioned earlier.

The prospect of using measured array temperature to describe the DC power, instead for the air temperature, was evaluated as well. For that, a consolidated method described in the literature was employed, providing nRMSE levels of 3.08 %, 1,73 %, 2.67 % and 6.61 %, respectively, for the p-Si, m-Si, bifacial and HCPV arrays. These error metrics are smaller than those obtained with the use of T_{air}, except for the HCPV modules. Considering that only three parameters were used as inputs (irradiance, cell temperature and air mass), the error levels suggest a good modeling performance, particularly when considering that models with significantly higher size and complexity (using up to 6 input variables) presented nRMSE of 3.04 %, 1.62 %, 2.43 % and 5.12 %, respectively, for p-Si, m-Si, bifacial and HCPV. The error levels are quite similar, except for the HCPV array, showing, again, that the model's performance is not necessarily enhanced with increasing complexity. All in all, it is shown that using measured array temperature instead of air temperature provided slightly better performance for p-Si and m-Si; however, the modeling quality was worse for the bifacial and HCPV technologies. The reason might be that the p-Si and m-Si modules are built in such a way that the temperature sensors, when attached to the rear of the modules, are closer to the PV cells, as in comparison with the bifacial and HCPV modules. It is worth recalling that the p-Si and m-Si modules present a thin EVA coating as the back cover, whereas the bifacial modules are glass-glass encapsulated; and the HCPV cells are contained within a metal box.

The STC ratings were once again experimentally determined, using measurement instruments and methods totally different from those considered in the I-V curve measurement campaign carried out before the modules were mounted on the tracker. Once again, the STC power levels referring to all PV arrays were found as smaller than the datasheet specifications.

As mentioned earlier, special attention was directed to the bifacial array, given the relevance of such a technology in the market. This way, assessments of a novel method to determine the effective irradiance G_E produced a 2.88 % nRMSE, relatively to the traditional method using front and rear-side irradiance measurements. In turn, the bifacial gain is a valuable metric for the performance of a bifacial PV plant, relatively to a regular system with monofacial devices. In this thesis, it is proposed to calculate the bifacial gain by means of assessing the individual power contributions of each side of the bifacial array. This avoids the use of a reference monofacial PV array for the BG determination. The method to compute the power referring only to the front-side of a PV array presented nRMSE of 2.68 %, relatively to assessments made using the international standard IEC-60891. The bifacial gain calculated using the novel method was 6.24 %, whereas the BG obtained using the traditional method – talking the m-Si system as the reference – produced BG = 6.69 %.

Finally, a summary of the PV arrays' performance showed normalized yields of 1536 h for p-Si; 1726 h for m-Si; 1833 h for bifacial; and 995 h for HCPV. The annual performance ratios resulted in 0.83 for p-Si; 0.94 for m-Si; 0.93 for bifacial; and 0.76 for HCPV. If the previous assessments highlighted the HCPV array's undesired sensitivity to several operating parameters, always to a greater extent than for the other technologies, the performance summary shows the definitive metrics that make the HCPV the worst-performing among all four technologies evaluated in this work.

SECTION 6
FINAL CONCLUSIONS

6 FINAL CONCLUSIONS

The study described in this thesis covers several phases concerning the assessment of the influencing parameters on the behavior of four different PV arrays. The initial objective – the performance comparison between the four PV arrays and the development of a sensitivity analysis – has been accomplished; however, it is the total set of methods and assessments that actually constitute the actual contribution of this work.

The thesis positively differs from other works in literature in the sense that extensive I-V curve measurement – with all PV modules involved – was carried out before the one-year measurement campaign started. Not only the modules integrity was checked; the I-V curves were used to determine the actual STC ratings of the modules, allowing the real reference performance to be quantified.

As this work concerned several different metering equipment, an uncertainty analysis was performed, ranging from the individual meters' uncertainty to the combined uncertainties for several parameters. The uncertainty levels were applied as references for setting data filters.

A considerable amount of effort was directed to the initial data-related work: data collection, synchronization, interpolation, aggregation and filtering. Although such a task does not directly relate with the scientific focus of the thesis, it should be acknowledged that working with data is an unavoidable part of any experimental work. In particular, the amount of data recorded and produced required a dedicated software application for data exploration and visualization, given the dataset size: over 450,000 records and over 100 data attributes, consisting of measured and calculated quantities.

The first step in the data analysis was the raking of the external parameters by relevance in describing the main output quantity of a PV array – the power. This was accomplished by means of a study based on the successive inclusion of different parameters to a multivariate model, which was optimized in each iteration, aiming to reduce the error between the predicted and measured power levels. For all PV arrays studied, as expected, the irradiance (GNI for p-Si, m-Si and bifacial; BNI for HCPV) was found as the most important variable, followed by the air temperature. In general, absolute humidity and wind speed were found as the least relevant parameters when describing the DC power, for all 4 PV arrays.

The temperature coefficients were experimentally calculated: for the p-Si and m-Si, the experimental coefficients are very close to the datasheet specifications. For the bifacial and HCPV, the differences found suggest that more in-depth analysis should be carried out, be it by means of calculating the equivalent cell temperature from the open-circuit voltage; or by partially disassembling the PV modules to attach temperature sensors directly in contact with the PV cells. The former was not feasible in the context of this thesis, since the PV arrays operate at the V_{mp}, not the V_{oc}; and the latter requires severely modifying the PV modules, which was outside the goals of this thesis.

The PV array's response to the external parameters (GNI, BNI, T_{air}, AM, V_{wind}, and AH, plus GNI_{rear} and NDF) was studied using two different approaches. The first was purely experimental, in the sense that the data were classified, filtered and analyzed, whereas seeking for patterns of dependency between the output DC power and the external parameters. It was found that it is extremely unlikely to have all parameters but one unchanged – a condition which would be ideal for the sensitivity analysis. It happens that, in practice, some parameters such as the irradiance components, the

humidity and the temperature and the air mass and the irradiance are well correlated. This means that usually, changing one parameter implies changing another. The experimental sensitivity analysis was, therefore, carried out based on filtered ranges in which the parameters, which were intended to be static, were allowed to change. This resulted in a set of graphics in which it was concluded that the most distinguished array is the HCPV. Not only its response is dictated mainly by the BNI; its response to temperature is also the highest among the four PV technologies studied. Also, the HCPV was found as the most sensitive to the air mass and humidity changes. These results were corroborated by an analysis considering different operating scenarios, selected by filtering the data.

The second data analysis approach was based on the experimental data; however, the data were used to build models. In fact, multivariable models were built for each PV array, and the error metrics were quantified. Such simple empirical models suffer from the collinearity between the input variables, resulting in an inaccurate coefficient attribution during the models' optimization. To overcome this issue, a strategy based on vectorial transformation (PCR) allowed building new models, based on a set of parameters which are linearly independent. This allowed a more assertive coefficient attribution to the terms within the models. However, simply applying the original data records referring to the external variables, to perform a sensitivity analysis, is not suitable. It should be recalled that the external parameters are precisely the source of collinearity, which in turn required the adoption of the PCR modeling strategy. This way, the models obtained via the PCR were used along with artificial independent variables, which simulated the external parameters, however, without the collinearity. This resulted in a more refined sensitivity analysis. It was found that most of the results obtained at this phase were in agreement with the sensitivity analysis carried out based entirely on the experimental data.

Another assessment concerned the use of the cell temperature, instead of the air temperature, as input for modeling. A consolidated empirical model was applied to the dataset, for the p-Si and m-Si arrays, and a better modeling performance was obtained, whereas using less input parameters – only GNI, T_c and AM. In turn, for the bifacial and HCPV arrays, modifications regarding the irradiance input were required, given the particularities shown by such PV arrays. In both cases, the modeling performance when using T_c instead of T_{air} was slightly worse. The same T_c based model was employed to calculate the STC power ratings, which were within 5% in agreement with the results obtained via the initial tests, carried out before the modules were assembled on the tracker. Thus, this consists of a double indication that the datasheet ratings should always be critically assessed, given that datasheets do not necessarily reflect the actual performance of particular PV modules. This is caused by manufacturing tolerances and differences between production batches. Manufacturers provide a single datasheet for a given part number; not for every module produced.

In addition, a novel method to calculate relevant metrics for bifacial modules was introduced in this thesis. Bifacial modules are among the most promising PV technologies, presenting the best cost-benefit to date. An important metric regarding bifacial systems is the equivalent irradiance. It represents the total amount of useful irradiance reaching the PV module, considering the difference in efficiency between the front and rear sides of the device. Usually, the effective irradiance requires the normal irradiance to be measured on the front and rear sides. This poses a problem, since the rear-side irradiance on a bifacial array is likely to be non-uniform. Thus, several sensors would be necessary

to account for the uneven irradiance distribution, resulting in an increased cost. This thesis proposes a novel method to compute the effective irradiance, based on the operating current, thus not requiring any rear-side irradiance measurements.

The metric which reflects the advantage of using a bifacial array is the bifacial gain. It expresses the extra energy obtained by the bifacial array, in comparison to a monofacial array of the same power. Traditionally, a side-measurement with a monofacial PV system is used to assess the bifacial gain. In this thesis, however, a novel method, based on the individual contributions of each side of the PV device, allows calculating the bifacial gain without the use of a monofacial reference system.

Finally, a summary of the PV arrays' performance allowed the visualization of the monthly average metrics, as well as the annual production-related features, for which final considerations were presented for all four PV arrays studied.

This work considered actual PV systems operating outdoors, supplying electricity to the grid. Therefore, the external parameters are uncontrollable, and the inverters define the operating point for the PV arrays. This is a limitation of this study since it is not possible to confirm that the PV arrays were operating at the maximum power point. However, such a setup allowed the assessments to produce realistic metrics and conclusions considering the non-idealities present.

All in all, it is expected that the results and methods presented in this thesis can somehow contribute to the PV scientific community and the PV industry.

REFERENCES

REFERENCES

Abe, C.F., Batista Dias, J., Notton, G., Faggianelli, G.A., Pigelet, G., Ouvrard, D., 2023. Estimation of the Effective Irradiance and Bifacial Gain for PV Arrays Using the Maximum Power Current. IEEE J. Photovoltaics 1–10. https://doi.org/10.1109/JPHOTOV.2023.3242117

Abe, C.F., Dias, J.B., Haeberle, F., Notton, G., Faggianelli, G.A., 2021. Simplified Approach to Adjust IEC-60891 Equation Coefficients from Experimental Measurements with Long-Term Validation. IEEE J. Photovoltaics 11, 496–503. https://doi.org/10.1109/JPHOTOV.2020.3043101

Abe, C.F., Dias, J.B., Notton, G., Faggianelli, G.A., 2020a. Experimental application of methods to compute solar irradiance and cell temperature of photovoltaic modules. Sensors (Switzerland) 20, 1–17. https://doi.org/10.3390/s20092490

Abe, C.F., Dias, J.B., Notton, G., Poggi, P., 2020b. Computing Solar Irradiance and Average Temperature of Photovoltaic Modules from the Maximum Power Point Coordinates. IEEE J. Photovoltaics. https://doi.org/10.1109/JPHOTOV.2020.2966362

Abe, C.F., Dias, J.B., Poggi, P., Pillot, B., 2019. Combining Identification and Translation Methods of the Single-Diode Model to Compute the Average Temperature of Photovoltaic Modules from the Open-Circuit Voltage. IEEE J. Photovoltaics. https://doi.org/10.1109/JPHOTOV.2019.2922540

Abe, C.F., Faggianelli, G.-A., Batista Dias, J., Notton, G., 2022. Using On-Site Measurements to Identify and Adjust PV Single-Diode Model Parameters for Real Operating Conditions. J. Energy Eng. 149. https://doi.org/10.1061/(asce)ey.1943-7897.0000873

Adar, M., Najih, Y., Gouskir, M., Chebak, A., Mabrouki, M., Bennouna, A., 2020. Three PV plants performance analysis using the principal component analysis method. Energy 207, 118315. https://doi.org/10.1016/j.energy.2020.118315

ASHRAE, 2009. Chapter 1: Psychometrics. 2009 ASHRAE Handb. - Fundam.

ASTM, 2020. Standard Tables for Reference Solar Spectral Irradiances: Direct Normal and Hemispherical on 37° Tilted Surface - ASTM G173.

Balaska, A., Tahri, A., Tahri, F., Stambouli, A.B., 2017. Performance assessment of five different photovoltaic module technologies under outdoor conditions in Algeria. Renew. Energy 107, 53–60. https://doi.org/10.1016/j.renene.2017.01.057

Baloch, A.A.B., Hammat, S., Figgis, B., Alharbi, F.H., Tabet, N., 2020. In-field characterization of key performance parameters for bifacial photovoltaic installation in a desert climate. Renew. Energy 159, 50–63. https://doi.org/10.1016/j.renene.2020.05.174

Benhammane, M., 2019. Développement d'un modèle opérationnel de puissance pour systèmes photovoltaïques à concentration (CPV). UNIVERSITE DE CORSE-PASCAL PAOLI, France.

Benhammane, M., Notton, G., Pichenot, G., Voarino, P., Ouvrard, D., 2021. Overview of electrical power models for concentrated photovoltaic systems and development of a new operational model with easily accessible inputs. Renew. Sustain. Energy Rev. 135. https://doi.org/10.1016/j.rser.2020.110221

Bërdufi, I., Berberi, P., Mitrushi, D., Muda, V., Topçiu, D., Buzra, U., 2016. The performance of a grid connected photovoltaic system Part I: Durisch and Evans energetic models. AIP Conf. Proc. 1722, 10–14. https://doi.org/10.1063/1.4944282

Bianchini, A., Gambuti, M., Pellegrini, M., Saccani, C., 2016. Performance analysis and economic assessment of different photovoltaic technologies based on experimental measurements. Renew. Energy 85, 1–11. https://doi.org/10.1016/j.renene.2015.06.017

Boutana, N., Mellit, A., Lughi, V., Massi Pavan, A., 2017. Assessment of implicit and explicit models for different photovoltaic modules technologies. Energy 122, 128–143.

Burnham, L., Riley, D., Walker, B., Pearce, J.M., 2019. Performance of Bifacial Photovoltaic Modules on a Dual-Axis Tracker in a High-Latitude, High-Albedo Environment. Conf. Rec. IEEE Photovolt. Spec. Conf. 1320–1327. https://doi.org/10.1109/PVSC40753.2019.8980964

Canadian Solar, 2020a. CS6K Poly-Crystalline PV module. Prod. Datasheet.

Canadian Solar, 2020b. HIGH POWER BIFACIAL POLY PERC MODULE 390 W ~ 415 W. Prod. Datasheet.

Canadian Solar, 2020c. HIGH POWER BIFACIAL MONO PERC MODULE 435 W ~ 460 W. Prod. Datasheet.

Cannizzaro, S., Piazza, M.C., Luna, M., Vitale, G., 2014a. Generalized classification of PV modules by simplified single-diode models, in: IEEE International Symposium on Industrial Electronics. pp. 2266–2273.

Cannizzaro, S., Piazza, M.C., Luna, M., Vitale, G., 2014b. PVID: An interactive Matlab application for parameter identification of complete and simplified single-diode PV models, in: 2014 IEEE 15th Workshop on Control and Modeling for Power Electronics, COMPEL 2014.

Chatterjee, A., Keyhani, A., Kapoor, D., 2011. Identification of photovoltaic source models. IEEE Trans. Energy Convers. 26, 883–889.

De Soto, W., Klein, S.A., Beckman, W.A., 2006. Improvement and validation of a model for photovoltaic array performance. Sol. Energy 80, 78–88.

Deline, C., Macalpine, S., Marion, B., Toor, F., Asgharzadeh, A., Stein, J.S., 2017. Assessment of Bifacial Photovoltaic Module Power Rating Methodologies—Inside and Out. 2017 IEEE 44th Photovolt. Spec. Conf. PVSC 2017 7, 1–6. https://doi.org/10.1109/PVSC.2017.8366887

Drury, E., Lopez, A., Denholm, P., Margolis, R., 2013. Relative performance of tracking versus fixed tilt photovoltaic systems in the USA. Prog. Photovoltaics Res. Appl. 20, 6–11. https://doi.org/10.1002/pip

Dubois, A.M., Badosa, J., Bourdin, V., Torres Aguilar, M.I., Bonnassieux, Y., 2021. Estimation of the Uncertainty due to Each Step of Simulating the Photovoltaic Conversion under Real Operating Conditions. Int. J. Photoenergy 2021. https://doi.org/10.1155/2021/4228658

Duffie, J.A., Beckman, W.A., 2020. Solar engineering of thermal processes, Design Studies. https://doi.org/10.1016/0142-694x(82)90016-3

Duran, E., Piliougine, M., Sidrach-De-Cardona, M., Galan, J., Andujar, J.M., 2008. Different methods to obtain the I-V curve of PV modules: A review, in: Conference Record of the IEEE Photovoltaic Specialists Conference.

Durisch, W., Bitnar, B., Mayor, J.C., Kiess, H., Lam, K. hang, Close, J., 2007. Efficiency model for photovoltaic modules and demonstration of its application to energy yield estimation. Sol. Energy Mater. Sol. Cells 91, 79–84. https://doi.org/10.1016/j.solmat.2006.05.011

Durisch, W., Struss, O., Robert, K., 2000. Efficiency of Selected Photovoltaic Modules Under Varying Climatic Conditions. World Renew. Energy Congr. VI 779–788. https://doi.org/10.1016/b978-008043865-8/50156-2

Elibol, E., Özmen, Ö.T., Tutkun, N., Köysal, O., 2017. Outdoor performance analysis of different PV panel types. Renew. Sustain. Energy Rev. 67, 651–661. https://doi.org/10.1016/j.rser.2016.09.051

Emery, K., 2016. Photovoltaic Calibrations at the National Renewable Energy Laboratory and Uncertainty Analysis Following the ISO 17025 Guidelines.

Faggianelli, G.A., Haurant, P., Rodler, A., Poggi, P., 2015. An outdoor platform for PV ageing studies: Electrical parameters extraction from IV curves, in: ISES Solar World Congress 2015, Conference Proceedings. pp. 409–418.

Femia, N., Petrone, G., Spagnuolo, G., Vitelli, M., 2017. Power Electronics and Control Techniques for Maximum Energy Harvesting in Photovoltaic Systems, Power Electronics and Control Techniques for Maximum Energy Harvesting in Photovoltaic Systems. Taylor & Francis, USA. https://doi.org/10.1201/b14303

Galarnyk, M., 2023. Understanding Boxplots [WWW Document]. kdnuggets.com. URL https://www.kdnuggets.com/2019/11/understanding-boxplots.html (accessed 5.10.23).

Gostein, M., Pelaez, S.A., Deline, C., Habte, A., Hansen, C.W., Marion, B., Newmiller, J., Sengupta, M., Stein, J.S., Suez, I., 2021. Measuring Irradiance for Bifacial PV Systems. Conf. Rec. IEEE Photovolt. Spec. Conf. 896–903. https://doi.org/10.1109/PVSC43889.2021.9518601

Gu, W., Li, S., Liu, X., Chen, Z., Zhang, X., Ma, T., 2021. Experimental investigation of the bifacial photovoltaic module under real conditions. Renew. Energy 173, 1111–1122. https://doi.org/10.1016/j.renene.2020.12.024

Gu, W., Ma, T., Ahmed, S., Zhang, Y., Peng, J., 2020. A comprehensive review and outlook of bifacial photovoltaic (bPV) technology. Energy Convers. Manag. 223, 113283.

https://doi.org/10.1016/j.enconman.2020.113283
Guenounou, A., Malek, A., Aillerie, M., 2016. Comparative performance of PV panels of different technologies over one year of exposure: Application to a coastal Mediterranean region of Algeria. Energy Convers. Manag. 114, 356–363. https://doi.org/10.1016/j.enconman.2016.02.044
Gueymard, C., 1995. A Simple Model of the Atmospheric Radiative Transfer of Sunshine: Algorithms and performance assessment. Florida Sol. Energy Cent.
Hamou, S., Zine, S., Abdellah, R., 2014. Efficiency of PV module under real working conditions. Energy Procedia 50, 553–558. https://doi.org/10.1016/j.egypro.2014.06.067
Hayibo, K.S., Petsiuk, A., Mayville, P., Brown, L., Pearce, J.M., 2022. Monofacial vs bifacial solar photovoltaic systems in snowy environments. Renew. Energy 193, 657–668. https://doi.org/10.1016/j.renene.2022.05.050
Hejri, M., Mokhtari, H., 2017. On the Comprehensive Parametrization of the Photovoltaic (PV) Cells and Modules. IEEE J. Photovoltaics 7, 250–258.
HeliosLite, 2019. HL39 PV Tracker Technical Datasheet HL39 PV Tracker. HeliosLIte Prod. Datasheet.
Hosseini, S., Taheri, S., Farzaneh, M., Taheri, H., Narimani, M., 2018. Determination of Photovoltaic Characteristics in Real Field Conditions. IEEE J. Photovoltaics 8, 572–580.
IEC, 2021a. Photovoltaic devices – Part 1-2: Measurement of current-voltage characteristics of bifacial photovoltaic (PV) devices. Int. Electrotech. Comm.
IEC, 2021b. Photovoltaic systems – Power conversion equipment performance – Energy evaluation method. IEC 63156.
IEC, 2019. Photovoltaic systems – Power conditioners – Procedure for measuring efficiency. IEC 61683 2019, 268.
IEC, 2016. IEC TS 61724-3: Photovoltaic system performance – Part 3: Energy evaluation method. Int. Electrotech. Comm.
IEC, 2011. Photovoltaic devices – Part 5: Determination of the equivalent cell temperature (ECT) of photovoltaic (PV) devices by the open-circuit method. IEC-60904-5.
IEC, 2009. Procedures for temperature and irradiance corrections to measured I-V characteristics. IEC-60891.
IEC, 2003. Photovoltaic devices – Part 1: Measurement of photovoltaic current-voltage characteristics. IEC-60904-1.
International Electrotechnical Comission, 2021. Photovoltaic system performance. IEC-61724.
Iqbal, M., 2012. An Introduction To Solar Radiation, Academic Press. Elsevier Science, UK.
Jordan, D.C., Deline, C., Kurtz, S.R., Kimball, G.M., Anderson, M., 2018. Robust PV Degradation Methodology and Application. IEEE J. Photovoltaics 8, 525–531. https://doi.org/10.1109/JPHOTOV.2017.2779779
Kalogirou, S., 2017. McEvoy's Handbook of Photovoltaics, Third Edition - Fundamentals and Applications.
Kasten, F., Young, A.T., 1989. Revised optical air mass tables and approximation formula. Appl. Opt. 28, 4735–4738.
Katz, M.H., 2006. Multivariable analysis: A practical guide for clinicians, second edition, Multivariable Analysis: A Practical Guide for Clinicians. https://doi.org/10.1017/CBO9780511811692
Kenny, R.P., Garcia Menendez, E., Lopez-Garcia, J., Haile, B., 2018. Characterizing the operating conditions of bifacial modules. AIP Conf. Proc. 1999. https://doi.org/10.1063/1.5049253
King, D.L., 2008. Photovoltaic module and array performance characterization methods for all system operating conditions 347, 347–368. https://doi.org/10.1063/1.52852
King, D.L., Boyson, W.E., Kratochvil, J.A., 2004. Photovoltaic array performance model. Sandia Rep. No. 2004-3535 8, 1–19. https://doi.org/10.2172/919131
Kipp&Zonen, 2021. Solar Irradiance Monitoring in Solar Energy Projects. https//www.kippzonen.com/, Prod. Cat. acessed June 21, 2021.
Kipp & Zonen, 2018. Kipp & Zonen Sun Tracker Selection Guide Sun Tracker Specification Comparison.
Kopecek, R., Libal, J., 2021. Bifacial photovoltaics 2021: Status, opportunities and challenges. Energies 14. https://doi.org/10.3390/en14082076

Kopecek, R., Libal, J., 2018. Towards large-scale deployment of bifacial photovoltaics. Nat. Energy 3, 443–446. https://doi.org/10.1038/s41560-018-0178-0

Krauter, S., Preiss, A., 2009. Comparison of module temperature measurement methods, in: Conference Record of the IEEE Photovoltaic Specialists Conference. https://doi.org/10.1109/PVSC.2009.5411669

Labouret, A., Villoz, M., 2010. Solar photovoltaic energy, Physics Today. https://doi.org/10.1063/1.2995731

Lappalainen, K., Manganiello, P., Piliougine, M., Spagnuolo, G., Valkealahti, S., 2020. Virtual Sensing of Photovoltaic Module Operating Parameters. IEEE J. Photovoltaics 10, 852–862.

LDK, 2018. LDK-240 mono-crystalline PV module.

Li, B., Karin, T., Meyers, B.E., Chen, X., Jordan, D.C., Hansen, C.W., King, B.H., Deceglie, M.G., Jain, A., 2023. Determining circuit model parameters from operation data for PV system degradation analysis: PVPRO. Sol. Energy 254, 168–181. https://doi.org/10.1016/j.solener.2023.03.011

Liang, T.S., Pravettoni, M., Deline, C., Stein, J.S., Kopecek, R., Singh, J.P., Luo, W., Wang, Y., Aberle, A.G., Khoo, Y.S., 2019. A review of crystalline silicon bifacial photovoltaic performance characterisation and simulation. Energy Environ. Sci. 12, 116–148. https://doi.org/10.1039/c8ee02184h

Libby, C., Kurtz, S., Coley, S., 2015. Field testing of flat-plate and concentrator photovoltaic systems at the Solar Technology Acceleration Center. 2015 IEEE 42nd Photovolt. Spec. Conf. PVSC 2015. https://doi.org/10.1109/PVSC.2015.7356001

Lindig, S., Moser, D., Curran, A.J., Rath, K., Khalilnejad, A., French, R.H., Herz, M., Müller, B., Makrides, G., Georghiou, G., Livera, A., Richter, M., Ascencio-Vásquez, J., van Iseghem, M., Meftah, M., Jordan, D., Deline, C., van Sark, W., Stein, J.S., Theristis, M., Meyers, B., Baumgartner, F., Luo, W., 2021. International collaboration framework for the calculation of performance loss rates: Data quality, benchmarks, and trends (towards a uniform methodology). Prog. Photovoltaics Res. Appl. 29, 573–602. https://doi.org/10.1002/pip.3397

Lineykin, S., Averbukh, M., Kuperman, A., 2014. An improved approach to extract the single-diode equivalent circuit parameters of a photovoltaic cell/panel. Renew. Sustain. Energy Rev. 30, 282–289.

Livera, A., Theristis, M., Koumpli, E., Makrides, G., Stein, J.S., Georghioul, G.E., 2020. GUIDELINES FOR ENSURING DATA QUALITY FOR PHOTOVOLTAIC SYSTEM PERFORMANCE.

Luo, W., Khoo, Y.S., Hacke, P., Jordan, D., Zhao, L., Ramakrishna, S., Aberle, A.G., Reindl, T., 2019. Analysis of the Long-Term Performance Degradation of Crystalline Silicon Photovoltaic Modules in Tropical Climates. IEEE J. Photovoltaics 9, 266–271. https://doi.org/10.1109/JPHOTOV.2018.2877007

Luque, A., Hegedus, S., 2011. Handbook of Photovoltaic Science and Engineering, Handbook of Photovoltaic Science and Engineering. https://doi.org/10.1002/9780470974704

Macêdo, W.N., Zilles, R., 2006. Operational Results of Grid-Connected Photovoltaic System With Different Inverter's Sizing Factors (ISF). Prog. Photovoltaics Res. Appl. 15, 337–352. https://doi.org/10.1002/pip

Marquis, A., Gostein, M., King, B.H., 2022. Validation of In-Situ I-V Measurement Unit for PV System Monitoring Applications 0291–0294. https://doi.org/10.1109/pvsc48317.2022.9938898

Mavromatakis, F., Kavoussanaki, E., Vignola, F., Franghiadakis, Y., 2014. Measuring and estimating the temperature of photovoltaic modules. Sol. Energy. https://doi.org/10.1016/j.solener.2014.10.009

Menicucci, D.F., 1985. PVFORM - A NEW APPROACH TO PHOTOVOLTAIC SYSTEM PERFORMANCE MODELLING., in: Conference Record of the IEEE Photovoltaic Specialists Conference.

Muehleisen, W., Loeschnig, J., Feichtner, M., Burgers, A.R., Bende, E.E., Zamini, S., Yerasimou, Y., Kosel, J., Hirschl, C., Georghiou, G.E., 2021. Energy yield measurement of an elevated PV system on a white flat roof and a performance comparison of monofacial and bifacial modules. Renew. Energy 170, 613–619. https://doi.org/10.1016/j.renene.2021.02.015

Myers, D.R., Gueymard, C.A., 2004. Description and availability of the SMARTS spectral model for photovoltaic applications. Org. Photovoltaics V 5520, 56. https://doi.org/10.1117/12.555943

Notton, G., Diaf, S., 2016. Available solar energy for flat-plate solar collectors mounted on a fixed or tracking structure. Int. J. Green Energy 13, 181–190. https://doi.org/10.1080/15435075.2014.937866

Notton, G., Lazarov, V., Stoyanov, L., 2010. Optimal sizing of a grid-connected PV system for various PV module technologies and inclinations, inverter efficiency characteristics and locations. Renew. Energy 35, 541–554. https://doi.org/10.1016/j.renene.2009.07.013

Nour-eddine, I. omar, Lahcen, B., Fahd, O.H., Amin, B., Aziz, O., 2020. Outdoor performance analysis of different PV technologies under hot semi-arid climate. Energy Reports 6, 36–48. https://doi.org/10.1016/j.egyr.2020.08.023

Øgaard, M.B., Riise, H.N., Haug, H., Sartori, S., Selj, J.H., 2020. Photovoltaic system monitoring for high latitude locations. Sol. Energy 207, 1045–1054. https://doi.org/10.1016/j.solener.2020.07.043

Paudyal, B.R., Imenes, A.G., 2021. Investigation of temperature coefficients of PV modules through field measured data. Sol. Energy 224, 425–439. https://doi.org/10.1016/j.solener.2021.06.013

Pérez-Higueras, P., Fernández, E.F., 2015. High Concentrator Photovoltaics: Fundamentals, Engineering and Power Plants, Springer.

Petrone, G., Ramos-Paja, C.A., Spagnuolo, G., 2017. Photovoltaic Sources Modeling, Photovoltaic Sources Modeling. Wiley, U.K. https://doi.org/10.1002/9781118755877

Photovoltaik, I., 2020. ISET Sensor. Prod. Man.

Piazza, M.C. Di, Luna, M., Petrone, G., Spagnuolo, G., 2017. Translation of the Single-Diode PV Model Parameters Identified by Using Explicit Formulas. IEEE J. Photovoltaics 7, 1009–1016.

Piazza, M.C., Luna, M., Petrone, G., Spagnuolo, G., 2015. About the identification of the single-diode model parameters of high-fill-factor photovoltaic modules, in: 5th International Conference on Clean Electrical Power: Renewable Energy Resources Impact, ICCEP 2015. pp. 85–91.

Piazza, M.C., Vitale, G., 2017. Photovoltaic Sources. Springer, U.K. https://doi.org/10.2174/97816080528511120101

Piliougine, M., Guejia-Burbano, R.A., Petrone, G., Sánchez-Pacheco, F.J., Mora-López, L., Sidrach-de-Cardona, M., 2021. Parameters extraction of single diode model for degraded photovoltaic modules. Renew. Energy 164, 674–686.

Quiroz, J.E., Stein, J.S., Carmignani, C.K., Gillispie, K., 2015. In-situ module-level I-V tracers for novel PV monitoring. 2015 IEEE 42nd Photovolt. Spec. Conf. PVSC 2015. https://doi.org/10.1109/PVSC.2015.7355608

Rampinelli, G.A., Krenzinger, A., Chenlo Romero, F., 2014. Mathematical models for efficiency of inverters used in grid connected photovoltaic systems. Renew. Sustain. Energy Rev. 34, 578–587. https://doi.org/10.1016/j.rser.2014.03.047

Rao Golive, Y., Kottantharayil, A., Shiradkar, N., 2022. Improving the accuracy of temperature coefficient measurement of a PV module by accounting for the transient temperature difference between cell and backsheet. Sol. Energy 237, 203–212. https://doi.org/10.1016/j.solener.2022.03.049

Razongles, G., Sicot, L., Joanny, M., Gerritsen, E., Lefillastre, P., Schroder, S., Lay, P., 2016. Bifacial Photovoltaic Modules: Measurement Challenges. Energy Procedia 92, 188–198. https://doi.org/10.1016/j.egypro.2016.07.056

Reise, C., Müller, B., IEA, 2018. Uncertainties in PV System Yield Predictions and Assessments, International Energy Agency.

Rodrigo, P., Fernández, E.F., Almonacid, F., Pérez-Higueras, P.J., 2014. Review of methods for the calculation of cell temperature in high concentration photovoltaic modules for electrical characterization. Renew. Sustain. Energy Rev. 38, 478–488. https://doi.org/10.1016/j.rser.2014.06.008

Rodrigues Neto, J.A., Torres, P.F., Teles, M.B., Pinho, J.T., Galhardo, M.A.B., Macêdo, W.N., 2020. Performance evaluation of a grid-connected photovoltaic system by comparing its theoretical model to experimental data. Proc. ISES Sol. World Congr. 2019 IEA SHC Int. Conf. Sol. Heat. Cool. Build. Ind. 2019 1061–1070. https://doi.org/10.18086/swc.2019.19.09

Rodríguez-Gallegos, C.D., Liu, H., Gandhi, O., Singh, J.P., Krishnamurthy, V., Kumar, A., Stein, J.S., Wang,

S., Li, L., Reindl, T., Peters, I.M., 2020. Global Techno-Economic Performance of Bifacial and Tracking Photovoltaic Systems. Joule 4, 1514–1541. https://doi.org/10.1016/j.joule.2020.05.005

Salis, E., Pavanello, D., Trentadue, G., Müllejans, H., 2018. Uncertainty budget assessment of temperature coefficient measurements performed via intra-laboratory comparison between various facilities for PV device calibration. Sol. Energy 170, 293–300. https://doi.org/10.1016/j.solener.2018.04.062

Seapan, M., Hishikawa, Y., Yoshita, M., Okajima, K., 2020. Temperature and irradiance dependences of the current and voltage at maximum power of crystalline silicon PV devices. Sol. Energy 204, 459–465. https://doi.org/10.1016/j.solener.2020.05.019

Sera, D., Teodorescu, R., Rodriguez, P., 2007. PV panel model based on datasheet values, in: IEEE International Symposium on Industrial Electronics. pp. 2392–2396.

Singh, J.P., Aberle, A.G., Walsh, T.M., 2014. Electrical characterization method for bifacial photovoltaic modules. Sol. Energy Mater. Sol. Cells 127, 136–142. https://doi.org/10.1016/j.solmat.2014.04.017

Spertino, F., Ahmad, J., Ciocia, A., Di Leo, P., Murtaza, A.F., Chiaberge, M., 2015. Capacitor charging method for I-V curve tracer and MPPT in photovoltaic systems. Sol. Energy 119, 461–473.

Stein, J.S., Riley, D., Lave, M., Hansen, C., Deline, C., Toor, F., 2018. Outdoor Field Performance from Bifacial Photovoltaic Modules and Systems 3184–3189. https://doi.org/10.1109/pvsc.2017.8366042

Tan, R.H.G., Tai, P.L.J., Mok, V.H., 2013. Solar irradiance estimation based on photovoltaic module short circuit current measurement. 2013 IEEE Int. Conf. Smart Instrumentation, Meas. Appl.

Tina, G.M., Bontempo Scavo, F., Merlo, L., Bizzarri, F., 2021. Comparative analysis of monofacial and bifacial photovoltaic modules for floating power plants. Appl. Energy 281, 116084. https://doi.org/10.1016/j.apenergy.2020.116084

Toreti Scarabelot, L., Arns Rampinelli, G., Rambo, C.R., 2021. Overirradiance effect on the electrical performance of photovoltaic systems of different inverter sizing factors. Sol. Energy 225, 561–568. https://doi.org/10.1016/j.solener.2021.07.055

Tossa, A.K., Soro, Y.M., Thiaw, L., Azoumah, Y., Sicot, L., Yamegueu, D., Lishou, C., Coulibaly, Y., Razongles, G., 2016. Energy performance of different silicon photovoltaic technologies under hot and harsh climate. Energy 103, 261–270. https://doi.org/10.1016/j.energy.2016.02.133

Trina Solar, 2019. Half-Cell Dual Glass 60 Layout Module 60 Layout - Monocrystalline Bifacial Module. Prod. Datasheet.

Visa, I., Burduhos, B., Neagoe, M., Moldovan, M., Duta, A., 2016. Comparative analysis of the infield response of five types of photovoltaic modules. Renew. Energy 95, 178–190. https://doi.org/10.1016/j.renene.2016.04.003

Wang, H.X., Muñoz-García, M.A., Moreda, G.P., Alonso-García, M.C., 2018. Optimum inverter sizing of grid-connected photovoltaic systems based on energetic and economic considerations. Renew. Energy 118, 709–717. https://doi.org/10.1016/j.renene.2017.11.063

Wenham, S.R., Green, M.A., Watt, M.E., Corkish, R., 2013. Applied photovoltaics, second edition, Applied Photovoltaics, Second Edition. https://doi.org/10.4324/9781849770491

Yastrebova, N. V, 2007. High-efficiency multi-junction solar cells : Current status and future potential. Cent. Res. Photonics, Univ. Ottawa.

Ye, M., Wang, X., Xu, Y., 2009. Parameter extraction of solar cells using particle swarm optimization. J. Appl. Phys. 105, 1–8.

Zarkov, Z., Stoyanov, L., Kanchev, H., Milenov, V., Lazarov, V., 2016. Study of photovoltaic systems' performances with different module types. Mater. Sci. Forum 856, 279–284. https://doi.org/10.4028/www.scientific.net/MSF.856.279

Zhao, Y., Lehman, B., Ball, R., Mosesian, J., De Palma, J.F., 2013. Outlier detection rules for fault detection in solar photovoltaic arrays. Conf. Proc. - IEEE Appl. Power Electron. Conf. Expo. - APEC 2913–2920. https://doi.org/10.1109/APEC.2013.6520712

Ziegel, E.R., 2002. Applied Multivariate Data Analysis. Technometrics 44, 407–407. https://doi.org/10.1198/tech.2002.s92

APPENDIX A

APPENDIX A: VALIDATION FOR THE METHOD INTRODUCED IN SECTION 3.7.1

A.1 Experimental resource: SPR-327 and TE-245 PV modules

The dataset considered in this validation study was experimentally obtained from the DURASOL project, located at the SPE Laboratory UMR CNRS 6134, at University of Corsica, in France. The DURASOL was a multi-site project, aimed at supporting studies on PV module ageing, under different climates (Faggianelli et al. 2015). The dataset consists of electric measurements (I-V curves) of two different PV modules, along with solar irradiance and module temperature measurements. The measurements were carried out by tracing I-V curves of the modules, with 100 points each, obtained in about 1 second. The data collection covered almost 16 months, and the curves of each module were measured in 5-minutes interval. The irradiance measurements were carried out using a Kipp & Zonen CMP10 pyranometer, installed close to the modules and at the same inclination and orientation. At the back of each of the PV modules, PT100 sensors (RTD) were installed to measure their temperature. The experimental PV system is illustrated in Fig. A-1.

(a) (b)

Figure A-1: (a) Modules under test at the DURASOL site at Corsica University and (b) the I-V curve measurement hardware and operator interface

Two monocrystalline modules were considered in this study. Their manufacturers and models are Tenesol TE-245 and Sunpower SPR-327. Relevant datasheet parameters are presented in Table A-1. It is worth recalling that datasheet specifications referring to electrical parameters under STC are not required. This way, the modeling is based only on experimental information, providing a reliable way to predict the behavior of those particular modules, which present different characteristics. It is worth mentioning that on PV module datasheets, α and β are usually provided in %/°C, however, in Eqs. (3.3) and (3.4), they must be entered in °C^{-1}. Thus, in Table A-1, the format has been converted to °C^{-1}. The coefficients α and β for the two models of module are relatively different, thus it is a good opportunity to test the method on two different conditions.

Table A-1: Datasheet information of the two modules under study

Module	Number of Cells	α (°C^{-1})	β (°C^{-1})	γ (°C^{-1})
TE-245	60	0.00056	-0.0035	-0.0043
SPR-327	96	0.0004	-0.0027	-0.0036

A.2 Influence of the selected A and B curves on translation error

The selection of the curves A and B is crucial for determining the performance of the translation method according to the target irradiance and temperature levels. In this section, four combinations of A and B curves are studied, aiming to compare the errors produced in each case and for each irradiance range, considering that curve A is translated to G levels from 200 to 1000 W/m² and different T_c.

Case 1: curve A under 1000 W/m², curve B under 700 W/m²: the parameters referring to curves A and B of Case 1 are presented in Table A-2.

Table A-2: Data referring to the reference curves of SPR-327: Case 1

G (W/m²)	T_c (°C)	V_{oc} (V)	I_{sc} (A)	V_{mp} (V)	I_{mp} (A)	P_{mp} (W)
1000	56.0	59.16	6.22	48.29	5.73	276.71
701	45.0	60.15	4.38	49.98	4.07	203.41

By applying the procedure introduced in section 3.7.1, the three parameters of Eq. (3.4) were computed and resulted in a = 0.0407, R_S = 0.6991 Ω and k = 0.0092 Ω/K. Also, $V_{oc,c}$ = 58.31 V and $P_{mp,c}$ = 197.96 W.

Using Eqs. (3.3) and (3.4) with the calculated parameters, curve A was translated to different conditions, ranging from 200 to 1000 W/m² and 25 to 56 °C. It is worth mentioning that in the data selected as reference for this section, each irradiance level has a different T_c associated to it. The temperature for each irradiance level is presented along with the irradiance levels in Figs. A-2 to A-5, in the horizontal axes. Concerning Case 1, the errors on each computed parameter, taking the measurements contained within the dataset as reference, are illustrated in Fig. A-2. In this figure, it is shown that the translations present error equal to zero for the point under 1000 W/m² and 56 °C, except for the P_{mp}, since it is adjusted using curve B. Thus, the P_{mp} presents error equal to zero for case G = 700 W/m². In Fig. A-2, the errors on V_{oc} and V_{mp} steadily increase as the irradiance decreases, since the adjustment has been made using curves under high levels of G.

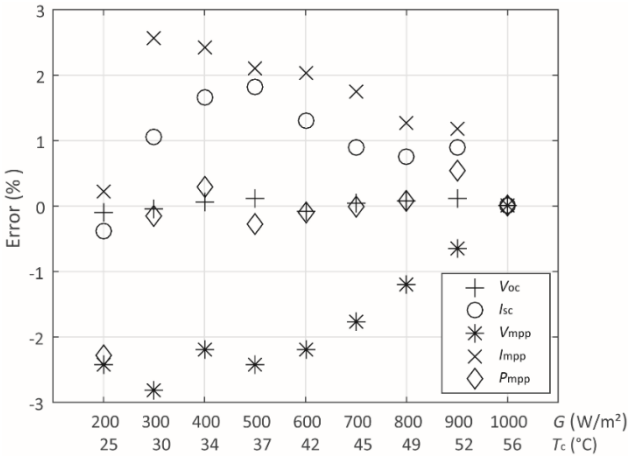

Figure A-2: Percent errors on translated parameters, Case 1

Case 2: curve A under 900 W/m²; curve B under 600 W/m²: application of the data in Table A-3 to the proposed parameter calculation procedure leads to a = 0.0460, R_S = 0.5050 Ω and k = 0.0103 Ω/K. Also, $V_{oc,c}$ = 58.50 V and $P_{mp,c}$ = 171.82 W.

Table A-3: Data referring to the reference curves of SPR-327: Case 2

G (W/m²)	T_c (°C)	V_{oc} (V)	I_{sc} (A)	V_{mp} (V)	I_{mp} (A)	P_{mp} (W)
900	52.0	59.63	5.64	48.98	5.21	255.19
600	42.1	60.18	3.76	50.31	3.49	175.58

The errors are presented in Fig. A-3, and show lower magnitudes compared to Case 1.

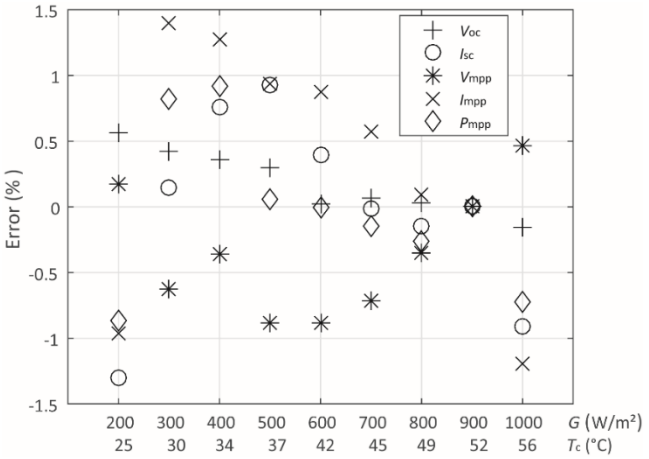

Figure A-3: Percent errors on translated parameters, Case 2

Case 3: curve A under 800 W/m²; curve B under 500 W/m²: in Case 3, the parameters of Eq. (3.4) were computed as a = 0.0414, R_S = 0.4310 Ω and k = 0.0132 Ω/K, using the data in Table A-4 whereas $V_{oc,c}$ = 58.66 V and $P_{mp,c}$ = 145.29 W.

Table A-4: Data referring to the reference curves of SPR-327: Case 3

G (W/m²)	T_c (°C)	V_{oc} (V)	I_{sc} (A)	V_{mp} (V)	I_{mp} (A)	P_{mp} (W)
800	49.1	59.81	5.00	49.40	4.63	228.72
501	37.0	60.7	3.15	51.04	2.91	148.53

This case, with errors illustrated in Fig. A-4, presents essentially the same error magnitudes as in Case 2. Slightly higher error levels can be observed referring to the higher irradiance levels, and this is due to the selection of the reference curves, which refer to lower irradiance levels, as in comparison to the previous cases.

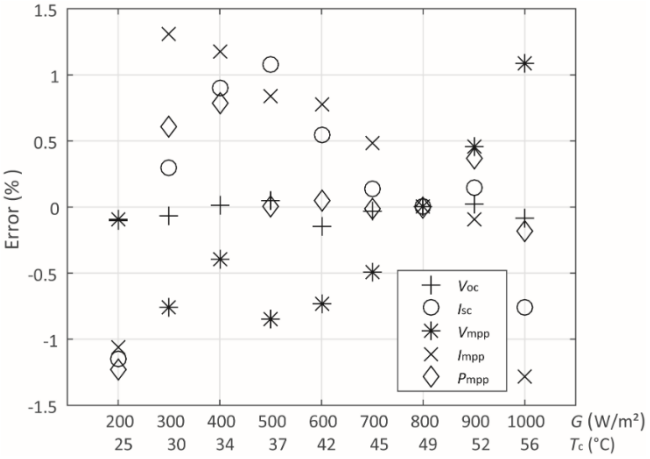

Figure A-4: Percent errors on translated parameters, Case 3

Case 4: curve A under 700 W/m²; curve B under 400 W/m²: case 4 refers to data in Table A-5, with $V_{oc,c}$ = 58.71 V and $P_{mp,c}$ = 115.67 W. The computed parameters of Eq. (3.4) are a = 0.0412, R_S = 0.5483 Ω and k = 0.0167 Ω/K.

Table A-5: Data referring to the reference curves of SPR-327: Case 4

G (W/m²)	T_c (°C)	V_{oc} (V)	I_{sc} (A)	V_{mp} (V)	I_{mp} (A)	P_{mp} (W)
701	45.0	60.15	4.38	49.98	4.07	203.41
402	33.9	60.65	2.52	51.49	2.34	120.49

The errors, per irradiance range, are illustrated in Fig. A-5. It shows error magnitudes similar to Case 1, however, in the opposite direction in terms of irradiance. It should be noted that in cases 1 and 4, the vertical scale of the graphics has changed in a 2:1 ratio, in comparison with cases 2 and 3. Therefore, Figs. A-2 to A-5 indicate that selecting curves A and B positioned close to the center of the irradiance range produces smaller overall errors. This criterion should be followed when selecting curves A and B. However, it should be recalled that the errors on all parameters reach error equal to zero under G_a and $T_{c,a}$, whereas the P_{mp} and V_{mp} present error very close to zero under G_b and $T_{c,b}$.

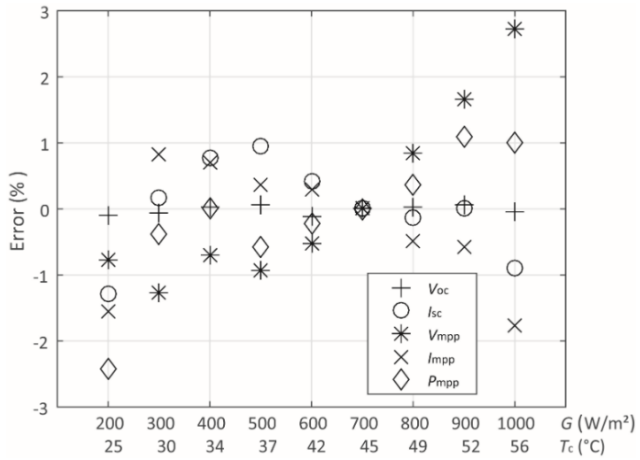

Figure A-5: Percent errors on translated parameters, Case 4

A.3 Using experimental data to determine $V_{oc,c}$ and $P_{mp,c}$

The prospect of using experimental data under G_b and $T_{c,a}$ to determine $V_{oc,c}$ and $P_{mp,c}$, thus avoiding their calculation via Eqs. (3.5) and (3.9), is presented in this section. Although measuring a third curve, under specified levels of G and T_c might initially be considered a disadvantage, it could be a way to apply the method proposed in this work for cases where α and β or γ are not known. Revisiting the four cases considered in Section A-2, the calculated values of $V_{oc,c}$ and $P_{mp,c}$, under the respective levels of G_b and $T_{c,a}$ were compared with actual measured data under the same irradiance and temperature condition, in each case. This leads to the construction of Table A-6, where the percent difference referring to the measured $V_{oc,c}$ and $P_{mp,c}$ is also presented, taking the calculated values of $V_{oc,c}$ and $P_{mp,c}$ (via Eqs. (3.5) and (3.9)) as reference.

Table A-6: Measured values of $V_{oc,c}$ and $P_{mp,c}$ and percent errors relative to the calculations by means of Eqs. (3.5) and (3.9)

G_b (W/m²)	$T_{c,a}$ (°C)	$V_{oc,c}$ (V)	$P_{mp,c}$ (W)	Error on $V_{oc,c}$ (%)	Error on $P_{mp,c}$ (%)
704	56	58.15	194.99	-0.28	-1.50
597	52	58.45	168.84	-0.08	-1.73
501	49	58.57	142.84	-0.16	-1.69
400	45	58.72	114.70	0.00	-0.84

The most significant errors reported in Table A-6 refer to the parameter $P_{mp,c}$, which is used to compute R_S. Given the differences found, a study of the influence on the calculation of a, R_S and k was carried out. Such parameters, referring to each of the four cases, were recalculated using the measured $V_{oc,c}$ and $P_{mp,c}$. They are organized in Table A-7, along with the respective percent error, taking the calculations made via Eqs. (3.5) and (3.9) as reference.

Table A-7: Values of a, R_S and k computed using measured values of $V_{oc,c}$ and $P_{mp,c}$

Case	Parameter values			Error on parameters (%)		
	a	R_S (Ω)	k (Ω/K)	a	R_S	k
1	0.0481	0.7380	0.0112	18.18	5.56	21.74
2	0.0488	0.4666	0.0143	6.09	-7.60	38.83
3	0.0443	0.6374	0.0052	7.00	47.89	-60.61
4	0.0428	0.3415	0.0327	3.88	-37.72	95.81

Although the errors in Table A-7 reach relatively high levels, especially for parameter k – with almost 2:1 ratio relative to Case 4 – the practical effect on the translation error, considering cases 1 to 4, is quite smaller. In fact, the highest differences in translation error are within 1%, when compared to the results presented in Section A-2.

A more general analysis regarding the influence of the selection of curves A and B, as well as the use of computed or measured values for $V_{oc,c}$ and $P_{mp,c}$ is presented in the following section.

A.4 Application of the adjusted equations for current and voltage translation: various G and T_c levels

This part of the experimental application refers to the whole dataset of the two modules. The combinations of curves A and B come from the cases presented in Section A-2, since the parameters of Eq. (3.4) were already calculated. In addition to that, the parameters of Eq. (3.4), calculated using measured $V_{oc,c}$ and $P_{mp,c}$ (Section A-3), were also considered in the present section, as a final comparison resource.

For each of the combinations of A and B curves in Section A-2, the translation method with Eqs. (3.3) and (3.4) was applied to translate curve A to the recorded values of G and T_c within the datasets, therefore allowing to obtain computed values of V_{oc}, I_{sc}, V_{mp}, I_{mp} and P_{mp}. These values were then compared with the measured values contained in the dataset, and the errors for each curve were calculated. These errors are expressed, for the whole dataset, as nRMSE, for each case and parameter. The errors, considering the SPR 327 module, are presented in Fig. A-6, and were calculated based on 18634 I-V curves.

As mentioned in Section A-3, the prospect of using a third measured I-V curve for the adjustment of the coefficients of Eq. (3.4) has been considered in this work. Thus, advancing on this subject, the parameters from Table A-7 were used with Eqs. (3.3) and (3.4) to translate the A curves to the conditions recorded in the dataset. The results, specified in terms of nRMSE, are also presented in Fig. A-6, for the V_{oc}, V_{mp} and P_{mp} parameters, since these are affected by Eq. (3.4). In turn, the nRMSE referring to I_{sc} and I_{mp} do not change, since they refer to Eq. (3.3), which is kept constant. For I_{sc}, nRMSE = 2.42%; for I_{mp}, nRMSE = 2.96%.

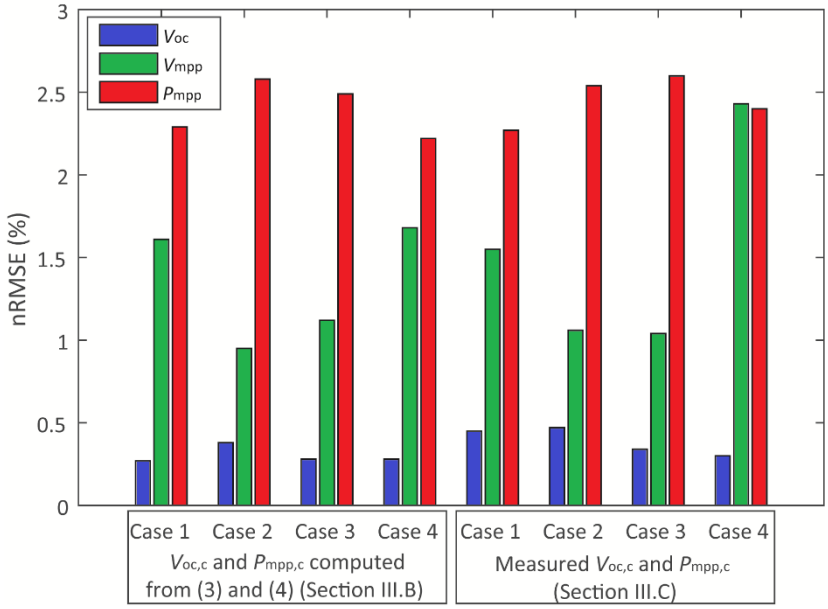

Figure A-6: nRMSE (%) values referring to the translated parameters: SPR-327 module

In Section A-3, it was stated that despite the difference between a, R_S and k, in comparison with the results from Section A-2, the resulting translations per irradiance range did not show expressive difference. Similarly, the nRMSE values in Fig. A-6, do not show significant deviations between the right and left portions, despite the expressive difference between the parameters employed in Eq. (3.4), in each phase of the study. Therefore, one important conclusion is that regardless of the selected A and B curves, the use of computed or measured $V_{oc,c}$ and $P_{mp,c}$ did not produce significant difference in the overall translation error, as illustrated in Fig. A-6.

As for the Tenesol TE-245 module, the same analysis as that of SPR-327 was carried out. The data regarding curves A and B, in each of the four considered cases, are organized in Table A-8.

Table A-8: Data for curves A and B of TE-245 module, for each of the four cases studied

Case	G (W/m²)	T_c (°C)	V_{oc} (V)	I_{sc} (A)	V_{mp} (V)	I_{mp} (A)	P_{mp} (W)
1	999	55	33.29	8.29	25.95	7.64	198.26
	800	47	33.85	6.63	26.98	6.16	166.20
2	899	51	33.59	7.48	26.47	6.93	183.44
	699	43	34.14	5.87	27.51	5.45	149.93
3	800	47	33.85	6.63	26.98	6.16	166.20
	599	40	34.16	4.89	27.79	4.64	128.95
4	699	43	34.14	5.87	27.51	5.45	149.93
	498	36	34.32	4.06	28.22	3.90	110.06

By applying the procedure presented in this section, the adjusted parameters of Eq. (3.4) were computed and are presented in Table A-9, which also shows the $V_{oc,c}$ and $P_{mp,c}$ values.

Table A-9: Parameters of Eq. (3.4), computed using the new procedure

Case	a	$V_{oc,c}$ (V)	R_S (Ω)	$P_{mp,c}$ (W)	k (Ω/K)
1	0.0264	33.09	0.4111	161.30	0.0025
2	0.0240	33.38	0.4956	145.65	0.0031
3	0.0365	33.49	0.4055	125.68	0.0037
4	0.0424	33.64	0.3228	107.27	0.0045

The application of Eqs. (3.3) and (3.4), after the adjustment of a, R_S and k, allows the translation of the A curves (in each case) to the condition of each of the 14559 curves within the Tenesol TE-245 module dataset. The resulting errors, in terms of nRMSE are organized in Table A-10, for each case and for each parameter.

Table A-10: nRMSE for each parameter and case, for TE-245 module

Case	nRMSE on parameters (%)				
	V_{oc}	I_{sc}	V_{mp}	I_{mp}	P_{mp}
1	0.65	2.44	1.47	2.99	2.69
2	0.67	2.44	2.17	2.99	2.48
3	0.65	2.44	1.22	2.99	2.68
4	0.71	2.44	0.76	2.99	2.91

The error levels presented in Table A-10 show that the proposed method performed similarly to the cases regarding the SPR-327 module, with nRMSE levels within 3% for P_{mp}.

The analysis carried out in this section allows assessing the performance of the proposed method concerning the use of different sources to adjust the parameters for the voltage equation of the 2nd procedure of IEC-60891, which is Eq. (3.4). Moreover, the application was directed to two large datasets. Thus, this analysis provides a view of how the method would perform in real applications, when multiple irradiance and cell temperature levels are combined.

A.5 Remarks for Section 3.7.1

A simplified approach for calculating the parameters of IEC-60891 (2nd procedure) has been presented in Section 3.7.1. The method does not require the reference curves to be obtained by means of a solar simulator, by advanced modeling methods, or from extensive experimental measurements, since only two I-V curves are required. These two curves have to differ both in terms of G and T_c, and they can be obtained experimentally under outdoor conditions. For the determination of the parameter a, the explicit solution of Eq. (3.6) has been proposed, which avoids the trial-and-error procedure originally proposed in the international standard. For the validation, the proposed method has been employed to predict the behavior of two PV modules, using large experimental datasets as reference, in three steps.

First, a study of the influence of the reference curves A and B on the translation results was carried out in Section A-2. When selecting curve A with high G, it has been found that all translated parameters presented absolute error of less than 3%, even when translating to low G levels. However,

even better performance was observed when the selected reference curves covered points closer to the center of the irradiance range considered, for example, between 900 and 500 W/m². In these cases, the maximum absolute errors were within 1.5 %, considering all the translated parameters and an irradiance range from 200 to 1000 W/m², referring to temperatures in the range of 30 – 56 °C.

Following, the prospect of employing measured data – instead of calculated from Eqs. (3.5) and (3.9) – to determine the parameters $V_{oc,c}$ and $P_{mp,c}$ was considered in Section A-3. It was found that although the parameters of Eq. (3.4) present relatively high difference when compared to the results from Section A-2, the resulting translation errors do not present relevant deviation.

Finally, in Section A-5, for two PV modules, thousands of translations were considered, presenting nRMSE levels below 3% for all the parameters referring to the two modules, making the proposed method suitable for a number of applications, due to its simplicity and straightforward application.

APPENDIX B

APPENDIX B: VALIDATION FOR THE METHOD INTRODUCED IN SECTION 3.7.2

B.1 Experimental resource: TE-245 and AC-250 PV modules

The experimental application was carried out using the experimental data recorded at the University of Corsica, during the DURASOL program (Faggianelli et al., 2015).

The two PV modules used in the present section were manufactured by Tenesol (model TE-245) and by Axitec (model AC-250). Both modules have 60 monocrystalline cells. The temperature coefficients for I_{sc} and V_{oc} are respectively 0.0564 %/°C and -0.348 %/°C for TE-245; 0.04 %/°C and -0.003 %/°C for AC-250.

Curves were measured every 5 minutes, with 100 I-V pairs each. For that, a variable electronic load was employed to change the operating voltage of the PV module, from -0.5 V to 102 % of V_{oc}. In turn, the current-voltage points were measured simultaneously since the measurement system has multiple data acquisition units (model Keysight 34411A), able to measure and record the I-V curves in less than 2 s. Each point of an I-V curve is associated with an irradiance level, measured using a calibrated PV cell at the same inclination and orientation as that of the PV modules. The dataset used in this section includes over 30,000 I-V curves, measured from 2017 to 2018. The data were filtered to exclude curves measured under partial shading conditions. Also, curves with G below 200 W/m² were not considered, given the fact that the SDM presents increased errors under low irradiance levels, as stated by (Petrone et al., 2017).

B.2 Parameter identification outdoors

The present section considers the I-V data rereferring to three different operating conditions outdoors, under which the SDM parameters were identified for the TE-245 and AC-250 modules. The study of different curves obtained outdoors allows studying the effect of G and T_c on the resulting SDM parameters, as well as the influence on the accuracy of the translations.

In Table B-1, the three reference curves for the TE-245 module are expressed in terms of G and T_c and the respective notable points. Data referring to the reference curves for the AC-250 module are organized in Table B-2. For both modules, the STC data obtained from the datasheets is also provided, however, it should be recalled that in this work, STC data was included only to provide a comparison resource in terms of operating condition.

The data in Tables B-1 and B-2 are enough to identify the SDM parameters through the 5-Par and 4-Par methods; however, the PSO method requires all the 200 I-V pairs of each curve, since it is a curve fitting procedure.

Table B-1: Reference curves for TE-245

Case	Condition		I-V curve notable points				
	G (W/m²)	T_c (°C)	V_{oc} (V)	I_{sc} (A)	V_{mp} (V)	I_{mp} (A)	P_{mp} (W)
1	990	60	32.75	8.4	25.41	7.73	196.45
2	798	51	33.25	6.74	26.58	6.2	164.69
3	600	42	33.83	5.04	27.71	4.66	129.1
STC	1000	25	37.4	8.7	29.8	8.3	245

Table B-2: Reference curves for AC-250

Case	Condition		I-V curve notable points				
	G (W/m²)	T_c (°C)	V_{oc} (V)	I_{sc} (A)	V_{mp} (V)	I_{mp} (A)	P_{mp} (W)
1	997	60	33.99	8.40	26.49	7.73	204.84
2	795	50	34.55	6.82	27.41	6.32	173.29
3	595	40	35.46	5.12	28.95	4.79	138.64
STC	1000	25	37.98	8.8	29.68	8.47	250

Tables B-3 and B-4 present the SDM parameters obtained, respectively, for the Tenesol and Axitec modules. The values of R_p referring to the 4-Par identification method are infinite because the SPR parameter is greater than one for the two PV modules.

Table B-3: SDM parameters for TE-245, per case and method

Method	Case	SDM parameters, TE-245				
		a	R_s (Ω)	R_p (Ω)	I_0 (A)	I_{ph} (A)
4-Par	1	1.165	0.293	∞	6.815E-07	8.40
	2	1.327	0.171	∞	2.149E-06	6.74
	3	1.371	0.076	∞	1.307E-06	5.04
	STC	0.8201	0.438	∞	1.026E-12	8.70
5-Par	1	0.8821	0.451	3.947E+03	3.632E-09	8.40
	2	1.038	0.362	2.162E+03	3.308E-08	6.74
	3	1.121	0.290	2.306E+03	4.469E-08	5.04
	STC	0.6744	0.522	1.827E+06	2.071E-15	8.70
PSO	1	1.076	0.315	282.8	1.753E-07	8.41
	2	1.065	0.317	297.6	5.325E-08	6.75
	3	1.060	0.310	546.4	1.526E-08	5.04
	STC	0.816	0.449	7.057E+04	1.053E-12	8.70

Table B-4: SDM parameters for AC-250, per case and method

Method	Case	SDM parameters, AC-250				
		a	R_s (Ω)	R_p (Ω)	I_0 (A)	I_{ph} (A)
4-Par	1	1.2250	0.2807	∞	8.354E-07	8.4
	2	1.2105	0.2939	∞	2.581E-07	6.82
	3	1.1766	0.2681	∞	4.261E-08	5.12
	STC	0.6179	0.6102	∞	4.244E-17	8.80
5-Par	1	0.9353	0.4417	3.54E+03	5.658E-09	8.40
	2	0.9881	0.4446	4.607E+03	5.509E-09	6.82
	3	1.0181	0.4119	8.966E+03	2.351E-09	5.12
	STC	0.5361	0.6601	7.155E+07	9.034E-20	8.80
PSO	1	1.1311	0.3137	391.5	2.220E-07	8.41
	2	1.1695	0.2941	458.8	1.447E-07	6.83
	3	1.0949	0.3076	539.9	1.071E-08	5.13
	STC	0.6198	0.6096	1.827E+08	4.790E-17	8.80

Some parameters present a wide variation according to the modeling approach employed: for example, Tables B-3 and B-4 show significantly higher R_p values for the 5-Par method, compared to the results for R_p provided by the PSO approach.

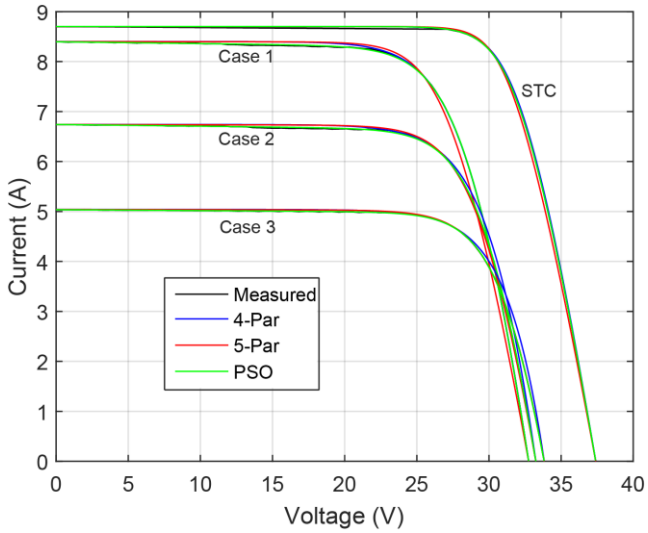

Figure B-1: Curves measured and calculated using Eq. (3.11), for each case and each method; Tenesol TE-245 module

To evaluate the suitability of the nine SDM parameter sets calculated for each module, the measured reference curves were copmpared with curves reproduced using Eq. (3.11) and the data from Tables B-3 and B-4. This way, Fig. A-1 shows the three measured curves for TE-245, and along with each of them, three calculated curves, referring to each of the identification methods. The same applies to Fig. B-2, which shows the curves for AC-250.

In Figs. B-1 and B-2, a good agreement between the measured and calculated curves is observed for all cases and for all methods, despite the fact that for a given condition, each identification method provided significantly different values for parameters R_p and I_0.

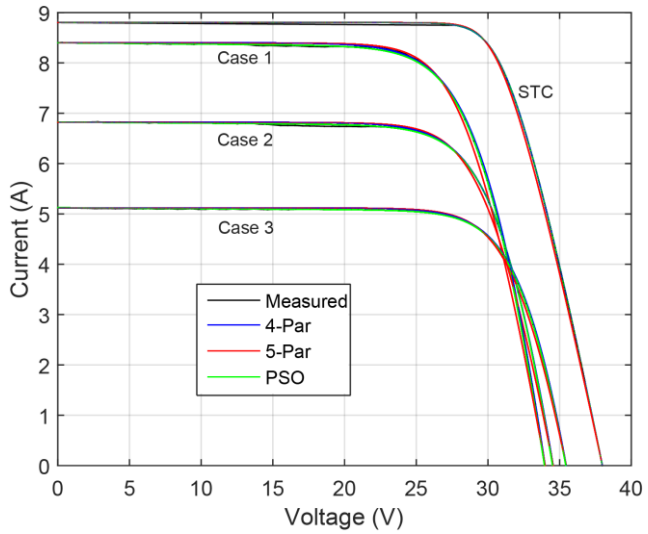

Figure B-2: Curves measured and calculated using Eq. (3.11), for each case and each method; Axitec AC-250 module.

The plots in Figs. B-1 and B-2 show the suitability for all three methods to reproduce the reference curves. Thus, it is possible to proceed to the next phase of the study, which is the introduction of the translation methods to correct the SDM parameters I_{ph} and I_0 according to the operating condition.

B.3 Experimental data

For this validation study, the datasets were obtained using the DURASOL platform, with I-V curves and the respective G and T_c levels recorded for 16 months. Therefore, the datasets contain information referring to all seasons of the year, which allowed considering a wide range of irradiance and cell temperature levels, as illustrated in B-3.

In the dataset for the TE-245 module, the measurements present an average G of 677 W/m², whereas the average T_c is 44 °C. In turn, the dataset referring to the AC-250 module presents average G of 683 W/m², and the average T_c is 47 °C. Over 14,000 measured curves are considered in the nRMSE calculations for the TE-245 module, and over 10,000 for AC-250.

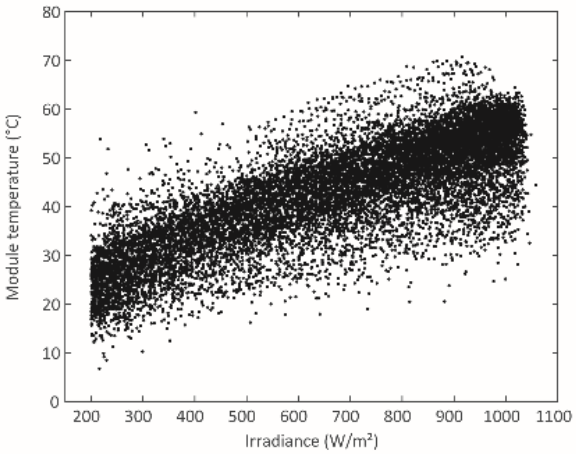

Figure B-3: Irradiance and cell temperature levels referring to the data recorded for TE-245 module

B-4 Performance assessment of the models: predicting the P_{mp}

In this section, the six possible combinations between identification and adjustment methods (4-Par,A / 5-Par,A / PSO,A / 4-Par,B / 5-Par,B / PSO,B) for the SDM parameters were used with the three reference curves previously presented. For both PV modules, the reference curve is denoted by a Case number, following the nomenclature given in Tables B-1 and B-2.

This assessment aims to provide a summarized error quantification when the adjustments are carried out to various arbitrary operating conditions. This was carried out by calculating the nRMSE levels for the predicted P_{mp}, for each combination of methods, and for each of the base curves (Cases). Results including IEC-60891 were also included for comparison. The resulting nRMSE levels are described in Fig B-4 for the TE-245 module and in Fig. B-5 for the AC-250 module. The plots in Figs. B-4 and B-5 were produced by calculating 28 curves (7 methods x 4 cases) for each of the 33,434 measurement points within the datasets of the two modules.

The plots in Figs. B-4 and B-5 show that for Cases 1 and 2, some combinations of SDM methods, particularly 5-Par,A, and PSO,B presented better performance than IEC-60891.

Overall, identification method 5-Par presented better performance when used with adjustment method A.

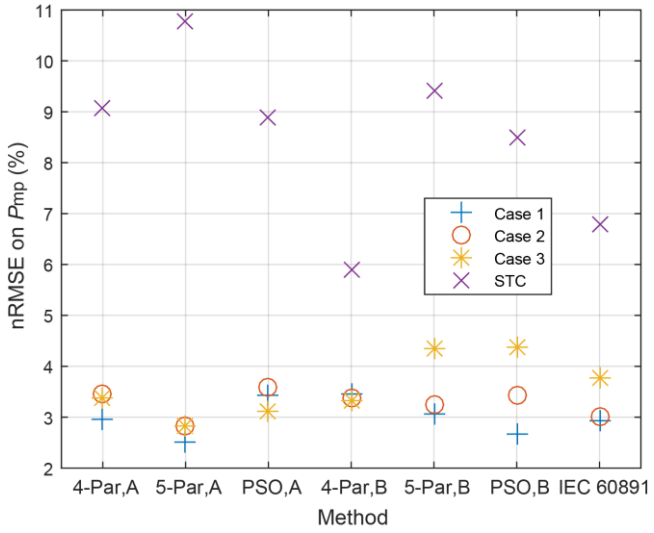

Figure B-4: nRMSE levels on P_{mp}: TE-245

For both PV modules studied – considering only Cases 1 to 3 – smallest nRMSE levels were achieved for Case 1, whereas the worst overall performance was achieved when using the reference curve of Case 4.

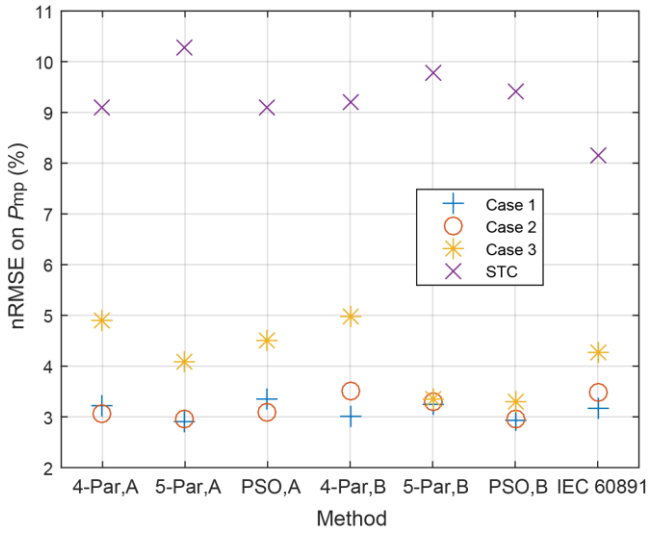

Figure B-5: nRMSE levels on P_{mp}: AC-251

Identification method 4-Par presented similar performance when applied in conjunction with methods A and B, for both PV modules; however, the performance of such combinations was slightly worse than that of IEC 60891. It is worth recalling that 4-Par,A presents a very straightforward application and requires only one reference I-V curve. It is the simplest method combination studied in this work. The methods 5-Par,A, and PSO,A also require only one reference curve. However, the parametric identification is not as simple as that of 4-Par method. The remaining methods (4-Par,B / 5-Par,B / PSO,B / IEC 609891) require two I-V curves; thus, they are subject to measurement error from two different sources.

In Case 1, despite its simplicity, 4-Par,A performed similarly to 5-Par,B – which presents more complex parametric identification and requires two I-V curves. This illustrates that method complexity and inclusion of more experimental data do not necessarily lead to better performance. Further examination of the nRMSE levels illustrated in Figs. B-4 and B-5 leads to the following considerations:

- Using STC data from datasheets as a reference source for parametric identification resulted in far greater nRMSE levels for all 7 methods and both PV modules. The two PV modules have been exposed to sunlight for over five years, therefore their actual ratings under STC are expected to be different from the datasheet ratings. However, it is not possible to determine to what extent the high error levels are due to module aging since it is known that STC datasheet information are not specific for each particular module that is manufactured.

- The calculations using the curve from Case 3 as the reference for parametric identification presented, in general, worse performance compared to Cases 1 and 2.

- Overall, the error differences found among Cases 1 – 2 are not expressive, for the two PV modules. Therefore, the reference curve for the parameter identification could be selected in the range of 800 – 1000 W/m². Tables V and VI focus on the two best-performing Cases (1 and 2), providing numerical values for the nRMSE calculations.

Table B-5 – nRMSE for Cases 1-2 and all methods (TE-245)

Case	TE-245: nRMSE per case and method (%)						
	4-Par,A	5-Par,A	PSO,A	4-Par,B	5-Par,B	PSO,B	IEC 60891
1	2.96	2.50	3.43	3.46	3.06	2.68	2.92
2	3.46	2.83	3.60	3.38	3.24	3.43	3.01
Average	3.21	2.67	3.51	3.42	3.15	3.05	2.96

Table B-6 – nRMSE for Cases 1-2 and all methods (AC-250)

Case	TE-245: nRMSE per case and method (%)						
	4-Par,A	5-Par,A	PSO,A	4-Par,B	5-Par,B	PSO,B	IEC 60891
1	3.21	2.90	3.34	3.00	3.25	2.93	3.18
2	3.06	2.97	3.09	3.51	3.31	2.95	3.49
Average	3.13	2.93	3.22	3.26	3.28	2.94	3.34

When analyzing the methods' performance in Tables B-5 and B-6, for the two PV modules, no regular pattern is found. In other words, it is not possible to determine the best or worst method for the two modules simultaneously. The nRMSE values are not very discrepant when different methods are compared. However, the methods' complexity is not similar, which is an advantage for the simple 4-Par method. For module TE-245, 4-Par,A (the most straightforward approach, requiring one curve only) performed better than PSO,A (more complex parametric identification); and for the AC-250 module, 4-Par,A provided better predictions than PSO,A, 4-Par,B (two curves required), 5-Par,B (the most complex identification method, two curves required), and IEC-60891 (two curves and the temperature coefficient for P_{mp} required).

B.5 The difference between datasheet specification and actual performance

The STC data described in the datasheets was taken as a comparison resource for the reference curves in this work. For TE-245 and AC-250 modules, using datasheet information under STC to model the devices provided significantly higher nRMSE levels than cases using outdoor measured data, as shown by the error metrics in Figs. B-4 and B-5. This behavior was observed even when using IEC 60891. It should be recalled that the modules employed in this work are not new.

To provide a quantitative view of the difference between the datasheet STC data and the actual module performance, IEC 60891 was used to adjust the three reference curves to STC. This allows evaluating the differences using the same operating condition for all cases. Concerning TE-245, the average adjusted P_{mp} is 231 W, whereas the datasheet informs 245 W – a 6 % higher P_{mp}. The average adjusted P_{mp} for AC-250 is 241 W, while the datasheet reports 250 W – a 3.7 % higher value.

B.6 Remarks for Section 3.7.2

Section 3.7.2 explored the extraction of the SDM parameters using outdoor measured data using three different identification methods. The main advantage of outdoor characterization of PV modules is that the actual performance of the PV device is considered without relying on STC data. To avoid the need for identifying the SDM parameters every time the operating condition changes, two parameter adjustment methods were considered. This way, once the SDM parameters were identified, the I-V characteristic could be adjusted to any operating condition specified in terms of G and T_c.

The relevance of the present study lies in evaluating how well particular identification and adjustment methods work together when using outdoor measured data to calculate the SDM parameters. This was done by evaluating the nRMSE levels associated with each combination when predicting the P_{mp} for two PV modules. The approach presented in this work complements the publications of Cannizzaro et al. (2014a), Di Piazza et al. (2015) and Sera et al. (2007). Thus, methods 5-Par and 4-Par, which originally employed datasheet information for the parametric identification, were now applied using outdoor measured data. The PSO method introduced by (Faggianelli et al., 2015) employed outdoor measured data. However, the authors did not use any adjustment methods. The present work thus allowed to assess the performance of PSO,A and PSO,B. Moreover, the present study also complements the studies of Lineykin et al. (2014) and Piazza et al. (2017), due to the application of the two adjustment methods with SDM parameters identified outdoors – again, avoiding the use of datasheet information.

The prospect of using datasheet information in STC was considered in this section for comparison. Using datasheet information to adjust the SDM parameters for modules which are not new provided significantly higher nRMSE levels than the cases using outdoor measurements.

APPENDIX C

APPENDIX C: INVESTIGATION ON THE PRODUCTION OF DATA OUTLIERS

This section presents a visual assessment regarding scatter plots of the efficiency and irradiance, for the four PV arrays considered in this thesis, after the application of the basic and power filters presented in Section 4. The aim is to investigate the reasons for the occurrence of sparse points, allowing to confidently delete records taken under undesired conditions. Such conditions include shading on the PV arrays, strong transient conditions, uneven irradiance reaching the PV arrays and the irradiance sensor, measurement errors and open-circuit operation, particularly at the beginning and end of the daily sunny period. It should be emphasized that the assessments in this Appendix are qualitative. Data filtering based on quantitative metrics is considered in Section 4.

C.1 Polycrystalline array

The general shape of the data points referring to the p-Si array (Fig. 4-2) is quite similar to the bifacial array's data (Fig. 4-4). These two PV arrays hold the similarity in that both are positioned well close to the ground at the sunrise, as shown in Fig. C-1, and thus, subject to partial shading caused by nearby objects. In cases where the PV arrays receive less irradiance than the irradiance sensor, abnormally low efficiency levels are likely to be found.

Figure C-1: The PV tracker position during sunrise

Also, the p-Si and bifacial arrays are held quite high on the PV tracker at the sunset – when the front-side PV sensor is positioned very close to the ground. In such a situation, surprisingly high efficiency levels are likely to be found, due to interferences on the radiation reaching the irradiance sensor. Both situations are undesirable in the context of this study, as it is desirable that uniform radiation levels reach the PV arrays and the irradiance sensors.

Figure C-2: The PV tracker position during sunset

Some high efficiency records are visible in Fig. 4-2; they are highlighted in Fig. C-3.

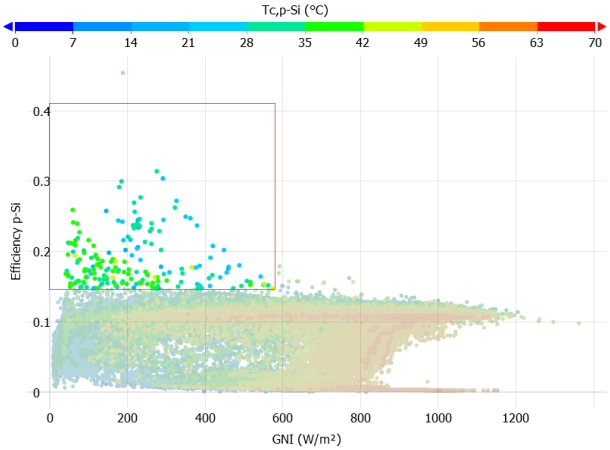

Figure C-3: High efficiency records highlighted.

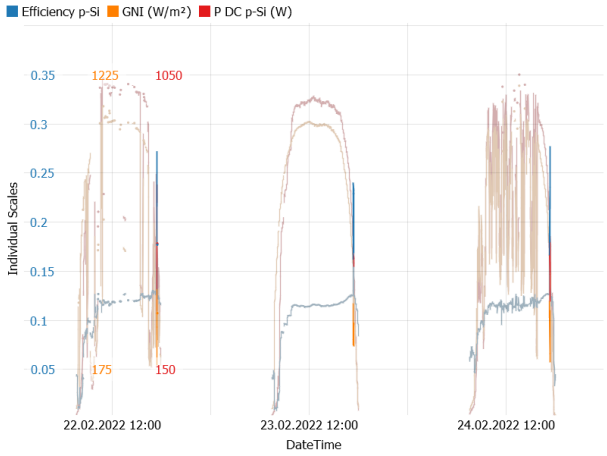

Figure C-4: Time series plot referring to Fig. C-3

In Figs. C-3 and C-4, the selected points are color-bright, whereas the non-selected points are color-faded. This allows easily finding the correspondence between the scatter and time series plots.

From Fig. A-3, it is seen that the unusually high efficiency records selected in Fig. A-4 are produced during sunset. Such an observation is valid for multiple days. To better understand the behavior of the variables involved, a zoom-in is applied and shown in Fig. A-5.

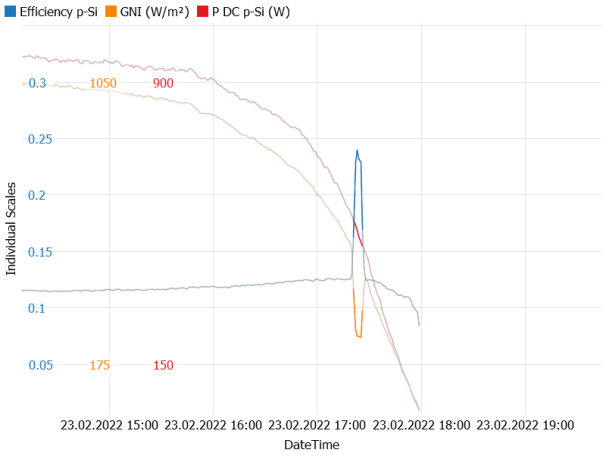

Figure C-5: A portion of Fig. A-4 shown in detail.

Figure C-5 clearly shows that while the DC power decreases steadily as sunset approaches, the irradiance shows an abrupt decrease. As a result, the calculated efficiency presents a sharp increase. After the transient, the GNI eventually resumes the original steady decrease path. As illustrated in Fig. C-2, the front irradiance sensor is kept at a very low position, close to the ground, during the sunset. Given the presence of several other structures and equipment near the tracker area, uneven irradiance between the GNI sensor and the p-Si array is likely to occur, which introduces invalid values for the PV efficiency.

On the other hand, very low efficiency levels for the p-Si array are found in Fig. 4-2, from low to high GNI values. Such records are highlighted in Fig. C-6, in a square-shaped selection.

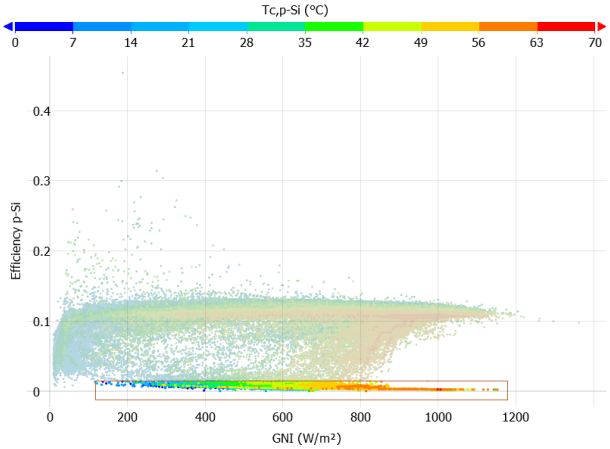

Figure C-6: Selection of low efficiency data records

The corresponding time series plot in Fig. A-7 shows that the points selected in Fig. C-6 refer to the beginning of the day, when the irradiance is increasing sharply. In Fig. C-7, the array's DC current is close to zero for the highlighted points, whereas the voltage is quite high, meaning that the PV array

is not yet operating on the maximum power. The array is actually near the open-circuit condition, where the power is close to zero. The mismatch between the irradiance and current levels is the cause for the low efficiency levels highlighted in Fig. C-6.

Figure C-7: Time series plot referring to Fig. C-6

Figure C-8 shows a portion of Fig. C-7 in detail. The efficiency increases once the current reaches a level in which the inverter's MPPT starts searching the maximum power. This is precisely when the power starts to increase and, eventually, reaches the maximum power point. In Fig. C-8, periodic oscillations are visible on the voltage and current; this is the effect of the MPPT's constant perturbations, seeking the maximum V-I product.

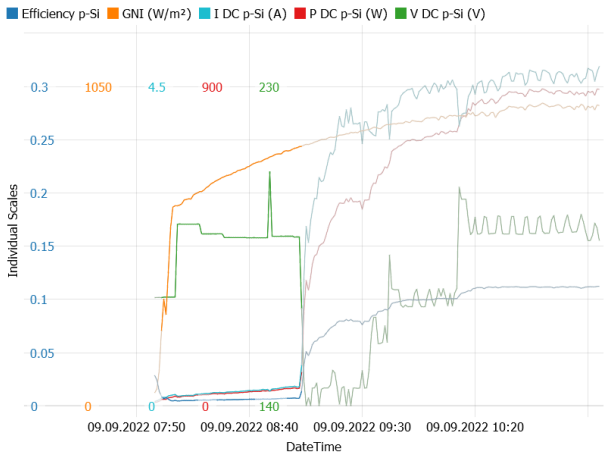

Figure C-8: Zoom-in Fig. C-7

In respect to other low efficiency data points under high GNI, when highlighting points on the region with irradiance above 500 W/m² and low efficiency values (Fig. C-9), the corresponding time series plot (Fig. C-10) shows that such points are related to the morning, that is, the sunrise.

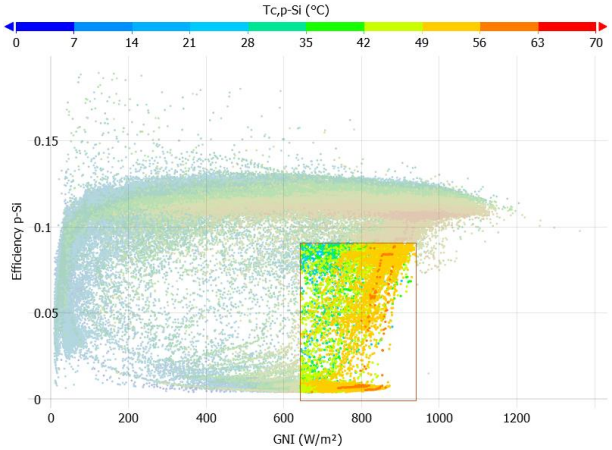

Figure C-9: Selecting low efficiency, high GNI data points.

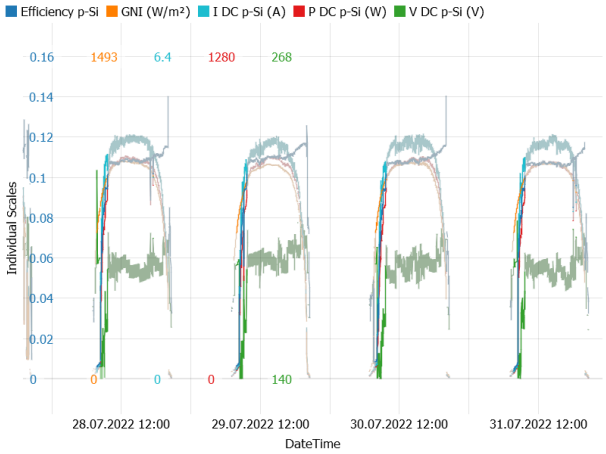

Figure C-10: Time series plot referring to Fig. C-9

When looking at Fig. C-10 in detail, in Fig. C-11, it is observed that although GNI is relatively high, the measured power is low, causing the efficiency to drop. This is similar to the behavior shown in Fig. C-8.

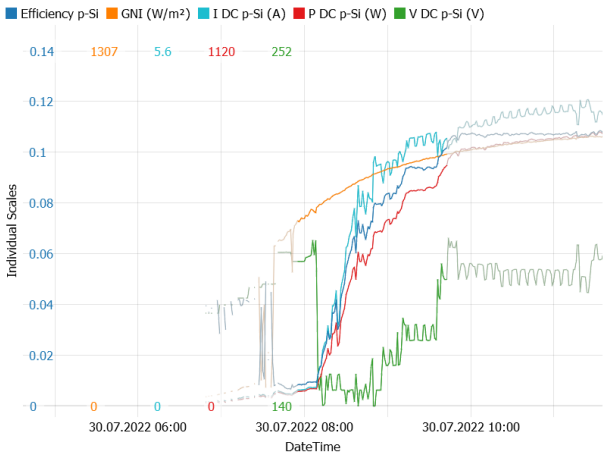

Figure C-11: Curves shown in Fig. C-10, in detail.

The reason for such a behavior is shading affecting the polycrystalline array at the beginning of the day, due to the fact that the polycrystalline array is very close to the ground in the early morning, as illustrated in Fig. C-1. In this situation, the polycrystalline array is shaded by bushes and by cabling structures of the PV tracker. The reason for such a shading caused by cables belonging to the tracker is that the p-Si array presents an area which is slightly above the tracker's rated holding capacity. However, shading caused by the structure cables occurs only in the early mornings.

In fact, when studying the remaining sparse points recorded with relatively low efficiency levels in Fig 4-2, it was found that they also refer to situations where the daily recordings are starting – that is, near the sunrise.

C.2 Monocrystalline array

A few points, highlighted in Fig. C-12, present unusually high efficiency levels.

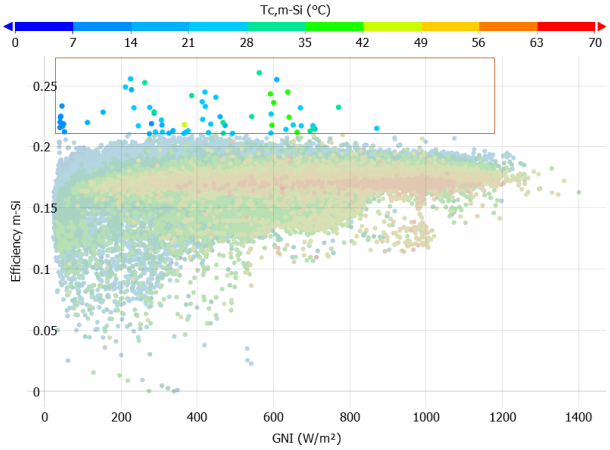

Figure C-12: High efficiency sparse points selection

Such points refer to cases in which the GNI varies widely and quickly, as shown in Fig. C-13.

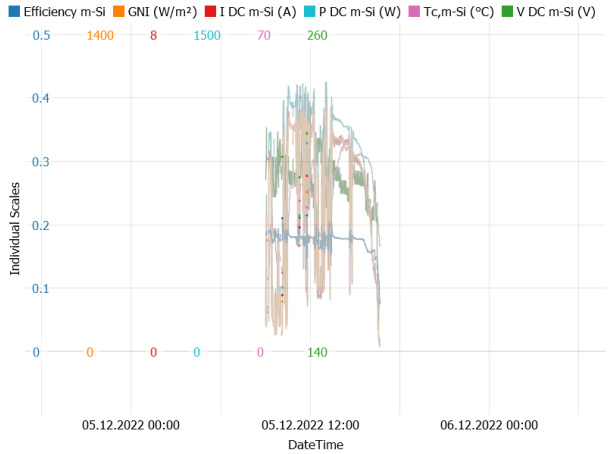

Figure C-13: Time series referring to the scatter plot in Fig. C-12

In some cases, the voltage presented relatively high levels, due to a steady temperature reduction caused by a temporary reduction in the irradiance levels. Then, when the irradiance suddenly increased, the array power reached a relatively high level, due to the previous temperature drop and the fact that the temperature does not rise instantaneously. However, there are not enough

data to strongly support such a hypothesis, given that very few records (around 0.07 %) fall into this category.

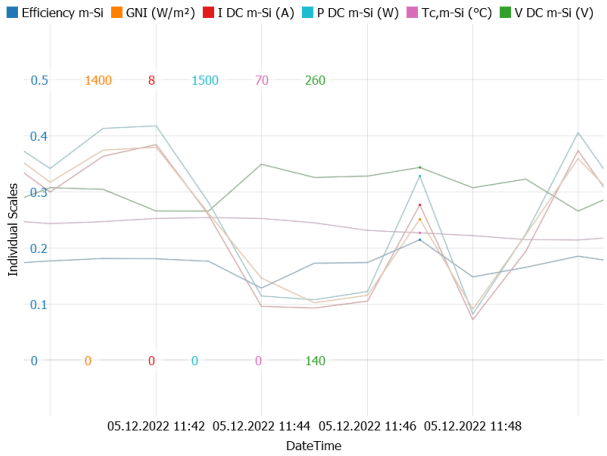

Figure C-14: Time series shown in Fig. C-13, in detail.

Next, low efficiency levels under low irradiance values are considered:

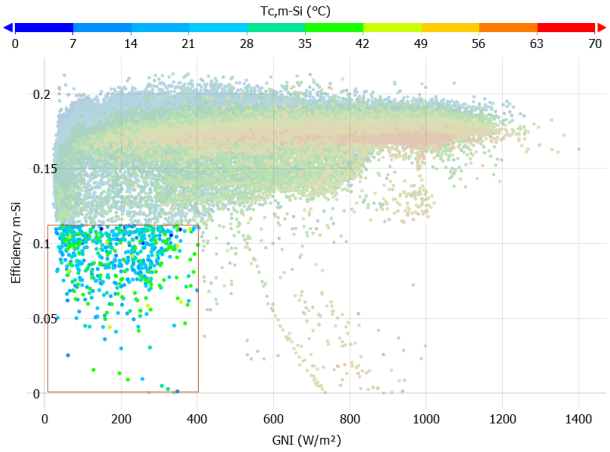

Figure C-15: Selecting low efficiency records under low GNI.

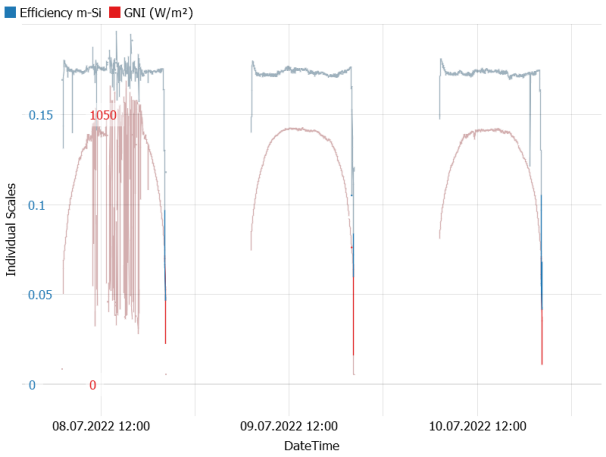

Figure C-16: Time series related to the scatter plot in Fig. C-15

Such points are related to the sunset, as illustrated in Fig. C-16. During this period, the monocrystalline array is at a very low position (Fig. C-2), close to the ground and thus, subject to

shading caused by nearby objects. In addition to that, the GNI sensor is also at a low position, also subject to shading.

The next assessment considers the sparse points below the main efficiency curve.

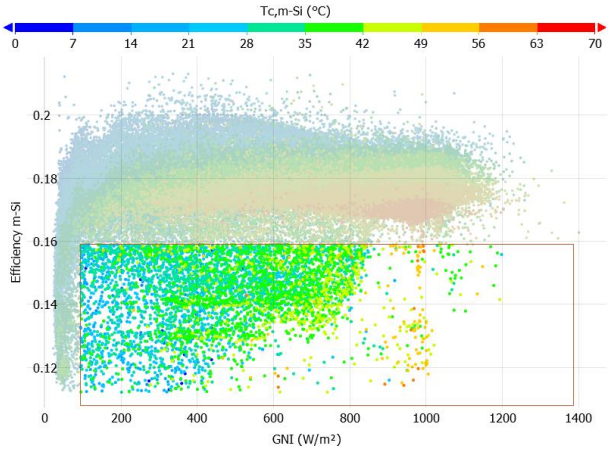

Figure C-17: Selection of sparse points below the main efficiency curve

As in the previous case, such points are related with the sunset. In the time series analysis shown in Fig. C-18, it is evident that the steep decrease in the efficiency is caused by a different rate of decrease of GNI and DC power – with the power decreasing at a rate greater than GNI. The air mass cannot be considered a source for such an effect because the GNI sensor uses a monocrystalline PV cell as a sensor, therefore, the GNI meter and the PV array under study are spectrally matched. This means that spectral effects causing a reduction in power would cause a decrease of the measured GNI levels as well, in a very close proportion, given that the PV sensor and the PV array are always at the same inclination and orientation. Therefore, such a group of points refer to situations in which the PV tracker's vertical position has acted as a source of interference, as in the previous case.

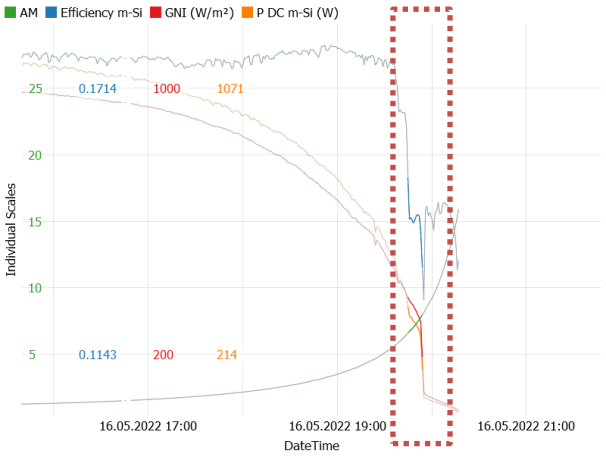

Figure C-18: Time series related to the scatter plot in Fig. C-17

C.3 Bifacial PV array

The efficiency referring to the bifacial array was calculated taking the concept of effective irradiance (G_E, Section 2.2.2) into account, since this way, the irradiance reaching the rear side of the array is considered. Conversely, if only the front-side irradiance was considered, unrealistically high

efficiency levels would be found. An in-depth study regarding the particularities of bifacial modules is presented in Section 5.7.

In the upper portion of the efficiency plot in Fig. 4-4, high efficiency levels are found in the range up to 600 W/m². These points are highlighted in Fig. C-19.

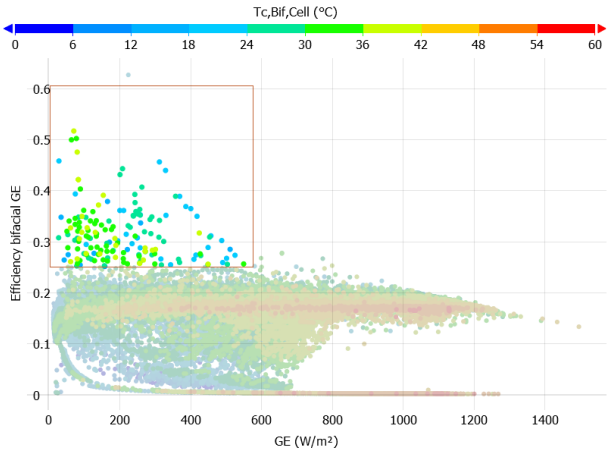

Figure C-19: Selecting high-efficiency sparse data records.

Such records refer to situations at the end of the day, as seen in the time series plot in Fig. C-20, where the points corresponding to the selection in Fig. C-19 are also highlighted.

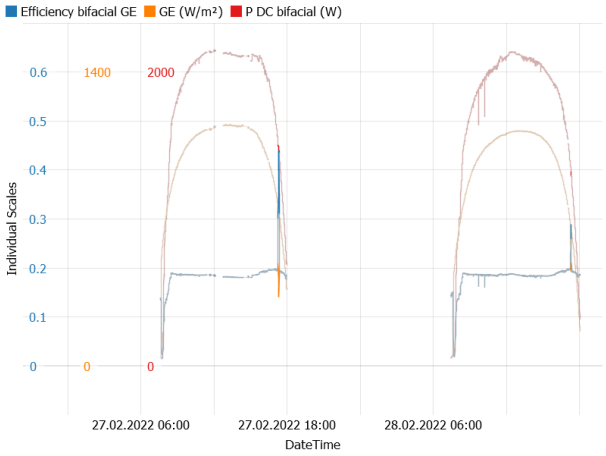

Figure C-20: Time series plot referring to Fig. C-19

Taking a closer look at the time series, it is observed that the high efficiency levels were produced due to an incoherence between the recorded values of power referring to the bifacial array and the G_E. Such a situation happens because the tracker reaches a position in which the front irradiance sensor is positioned well below the bifacial array (Fig. C-2), around 50 cm from the ground, thus the sensor is subject to shading from nearby objects.

In turn, the data selection in Fig. C-21 shows data records close to zero highlighted.

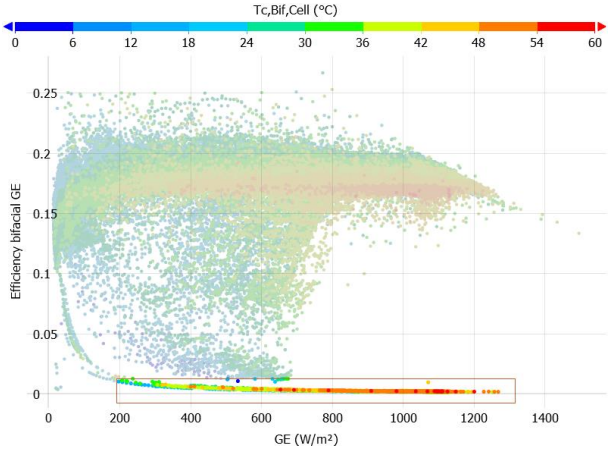

Figure C-21: Selecting data records close to zero efficiency.

Such records refer to a specific day in July, in which power levels were zero, as observed in Fig. C-22. This was likely to be caused by a failure in recording the data from the tracker.

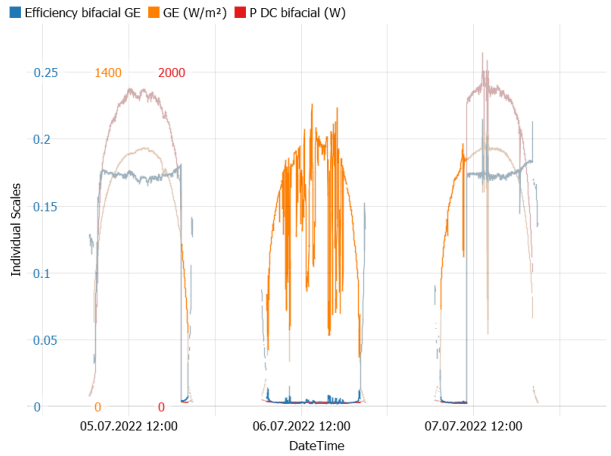

Figure C-22: Time series plot referring to Fig. C-21.

Advancing on the analysis, the sparse low efficiency levels selected in Fig. C-23 refer to cases at the beginning of the day, where the PV array is not yet operating at the MPP, as noticed by the analysis of the respective time series in Fig. C-24.

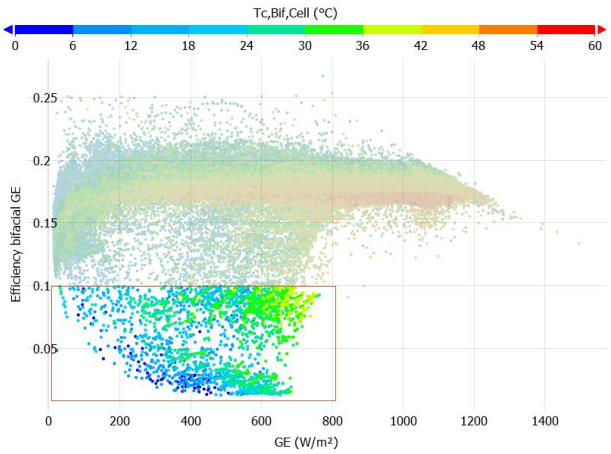

Figure C-23: Selection of low efficiency sparse data records

When analyzing the time series in Fig. C-24, it is found that the PV array voltage recording starts close to the V_{oc} and then steadily decreases while the PV array current rises. This is a common behavior at the beginning of the sunny period, when the PV array is starting to operate along with the inverter's MPPT.

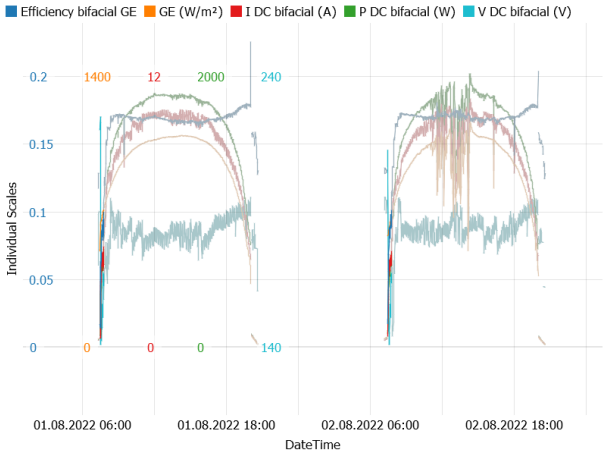

Figure C-24: Time series referring to Fig. C-23

Figure C-25 shows the plots of Fig. C-24 in detail, focusing on the beginning of a day, when the PV array is starting its operation.

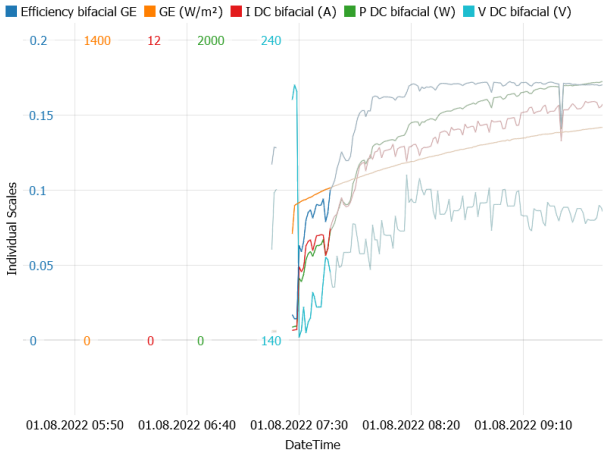

Figure C-25: Zoom-in of Fig. C-24, focusing on the sunrise.

Next, the efficiency of the bifacial array shows a ramp-shaped decrease at the far right-hand side of Fig. C-26.

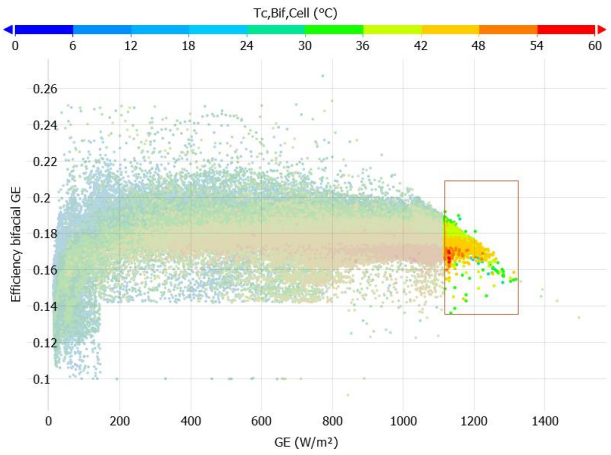

Figure C-26: Selection of data records under high irradiance

By analyzing the respective time series in Fig. C-27, it was found that the points referring to decreasing efficiency at high values of G_E are related with cases where the bifacial array power is unusually high. Such cases are usually related to GNI above 1000 W/m² and GNI_{rear} above 200 W/m². This leads to a situation in which the AC power rating of the inverter is reached. As a result, the inverter's control unit shifts the operating point of both arrays (bifacial and p-Si, for inverter 2) to a region outside the MPP, to keep the output power within 3000 W. The time series plot shows two situations in which the AC power of inverter 2 reached 3000 W; these points refer to the low efficiency cases under high G_E of the previous scatter plot. The data records referring to inverter saturation were removed by using the strategies presented in Section 4.2.

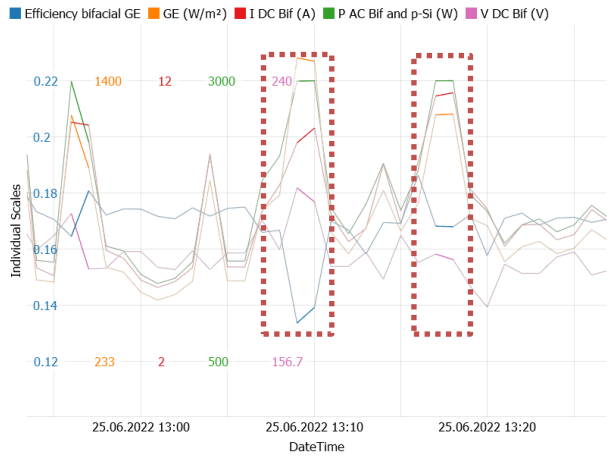

Figure C-27: Time series plot referring to Fig. C-26, showing inverter saturation.

C.4 HCPV array

The HVPC array efficiency is plotted against the BNI, given that such a PV technology only converts the beam irradiance due to the use of Fresnel lenses for the radiation concentration.

The first region to be noted is the group of points showing unusually high efficiency levels. It should be mentioned that, as opposed to the previous cases, the irradiance measurements (BNI) come from another source, the Solys 2 station.

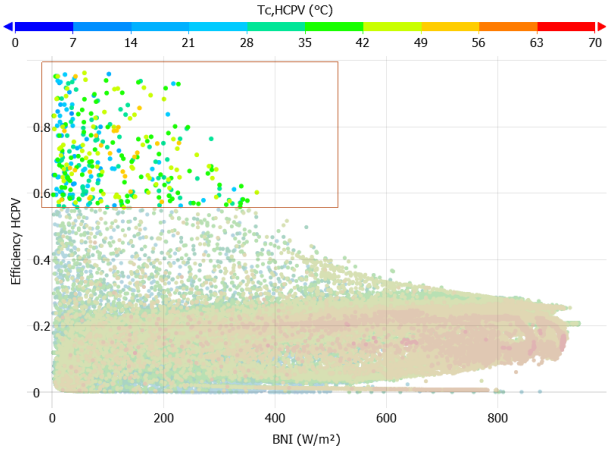

Figure C-28: Selection of high efficiency data records

The points highlighted in Fig. C-28 refer to transient situations, in which the beam irradiance is quickly changing as shown in Fig. C-29. Given that the power measurements are instantaneous (taken every one minute), a possible reason for such an anomality is the Solys 2-measured BNI values resulting from an internally calculated average, therefore causing a short-term difference when compared to the instantaneously measured power values. In fact, in most of the times the HCPV array's power and the BNI agree. The cases originating the highlighted high-efficiency levels are actually produced by isolated – incoherent – records, taken under transient conditions, as seen in the time series plotted in Fig. C-29. It is also noted that, in a clear sky day – such as on 14 November – such points related to unusually high efficiency are not present.

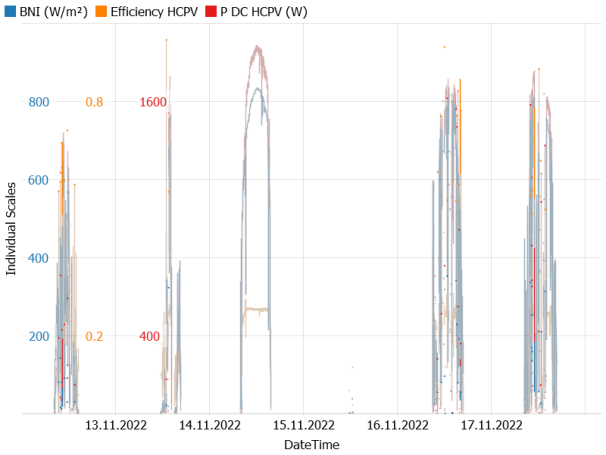

Figure C-29: Time series related to the scatter plot in Fig. C-28

The next step considers the records showing efficiency close to zero, highlighted in Fig. C-30.

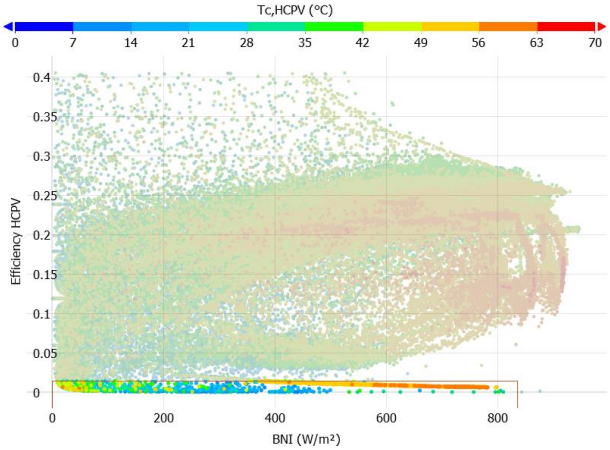

Figure C-30: Selecting data points with close-to-zero efficiency.

The time series analysis in Fig. C-31 reveals that such points refer to the very bottom of the curves, covering cases where the BNI is greater than zero, whereas the HCPV array is not yet supplying power. It should be emphasized that the inverter's MPPT is responsible for positioning the array's operating point at the MPP; however, such a tracking system presents practical limitations to operate, mainly in terms of minimum voltage and current levels for the DC-DC converters to work properly and within an adequate range of conversion efficiency.

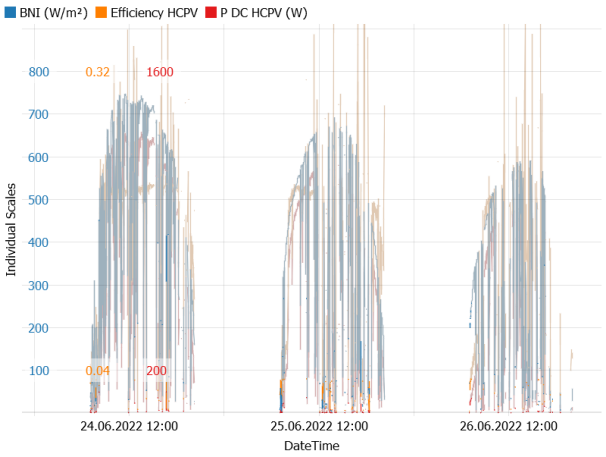

Figure C-31: Time series referring to the scatter plot in Fig. C-30

The attention now turns to the to the sparse distribution above the main curve, as illustrated in Fig. C-32.

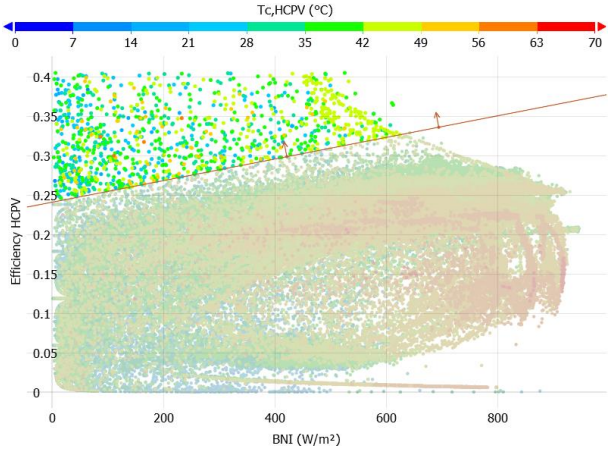

Figure C-32: Selecting sparse high-efficiency data points above the main curve.

These points are related to steep variations of BNI and consequently, DC power. For the reasons mentioned earlier, short-term deviations between the measured BNI and power might produce unrealistic efficiency levels. For instance, unusually high efficiency values might be produced when the tracker's measuring system instantaneously records a relatively high DC power level, while the Solys 2 provides a relatively low BNI level, coming from an internal averaging calculation.

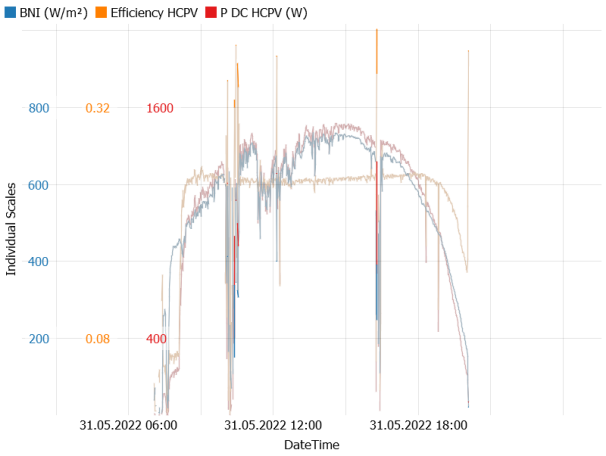

Figure C-33: Time series plot referring to the scatter plot in Fig. C-32

Finally, the sparse points below the main curve are selected, as shown in Fig. C-34.

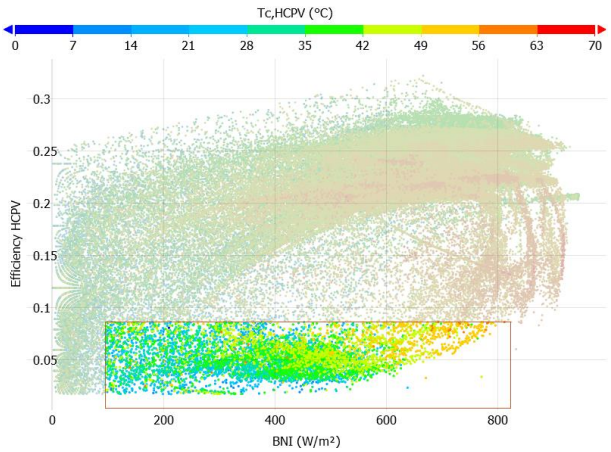

Figure C-34: Selection of low efficiency data points

The records highlighted in Fig. C-34 are related to the HCPV array's start of operation, as seen in Fig. C-35. Once the current level increases, so does the power, and the inverter's MPPT starts seeking the maximum power.

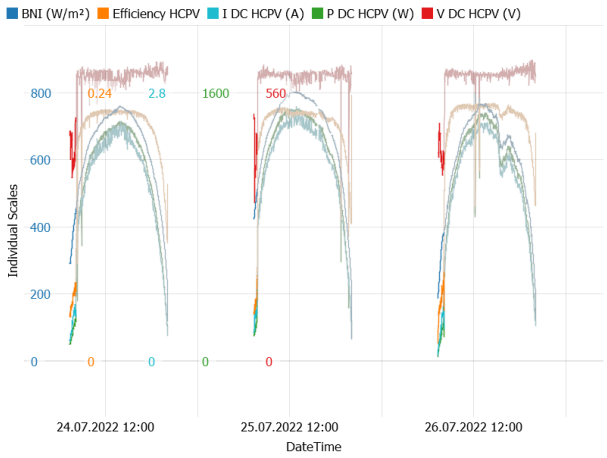

Figure C-35: Time series plot related to the selected points in Fig. C-34

APPENDIX D

APPENDIX D: MULTIVARIATE REGRESSION USED IN SECTION 5.3

Tables D-1 to D-4 present the terms and coefficients for the polynomial multivariate regression performed using the air temperature. In turn, Tables D-5 to D-8 present the models using the measured array temperature. Such models were created aiming to determine the order of relevance of the external parameters, for each PV array, regardless of model complexity and size. The composition of the polynomial terms and the values for the coefficients were automatically set by the Visplore® data visualization application, via RMSE minimization.

Table D-1: Polynomial model for the p-Si array (T_{air})

Terms	Coefficients
GNI	0.906
Temperature air ^2	-0.00913
GNI * AM	0.01726
Wind speed	0.992
GNI * Abs. humidity	-1.295
Temperature air ^2 * BNI	-7.2E-05
Wind speed * BNI	0.00221
GNI * AM * Wind speed	0.003282
GNI * AM * BNI	-1.9E-05
BNI ^2	3.7E-05
AM^2	0.03493
AM^2 * Wind speed	-0.1391
Temperature air ^2 * BNI * AM	3.63E-06
y-intercept	-0.0504

Table D-2: Polynomial model for the m-Si array (T_{air})

Terms	Coefficients
GNI	1.238
Temperature air	-6.42
Temperature air * BNI	0.000785
Wind speed * BNI	-0.0017
BNI	-0.02077
Temperature air * BNI * AM	0.000906
Temperature air * BNI * AM * Normal global clearness index	-0.00189
AM^2 * Temperature air	-0.0037
AM^2 * Temperature air * GNI	-3.1E-05
AM^2 * Temperature air * GNI * Wind speed	-1.9E-05
Wind speed * BNI * AM	0.001969
Temperature air ^2	0.1554
Temperature air ^2 * GNI	-0.00013
Wind speed * Normal global clearness index	5.63
y-intercept	59.5

Table D-3: Polynomial model for the bifacial array (T_{air})

Terms	Coefficients
GNI	1.93
Temperature air	-11.39
Wind speed	1.666
GNI,rear	0.0915
GNI,rear * AM	0.995
Temperature air * BNI	-0.005
AM^2	1.788
GNI,rear * AM * Abs. humidity	-17.99
AM^2 * GNI	0.004005
BNI ^2	4.7E-05
AM	-52.7
Wind speed * BNI	-0.0081
Temperature air * AM	0.858
Abs. humidity ^2	68244
Temperature air ^2	0.1205
GNI * AM	-0.0569
Wind speed * BNI * AM	0.01307
AM^2 * GNI * Wind speed	-0.00024
AM^2 * GNI * BNI * Wind speed	-1.7E-06
y-intercept	223.4

Table D-4: Polynomial model for the HCPV array (T_{air})

Terms	Coefficients
BNI	2.067
Temperature air ^2	0.2618
AM^2	-18.35
Temperature air ^2 * AM	-0.1264
Normal diffuse fraction^2	809
BNI * AM	0.0958
Rel. humidity ^2	0.03604
Abs. humidity ^2	631971
AM^2 * Normal diffuse fraction	-14.01
BNI * Normal diffuse fraction	7.96
AM^2 * Abs. humidity	939
AM^2 * Temperature air	0.4466
BNI * Normal diffuse fraction * Temperature air	-0.1482
BNI * AM * Abs. humidity	-74.8
BNI * AM * Abs. humidity * GNI	0.0758
BNI * Normal diffuse fraction * Temperature air * Rel. humidity	0.000391
BNI * Normal diffuse fraction * GNI	-0.00051
BNI * Normal diffuse fraction * Temperature air * Rel. humidity * GNI	-1.7E-06
BNI * Normal diffuse fraction * GNI * AM	-0.00157
BNI * Normal diffuse fraction * Temperature air * Rel. humidity * AM	0.000518
BNI * AM * Temperature air	0.004976
Normal diffuse fraction^2 * GNI * BNI	0.001281
Normal diffuse fraction^2 * Abs. humidity	-29510
Rel. humidity ^2 * Abs. humidity	-2.388
BNI * Normal diffuse fraction * GNI * Wind speed	-8.7E-06
AM	124.4
AM * Temperature air	1.437
Normal diffuse fraction^2 * GNI * BNI * Temperature air	4.34E-05
Normal diffuse fraction^2 * BNI	-3.145
y-intercept	-826

Table D-5: Polynomial model for the p-Si array (T_c)

Terms	Coefficients
GNI (W/m²)	0.971
Tc,p-Si (°C)^2	-0.01317
Tc,p-Si (°C)^2 * AM	0.003194
Wind speed (m/s)	0.3601
Tc,p-Si (°C)^2 * BNI (W/m²)	-1.6E-05
GNI (W/m²) * AM	0.001661
Tc,p-Si (°C)^2 * AM * GNI (W/m²)	-5.8E-06
AM^2	-0.3454
BNI (W/m²)^2	3.17E-05
GNI (W/m²) * AM * Wind speed (m/s)	0.001694
Tc,p-Si (°C)^2 * BNI (W/m²) * Wind speed (m/s)	-1.2E-06
AM^2 * GNI (W/m²)	0.001284
Tc,p-Si (°C)^2 * GNI (W/m²)	-1.6E-05
Tc,p-Si (°C)	0.2198
y-intercept	-7.56

Table D-6: Polynomial model for the m-Si array (T_c)

Terms	Coefficients
GNI (W/m²)	1.219
Abs. humidity (kgH2O/kgda)	883
Rel. humidity (%)	-0.0548
DNI (W/m²)	0.02837
Tc,m-Si (°C)^2	-0.02628
AM^2	0.529
Abs. humidity (kgH2O/kgda) * BNI (W/m²)	-3.973
Tc,m-Si (°C)^2 * AM	0.01039
Tc,m-Si (°C)^2 * AM * Wind speed (m/s)	-0.0004
Rel. humidity (%) * BNI (W/m²)	0.000964
Abs. humidity (kgH2O/kgda) * BNI (W/m²) * DNI (W/m²)	-0.00554
Rel. humidity (%) * BNI (W/m²) * Wind speed (m/s)	1.91E-05
Tc,m-Si (°C)^2 * AM * GNI (W/m²)	-1.3E-05
GNI (W/m²) * AM	0.00841
AM^2 * Tc,m-Si (°C)	-0.0502
GNI (W/m²) * AM * Abs. humidity (kgH2O/kgda)	-0.4494
Tc,m-Si (°C)^2 * AM * Wind speed (m/s) * DNI (W/m²)	-1.3E-06
Wind speed (m/s)^2	0.3063
GNI (W/m²) * AM * Abs. humidity (kgH2O/kgda) * DNI (W/m²)	-0.00021
y-intercept	-9.19

Table D-7: Polynomial model for the bifacial array (T_c)

Terms	Coefficients
GNI (W/m²)	1.975
Tc,Bif,Cell (°C)^2	-0.1874
Rel. humidity (%)^2	-0.00199
Rel. humidity (%)^2 * GNI,rear (W/m²)	0.000135
GNI (W/m²) * Abs. humidity (kgH2O/kgda)	-13.62
GNI (W/m²) * Abs. humidity (kgH2O/kgda) * AM	1.075
Wind speed (m/s)	2.048
AM * GNI,rear (W/m²)	0.2282
Abs. humidity (kgH2O/kgda)^2	-185213
AM * GNI (W/m²)	-0.01121
GNI,rear (W/m²)^2	-0.00902
GNI (W/m²) * Abs. humidity (kgH2O/kgda) * AM * Normal beam clearness index	-4.545
AM * GNI,rear (W/m²) * Normal beam clearness index	0.3575
Tc,Bif,Cell (°C)^2 * Abs. humidity (kgH2O/kgda)	6.16
Tc,Bif,Cell (°C)	4.912
GNI,rear (W/m²)	2.174
Rel. humidity (%)^2 * AM	-0.00034
Rel. humidity (%)^2 * AM * GNI (W/m²)	-8E-07
y-intercept	-75.1

Table D-8: Polynomial model for the HCPV array (T_c)

Terms	Coefficients
BNI (W/m²)	1.163
Tc,HCPV (°C)^2	-0.3924
AM^2	-9.87
Rel. humidity (%)	17.02
Abs. humidity (kgH2O/kgda)^2	6488628
Tc,HCPV (°C)^2 * AM	-0.02929
GNI (W/m²)^2	-0.00025
GNI (W/m²)^2 * AM	-0.0002
GNI (W/m²)^2 * AM * BNI (W/m²)	1.93E-07
AM^2 * BNI (W/m²)	0.0125
Tc,HCPV (°C)^2 * BNI (W/m²)	0.000156
AM^2 * Abs. humidity (kgH2O/kgda)	-476.5
Abs. humidity (kgH2O/kgda)^2 * AM	-2304772
GNI (W/m²)^2 * Abs. humidity (kgH2O/kgda)	-0.0565
GNI (W/m²)^2 * AM * BNI (W/m²) * Abs. humidity (kgH2O/kgda)	2.77E-05
AM^2 * BNI (W/m²) * Rel. humidity (%)	-0.00043
Tc,HCPV (°C)^2 * AM * Rel. humidity (%)	-0.0004
AM^2 * Abs. humidity (kgH2O/kgda) * Tc,HCPV (°C)	51
Abs. humidity (kgH2O/kgda)^2 * AM * Rel. humidity (%)	18629
GNI (W/m²)^2 * Abs. humidity (kgH2O/kgda) * Rel. humidity (%)	0.000675
GNI (W/m²)^2 * BNI (W/m²)	2.73E-07
GNI (W/m²)	1.059
Rel. humidity (%) * Abs. humidity (kgH2O/kgda)	-1925
Tc,HCPV (°C)	30.93
AM	79.4
GNI (W/m²)^2 * BNI (W/m²) * Rel. humidity (%)	-6.7E-09
AM * Abs. humidity (kgH2O/kgda)	10957
Rel. humidity (%) * Abs. humidity (kgH2O/kgda) * GNI (W/m²)	0.3691
Abs. humidity (kgH2O/kgda)^2 * GNI (W/m²)	-3042
y-intercept	-1323